

Mathematical Modelling of MHD Waves in Asymmetric Waveguides with Applications to Solar Physics



The
University
Of
Sheffield.

Noemi Kinga Zsamberger
School of Mathematics and Statistics
University of Sheffield

Under supervision of
Professor Robertus Erdelyi

This thesis is submitted for the degree of Doctor of Philosophy

2022

Declaration of Authorship

I hereby confirm that the work submitted is my own, except where specific reference is made to the work of others. The contribution of other authors to this work has been explicitly indicated. The contents of this dissertation are original and have not been submitted for consideration for any other degree or qualification.

Abstract

The highly structured, complex and coupled system constituted by the solar atmosphere is permeated by ubiquitous magnetic fields. Together with gravity, they create a wide variety of waveguides which are able to support magnetohydrodynamic (MHD) waves.

The aim of the present work is to study these waves using a family of multi-layered Cartesian waveguide configurations of solar atmospheric features, in order to develop models and diagnostic tools applicable to a collection of features within the solar atmosphere. In particular, I investigate the effect of incorporating various sources of asymmetry into the classical model of a magnetic slab on the waves supported by the system.

The initially considered configuration is a static magnetic slab filled with uniform, inviscid, ideal plasma, which is embedded in an asymmetric, magnetic environment. I derive the equation governing the dispersion of magneto-acoustic waves in this slab system, and describe the behaviour of quasi-kink and quasi-sausage eigenmodes.

I proceed to conduct a detailed analytical and numerical investigation of trapped waves that may be supported by this slab system under various orderings of the characteristic speeds. I utilise these approximations to provide a list of potential applications of this slab model to solar atmospheric waveguides, from the global stratification of the layers of the solar atmosphere down to small-scale phenomena such as the environment of magnetic bright points.

Finally, I focus on generalising pre-existent and developing new techniques of solar magneto-seismology. I investigate both propagating and standing waves in asymmetric magnetic and non-magnetic slab systems, and I use the mixed character of the eigenmodes to provide tools for diagnosing the solar atmospheric plasma and determining unknown parameters that would be difficult to measure directly, such as Alfvén speed values.

Acknowledgements

I would like to offer my thanks to all the people and institutions who have made the research summarised in this thesis possible.

First and foremost, I would like to thank my Supervisor, Professor Robertus von Fáy-Siebenbürgen, who has opened my eyes to a whole new and fascinating field of astronomy and astrophysics and has been nothing but patient, supportive and encouraging all throughout my studies.

I am grateful for the support received from the members of SP²RC at the University of Sheffield, the Hungarian Solar Physics Foundation, and the University of Debrecen. I owe further thanks to the tireless organisers of the SURE and UGRI schemes at the University of Sheffield, whose efforts have allowed me to work together with some of the best undergraduate students at School of Mathematics and Statistics. I am especially thankful to Mihai Berbulescu for swiftly sharing the extremely useful PyTES root finding codes with me, and to Norbert Gyenge, Fionnlagh Dover and Matthew Allcock for all the useful coding advice. Thank you to all my co-authors and all the postgraduate students making our office (and later, our computer screens) a lively and understanding environment. Thank you to my close friends, wherever your roads have taken you these past years.

Last but definitely not least, I would like to give thanks to my family for the incredible support and all their love, which, I am certain, would be enough to move the Sun and all other stars.

Publications

Parts of this Thesis are based on the following publications:

- Zsámberger, N. K., Allcock, M. and Erdélyi, R. (2018): Magneto-acoustic Waves in a Magnetic Slab Embedded in an Asymmetric Magnetic Environment: The Effects of Asymmetry. *The Astrophysical Journal*, Volume 853, 136.
- Allcock, M., Shukhobodskaya, D., Zsámberger, N. K. and Erdélyi, R. (2019): Magnetohydrodynamic waves in multi-layered asymmetric waveguides: solar magneto-seismology theory and application. *Frontiers in Astronomy and Space Sciences*, Volume 6, 48.
- Oxley, W., Zsámberger, N. K. and Erdélyi, R. (2020): Standing MHD Waves in a Magnetic Slab Embedded in an Asymmetric Plasma Environment: Slow Surface Waves *The Astrophysical Journal*, Volume 890, 109.
- Oxley, W., Zsámberger, N. K. and Erdélyi, R. (2020): Standing MHD Waves in a Magnetic Slab Embedded in an Asymmetric Magnetic Plasma Environment: Surface Waves *The Astrophysical Journal*, Volume 898, 19.
- Zsámberger, N. K. and Erdélyi, R. (2020): Magnetoacoustic Waves in a Magnetic Slab Embedded in an Asymmetric Magnetic Environment. II. Thin and Wide Slabs, Hot and Cold Plasmas. *The Astrophysical Journal*, Volume 894, 123.
- Zsámberger, N. K. and Erdélyi, R. (2021): Magnetoacoustic Waves in a Magnetic Slab Embedded in an Asymmetric Magnetic Environment. III. Applications to the Solar Atmosphere. *The Astrophysical Journal*, Volume 906, 122.

More details on the parts of the listed papers and the corresponding thesis Chapters can be found in the Abstract of each Chapter.

Contents

1	Introduction	1
1.1	The Sun	1
1.2	The Equations of Magnetohydrodynamics	4
1.2.1	The Induction Equation	5
1.2.2	The Equation of Continuity	6
1.2.3	The Energy Equation	7
1.2.4	The Equation of Motion	7
1.2.5	Summary of the Ideal MHD Equations	8
1.3	The Study of Waves in the Solar Atmosphere	8
1.3.1	Magnetohydrodynamic Waves	8
1.3.2	MHD Waves in Magnetic Slabs	10
1.3.3	Solar Magneto-Seismology	11
1.4	Outline	13
2	Propagating Waves in an Asymmetric Magnetic Slab	15
2.1	Chapter Introduction	15
2.2	The General Dispersion Relation for a Slab in an Asymmetric Magnetic Environment	17
2.2.1	Description of the equilibrium	17
2.2.2	Derivation of the dispersion relation	18
2.2.3	Validation with earlier studies	23
2.2.4	On asymmetric eigenmodes	25
2.3	A mechanical analogy and quasi-symmetric oscillations	27
2.4	Parametric solutions for the general case	29
2.4.1	The effect of varying magnetic field and density ratios	31
2.5	Conclusion	34
3	Approximations of the Dispersion Relation	36
3.1	Chapter Introduction	36
3.2	Thin-slab approximation	37
3.2.1	Surface modes	37
3.2.2	Body modes	42
3.3	Wide-slab approximation	45
3.3.1	Surface modes	45
3.3.2	Body modes	46
3.3.3	Thin- and wide-slab approximations based on the full dispersion relation	47
3.4	Low- β approximation	51
3.4.1	Low plasma- β in all three domains	51

3.4.2	Zero- β limit	54
3.5	High- β approximation	55
3.5.1	High plasma- β in all three domains	55
3.5.2	Infinite- β limit	57
3.5.3	Low- and high- β approximations based on the full dispersion relation	58
3.6	The incompressible limit	60
3.7	Conclusion	64
4	Solar Atmospheric Applications of the Asymmetric Magnetic Slab Model	66
4.1	Chapter Introduction	66
4.2	From the photosphere to the corona with a global view	67
4.2.1	The transition region	72
4.3	Coronal hole boundaries	76
4.4	Prominences	78
4.5	Light bridges	81
4.6	Magnetic bright points	88
4.7	Conclusion	92
5	Solar Magneto-Seismology of an Asymmetric Magnetic Slab	95
5.1	Chapter Introduction	95
5.2	Amplitude ratios	96
5.2.1	Quasi-sausage modes	97
5.2.2	Quasi-kink modes	100
5.2.3	Approximation of amplitude ratios in a weakly asymmetric slab	103
5.2.4	Quasi-symmetric modes	106
5.3	Minimum perturbation shift	110
5.3.1	Quasi-sausage modes	111
5.3.2	Quasi-kink modes	112
5.3.3	The incompressible limit	114
5.4	Conclusion	114
6	Standing Waves in an Asymmetric Slab	116
6.1	Chapter Introduction	116
6.2	The Slab in a Non-Magnetic Environment	117
6.3	Derivation of the Dispersion Relation	118
6.3.1	Frequencies of the Standing Harmonic Modes	121
6.3.2	Amplitudes of the Standing Harmonic Modes	127
6.3.3	Numerical Solutions of the Dispersion Relation	129
6.4	The Rayleigh-Ritz Technique	130
6.5	The Slab in a Magnetic Environment	132
6.5.1	The Equilibrium Magnetic Slab	133
6.5.2	Boundary Conditions	133
6.5.3	Derivation of the Dispersion Relation	134
6.5.4	Eigenfrequencies of Standing Harmonic Modes	135
6.5.5	Amplitudes of Standing Harmonic Modes	139
6.6	Conclusion	141

7	Conclusion	143
7.1	Overview of the Thesis	143
7.2	Summary of the main results	145
7.2.1	The Magnetic Slab Embedded in an Asymmetric Magnetic Environment	145
7.2.2	Standing Waves in Asymmetric Slab Waveguides	148
7.3	Asymmetric Slab Waveguides and Their Applications in Solar Magneto-Seismology	149
7.4	Future Aims	151

List of Figures

1.1	The structure of our Sun. The source of this figure is ESA (2019).	2
1.2	The height variation of temperature and density in the solar atmosphere in the VAL model. Image credit:Avrett and Loeser (2008).	3
1.3	Model and eigenmodes of a symmetric magnetic slab of width $2a$. Panel (a) illustrates the equilibrium configuration, panel (b) depicts a sausage mode, while panel (c) shows a kink mode oscillation. The source of this figure is Priest (2014).	11
2.1	Illustration of the equilibrium configuration for a magnetic slab embedded in an asymmetric non-magnetic environment. Figure adapted from Allcock et al. (2019).	16
2.2	The equilibrium conditions: inside the slab, $ x \leq x_0$ (medium grey), and outside the slab, $x < -x_0$ and $x > x_0$ (light and dark grey). The red arrows illustrate the vertical magnetic fields, $B_0\hat{\mathbf{z}}$, $B_1\hat{\mathbf{z}}$, and $B_2\hat{\mathbf{z}}$; the dashed black lines outline the boundaries of the slab.	18
2.3	Illustration of eigenmodes along a slab in an asymmetric magnetic environment. The red arrows illustrate the perturbed magnetic fields, the thick solid black lines denote the perturbed slab boundaries, and the dashed grey lines indicate the position of the slab boundaries after half a period.	26
2.4	Distribution of the transverse velocity perturbation amplitude (\hat{v}_x) in a strongly magnetised slab and its rarefied asymmetric environment, plotted with solid black curves, as a function of the transverse spatial coordinate, x . Lighter gray shading represents lower background densities, while the blue arrows show the equilibrium magnetic fields, and darker grey shading corresponds to higher background densities. In Panel (a), a slow quasi-kink surface mode, in Panel (b), a slow quasi-sausage surface mode, in Panel (c), a fast quasi-kink body mode of order one, and in Panel (d), a fast quasi-sausage body mode of order one is presented. Panels (a) and (b) correspond to a thin slab ($kx_0 = 0.685$), while Panels (c) and (d) represent a wide slab ($kx_0 = 2.790$). These solutions to the dispersion relation (Equation 2.31) were obtained numerically, for a slab system characterized by $v_{A0} = 0.7c_0$, $v_{A1} = 0.2c_0$, $v_{A2} = 0.1c_0$, $c_1 = 2.2279c_0$, $c_2 = 1.8742c_0$, $\rho_1/\rho_0 = 0.28$, and $\rho_2/\rho_0 = 0.4$	27

- 2.5 Illustration of a coupled mechanical oscillator system as an analogy to the asymmetric slab geometry. Thicker springs correspond to higher spring constants k_{ij} . Figures (a), (d) and (g) show the symmetric, asymmetric and quasi-symmetric spring systems in equilibrium. Figures (b) and (c) show the normal modes of a symmetric system. Figures (e) and (f) show the normal modes of an asymmetric system, while Figures (h) and (i) show the quasi-symmetric system. In each panel, the vertical dashed lines correspond to the positions of the gray plates at equilibrium. 28
- 2.6 Diagnostic diagrams for the dispersion relation, Equation (2.31). Quasi-sausage (quasi-kink) modes are plotted in blue (red). **(a)** Slow and fast body modes, as well as slow surface mode waves can exist if the Alfvén speed of each domain is smaller than the corresponding sound speed. The characteristic speeds used in this case are: $v_{A0} = 0.7c_0$, $v_{A1} = 0.2c_0$, $v_{A2} = 0.1c_0$, $c_1 \approx 1.7c_0$, $c_2 \approx 1.9c_0$, with $\rho_1/\rho_0 = 0.5$, $\rho_2/\rho_0 = 0.4$. **(b)** Both fast and slow surface and body modes occur when the internal Alfvén speed is smaller than the internal sound speed, but the external Alfvén speeds are both higher than their corresponding sound speeds. The characteristic speed ordering used to obtain this figure is $v_{A0} = 0.5c_0$, $v_{A1} = 1.5c_0$, $v_{A2} = 1.7c_0$, $c_1 = 0.9c_0$, $c_2 = 0.85c_0$, $\rho_1/\rho_0 = 0.45$, $\rho_2/\rho_0 = 0.39$ 30
- 2.7 The dependence of the phase speeds of slow surface mode solutions of Equation (3.99) on the dimensionless slab width and left-hand-side density ratio in the incompressible limit. The blue surface shows the quasi-sausage mode, while the red one displays the quasi-kink mode. Here, $c_1 = 100.0$, $v_{A0} = 1.0$, $v_{A1} = 0.5$ and $v_{A2} = 0.7$ were used, while c_0 and c_2 were continuously changing in order to sustain total pressure balance between the domains. The black line indicates the values of the density ratio and the dimensionless slab width, for which the phase speeds of the quasi-sausage and quasi-kink modes perform a close approach and avoided crossing. 32
- 2.8 (a) The spatial variation of the transverse displacement perturbation ($\hat{\xi}_x$) throughout the slab and its environment. The upper (lower) parts of the panel represent the quasi-sausage (quasi-kink) mode solutions. Negative amplitude regions are filled with blue, while positive ones are coloured red. In each column, the left-hand-side density ratio remains constant, while in each row, the ratio of the left-hand-side external magnetic field to the internal one ($B_1^* = B_1/B_0$) is kept at the same value. The right-hand-side density ratio is held fixed at $\rho_2/\rho_0 = 0.4$. The characteristic speeds used to obtain these plots are: $v_{A0} = 0.7c_0$, $v_{A1} = 0.2c_0$, $v_{A2} = 0.1c_0$, $c_2 = 1.8742c_0$, but c_1 varies to satisfy equilibrium pressure balance. Panel (b) displays phase speeds of solutions corresponding to different values of B_1^* , for specific fixed values of the non-dimensional slab width (kx_0). 33

- 3.1 The phase speed (ω/k) of magnetoacoustic waves in various low- β situations characterised by typical choices of c_i, v_{Ai}, ρ_i . Blue (red) curves show quasi-sausage (quasi-kink) modes. Hatching represents regions in which no propagating modes are permitted. **(a)** Slow and fast mode body waves are seen when $v_{A0} = 1.5c_0, v_{A1} = 4c_0, v_{A2} = 3c_0, c_1 = 0.5976c_0, c_2 = 0.6972c_0, \rho_1/\rho_0 = 0.21, \rho_2/\rho_0 = 0.36$. **(b)** One band of slow-, and two bands of fast body modes appear when $v_{A0} = 1.2c_0, v_{A1} = 3c_0, v_{A2} = 3.5c_0, c_1 = 1.5811c_0, c_2 = 1.6531c_0, \rho_1/\rho_0 = 0.22, \rho_2/\rho_0 = 0.17$. **(c)** Only slow body modes can be found when $v_{A1} = 0.7v_{A0}, v_{A2} = 0.6v_{A0}, c_0 = 0.5v_{A0}, c_1 = 0.2504v_{A0}, c_2 = 0.2472v_{A0}, \rho_1/\rho_0 = 2.3, \rho_2/\rho_0 = 3.0$. **(d)** Even with more prominent asymmetry, one band of slow-, and one band of fast body modes exist when, e.g., $v_{A0} = 0.3v_{A2}, v_{A1} = 0.6v_{A2}, c_0 = 0.2v_{A2}, c_1 = 0.1v_{A2}, c_2 = 0.8v_{A2}, \rho_1/\rho_0 = 0.3710, \rho_2/\rho_0 = 0.0871$. In each panel, for the sake of clarity, only a couple of examples in each band of body modes are displayed. 53
- 3.2 Solutions to the dispersion relation, similar to Figure 3.1, obtained for various high- β cases. **(a)** Slow and fast mode body waves, as well as slow surface waves are present when $v_{A0} = 0.7c_0, v_{A1} = 0.2c_0, v_{A2} = 0.1c_0, c_1 = 1.6683c_0, c_2 = 1.8742c_0, \rho_1/\rho_0 = 0.5, \rho_2/\rho_0 = 0.4$. **(b)** The same modes appear when $v_{A0} = 0.6c_0, v_{A1} = 0.95c_0, v_{A2} = 0.9c_0, c_1 = 1.5c_0, c_2 = 1.4c_0, \rho_1/\rho_0 = 0.433, \rho_2/\rho_0 = 0.4934$. **(c)** Only the slow surface and body modes can be observed when $v_{A1} = 0.4v_{A0}, v_{A2} = 0.3v_{A0}, c_0 = 1.4v_{A0}, c_1 = 1.15v_{A0}, c_2 = 1.1v_{A0}, \rho_1/\rho_0 = 1.9188, \rho_2/\rho_0 = 2.1738$. **(d)** Three bands of fast body modes, one band of slow body modes, and a pair of slow surface modes exist when $v_{A0} = 0.2v_{A2}, v_{A1} = 0.7v_{A2}, c_0 = 0.5v_{A2}, c_1 = 1.1v_{A2}, c_2 = 1.8v_{A2}, \rho_1/\rho_0 = 0.1751, \rho_2/\rho_0 = 0.071$. As before, in each panel, only a couple of examples in each band of body modes are displayed. 57
- 3.3 Solutions of Equation (3.88) for $R = 0.5$ (left panel) and $R = 1.0$ (right panel), showing the behaviour of magneto-acoustic waves in the limiting case of an incompressible plasma. The blue line indicates the quasi-sausage mode, while the red line shows the quasi-kink mode. Hatching denotes regions in which no modes occur. For the left panel $c_0 \approx 105, c_1 = 100, c_2 \approx 62, v_{A0} = 1.0, v_{A1} = 0.5, v_{A2} = 0.7, \rho_0/\rho_1 = 1.1, \rho_0/\rho_2 = 2.9$, while for the right panel $c_0 \approx 105, c_1 = 100, c_2 \approx 111, v_{A0} = 1.0, v_{A1} = 0.5, v_{A2} = 0.7, \rho_0/\rho_1 = 1.1, \rho_0/\rho_2 = 0.9$ were used. 61
- 3.4 Slow surface mode solutions of Equation (3.99) in the incompressible limit, showing the dependence of the common phase speed limit on the density ratio ρ_1/ρ_0 . Blue indicates the quasi-sausage mode, while red applies to the quasi-kink mode. Here, $c_1 = 100.0, v_{A0} = 1.0, v_{A1} = 0.5$ and $v_{A2} = 0.7$ were used, while c_0 and c_2 were continuously changing in order to sustain total pressure balance between the domains. The black line indicates the values of the density ratio and the dimensionless slab width, for which the phase speeds of the quasi-sausage and quasi-kink modes perform a close approach and avoided crossing. 63

- 3.5 Two-dimensional projections of Figure 3.4 illustrating what the effects of varying the values of the equilibrium **(a)** slab width, kx_0 , and **(b)** density ratio ($R_1 = \rho_0/\rho_1$) are on the incompressible eigenmodes of an asymmetric magnetic slab. Solid (dashed) lines represent quasi-sausage (quasi-kink) modes, and colour coding indicates which pair of solutions is valid for which value of the equilibrium parameters. . . . 64
- 4.1 The layers of the solar atmosphere modelled as an asymmetric slab configuration. The illustration on the left puts this suggested application in the context of the magnetic fields and network elements of the solar atmosphere, and the dashed red box is used to highlight where exactly the slab is placed in this model. For the sake of clarity, we included the same numbering of the regions that is used in the simplified slab model on the right-hand side: the number and index 1 denotes the photosphere, 0 shows the interface region, while 2 indicates the corona. Compared to the original model, the coordinate system was rotated by 90° , therefore, now, the black arrows on the right illustrate the horizontal magnetic fields, $B_0\hat{z}$, $B_1\hat{z}$ and $B_2\hat{z}$. As before, the dashed black lines denote the boundaries of the slab. The illustration on the left was prepared using Figure 5 of Bushby (2008). 67
- 4.2 The phase speed of magnetoacoustic waves as a function of kx_0 in the photosphere-interface region-corona system. Blue (red) lines denote sausage (kink) modes. The diagram was produced by setting $c_0 = 1.044v_{A0}$, $c_1 = 0.783v_{A0}$, $c_2 = 13.1v_{A0}$, $v_{A1} = 0.267v_{A0}$, $v_{A2} = 130.6v_{A0}$ for the characteristic velocities in the three domains. The density ratios between the three regions were set to be $\rho_1/\rho_0 = 2.1503$ and $\rho_2/\rho_0 = 0.0001$. The black circle (diamond) denotes a trapped (leaky) solution, for which the transverse velocity perturbation throughout the slab system is displayed on the left (right) side of Figure 4.3. 71
- 4.3 The amplitude of the transverse velocity perturbation of a trapped and a leaky solution in the photosphere - interface region - corona system. The wavenumber and phase speed values representing the trapped (leaky) solution are denoted with a black circle (diamond) symbol in Figure 4.2. 73
- 4.4 The upper layers of the solar atmosphere modelled as an asymmetric slab configuration. Like in Figure 4.1, the image on the left places this suggested application in the context of the magnetic fields and network elements of the atmosphere, and the dashed red box is used to indicate the position of the slab, illustrated in detail on the right. The different layers have the same numbering on both sides: index 1 identifies the chromosphere, 0 stands for the transition region, and 2 denotes the corona. Compared to the original mathematical model, the coordinate system is now rotated by 90° , therefore the black arrows illustrate the horizontal magnetic fields, $B_0\hat{z}$, $B_1\hat{z}$ and $B_2\hat{z}$; the dashed black lines outline the boundaries of the slab. The illustration on the left was prepared using Figure 5 of Hansteen and Carlsson (2009). 74

- 4.5 The phase speed of magnetoacoustic waves as a function of kx_0 in a the chromosphere - transition region - corona system. The diagram was produced by setting $c_0 = 0.5v_{A0}$, $c_1 = 0.475v_{A0}$, $c_2 = 1.15v_{A0}$, $v_{A1} = 0.52v_{A0}$, $v_{A2} = 12.5v_{A0}$ for the characteristic speeds in the three domains, and density ratios of $\rho_1/\rho_0 = 2.402291$ and $\rho_2/\rho_0 = 0.008236$. 75
- 4.6 Polar plumes modelled as an asymmetric slab configuration. On the left, the red lines show the boundaries of the slab in the context of the solar atmosphere. The numbering of the three regions is identical on the left- and right-hand-side images, with 1 denoting a coronal hole region, 0 the coronal hole boundary region, and 2 the quiet Sun. On the right, as before, the dark red arrows illustrate the vertical magnetic fields, $B_0\hat{z}$, $B_1\hat{z}$ and $B_2\hat{z}$; and the dashed black lines denote the boundaries of the slab. The illustration on the left was prepared using Figure 1 of Poletto (2015). 77
- 4.7 The phase speed (ω/k) of magnetoacoustic waves that occur in a low-beta situation. Blue lines show sausage modes, while red lines indicate kink modes. The figure illustrates the case when $c_0 = 0.19v_{A0}$, $c_1 = 0.18v_{A0}$, $c_2 = 0.62v_{A0}$, $v_{A1} = 1.6v_{A0}$, $v_{A2} = 1.3v_{A0}$ are the characteristic speeds in the three domains, and the ratios of the external densities to the internal one are $\rho_1/\rho_0 = 0.407429$ and $\rho_2/\rho_0 = 0.513077$. 79
- 4.8 Stratification around a solar prominence viewed as an asymmetric slab configuration. The picture on the left shows the orientation and position of the slab in the context of the solar atmosphere using an SDO 304 Å observation from July 20, 2013. The dashed yellow box shows the region of space suggested for modelling, and the dotted yellow lines delimit the slab boundaries. In both the left- and right-hand-side images, the index 1 denotes the coronal region beneath the prominence, 2 the one above the prominence, while 0 stand for the volume of the prominence itself. On the right, once again, the coordinate system was rotated by 90° , therefore now the dark red arrows illustrate the horizontal magnetic fields, $B_0\hat{z}$, $B_1\hat{z}$ and $B_2\hat{z}$; while the dashed black lines still denote the boundaries of the slab. 80
- 4.9 Phase speeds of magnetoacoustic waves in a prominence examined as a low-beta slab. In the examined configuration $c_0 = 0.09v_{A0}$, $c_1 = 2.73v_{A0}$, $c_2 = 2.23v_{A0}$, $v_{A1} = 10.92v_{A0}$, $v_{A2} = 10.94v_{A0}$, $\rho_1/\rho_0 = 0.007872$ and $\rho_2/\rho_0 = 0.008043$. The phase speed range between v_{A0} and c_2 contains multiple bans of leaky modes, where solutions are not plotted, and therefore the first fast body mode solution appearing in this figure appears as a line broken into three parts. 81
- 4.10 A light bridge examined as an asymmetric slab. The bright region of the light bridge between the two umbral blobs (or cores) is the slab itself, while physical parameters (density, temperature, magnetic field strength) on either side of it in the umbrae are slightly different from one another. The original picture (in the top right corner) used for the graphic is a slit-jaw image observed by the Interface Region Imaging Spectrograph (IRIS) in 1400 Å, on 2014 July 3. 83

-
- 4.11 The phase speed (ω/k) of magnetoacoustic waves that may be supported by light bridges under various possible characteristic speed orderings suggested by observations. **(a)** $v_{A1} = 35v_{A0}$, $v_{A2} = 14v_{A0}$, $c_0 = 7v_{A0}$, $c_1 = 5.5v_{A0}$, $c_2 = 6.5v_{A0}$, $\rho_1/\rho_0 = 0.046122$ and $\rho_2/\rho_0 = 0.242400$. **(b)** $v_{A1} = 11.83v_{A0}$, $v_{A2} = 2v_{A0}$, $c_0 = 2.33v_{A0}$, $c_1 = 1.83v_{A0}$, $c_2 = 2.17v_{A0}$, $\rho_1/\rho_0 = 0.076943$ and $\rho_2/\rho_0 = 1.150634$. **(c)** $v_{A1} = 5.55v_{A0}$, $v_{A2} = 2.19v_{A0}$, $c_0 = 1.093v_{A0}$, $c_1 = 0.86v_{A0}$, $c_2 = 1.02v_{A0}$, $\rho_1/\rho_0 = 0.076943$ and $\rho_2/\rho_0 = 0.404378$. **(d)** $v_{A1} = 5.55v_{A0}$, $v_{A2} = 0.94v_{A0}$, $c_0 = 1.09v_{A0}$, $c_1 = 0.86v_{A0}$, $c_2 = 1.02v_{A0}$, $\rho_1/\rho_0 = 0.076943$ and $\rho_2/\rho_0 = 1.150634$ 86
- 4.12 An elongated MBP can be considered as an asymmetric magnetic slab. The bright region at the centre itself is the slab, while physical parameters (density, temperature, magnetic field strength) on either side of it in the intergranular lane are slightly different from one another. The illustration was prepared using Figure 11 of (Liu et al., 2018), showing TiO 7058 Å observations taken by the New Vacuum Solar Telescope. 89
- 4.13 Numerical solutions for the phase speed (ω/k) of magnetoacoustic waves supported by an elongated MBP in a high- β asymmetric magnetic environment. Solutions in panel **(a)** were obtained using characteristic speeds and density ratios of $v_{A1} = 0.205v_{A0}$, $v_{A2} = 0.3v_{A0}$, $c_0 = 1.2v_{A0}$, $c_1 = 0.7v_{A0}$, $c_2 = 0.8v_{A0}$, $\rho_1/\rho_0 = 4.329987$ and $\rho_2/\rho_0 = 3.179487$, in which case the MBP itself is a high-*beta* slab as well. Panel **(b)** shows solutions obtained in a slab system characterised by $v_{A1} = 0.170v_{A0}$, $v_{A2} = 0.249v_{A0}$, $c_0 = 0.913v_{A0}$, $c_1 = 0.581v_{A0}$, $c_2 = 0.663v_{A0}$, $\rho_1/\rho_0 = 4.609381$ and $\rho_2/\rho_0 = 3.384645$, in which case the MBP itself is described by a plasma-*beta* value of one. Finally, panel **(c)** shows trapped solutions when $v_{A1} = 0.0137v_{A0}$, $v_{A2} = 0.2v_{A0}$, $c_0 = 0.733v_{A0}$, $c_1 = 0.47v_{A0}$, $c_2 = 0.53v_{A0}$, $\rho_1/\rho_0 = 5.875957$ and $\rho_2/\rho_0 = 4.314685$, and therefore the MBP itself is a low-*beta* slab. 93
- 5.1 Illustration of the principle of the amplitude ratio method: the ratio of transverse displacement (or velocity) amplitudes at the two boundaries of the slab, A_1 and A_2 , is calculated and measured. 96
- 5.2 Trapped surface mode solutions in an asymmetric slab with $v_{A0} = 1$, $c_0 = 1.4$, $v_{A1} = 0.19$, $c_1 = 1.2$, $\rho_1/\rho_0 = 1.9$, $v_{A2} = 0.18$, $c_2 = 1.09$, $\rho_2/\rho_0 = 2.28$. The blue (red) line displays the quasi-sausage (quasi-kink) surface mode, with other types of solutions not displayed in the figure. 100
- 5.3 Amplitude ratios of the quasi-sausage mode as a function of kx_0 . The exact amplitude ratio is plotted with blue, the approximation with red, using the same background parameters as Figure 5.2. For small slab widths, as expected, the approximation follows the exact solutions closely, but for wide slabs, the difference between the two grows quickly. 101
- 5.4 Dependence of the amplitude ratio on δ , for $\epsilon = 0.1$ and $kx_0 = 0.1$. for the quasi-sausage mode. 105

5.5	Dependence of the amplitude ratio on δ , for $\epsilon = 0.5$ and $kx_0 = 0.5$. for the quasi-sausage mode.	106
5.6	Dependence of the amplitude ratio on δ , for $\epsilon = 0.1$ and $kx_0 = 0.1$. for the quasi-kink mode.	107
5.7	Dependence of the amplitude ratio on δ , for $\epsilon = 0.1$ and $kx_0 = 0.5$. for the quasi-kink mode.	107
5.8	The principle of the minimum perturbation shift method. Figure courtesy of Allcock and Erdélyi (2018).	111
5.9	Dependence of the minimum perturbation shift of the quasi-sausage (blue) and quasi-kink mode (red) on δ , for $\epsilon = 0.1$ and $kx_0 = 0.1$	113
5.10	Dependence of the minimum perturbation shift of the quasi-sausage (blue) and quasi-kink mode (red) on δ , for $\epsilon = 0.1$ and $kx_0 = 0.5$	113
6.1	The equilibrium state inside ($ x \leq x_0$) and outside of the magnetic slab ($x < -x_0$ and $x > x_0$), with the magnetic field lines indicated in red. The source of the Figure is: Oxley et al. (2020a).	118
6.2	The phase speed for the fundamental mode ($n = 1$, panel (a)) and the first harmonic ($n = 2$, displayed in panel (b)) as a function of ϵ ranging from 0 to 0.4, and δ ranging from 0 to 2. The purple plane represents the value of c_T , and the green line illustrates the maximum plotted value, which is $\omega_1/k \approx 2.89$ in panel (a), and $\omega_2/k \approx 4.09$ in panel (b), by joining it to the vertical axis. The source of the Figure is: Oxley et al. (2020a).	122
6.3	The phase speed for the fundamental mode ($n = 1$) and the first harmonic ($n = 2$) of the quasi-sausage waves (given by Equation 6.14) and the quasi-kink waves (given by Equation 6.15), (a) as a function of ϵ , with $\delta = 1$ fixed, and (b) as a function of δ , with $\epsilon = 0.1$ fixed. The source of the Figure is: Oxley et al. (2020a).	122
6.4	Illustration of a fundamental standing quasi-sausage mode oscillation in the asymmetric magnetic slab. The source of the Figure is: Oxley et al. (2020a).	123
6.5	Same as Figure 6.4 but for the first harmonic. The source of the Figure is: Oxley et al. (2020a).	123

6.6	The phase speed for the fundamental mode ($n = 1$) and the first harmonic ($n = 2$) of the quasi-sausage waves (given by Equation 6.19) and the quasi-kink waves (given by Equation 6.24), (a) as a function of ε , with $\delta = 0.03$ fixed and (b) as a function of δ , with $\varepsilon = 0.12$ fixed. The source of the Figure is: Oxley et al. (2020a).	124
6.7	The ratio of the frequencies of the first harmonic to the fundamental mode of the quasi-sausage waves (given by Equation 6.20) and the quasi-kink waves (given by Equation 6.25), (a) as a function of ε , with $\delta = 0.03$ fixed, and (b) as a function of δ , with $\varepsilon = 0.12$ fixed. The source of the Figure is: Oxley et al. (2020a).	125
6.8	The frequency difference due to asymmetry of the fundamental mode ($n = 1$) and the first harmonic ($n = 2$) quasi-sausage waves (given by Equation 6.21) and the quasi-kink waves (given by Equation 6.26), (a) as a function of ε , with $\delta = 0.03$ fixed, and (b) as a function of δ , with $\varepsilon = 0.12$ fixed. The source of the Figure is: Oxley et al. (2020a).	125
6.9	Illustration of a fundamental standing quasi-kink mode oscillation in the asymmetric magnetic slab. The source of the Figure is: Oxley et al. (2020a).	126
6.10	Same as Figure 6.9 but for the first harmonic. The source of the Figure is: Oxley et al. (2020a).	126
6.11	The amplitude difference between the two sides of the slab for the quasi-sausage waves (given by Equation 6.29) and both the fundamental mode ($n = 1$) and the first harmonic ($n = 2$) quasi-kink waves (given by Equation 6.35), (a) as a function of ε , with $\delta = 0.03$ fixed, and (b) as a function of δ , with $\varepsilon = 0.12$ fixed. The source of the Figure is: Oxley et al. (2020a).	128
6.12	(a) The phase speed for the fundamental mode ($n = 1$) of the quasi-sausage waves as a function of ε and δ . Panel (b) displays the same, but for the quasi-kink mode. The source of the Figure is: Oxley et al. (2020a).	130
6.13	Visualisation of the equilibrium state inside ($ x \leq x_0$) and outside of the magnetic slab ($x < -x_0$ and $x > x_0$), where the magnetic field is indicated by the red lines. The source of the Figure is: Oxley et al. (2020b).	133
6.14	Illustration of a fundamental standing quasi-sausage mode oscillation in the magnetic slab embedded in a magnetically asymmetric environment. The source of the Figure is: Oxley et al. (2020b).	138
6.15	Same as Figure 6.14 but for the first harmonic. The source of the Figure is: Oxley et al. (2020b).	138
6.16	The ratio of the frequencies of the first harmonic to the fundamental mode of the quasi-sausage waves (Solution 1 given by Equation (6.64) and Solution 2 by Equation 6.67), (a) as a function of ε , with $\zeta = 0.2$ fixed, and (b) as a function of ζ , with $\varepsilon = 0.2$ fixed. The source of the Figure is: Oxley et al. (2020b).	138
6.17	Illustration of a fundamental standing quasi-kink mode oscillation in the slab embedded in a magnetically asymmetric environment. The source of the Figure is: Oxley et al. (2020b).	140

6.18 Same as Figure 6.17 but for the first harmonic. The source of the
Figure is: Oxley et al. (2020b). 140

List of accompanying materials

Interactive Figures for Chapter 5

- SM-S1: The exact and thin-slab quasi-sausage mode amplitude ratios as a function of the density asymmetry, δ , with fixed magnetic asymmetry, ϵ , and changing slab width, kx_0
- SM-S2: The exact and thin-slab quasi-kink mode amplitude ratios as a function of the density asymmetry, δ , with fixed magnetic asymmetry, ϵ , and changing slab width, kx_0

These Figures are part of a collection at <https://www.overleaf.com/read/hffdchcsdxdg>.

Interactive Figures for Chapter 6

- SM-A1: The phase speeds of the quasi-sausage and quasi-kink fundamental mode calculated from the approximate solutions
- SM-A2: The phase speeds of the quasi-sausage and quasi-kink first harmonics calculated from the approximate solutions
- SM-C1: Comparison of the approximation and the exact phase speeds of the quasi-sausage fundamental mode
- SM-C2: Comparison of the approximation and the exact phase speeds of the quasi-kink fundamental mode

These Figures are are part of a collection at <https://www.overleaf.com/read/hffdchcsdxdg> and also available as part of the published article Oxley et al. (2020a).

Chapter 1

Introduction

Abstract

This Introduction provides an overview of the background and main topics covered by our research conducted about MHD wave propagation in asymmetric solar waveguides. We provide a description of the fundamental structures of the Sun and its atmosphere, and then we proceed to summarise the equations of ideal MHD, which the calculations carried out in the following Chapters will be based on. Next, we discuss the basics of MHD wave propagation in a uniform and in a structured medium, before we present some key historical developments in the magneto-seismology of solar structures. This Chapter follows the fundamentals of MHD theory from Priest (2014) and Goedbloed and Poedts (2004), and relies on Zsámberger et al. (2018), Allcock et al. (2019), Zsámberger and Erdélyi (2020), and Zsámberger and Erdélyi (2021) for the overview of magnetic slab models and developments in solar magneto-seismology.

1.1 The Sun

Our Sun has been a subject of continued fascination and ceaseless study in some form through most of human history. It is an “average”, G-type star, but one that is located far closer to our planet than any of its cosmic relatives. This allows us to observe it in unparalleled detail and use it as a “laboratory” for testing any expectations derived from our theories, simulations and models. Here, we provide a brief overview of our star’s structure deduced from many years of observations and helioseismological studies, based on Golub and Pasachoff (2009) and Priest (2014). To complement this description, Figure 1.1 provides an illustration of the main layers and features of the solar interior and atmosphere.

The Sun is the largest object in our solar system. It also represents over 99% of the total mass in our solar system and serves as the main energy source for most of its various other objects. This energy is generated at the heart of our star, in its *core*, at a temperature of around 15 million K and a particle density of 10^{32} m^{-3} magnitude. Under such conditions, the stellar material is in a plasma state, with its particles being energetic enough to overcome electromagnetic forces pushing the same charges apart, and the nuclear fusion of four hydrogen nuclei becomes possible, resulting in the creation of a helium nucleus. A small fraction of the initial mass is converted into energy in the process, which is then carried away by the γ -rays and

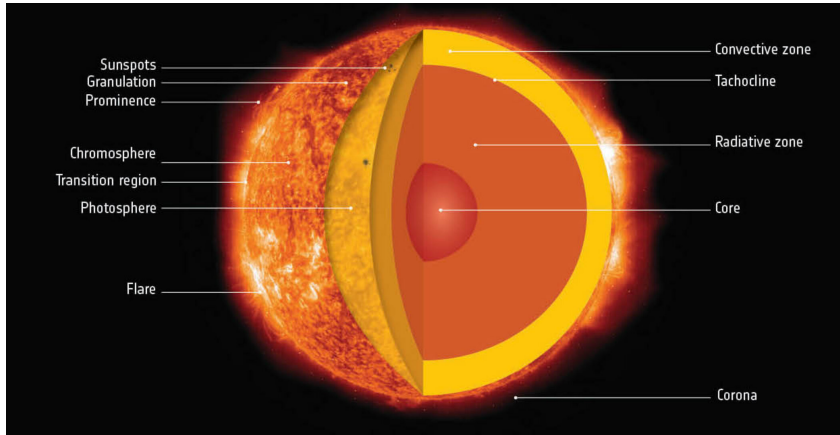


Figure 1.1: The structure of our Sun. The source of this figure is ESA (2019).

electron neutrinos generated in the reaction.

The core extends to about 25% of the 700 Mm solar radius (R_{\odot}), giving its place to the *radiative zone* located at radii of $0.25R_{\odot} < r < 0.75R_{\odot}$. In this layer of the solar interior, the photons leaking out from the core perform a lengthy random walk process, going through numerous collisions, absorbtions and re-emmissions. During their slow radiative diffusion, they suffer energy losses and their wavelength is shifted from the high-energy γ range towards the visible spectrum.

The outermost layer of the solar interior is the *convective zone*, separated from the radiative zone by a thin shear layer called the *tachocline*, which is suspected to play an important role in the generation of the global solar magnetic field. Above this layer, the dominant energy transport process becomes convection. The high temperature gradient is able to induce convective instability, displacing blobs of plasma vertically upwards. The buoyant plasma radiates its energy into the solar atmosphere once it reaches the surface, cooling down in the process, before it sinks and the cycle of convection starts over again.

The solar atmosphere is defined as the part of our star from which photons escape directly into space. Unlike the opaque interior, this segment of our star as been the subject of numerous, continually improving direct observations. The atmosphere consists of three main layers, the lowest one of which is called the *photosphere*. This very thin layer of relatively dense and opaque plasma is regarded as the solar surface, which is where the majority of visible solar radiation is emitted from. This is where the plasma rising in convective cells cools and sinks back down from, resulting in most of the photosphere being covered in irregularly shaped, bubbling convective cells called granules. The bright and hot centres of granules, where plasma rises from the convective zone, are separated from one another by darker intergranular lanes, which are cooler regions of downflow. Motions and structuring are present in larger scales as well, in the form of mesogranulation and giant cells. Concentrations of strong magnetic fields may partially or fully inhibit convection, interrupting this structure in the form of sunspots. Within these areas, the average photospheric temperature of about 6000 K decreases by 1000-2000 K, lending them their dark appearance.

The photosphere is also where the temperature of our Sun reaches its minimum value. It has long been a puzzling observation that after dropping from about 15 million to 6000 K as we move radially outwards from the core of the Sun to the

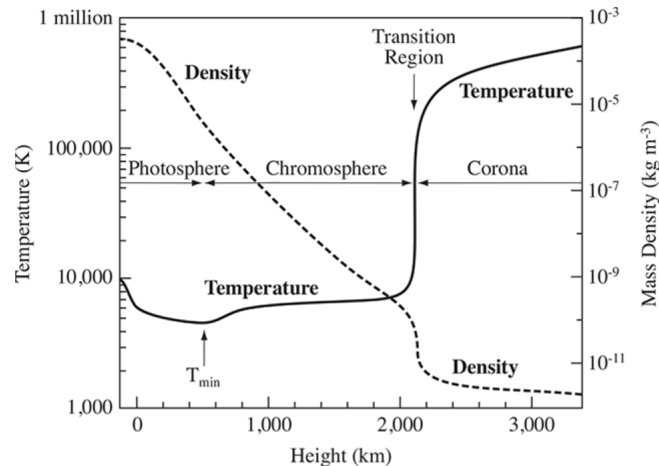


Figure 1.2: The height variation of temperature and density in the solar atmosphere in the VAL model. Image credit:Avrett and Loeser (2008).

photosphere, the temperature starts rising once again, until it reaches values of one to a few million K again in the outermost layers of the solar atmosphere. This unexpected behaviour gave rise to the question of solar atmospheric heating, which is a multi-faceted issue with no single clear answer. Figure 1.2 displays this surprising temperature distribution throughout the solar atmosphere.

Directly above the photosphere, the next spherical shell of the Sun is the *chromosphere*, located between heights of 0.5-2.5 Mm. This layer shows complex structuring, its most notable feature being the forest of spicules, which are thin, short-lived plasma jets. The temperature in the chromosphere keeps rising slowly, until at heights of about 2 Mm above the solar surface, it suddenly jumps by two orders of magnitude. This narrow layer of swiftly warming plasma is called the *transition region*, above which we find the outermost shell of the solar atmosphere: the rare and hot *solar corona*.

The corona is dominated by the presence of magnetic fields and shows various forms of large-scale structuring. Its main features are helmet-shaped streamers near mid-latitudes and regions of open magnetic field lines appearing especially near the poles called coronal holes. The corona also contains numerous arcs of magnetic field lines. Concentrations of ionised plasma follow these arcs, forming coronal loops, which are one of the most thoroughly studied structures in the field of coronal seismology. The outer corona expands outwards continuously in a stream of particles forming the solar wind.

The change in mean temperatures and densities throughout the layers of the solar atmosphere are commonly described by the VAL (Vernazza-Avrett-Loeser) model (Avrett and Loeser, 2008). This model shows that both the temperature and the density first go through a gradual change from their photospheric values, and then a sudden jump in the transition region, before they reach their coronal values. The drastic temperature increase from the photosphere to the corona as we move further away from the main energy source of the Sun (the nuclear fusion occurring in the core) requires that there should be an alternate energy transport mechanism which is able to balance out radiative losses in the atmosphere. Numerous processes have been nominated as this additional energy source to provide the energy required for atmospheric heating and for the acceleration of the solar wind. In reality, the high

chromospheric and coronal temperatures likely owe their existence to a combination of different processes operating on various scales. Thus, the answers to the enigma of atmospheric heating include both hydrodynamic processes (such as acoustic and pulsation waves), and magnetic heating mechanisms (waves and reconnection). For an overview of these possibilities, see Erdélyi and Nelson (2016a)).

1.2 The Equations of Magnetohydrodynamics

Section 1.1 has shed light on what a dynamic and complex plasma environment the solar atmosphere is. The main sources of the global and fine structure are gravity and the ubiquitous magnetic fields present in the entirety of its volume. While gravity is responsible mainly for the global vertical stratification of the atmosphere, the non-uniformly distributed magnetic fields also create sub-structures on various scales, from the sunspots and pores in the photosphere, the spicule forest in the chromosphere, all the way up to prominences, coronal loops, and even coronal plumes that extend far into the solar wind (Roberts, 1984, Goossens et al., 2002).

The interactions of the hot solar plasma and the magnetic fields that permeate it are mathematically described by the theory of magnetohydrodynamics (MHD). As later Sections will illustrate, these interactions of magnetic fields and plasma particles can give rise to a plethora of wave phenomena in all layers of the solar atmosphere (De Pontieu et al., 2005; Komm et al., 2015). In order to understand these observations and events, in the current Section, we provide a summary of the fundamental assumptions and equations of MHD, which we will use in the remaining Chapters to derive dispersion relations for various slab models.

The equations of MHD provide a mathematical framework for describing the macroscopic behaviour of magnetised plasmas. For this type of description to be applicable, a number of basic assumptions have to be made. Based on the relevant sections of Goedbloed and Poedts (2004) and Priest (2014), the first of these assumptions is that over distances exceeding the so-called Debye length, λ_D , the plasma is considered to be approximately charge-neutral. Deviations from charge neutrality occur only in small regions defined by the size of the Debye length

$$\lambda_D = \sqrt{\frac{\epsilon_0 k_B T}{nq}}. \quad (1.1)$$

Here, the constituent quantities used are defined in the following manner: $k_B \approx 1.38 \times 10^{-23} \text{ J K}^{-1}$ is Boltzmann's constant, and n is the particle density, and q is the charge of a particle. Further, the permittivity of free space is

$$\epsilon_0 = \frac{1}{\mu_0 c^2} \approx 8.85 \times 10^{-12} \text{ F s}^{-1}, \quad (1.2)$$

where the factors are $\mu_0 = 4\pi \times 10^{-7} \text{ N A}^{-2}$, the permeability of free space, and $c = 299792458 \text{ m s}^{-1}$, the speed of light. A large collection of charged particles can then be considered a plasma if the number density of particles is very large in a sphere with radius $r = \lambda_D$, that is

$$\frac{4\pi n \lambda_D^3}{3} \gg 1. \quad (1.3)$$

The second important condition is that any variation occurs on a length scale much larger than the internal plasma lengths such as the Larmor-radius (or gyroradius),

$$r_L = \frac{mv_p}{|q|B}, \quad (1.4)$$

defined in relation to the motion of a charged particle in a magnetic field. In Equation (1.4), m denotes the mass of the particle, q its charge, v_p the component of its velocity perpendicular to the magnetic field of strength B .

The plasma is also assumed to be in thermodynamic equilibrium, with its distribution functions being close to Maxwellian. This condition is fulfilled on time- and length-scales much larger than the collision times and mean free paths of particles, respectively. The plasma is considered as a single fluid, although this assumption may need to be re-examined in the coolest or rarest parts of the Sun's atmosphere. Important parameters such as the diffusivity, η , or the permeability, μ , are assumed to be uniform within this work, and typical plasma velocities (flow speeds, Alfvén speeds, sound speeds) are treated as non-relativistic. While the inclusion of various other effects is possible, the equations in the following parts are formulated for an inertial (non-rotating) frame. Any terms arising from heat transfer, resistivity, and viscosity are neglected, and only adiabatic, ideal, inviscid plasmas are considered.

Keeping these assumptions in mind, the equations of magnetohydrodynamics may be obtained by averaging the kinetic equations of plasma physics, or as we will proceed to do now, by combining the Maxwell-equations with the equations describing fluid motion and continuity.

1.2.1 The Induction Equation

In order to describe the connection between the generation of magnetic fields and the motion of charged plasma particles, we need to start from Maxwell's equations of electrodynamics. Firstly, Gauss' law

$$\nabla \cdot \mathbf{E} = \frac{\rho^*}{\epsilon_0} \quad (1.5)$$

states that the divergence of the electric field, \mathbf{E} , is given by the electric charge density, ρ^* divided by the permittivity constant ϵ_0 .

Next, Gauss' magnetic law states that no magnetic monopoles exist, as magnetic fields must be solenoidal vector fields:

$$\nabla \cdot \mathbf{B} = 0. \quad (1.6)$$

The third equation can be written as

$$\nabla \times \mathbf{E} = -\frac{\partial \mathbf{B}}{\partial t}. \quad (1.7)$$

This is the Maxwell-Faraday equation stating that a temporally changing magnetic field will generate a spatially varying electric field, and, in turn, a spatially varying electric field will result in the induction of a changing magnetic field.

Finally, we have

$$\nabla \times \mathbf{B} = \mu_0 \mathbf{j} + \frac{1}{c^2} \frac{\partial \mathbf{E}}{\partial t}, \quad (1.8)$$

known as Ampère's law. This equation describes how magnetic fields can be generated by a change in the electric field or an electric current (\mathbf{j}). If we take the assumption of MHD requiring the plasma velocities to be significantly smaller than the speed of light, then the second term of Ampère's law is negligible, and the equation can be re-stated as

$$\nabla \times \mathbf{B} = \mu_0 \mathbf{j}. \quad (1.9)$$

Similarly, the right-hand-side of Equation (1.5) is assumed zero.

Now, we proceed to use Ohm's law to connect the electric, magnetic and velocity fields with the current density:

$$\mathbf{E} + \mathbf{v} \times \mathbf{B} = \eta \mathbf{j}, \quad (1.10)$$

where $\eta = 1/(\mu\sigma)$ is the magnetic diffusivity and σ is the electrical conductivity. Since we are only investigating ideal MHD effects, we can use $\eta = 0$ to simplify Ohm's law to

$$\mathbf{E} + \mathbf{v} \times \mathbf{B} = 0. \quad (1.11)$$

We can express \mathbf{E} from Equation (1.11), and substitute the expression into Equation (1.7) to obtain the induction equation for ideal MHD as

$$\frac{\partial \mathbf{B}}{\partial t} = \nabla \times (\mathbf{v} \times \mathbf{B}). \quad (1.12)$$

This equation describes the generation of magnetic fields. If non-ideal effects can not be neglected, this equation has a second, competing term as well, which is responsible for diffusing away the magnetic fields generated by the first term:

$$\frac{\partial \mathbf{B}}{\partial t} = \nabla \times (\mathbf{v} \times \mathbf{B}) + \eta \nabla^2 \mathbf{B}. \quad (1.13)$$

1.2.2 The Equation of Continuity

The motion of plasma is governed by three other equations: the equation of continuity, motion, and energy, which are coupled to the induction equation through the presence of the velocity term in Equation (1.12). The equation of continuity expresses the conservation of mass, and it may be written in one of the following forms:

$$\frac{D\rho}{Dt} + \rho \nabla \cdot \mathbf{v} = 0, \quad \text{or} \quad \frac{\partial \rho}{\partial t} + \nabla \cdot (\rho \mathbf{v}) = 0, \quad (1.14)$$

where ρ is the mass density, and $D/Dt = \partial/\partial t + \mathbf{v} \cdot \nabla$ is the material or total derivative. In either form, the equation of continuity expresses the fact that the density at a point increases if mass flows into its surrounding region. The opposite is also true, of course, if mass flows out from the environment of a point, the density decreases there.

1.2.3 The Energy Equation

Energy gains and losses within the medium are described by the heat equation,

$$\rho \frac{De}{Dt} + \frac{p D\rho}{\rho Dt} = -\mathcal{L}, \quad (1.15)$$

where \mathcal{L} is the energy loss function, and e is the internal energy per unit mass within the plasma. We restrict our focus to adiabatic processes, which has two consequences. First, the ratio of specific heats, $\gamma = c_p/c_v$ takes the value of 5/3. Secondly, any energy lost is balanced by energy gains, therefore $\mathcal{L} = 0$. To complete the system of MHD equations and simplify the energy equation, we require an equation of state to determine the gas pressure, p . For simplicity, we use the perfect (or ideal) gas law:

$$p = \frac{\bar{R}}{\bar{\mu}} \rho T = \frac{k_B}{m} \rho T, \quad (1.16)$$

which describes in what manner the pressure, density and temperature of the medium are connected using the gas constant \bar{R} , and the mean atomic weight, $\bar{\mu}$, or the mean particle mass (m) and Boltzmann's constant (k_B). For an ideal gas, the internal energy can be expressed as

$$e = c_v T, \quad (1.17)$$

where

$$c_v = \frac{1}{\gamma - 1} \frac{k_B}{m} \quad (1.18)$$

is the specific heat at constant volume. From Equations (1.16), (1.17) and (1.18), the internal energy can be expressed in terms of γ , the gas pressure and the density:

$$e = \frac{1}{\gamma - 1} \frac{k_B p}{m \rho}, \quad (1.19)$$

and the energy equation takes the following form:

$$\rho \frac{D\rho}{Dt} + \frac{\gamma p D\rho}{\rho Dt} = 0. \quad (1.20)$$

1.2.4 The Equation of Motion

Newton's equation of motion for a fluid (plasma) element can be written in the following form:

$$\rho \frac{D\mathbf{v}}{Dt} = \mathbf{F} = -\nabla p + \rho \mathbf{g} + \mathbf{j} \times \mathbf{B} + \rho * \mathbf{E} + \mathbf{F}_v, \quad (1.21)$$

which expresses the acceleration of a fluid element under the effect of a general force \mathbf{F} consisting of a pressure gradient ($-\nabla p$), gravity ($\rho \mathbf{g}$), as well as electromagnetic ($\mathbf{j} \times \mathbf{B} + \rho * \mathbf{E}$) and viscous forces (\mathbf{F}_v). With the consequences of the MHD approximation we have already utilised, and ignoring gravity, our equation of motion in ideal MHD becomes

$$\rho \frac{D\mathbf{v}}{Dt} = \mathbf{F} = -\nabla p + \mathbf{j} \times \mathbf{B}. \quad (1.22)$$

Here, $\mathbf{j} \times \mathbf{B}$ is the Lorentz force, which we can break down into two terms using Ampère's law:

$$\begin{aligned}\mathbf{F}_L &= \mathbf{j} \times \mathbf{B} = \frac{1}{\mu_0} \nabla \times \mathbf{B} \times \mathbf{B} \\ &= \frac{(\mathbf{B} \cdot \nabla) \mathbf{B}}{\mu_0} - \nabla \frac{B^2}{2\mu_0}.\end{aligned}\tag{1.23}$$

The first term in Equation (1.23) is called the magnetic tension force, which is a negative stress in the direction parallel to the field. The second term is the magnetic pressure force, which results in a positive stress in the direction normal to \mathbf{B} .

1.2.5 Summary of the Ideal MHD Equations

Subject to the conditions and simplifications detailed in the sections above, the set of ideal MHD equations governing the behaviour of a continuous plasma permeated by a magnetic field can be summarised as follows:

$$\frac{\partial \rho}{\partial t} + \nabla \cdot (\rho \mathbf{v}) = 0\tag{1.24}$$

$$\rho \frac{D\mathbf{v}}{Dt} = -\nabla p - \frac{1}{\mu} \mathbf{B} \times (\nabla \times \mathbf{B})\tag{1.25}$$

$$\frac{\partial \mathbf{B}}{\partial t} = \nabla \times (\mathbf{v} \times \mathbf{B})\tag{1.26}$$

$$\frac{D}{Dt} \left(\frac{p}{\rho^\gamma} \right) = 0,\tag{1.27}$$

where $\mathbf{v} = (v_x, v_y, v_z)$, \mathbf{B} , p , and ρ are the velocity, magnetic field strength, pressure, and density, respectively, and $\nabla \cdot \mathbf{B} = 0$. Equation (1.24) expresses the conservation of mass, Equations (1.25) and (1.26) are the momentum and induction equations, respectively, and Equation (1.27) is the form of the energy equation for adiabatic processes. This system of equations will be utilised in later Chapters as the starting point for the derivation of dispersion relations for various asymmetric magnetic slab configurations.

1.3 The Study of Waves in the Solar Atmosphere

Numerous observations of oscillatory behaviour in solar atmospheric structures have been made (see eg. Nakariakov and Verwichte (2005); Banerjee et al. (2007); De Pontieu et al. (2007b); Erdélyi and Fedun (2007); Jess et al. (2009); Taroyan and Erdélyi (2009); McIntosh et al. (2011); Morton et al. (2012); Morton et al. (2013)). Since the solar atmosphere is a finely structured magnetised plasma environment, these oscillations can be described within the framework of MHD, using the theory of magnetohydrodynamic waves (MHD waves), which we provide a brief introduction to in the current Section.

1.3.1 Magnetohydrodynamic Waves

We first consider a uniform magnetised plasma environment, where the background physical quantities come under the effect of a small, time-dependent perturbation.

These small perturbations (denoted by index “I”) are added to the background physical parameters (denoted by index “eq”) such that

$$f(\mathbf{r}, t) = f_{eq} + f_I(\mathbf{r}, t), \quad (1.28)$$

where the small perturbation $f_I \ll f$, and the generic parameter f here can stand for the pressure, p , the density, ρ , or the components of the magnetic field strength (B_x, B_y, B_z) and the velocity (v_x, v_y, v_z). Substituting these variables into the ideal MHD equations, and keeping terms only up to first order, we perform a linearisation of the system. Here, we assume that there are no bulk background motions in the plasma, therefore $\mathbf{v}_{eq} = 0$. For more details on such a linearisation of the ideal MHD equations, see e.g. Priest (2014). In brief, it is possible to arrive at a single generalised wave equation for disturbances in a uniform plasma, which has the following form:

$$\frac{\partial^2 \mathbf{v}_I}{\partial t^2} = c_{eq}^2 \nabla(\nabla \cdot \mathbf{v}_I) + (\nabla \times [\nabla \times \{\mathbf{v}_I \times \mathbf{B}_{eq}\}]) \times \frac{\mathbf{B}_{eq}}{\mu_0 \rho_{eq}}. \quad (1.29)$$

We seek plane wave solutions to this equation in the form of

$$\mathbf{v}_I(\mathbf{r}, t) = \mathbf{v}_I \exp(i[\mathbf{k} \cdot \mathbf{r} - \omega t]), \quad (1.30)$$

where \mathbf{k} is the wavenumber vector and ω is the angular frequency. After some algebra, this leads us to

$$\begin{aligned} \omega^2 \mathbf{v}_I = & v_A^2 k^2 \cos^2(\theta_B) - (\mathbf{k} \cdot \mathbf{v}_I) k \cos(\theta_B) \widehat{\mathbf{B}}_{eq} \\ & + ([1 + c_{eq}^2 v_A^2][\mathbf{k} \cdot \mathbf{v}_I] - k \cos(\theta_B)[\widehat{\mathbf{B}}_{eq} \cdot \mathbf{v}_I]) \mathbf{k}. \end{aligned} \quad (1.31)$$

Here, θ_B is the angle between the direction of propagation and the magnetic field, k is the magnitude of the wavenumber vector, $\widehat{\mathbf{B}}_{eq}$ is the unit vector in the direction of the magnetic field, and v_A is the equilibrium Alfvén speed defined as

$$v_A^2 = \frac{B_{eq}^2}{\mu_0 \rho_{eq}}. \quad (1.32)$$

This can be further transformed to give

$$\begin{aligned} (-\omega^2 + k^2 c_{eq}^2 + k^2 v_A^2)(\mathbf{k} \cdot \mathbf{v}_I) &= k^3 v_A^2 \cos(\theta_B) (\widehat{\mathbf{B}}_{eq} \cdot \mathbf{v}_I), \text{ and} \\ k \cos(\theta_B) c_{eq}^2 (\mathbf{k} \cdot \mathbf{v}_I) &= \omega^2 (\widehat{\mathbf{B}}_{eq} \cdot \mathbf{v}_I) \end{aligned} \quad (1.33)$$

There are two types of solutions to Equation (1.33). Firstly, if $(\mathbf{k} \cdot \mathbf{v}_I)$ vanishes, we get the Alfvén wave solutions, propagating with $\omega = \pm \omega_A = \pm k v_A \cos(\theta_B)$. These waves are purely transverse, and they are incompressible perturbations.

The second class of solutions are called magneto-acoustic waves, which are obtained by eliminating $(\mathbf{k} \cdot \mathbf{v}_I)/(\widehat{\mathbf{B}}_{eq} \cdot \mathbf{v}_I)$ between the two equations in Equation (1.33). This leads to a quadratic equation in ω^2 :

$$\omega^4 - \omega^2 k^2 (c_{eq}^2 + v_A^2) + c_{eq}^2 v_A^2 k^4 \cos^2(\theta_B) = 0. \quad (1.34)$$

The magneto-acoustic (or magnetosonic) waves further split into two sub-types, namely, fast and slow modes, which propagate with the fast- and slow-frequencies, defined as:

$$\begin{aligned}\omega_{slow} &= \frac{1}{2}k^2(c_{eq}^2 + v_A^2) \left(1 + \sqrt{1 - 4c_T^2 \cos^2(\theta_B)} \right), \\ \omega_{fast} &= \frac{1}{2}k^2(c_{eq}^2 + v_A^2) \left(1 + \sqrt{1 + 4c_T^2 \cos^2(\theta_B)} \right),\end{aligned}\quad (1.35)$$

where $c_T^2 = (c_{eq}^2 v_A^2)/(c_{eq}^2 + v_A^2)$ is the so-called tube speed or cusp speed. Both the Alfvén and the magneto-acoustic waves can propagate forward along the magnetic field lines ($\omega = \omega_j$, where $j = A, slow, fast$ for Alfvén, slow, and fast modes, respectively), or backward, opposite the direction of the field ($\omega = -\omega_j$).

1.3.2 MHD Waves in Magnetic Slabs

The solar atmosphere is very finely structured by gravity and magnetic fields, therefore, it is worthwhile to examine wave propagation in structured media as well. The two fundamental configurations often examined and applied in solar physics are those of the magnetic slab and the magnetic flux tube. Here, we only focus on magnetic slabs, but for a brief summary of wave propagation in flux tubes, see e.g. Priest (2014), or, for a full derivation and investigation, compare with Edwin and Roberts (1983). In a series of seminal studies, Roberts (1981a) and Edwin and Roberts (1982) described the properties of magneto-acoustic waves first at an interface (Roberts, 1981a), then in a magnetic slab sandwiched between two, symmetric regions of a non-magnetic environment (Roberts, 1981b), and, finally, in a magnetic slab embedded in a symmetric, magnetic environment (Edwin and Roberts, 1982). These studies only looked at structuring normal to the magnetic field, and sought plane wave solutions propagating along the magnetic field lines, which is the approach we adopt in our later, asymmetric studies as well.

In this section, we briefly summarise the study conducted about the magnetic slab in a symmetric, magnetic environment, as the other two cases mentioned above can be considered building blocks towards establishing this model. To be more exact, a slab can be considered a region of magnetised plasma embedded between two magnetic interfaces. Furthermore, the case of the slab in a non-magnetic environment can be recovered from the more general configuration of the slab being placed in a magnetic environment, if in the last step, the magnetic fields are chosen to be zero.

In their study, Edwin and Roberts (1982) considered a slab of plasma with width $2x_0$ permeated by an equilibrium magnetic field, located between two interfaces linking it to a symmetric plasma environment also woven through by an equilibrium magnetic field. By linearising the ideal MHD equations, and looking for plane wave solutions propagating along the field, they obtained a dispersion relation for the eigenmodes of the symmetric magnetic slab in the following form:

$$\rho_e(v_{Ae}^2 - \omega^2)m_0 \begin{pmatrix} \tanh(m_0 x_0) \\ \coth(m_0 x_0) \end{pmatrix} + \rho_0(k^2 v_{A0}^2 - \omega^2)m_e = 0. \quad (1.36)$$

Here, each quantity indexed with 0 refers to the inside of the slab, while parameters with the index e describe the environment. The coefficients m_e and m_0 are related

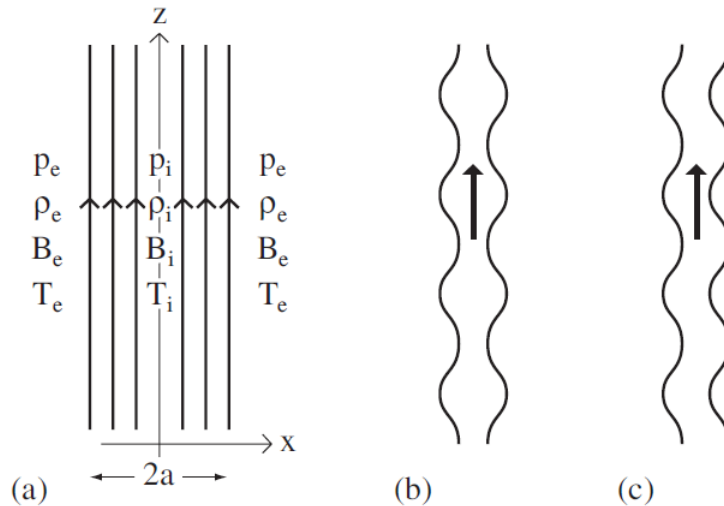


Figure 1.3: Model and eigenmodes of a symmetric magnetic slab of width $2a$. Panel (a) illustrates the equilibrium configuration, panel (b) depicts a sausage mode, while panel (c) shows a kink mode oscillation. The source of this figure is Priest (2014).

to the characteristic speeds (Alfvén, sound and tube speeds) in each region:

$$m_j^2 = \frac{(k^2 v_{Aj}^2 - \omega^2)(k^2 c_j^2 - \omega^2)}{(v_{Aj}^2 + c_j^2)(k^2 c_{Tj}^2 - \omega^2)}, \quad j = 0, e. \quad (1.37)$$

The top line of Equation (1.36) describes so-called sausage modes, while the bottom line pertains to kink modes. Sausage modes are waves which show amplitudes distributed in an antisymmetric manner around the centre of the slab ($x = 0$), while kink modes show a symmetric distribution of wave power. An illustration of these eigenmodes can be seen in Figure 1.3. The eigenmodes can further be classified as surface or body waves, depending on whether they are evanescent or oscillatory within the slab. A more detailed discussion of these modes and their asymmetric counterparts can be found in Chapter 2.

1.3.3 Solar Magneto-Seismology

The solar atmosphere is a dynamic plasma environment that shows complex structuring thanks to its ubiquitous magnetic fields. In understanding and measuring the properties of this rich variety of solar waveguides, the constantly evolving methods of solar magneto-seismology (SMS) provide a useful and versatile toolkit. These methods of SMS rely on the fact that the physical parameters and the geometric structuring of the medium determine the properties of the supported waves. From direct observations, we are able to determine some of these parameters, such as temperature, density, or geometric size. We can also measure temporal and spatial wave properties like frequencies, periods and amplitudes, which is often more easily accomplished than a direct measurement of e.g. magnetic field strength or transport coefficients could be carried out. Furthermore, from theoretical investigations, we can obtain a mathematical relationship between these quantities (see for example the magnetic slab system summarised in Section 1.3.2). The combination of these

models and observations is then utilised to solve (often difficult) inversion problems, and so allow us to draw conclusions about “missing” parameters of the solar atmospheric plasma, which would be difficult to measure directly (Erdélyi (2006a); Erdélyi (2006b); Banerjee et al. (2007); Andries et al. (2009); Arregui and Goossens (2019)).

MHD waves have played a two-fold role in improving our understanding of the solar plasma environment. Beyond their newer, diagnostic role in SMS, these waves have always been thought to serve as one possible solution to the atmospheric heating problem described at the beginning of this introduction. Their widespread presence within the solar atmosphere and fundamental part in our physical understanding meant that the theory of MHD wave propagation developed rapidly (De Moortel and Nakariakov, 2012), and the first magneto-seismological studies were conducted very early in the process (such as Rosenberg (1970); Roberts et al. (1984)). The majority of these investigations employed methods of temporal seismology, which encompasses methods relying on the observed frequency (or period) of MHD waves to be used in the estimation of background quantities. The maximum available telescopic resolution limited the range of fine-scale results achievable by both temporal and spatial seismology, the latter of which focuses on detecting the wave power distribution of eigenfunctions corresponding to a theoretical model. As one of the first examples of using spatial SMS techniques, Uchida gave an estimate of the magnetic field structure in the solar corona based on observations and theoretical analyses of Moreton waves (Uchida, 1970). An brief overview of early seismological studies can be found in e.g. Allcock and Erdélyi (2018) and Allcock et al. (2019).

Generally speaking, the theory of MHD waves could advance faster than the resolution of detectors improved. The existence of MHD waves in the solar atmosphere, especially in the corona, was predicted nearly half a century ago (Uchida, 1968, Habbal et al., 1979, Roberts, 1981a). However, in the past few decades, we have essentially entered a “golden age” of magneto-seismology, as unprecedented spatial and temporal resolutions were achieved. The detection of transversal (fast magneto-acoustic) waves in coronal loops, in 1998, with the help of TRACE [Transition Region and Coronal Explorer], has become a symbol of this scientific turning point (Aschwanden et al. (1999); Nakariakov et al. (1999); Ruderman and Erdélyi (2009a); De Moortel and Nakariakov (2012)). These oscillations were classified as fast kink modes, although the nomenclature is the subject of some debate in the literature, with some sources emphasising the similarities between Alfvén and kink mode properties and advocating for calling these oscillations Alfvénic (Aschwanden et al. (1999); Nakariakov et al. (1999); Goossens et al. (2009)). Since this first and historic direct observational detection of MHD waves in coronal loops, a number of other magnetic structures, such as spicules, flares, coronal arcades, and plumes, have also been observed as drivers or waveguides for perturbations in the solar atmospheric plasma (Aschwanden, 2005; De Moortel, 2005; Banerjee et al., 2007; de Moortel, 2009, Mathioudakis et al., 2013, Arregui, 2015). This is for the most part thanks to the continuing improvements in both the temporal and spatial resolution of detectors, allowing us to apply our theories and test our predictions in ever newer environment, down to the smallest elements of the fine structure. Additionally, the availability and variety of both space-based observatories, for example SOHO [Solar and Heliospheric Observatory], SDO [Solar Dynamics Observatory], and STEREO [Solar-Terrestrial RElations Observatory], and ground-based telescopes, such as

DST [Richard B. Dunn Solar Telescope], and SST [Swedish Solar Telescope] has been increasing (Nakariakov and Verwichte (2005); Banerjee et al. (2007); Ruderman and Erdélyi (2009a); Wang (2011); Arregui et al. (2012); De Moortel and Nakariakov (2012); Mathioudakis et al. (2013)). Currently, we are living in the age of the next generation of observational mega-projects, such as the DKIST (Daniel K. Inouye Solar Telescope), which has recently begun its operations, and, within a decade, the planned completion of EST (European Solar Telescope).

1.4 Outline

The aim of this study is to investigate the standing and propagating MHD waves in various asymmetric solar waveguides, through providing analytical and numerical solutions to the equations describing wave dispersion, as well as developing tools for solar magneto-seismology. The research carried out so far has been summarised in 8 Chapters. This current Chapter contains an introduction to the topic and an overview of previous studies in the area.

Chapter 2 sets up the first model we investigated in detail, namely, that of a magnetic slab embedded in an asymmetric magnetic environment. The detailed description of the equilibrium is followed by the derivation of the dispersion relation governing magneto-acoustic waves propagating along the field lines in this slab system. Next, we compare our results to earlier studies describing either magnetic or asymmetric environments of the central slab. In the last part of Section 2.2, we describe the important features of quasi-sausage and quasi-kink eigenmodes in an asymmetric magnetic slab in detail. Next, we aim to ease the understanding of these asymmetric eigenmodes through a mechanical analogy, and by presenting a couple of illustrative cases of numerical results. We explore the effects of density and magnetic asymmetries and describe the phenomenon of avoided crossing between the eigenmodes.

Chapter 3 deals with the further analytical investigation of this multi-layered waveguide system. We provide approximate analytical solutions to the dispersion relation from Chapter 2 in various geometric and magnetic limits relevant to applications in solar physics. First, we describe the limiting behaviour of surface and body modes in thin and wide slabs, then we move on to investigate the dispersion relation in the high- and low plasma- β limits. In addition, we also discuss the case when the slab system is considered incompressible.

In Chapter 4, we suggest and develop applications of the slab model to various features of the solar atmosphere. We achieve this by combining our analytical approximations from Chapter 3, and complementing them with a numerical investigation of MHD waves we expect to observe in a given solar structure based on information on characteristic speeds, densities, and physical sizes of solar atmospheric waveguides currently available in the literature. The suggested applications move from the global structuring of the solar atmosphere (Sections 4.2 and 4.2.1) to more localised features. First, we discuss potential coronal waveguides (Sections 4.3 and 4.4) in the form of plumes and prominences. Finally, we present suggested lower atmospheric applications in the environments of sunspot light bridges (Section 4.5) and magnetic bright points (Section 4.6).

Chapter 5 further generalises solar magneto-seismological tools developed for non-magnetic asymmetric waveguides by Allcock and Erdélyi (2017). These seis-

mology techniques rely on the effects that the environmental asymmetry has on the distribution of wave power within the eigenmodes of the slab system. In Section 5.2, we describe the amplitude ratio method, providing analytical and numerical results for the cases of both quasi-sausage and quasi-kink modes. We also utilise the observable displacement amplitudes on the slab boundaries to define and investigate so-called quasi-symmetric waves, which appear symmetric but propagate in an asymmetric waveguide. Then in Section 5.3, we calculate the minimum perturbation shift of quasi-sausage and quasi-kink modes, also providing further estimates of the internal Alfvén speed of the central slab in the process.

In Chapter 6, we focus on standing waves in asymmetric waveguides, and the additional seismological tools we can develop based on their characteristics. First, we investigate standing waves in an asymmetric non-magnetic slab system, before we move on to generalising the results for the case of an asymmetric magnetic environment.

Finally, in Chapter 7, we summarise the main results of the above-mentioned series of studies, and suggest further improvements of the model of slab families which could be investigated in the future as a natural extension of our research.

Chapter 2

Propagating Waves in an Asymmetric Magnetic Slab

Abstract

Building on previous slab models of the solar atmosphere, the current Chapter further generalises the model of a magnetic slab embedded in an asymmetric environment by introducing external asymmetric magnetic fields. The dispersion relation is for magneto-acoustic waves propagating along the slab is derived for unspecified and then for weak asymmetry. The asymmetric eigenmodes of the asymmetric magnetic slab are described, and a mechanical analogy to the asymmetric slab model is presented. Finally, the avoided crossings of quasi-sausage and quasi-kink eigenmodes are studied and a few examples of numerical solutions of the full dispersion relation are explored in detail. This Chapter was based on the publications Zsámberger et al. (2018), Section 7 of Zsámberger and Erdélyi (2020) and Section 3.2 of Allcock et al. (2019). In more detail, the author of this thesis is primarily responsible for Zsámberger et al. (2018), with the calculations in its Section 4 being shared between and concurrently checked by all authors. Furthermore, Zsámberger and Erdélyi (2020) and the referenced Section of Allcock et al. (2019) are also the author’s own work.

2.1 Chapter Introduction

As mentioned before, MHD theory and MHD waves, specifically, play an important role in understanding and describing various structures and processes of our Sun, with their two main applications being methods of energy transfer and tools for diagnosing the solar plasma (Andries et al., 2009; Mathioudakis et al., 2013).

The focus of this study is on constructing simple slab models of solar atmospheric waveguides, building on a long tradition of continually evolving Cartesian theoretical modelling (Roberts (1981a); Roberts (1981b); Edwin and Roberts (1982); Joarder and Roberts (1992a); Joarder and Roberts (1992b); Joarder and Roberts (1993); Allcock and Erdélyi (2017); Barbulescu and Erdélyi (2018); Shukhobodskaja and Erdélyi (2018)). While the “classical” models of magnetic slabs (Roberts, 1981a,b) were built upon the assumption that the environment surrounding the magnetic slab was symmetric, recent advances in the field have generalised this geometry to include various sources of external asymmetry.

The first such study was published by Allcock and Erdélyi (2017), and it con-

ducted a detailed analytical examination of waves propagating in a magnetic slab which was enclosed between two semi-infinite regions of non-magnetised plasma, where the densities, ρ , pressures, p , and temperatures, T , were allowed to be different from one another in all three regions delineated by the two interfaces (see Figure 2.1). Their work also conducted a parametric analysis into the influence of the relative magnitudes of the external densities on wave dispersion in this configuration.

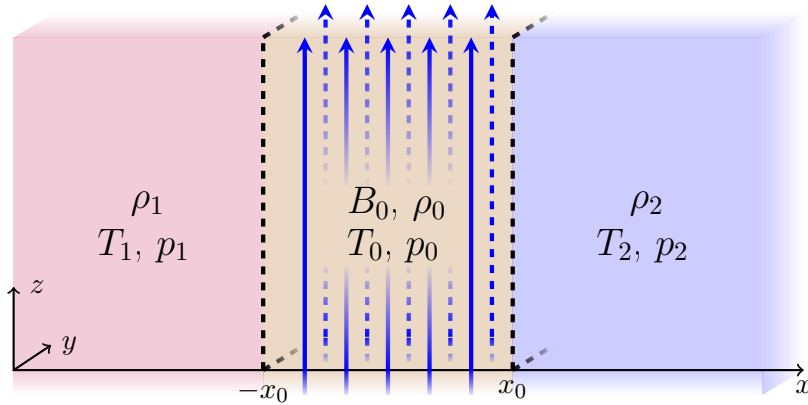


Figure 2.1: Illustration of the equilibrium configuration for a magnetic slab embedded in an asymmetric non-magnetic environment. Figure adapted from Allcock et al. (2019).

It was found that the general dispersion relation for magneto-acoustic waves propagating along the slab, parallel to the magnetic field lines, does not decouple into two separate equations for sausage- and kink-type modes. This mathematically reflects that the eigenmodes of the such a slab possess mixed characteristics of sausage and kink modes once asymmetry is introduced into the system (as also explained in Section 2.2). The model described in Allcock and Erdélyi (2017) was then used to develop new methods to be applied in solar magneto-seismology based on the fact that the amplitudes of the eigenmodes across the slab are affected by the asymmetric thermodynamic equilibrium conditions (Allcock and Erdélyi, 2018), which will be discussed further in Chapter (5).

The model of a magnetic slab in an asymmetric environment which will be introduced in this Chapter possesses an intermediate position among multi-layered waveguide models of the solar atmosphere. It serves as a generalisation of modelling the magnetic slab in an asymmetric, non-magnetic environment Allcock and Erdélyi (2017). At the same time, it can be considered a special case of the n -slab system described in Allcock et al. (2019), when $n = 1$ and a single slab is enclosed between asymmetric external regions.

In this Chapter, we expand upon the results contained Zsámberger et al. (2018), Zsámberger and Erdélyi (2020), and Allcock et al. (2019) to describe the effects of introducing asymmetric magnetic fields into the magnetic slab model of solar atmospheric structures. In Section 2.2, we summarise the modelling assumptions and the process of deriving the dispersion relation for waves propagating in an asymmetric magnetic slab. We further compare our results with previous studies, and describe the behaviour of eigenmodes in an asymmetric slab system in more detail. In Section 2.3, we include a generalisation of the mechanical analogy for asymmetric eigenmodes introduced by Allcock and Erdélyi (2017). In Section 2.4,

we investigate how any changes in the relative magnitudes of the external densities and magnetic field strengths affect the angular frequencies of the solutions. Finally, in Section 2.5, we provide a summary and brief discussion of the results contained in this Chapter.

2.2 The General Dispersion Relation for a Slab in an Asymmetric Magnetic Environment

This Section provides a detailed explanation of the equilibrium configuration of an asymmetric magnetic slab, as well as the steps of deriving the equation governing wave dispersion in such a geometry. The study of magnetic asymmetry in the system is motivated by the fact that magnetic fields are woven through and through the interconnected solar atmosphere, creating a fine structuring of the solar plasma (Roberts (1981a); De Pontieu et al. (2005); Komm et al. (2015)). In such a complex and dynamic environment, it is reasonable to expect that we should find asymmetries on various scales, rather than the perfectly symmetric environments studied in detail in classical slab models ((Roberts, 1981b); Edwin and Roberts (1982)). Therefore, it is a worthwhile endeavour to further the process of including various sources of asymmetry in well-understood slab systems, and investigating the additional wave physics arising with each added step of complexity. After the study of the magnetic slab in an asymmetric, non-magnetic environment carried out by (Allcock and Erdélyi, 2017), one of the next logical steps in the further generalisation of the slab model is to re-introduce the external magnetic fields, similarly to the configuration of a slab in a magnetic environment described by Edwin and Roberts (1982), however, with the new addition of magnetic asymmetry outside of the slab.

2.2.1 Description of the equilibrium

The equilibrium configuration investigated here is a three-dimensional slab system filled with inviscid, static, ideal plasma, permeated by an equilibrium magnetic field, $B_j(x)\hat{\mathbf{z}}$, where $j = 0, 1, 2$ and $\hat{\mathbf{z}}$ is the unit vector in the vertical direction. Two interfaces, placed at $x = \pm x_0$, divide this volume up into three separate domains of uniform plasma with different thermodynamic and magnetic parameters across the domains:

$$N(x) = \begin{cases} N_1 & x < -x_0, \\ N_0 & |x| < x_0, \\ N_2 & x_0 < x, \end{cases} \quad (2.1)$$

where N_j denotes any of the following physical parameters: densities, ρ , pressures, p , temperatures, T , and magnetic field strengths, B , and $N_j = \text{constant}$ (for $j = 0, 1, 2$). Throughout the study, quantities describing the inside of the slab are denoted by the subscript $j = 0$, while the parameters of the left- and right-hand-side environmental regions carry the subscripts $j = 1, 2$, respectively. The slab system is unbounded in the y - and z - directions. In this model, the effects of gravity or background bulk motions are neglected, in order to focus on the physical consequences of the thermodynamic and magnetic asymmetry present in the system.

Figure 2.2 provides an illustration of the equilibrium configuration described here. The magnetic slab of pressure p_0 , density ρ_0 and temperature T_0 is depicted

2.2. THE GENERAL DISPERSION RELATION FOR A SLAB IN AN ASYMMETRIC MAGNETIC ENVIRONMENT

with the shaded orange region in the centre, where $|x| \leq x_0$. The different colouring (pink and blue) illustrates the density, temperature and pressure asymmetry of the two semi-infinite environmental regions, $x < -x_0$ and $x > x_0$. The blue arrows illustrate the asymmetric magnetic fields permeating the entire volume, $B_0\hat{z}$, $B_1\hat{z}$ and $B_2\hat{z}$, while the dashed black lines outline the boundaries of the slab.

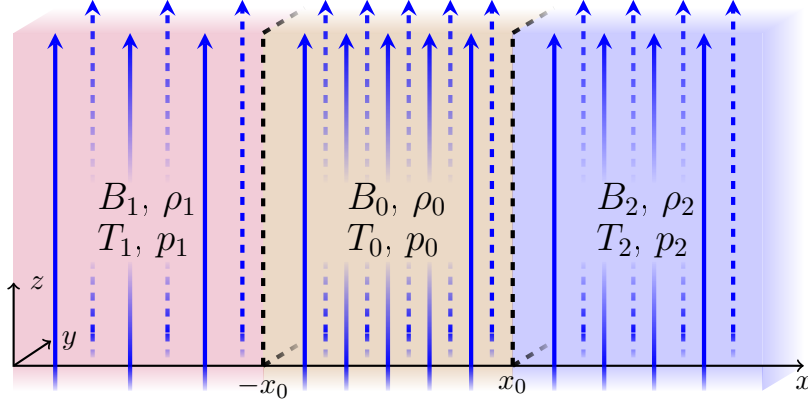


Figure 2.2: The equilibrium conditions: inside the slab, $|x| \leq x_0$ (medium grey), and outside the slab, $x < -x_0$ and $x > x_0$ (light and dark grey). The red arrows illustrate the vertical magnetic fields, $B_0\hat{z}$, $B_1\hat{z}$, and $B_2\hat{z}$; the dashed black lines outline the boundaries of the slab.

For the stability of the equilibrium conditions, the condition of equilibrium total pressure balance must be fulfilled at each interface. This required that the total (gas plus magnetic) pressure should be constant in all three domains:

$$p_1 + \frac{B_1^2}{2\mu} = p_0 + \frac{B_0^2}{2\mu} = p_2 + \frac{B_2^2}{2\mu}, \quad (2.2)$$

where μ is the permeability of free space. It is possible to rewrite this pressure balance condition in terms of the characteristic speeds and densities of each region. The sound speed is defined as $c_j = \sqrt{\gamma p_j / \rho_j}$, for $j = 0, 1, 2$. Here, γ denotes the adiabatic index. Since we assume that the plasma composition is the same in the entire volume, both γ and μ are uniform across the entire slab system. The Alfvén speeds can then be expressed as $v_{Aj} = B_j / \sqrt{\rho_j \mu}$, for $j = 0, 1, 2$. With these definitions, Equation (2.2) can be transformed into a relationship between the characteristic speeds and the density ratios of any two of the three domains:

$$\frac{\rho_j}{\rho_k} = \frac{c_k^2 + \frac{1}{2}\gamma v_{Ak}^2}{c_j^2 + \frac{1}{2}\gamma v_{Aj}^2}, \quad \text{where } j = 0, 1, 2; \quad k = 0, 1, 2; \quad j \neq k. \quad (2.3)$$

Equation (2.3) expresses a useful connection between the three domains, which will be utilised in various analytical approximations of the dispersion relation.

2.2.2 Derivation of the dispersion relation

The behaviour of any material or disturbances within the slab and its magnetic environment are governed by the ideal MHD equations (Equations 1.24 - 1.27) stated in Section 1.2.5.

In order to proceed, these equations are linearised about a static basic state. Since all three regions of the volume are magnetic and have the same configuration, we only demonstrate the intermediate steps of transforming the equations on the parameters describing the slab itself. Small perturbations are added to the equilibrium quantities as

$$\begin{aligned}\mathbf{v}(\mathbf{r}, t) &= \mathbf{v}_I(\mathbf{r}, t), & \rho(\mathbf{r}, t) &= \rho_{eq} + \rho_I(\mathbf{r}, t), \\ \mathbf{B}(\mathbf{r}, t) &= \mathbf{B}_{eq} + \mathbf{B}_I(\mathbf{r}, t), & p(\mathbf{r}, t) &= p_{eq} + p_I(\mathbf{r}, t),\end{aligned}\quad (2.4)$$

where the subscripts eq and I denote equilibrium quantities and perturbations, respectively. Where f may be any of the four parameters above, we impose the condition that $|f_I/f_{eq}| < 0.1$, in order for the perturbations to be considered linear.

We substituting the perturbed variables from (2.4) into the system of ideal MHD equations (Equations 1.24 - 1.27), and neglect second-order terms to arrive at the following set of first-order equations:

$$\frac{\partial \rho_I}{\partial t} + \rho_{eq} \nabla \cdot \mathbf{v}_I = 0 \quad (2.5)$$

$$\rho_{eq} \frac{\partial \mathbf{v}_I}{\partial t} = -\nabla \left(p_I + \frac{1}{\mu} \mathbf{B}_{eq} \mathbf{B}_I \right) + \frac{1}{\mu} \mathbf{B}_{eq} \frac{\partial \mathbf{B}_I}{\partial z} \quad (2.6)$$

$$\frac{\partial \mathbf{B}_I}{\partial t} = -\mathbf{B}_{eq} (\nabla \cdot \mathbf{v}_I) + \mathbf{B}_{eq} \frac{\partial \mathbf{v}_I}{\partial t} \quad (2.7)$$

$$\frac{\partial p_I}{\partial t} = -c_{eq}^2 \rho_{eq} \nabla \cdot \mathbf{v}_I. \quad (2.8)$$

Here $c_{eq} = \sqrt{\gamma p_{eq} / \rho_{eq}}$ is the sound speed in the actual domain. Consequently, when we consider the full slab system again at the end of the derivation process, c_{eq} will take the values c_0 , c_1 , and c_2 for the slab and the left- and right-hand-side of its environment, respectively. Note that the same indexing will apply to the Alfvén- and tube-speeds later.

The components of the induction equation (Equation 2.7) show how the components of the velocity- and magnetic field perturbations affect one another:

$$\begin{aligned}\frac{\partial B_{I,x}}{\partial t} &= B_{eq} \frac{\partial v_{I,x}}{\partial z} \\ \frac{\partial B_{I,y}}{\partial t} &= B_{eq} \frac{\partial v_{I,y}}{\partial z} \\ \frac{\partial B_{I,z}}{\partial t} &= B_{eq} (-\nabla \cdot \mathbf{v}_I) \frac{\partial v_I}{\partial z}.\end{aligned}\quad (2.9)$$

With p_{eq} and ρ_{eq} being constants, the equations can be further transformed, and, using the components of the induction equation, the components of the momentum equation can be rewritten as

$$\begin{aligned}\frac{\partial^2 v_{I,x}}{\partial t^2} &= \frac{\partial}{\partial x} \left(\left(c_{eq}^2 + v_{eq,A}^2 \right) \nabla \cdot \mathbf{v}_I - v_{eq,A}^2 \frac{\partial v_{I,z}}{\partial z} \right) + v_{eq,A}^2 \frac{\partial^2 v_{I,x}}{\partial z^2} \\ \frac{\partial^2 v_{I,y}}{\partial t^2} &= \frac{\partial}{\partial y} \left(\left(c_{eq}^2 + v_{eq,A}^2 \right) \nabla \cdot \mathbf{v}_I - v_{eq,A}^2 \frac{\partial v_{I,z}}{\partial z} \right) + v_{eq,A}^2 \frac{\partial^2 v_{I,y}}{\partial z^2} \\ \frac{\partial^2 v_{I,z}}{\partial t^2} &= c_{eq}^2 \frac{\partial}{\partial z} (\nabla \cdot \mathbf{v}_I),\end{aligned}\quad (2.10)$$

2.2. THE GENERAL DISPERSION RELATION FOR A SLAB IN AN ASYMMETRIC MAGNETIC ENVIRONMENT

where $v_{eq,A} = \frac{B_{eq}}{\sqrt{\rho_{eq}\mu}}$ is the Alfvén speed in the central domain, and the same indexing will apply to it as to the sound speeds before.

We seek to describe MHD waves guided along the slab (in the z -direction), therefore we look for plane wave solutions of the form

$$\begin{aligned} v_{I,x}(\mathbf{x}, t) &= \hat{v}_x(x)e^{i(kz-\omega t)}, \\ v_{I,y}(\mathbf{x}, t) &= 0, \\ v_{I,z}(\mathbf{x}, t) &= \hat{v}_z(x)e^{i(kz-\omega t)}. \end{aligned} \quad (2.11)$$

Here, $\mathbf{x} = x\hat{\mathbf{x}} + y\hat{\mathbf{y}} + z\hat{\mathbf{z}}$ is the displacement vector, ω is the angular frequency of waves, and k denotes the z -component of the wavenumber vector defined as $\mathbf{k} = (0, 0, k)$. The perturbations in the other variables (p , ρ , $B_{I,x}$, $B_{I,y}$, $B_{I,z}$) are written in an analogous form with an x -dependent amplitude.

Substituting these Fourier-forms into the components of the momentum equation (Equations (2.10)), we obtain the following equations (where $'$ denotes $\frac{\partial}{\partial x}$ derivatives):

$$-\omega^2 \hat{v}_{I,x} = \left(c_{eq}^2 + v_{eq,A}^2\right) \left(\hat{v}_{I,x}'' + ik\hat{v}_{I,z}'\right) - v_{eq,A}^2 ik\hat{v}_{I,z}' - v_{eq,A}^2 k^2 \hat{v}_{I,x} \quad (2.12)$$

$$-\omega^2 \hat{v}_{I,z} = c_{eq}^2 ik \left(\hat{v}_{I,x}' + ik\hat{v}_{I,z}\right) \quad (2.13)$$

Now, taking the partial derivative of (2.13) with respect to x yields the relation

$$\hat{v}_{I,z}' = \frac{ic_{eq}^2 k}{\left(k^2 c_{eq}^2 - \omega^2\right)} \hat{v}_{I,x}'' \quad (2.14)$$

Combining Equation (2.14) with equation (2.12) leads to an ordinary differential equation (ODE) governing plasma behaviour inside the slab. The derivation presented above may be repeated for the other two domains as well, now introducing the indices to $j = 0, 1, 2$ for quantities inside, to the left, and to the right of the slab, respectively. The ODEs governing the three domains may be summarised as:

$$\hat{v}_x'' - m_j^2 \hat{v}_x = 0, \quad (2.15)$$

where

$$m_j^2 = \frac{\left(k^2 v_{Aj}^2 - \omega^2\right) \left(k^2 c_j^2 - \omega^2\right)}{\left(v_{Aj}^2 + c_j^2\right) \left(k^2 c_{Tj}^2 - \omega^2\right)}, \quad j = 0, 1, 2, \quad (2.16)$$

are wavenumber coefficients and

$$c_{Tj}^2 = \frac{v_{Aj}^2 c_j^2}{v_{Aj}^2 + c_j^2} \quad (2.17)$$

are the tube speeds for each domain ($j = 0, 1, 2$).

The solutions to Equations (2.15) in each region are linear combinations of the hyperbolic functions. These Equations provide a full description of magneto-acoustic waves guided by the slab system, including both trapped and leaky, as well as surface and body mode oscillations (further details on these will be provided below). We aim to find “sustainable” eigenmodes of the asymmetric slab system, meaning that

the modes should be able to persist without the presence of a continuous source of energy / driver. Leaky modes would keep radiating energy away from the slab, which is why we do not further consider them in our investigation. Therefore, the physically realistic solutions we are looking for require the perturbations in the slab to have no effect on plasma far away from the system. This means that the waves must be evanescent outside the slab and imposes the restriction on the amplitude \hat{v}_x that, as $x \rightarrow \pm\infty$, $\hat{v}_x \rightarrow 0$. For the ODEs describing the external regions, this means that the parameters m_1 and m_2 must fulfil $m_1^2 > 0$ and $m_2^2 > 0$. Note, however, that inside the slab, solutions can still be either evanescent (surface waves) or oscillatory (body waves).

With these restrictions in observed, the general solution to ODEs Equation (2.15) takes the form

$$\hat{v}_x(x) = \begin{cases} A (\cosh m_1 x + \sinh m_1 x), & x < -x_0, \\ B \cosh m_0 x + C \sinh m_0 x, & |x| < x_0, \\ D (\cosh m_2 x - \sinh m_2 x), & x_0 < x. \end{cases} \quad (2.18)$$

Here, A , B , C and D are arbitrarily chosen real constants. Physical solutions further require that all solutions fulfil two boundary conditions, namely, the continuity of total pressure and velocity perturbations across the slab boundaries at $x = \pm x_0$.

A useful step before imposing the boundary conditions on the solutions described by (2.18) is to examine the relationship between the total pressure perturbation ($P = P(x)$) and the velocity perturbation. This can be found from combining the continuity (2.5) and the energy (2.8) equations, which yields

$$\frac{\partial p}{\partial t} = -\rho_j c_j^2 \nabla \cdot \mathbf{v} \quad (2.19)$$

for $j = 0, 1, 2$. The total pressure perturbation is the sum of the gas- and the magnetic pressure perturbation. In this case, it can be expressed as

$$P(x) = p_g + \frac{B_j}{\mu} b_z \quad (\text{for } j = 0, 1, 2). \quad (2.20)$$

Substituting the Fourier forms of the solutions $p(\mathbf{r}, t) = \hat{p}(x)e^{i(kz - \omega t)}$ and similar forms for other variables as defined above into (2.19), and then into the expression of the total (plasma + magnetic) pressure (2.20) leads to

$$\hat{P} = -\frac{i\rho_j}{\omega} \frac{k^2 v_{Aj}^2 - \omega^2}{m_j^2} \hat{v}'_x = \frac{\Lambda_j}{m_j} \hat{v}'_x, \quad (2.21)$$

for the expression of the total pressure variation, where

$$\Lambda_j = -\frac{i\rho_j}{\omega} \frac{k^2 v_{Aj}^2 - \omega^2}{m_j} \quad (j = 0, 1, 2). \quad (2.22)$$

Now applying the boundary conditions yields four homogeneous algebraic equations in terms of the constants A , B , C , and D listed below:

- continuity of \hat{v}_x at $x = -x_0$

$$A (\cosh m_1 x_0 - \sinh m_1 x_0) = B \cosh m_0 x_0 - C \sinh m_0 x_0 \quad (2.23)$$

2.2. THE GENERAL DISPERSION RELATION FOR A SLAB IN AN
ASYMMETRIC MAGNETIC ENVIRONMENT

- continuity of \hat{v}_x at $x = x_0$

$$B \cosh m_0 x_0 + C \sinh m_0 x_0 = D (\cosh m_2 x_0 - \sinh m_2 x_0) \quad (2.24)$$

- continuity of \hat{P} at $x = -x_0$

$$\begin{aligned} & -\frac{i\rho_1}{\omega} \frac{k^2 v_{A1}^2 - \omega^2}{m_1^2} A m_1 (-\sinh m_1 x_0 + \cosh m_1 x_0) = \\ & -\frac{i\rho_0}{\omega} \frac{k^2 v_{A0}^2 - \omega^2}{m_0^2} m_0 (C \cosh m_0 x_0 - B \sinh m_0 x_0) \end{aligned} \quad (2.25)$$

- continuity of \hat{P} at $x = x_0$

$$\begin{aligned} & -\frac{i\rho_0}{\omega} \frac{k^2 v_{A0}^2 - \omega^2}{m_0^2} m_0 (C \cosh m_0 x_0 + B \sinh m_0 x_0) = \\ & -\frac{i\rho_2}{\omega} \frac{k^2 v_{A2}^2 - \omega^2}{m_2^2} D m_2 (\sinh m_2 x_0 - \cosh m_2 x_0) \end{aligned} \quad (2.26)$$

To make the derivation more concise, from this point onwards the notation

$$\begin{aligned} C_1 &= \cosh m_1 x_0, & S_1 &= \sinh m_1 x_0, \\ C_0 &= \cosh m_0 x_0, & S_0 &= \sinh m_0 x_0, \\ C_2 &= \cosh m_2 x_0, & S_2 &= \sinh m_2 x_0. \end{aligned} \quad (2.27)$$

shall be applied. This way, the system of equations (2.23) - (2.26) can be summarized in a matrix form as

$$\begin{bmatrix} C_1 - S_1 & -C_0 & S_0 & 0 \\ 0 & C_0 & S_0 & S_2 - C_2 \\ -\Lambda_1 (C_1 - S_1) & -\Lambda_0 S_0 & \Lambda_0 C_0 & 0 \\ 0 & \Lambda_0 S_0 & \Lambda_0 C_0 & -\Lambda_2 (S_2 - C_2) \end{bmatrix} \begin{bmatrix} A \\ B \\ C \\ D \end{bmatrix} = \begin{bmatrix} 0 \\ 0 \\ 0 \\ 0 \end{bmatrix}.$$

In order for non-trivial solutions to exist, the determinant of this matrix (M_0) should be zero. By further introducing the notation

$$\tau_0 = \tanh m_0 x_0, \quad (2.28)$$

and using the definition of Λ_j provided in Equation (2.22), this condition can be expressed as

$$0 = -2\Lambda_0^2 - \Lambda_0 \Lambda_2 \tau_0 - \Lambda_0 \Lambda_1 \frac{1}{\tau_0} - 2\Lambda_1 \Lambda_2 - \Lambda_0 \Lambda_2 \frac{1}{\tau_0} - \Lambda_0 \Lambda_1. \quad (2.29)$$

By collecting the terms containing τ_0 or $1/\tau_0$, respectively, we obtain the full dispersion relation for the model of the magnetic slab embedded in an asymmetric magnetic environment as

$$2(\Lambda_0^2 + \Lambda_1 \Lambda_2) + \Lambda_0 (\Lambda_1 + \Lambda_2) \left[\tau_0 + \frac{1}{\tau_0} \right] = 0. \quad (2.30)$$

By substituting Λ_j , for $j = 0, 1, 2$, into Equation (2.30), we can express the dispersion relation in a physically more understandable form, i.e. terms of wavenumbers, frequencies and characteristic speeds:

$$2m_0^2 (k^2 v_{A1}^2 - \omega^2) (k^2 v_{A2}^2 - \omega^2) + 2 \frac{\rho_0}{\rho_1} m_1 \frac{\rho_0}{\rho_2} m_2 (k^2 v_{A0}^2 - \omega^2)^2 + \rho_0 m_0 (k^2 v_{A0}^2 - \omega^2) \left[\frac{m_2}{\rho_2} (k^2 v_{A1}^2 - \omega^2) + \frac{m_1}{\rho_1} (k^2 v_{A2}^2 - \omega^2) \right] \left[\tau_0 + \frac{1}{\tau_0} \right] = 0. \quad (2.31)$$

Any combination of wave properties that satisfy this dispersion relation describes a wave supported by the asymmetric magnetic slab, except for any spurious solutions brought in through the derivation process. There are a few special cases that require separate treatment, namely, when the phase speed of waves equals one of the characteristic speeds in the slab system. We do not carry out a detailed investigation of the case giving rise to the Alfvén resonance, that is, when $\omega^2 = k^2 v_{A0}^2$ (for more information see Goossens et al. 2011). Since we do not consider propagation in the y direction, only in the z direction, the Alfvén waves (described by the v_y and B_y components) become decoupled from the system anyway. Another case we exclude from our study is when $\omega^2 = k^2 c_{T0}^2$, and the governing equation (2.15) becomes singular, which means that the ideal MHD equations break, and dissipations should be considered. These cases would correspond to resonances for a driven problem, and if the slab would be non-uniform, they would result in resonant absorption. In this study, however, we focus on uniform slabs and restrict our analysis to the cases when the phase speed does not correspond to any of the characteristic speeds.

2.2.3 Validation with earlier studies

The dispersion relation derived for this slab model should remain consistent with the results of at least two earlier studies. Firstly, if we keep the thermodynamic asymmetry of the environment enclosing the magnetic slab, but we set $B_1 = B_2 = 0$, thus $v_{A1} = v_{A2} = 0$, the wavenumber coefficients m_1 and m_2 reduce to

$$m_j^2 = \frac{(k^2 c_j^2 - \omega^2)}{c_j^2}, \quad \text{for } j = 1, 2. \quad (2.32)$$

Furthermore, the factors containing the external Alfvén speeds ($k^2 v_{Aj}^2 - \omega^2$) in the full dispersion relation (Equation 2.31) also reduce to $-\omega^2$ terms, which allows the equation to be simplified to

$$\omega^4 m_0^2 + \frac{\rho_0}{\rho_1} m_1 \frac{\rho_0}{\rho_2} m_2 (k^2 v_{A0}^2 - \omega^2)^2 - \frac{1}{2} m_0 \omega^2 (k^2 v_{A0}^2 - \omega^2) \left(\frac{\rho_0}{\rho_1} m_1 + \frac{\rho_0}{\rho_2} m_2 \right) \left[\tau_0 + \frac{1}{\tau_0} \right] = 0. \quad (2.33)$$

This is exactly the same result that was obtained for the magnetic slab embedded in a non-magnetic asymmetric environment by Allcock and Erdélyi (2017).

The second possibility to approach the current model is to consider its connection to the symmetric slab model incorporating magnetic fields in the external regions

2.2. THE GENERAL DISPERSION RELATION FOR A SLAB IN AN ASYMMETRIC MAGNETIC ENVIRONMENT

described by Edwin and Roberts (1982). The dispersion relation given there is

$$\rho_e(k^2 v_{Ae}^2 - \omega^2) m_0 \begin{pmatrix} \tanh \\ \coth \end{pmatrix} \{m_0 x_0\} + \rho_0(k^2 v_{A0}^2 - \omega^2) m_e = 0, \quad (2.34)$$

where the index e denotes all external parameters on both the left- and right-hand side of the slab, since the system is now symmetric. However, as Equation (2.34) shows, this case leads to two decoupled equations: one for the sausage ($\tanh(m_0 x_0)$ line) and one for the kink modes ($\coth(m_0 x_0)$ line). In contrast, in the general case of the asymmetric slab in a magnetic environment, the dispersion relation does not decouple into separate equations for sausage- and kink-type modes.

A connection can still be made if we require that the densities, pressures, and magnetic field strengths on the two sides of the asymmetric slab should be of the same order ($\rho_1 \approx \rho_2$, $p_1 \approx p_2$, $B_1 \approx B_2$), and so Λ_2 is of the same order as Λ_1 . This can be expressed by writing $\Lambda_2 = \Lambda_1 + \epsilon$ for some $|\epsilon| \ll 1$. Then, the same quantity can be introduced as in the case of the slab in a non-magnetic asymmetric environment (Allcock and Erdélyi, 2017):

$$1 = \frac{1}{4} \frac{(\Lambda_1 + \Lambda_2)^2}{\Lambda_1 \Lambda_2} + \mathcal{O}(\epsilon^2) \approx \frac{1}{4} \frac{(\Lambda_1 + \Lambda_2)^2}{\Lambda_1 \Lambda_2}. \quad (2.35)$$

Substituting this into Equation (2.31), the full dispersion relation, multiplying by $2\Lambda_1\Lambda_2$ (which is a non-zero quantity) and factorising gives us

$$[\Lambda_0(\Lambda_1 + \Lambda_2) + 2\Lambda_1\Lambda_2\tau_0] \left[\Lambda_0(\Lambda_1 + \Lambda_2) + 2\Lambda_0\Lambda_1\Lambda_2 \frac{1}{\tau_0} \right] = 0. \quad (2.36)$$

Setting either factor of this product as zero yields an approximate dispersion relation for sausage- and kink-type modes each, which are quite similar to the case of the symmetric slab in a magnetic environment.

$$\Lambda_0(\Lambda_1 + \Lambda_2) + 2\Lambda_1\Lambda_2\tau_0 = 0 \quad (2.37)$$

gives us the dispersion relation describing the sausage-type mode, while

$$\Lambda_0(\Lambda_1 + \Lambda_2) + 2\Lambda_0\Lambda_1\Lambda_2 \frac{1}{\tau_0} = 0 \quad (2.38)$$

leads to the equation governing the kink-type mode. Therefore, we now have a decoupled dispersion relation for the asymmetric eigenmodes in the form of

$$(k^2 v_{A0}^2 - \omega^2) \left[\frac{\rho_0}{\rho_1} \frac{m_1}{(k^2 v_{A1}^2 - \omega^2)} + \frac{\rho_0}{\rho_2} \frac{m_2}{(k^2 v_{A2}^2 - \omega^2)} \right] + 2m_0 \begin{pmatrix} \tanh \\ \coth \end{pmatrix} \{m_0 x_0\} = 0. \quad (2.39)$$

If we now make the environment fully symmetric so that $\rho_1 = \rho_2 = \rho_e$, $p_1 = p_2 = p_e$, $B_1 = B_2 = B_e$, Equation (2.39) reduces to Equation (2.34), the dispersion relation for the slab in a symmetric magnetic environment derived by Edwin and Roberts (1982). In the following Section, we discuss some consequences of this factorisation of the dispersion relation.

2.2.4 On asymmetric eigenmodes

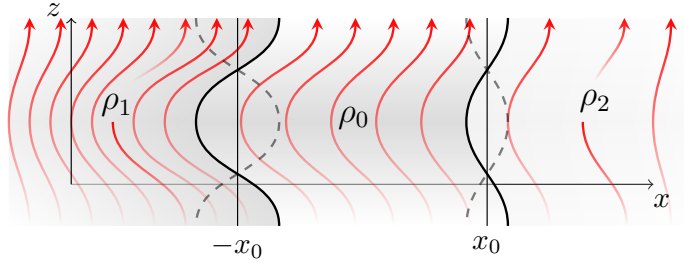
In a symmetric slab system, dispersion relation (Equation 2.34) in its full form consists of two separate equations without approximation, irrespective of the presence or absence of external magnetic fields (see also Roberts (1981b) and Edwin and Roberts (1982)). The line of this equation containing the $\tanh(m_0 x_0)$ function represents the sausage mode, where the velocity perturbation amplitude \hat{v}_x is described by an odd function, as the two boundaries of the slab oscillate in anti-phase. The line of the equation containing the $\coth(m_0 x_0)$ function describes kink waves, where \hat{v}_x is an even function, and slab boundaries oscillate in phase (Roberts, 1981b).

As opposed to this, the full and exact dispersion relation of an asymmetric slab system (either including (Zsámberger et al., 2018) or neglecting (Allcock and Erdélyi, 2017) external magnetic fields) does not decouple into separate equations governing sausage and kink modes, as the form of Equation (2.31) clearly shows and was discussed in Section 2.2.3. The presence of various sources of asymmetry (density, pressure, magnetic field strength) affects both "sausage" and "kink" mode solutions, which leads to the asymmetric eigenmodes having mixed characteristics of the traditional (symmetric) sausage and kink modes. Therefore we adopt the nomenclature introduced by Allcock and Erdélyi (2017), and from now on, we label the eigenmodes of asymmetric slab systems as quasi-sausage and quasi-kink modes. This both follows the widely used convention of classifying the in-phase oscillations as sausage modes and the in-antiphase oscillations as kink waves, which makes it easy to relate our findings to e.g. the symmetric slab models described by Roberts (1981b) and Edwin and Roberts (1982); at the same time, it also emphasizes the differences between waves in asymmetric waveguides and those in their symmetric counterparts. Perhaps the most easily noticeable such difference is that the transverse velocity of the quasi-sausage and quasi-kink eigenmodes shows an asymmetric distribution across the slab and its environment, resulting in different amplitudes at the two interfaces.

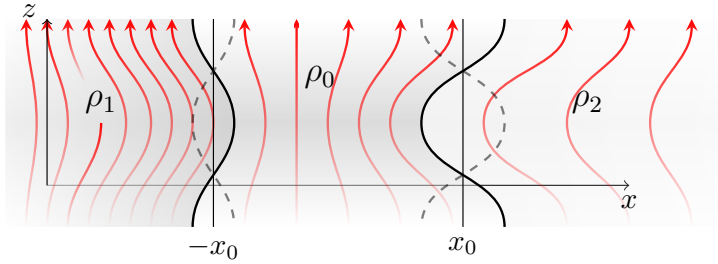
Figure 2.3 illustrates the basic identifying marks of quasi-kink (top) and quasi-sausage modes (bottom). The red arrows show the perturbed magnetic field lines, the thick solid black lines indicate the perturbed slab boundaries, and the dashed grey lines indicate the position of the slab boundaries after half a period.

To further elaborate on the characteristics demonstrated in Figure 2.3, Figure 2.4 contains numerical results for the distribution of the transverse velocity perturbation ($\hat{v}_x(x)$) as a function of the transverse spatial coordinate, x , overlaid on the illustration of a strongly magnetised, dense slab in a rarefied asymmetric environment permeated by weaker magnetic fields. Here, the blue arrows represent the equilibrium magnetic fields, and the grey shading (darker to lighter) indicate higher or lower background densities. The amplitude of the transverse velocity perturbation is plotted with a solid black curve in each case. Figure 2.4a displays a slow quasi-sausage surface mode, 2.4b a slow quasi-kink surface mode, while Figure 2.4c shows a fast quasi-sausage body mode of order one, 2.4d plots a fast quasi-kink body mode of order one. The results were obtained by setting the values of characteristic speeds and densities in each of the three regions so that pressure balance is maintained. Specifically, the values of $v_{A0} = 0.7c_0$, $v_{A1} = 0.2c_0$, $v_{A2} = 0.1c_0$, $c_1 = 2.2279c_0$, $c_2 = 1.8742c_0$, $\rho_1/\rho_0 = 0.28$, and $\rho_2/\rho_0 = 0.4$ were used for all four panels. Then using these speeds and densities, numerical solutions were obtained for the full dispersion relation, and the transverse velocity distributions of solutions

2.2. THE GENERAL DISPERSION RELATION FOR A SLAB IN AN ASYMMETRIC MAGNETIC ENVIRONMENT



(a) Illustration of a quasi-kink mode with $\rho_1 > \rho_2$ and $B_1 > B_2$.



(b) Illustration of a quasi-sausage mode with $\rho_1 > \rho_2$ and $B_1 > B_2$.

Figure 2.3: Illustration of eigenmodes along a slab in an asymmetric magnetic environment. The red arrows illustrate the perturbed magnetic fields, the thick solid black lines denote the perturbed slab boundaries, and the dashed grey lines indicate the position of the slab boundaries after half a period.

with a particular dimensionless slab width and wavenumber, kx_0 were calculated. For Figures 2.4a and 2.4b, $kx_0 = 0.685$ was chosen, while for Figures 2.4c and 2.4d, eigenmodes of a wider slab with $kx_0 = 2.790$ were plotted for visual clarity.

As explained in Section 1.3.2, sausage modes in a symmetric slab have an unperturbed magnetic surface in the centre of the slab (see Roberts (1981b), Edwin and Roberts (1982), Priest (2014)). However, in an asymmetric configuration, the unperturbed magnetic surface of quasi-sausage modes is shifted away from the mid-point of the central domain. In an asymmetric system with no external magnetic field, this surface of zero perturbation is simply moved closer the side where the transverse displacement perturbation is smallest, which corresponds to the side of the slab bounded by the denser external region (Allcock and Erdélyi, 2017). If the magnetic slab is also sandwiched between asymmetric magnetic fields, such as in Figure 2.4b, the location of the unperturbed surface can shift towards the side with higher density and weaker magnetic field strength.

While both kink and quasi-kink modes still oscillate in phase, kink modes of a symmetric system leave the cross-sectional width of the slab unchanged, while asymmetric quasi-kink modes do not preserve the slab's area (or volume) in this manner. This behaviour is shown in Figure 2.3a, and it can also be deduced from the velocity amplitudes plotted in Figure 2.4a. Furthermore, similarly to the case of sausage-type modes, symmetric kink modes also possess a surface of minimum (although not necessarily zero) perturbation, which is located in the centre of the slab. The position of this minimally perturbed surface is shifted away from the

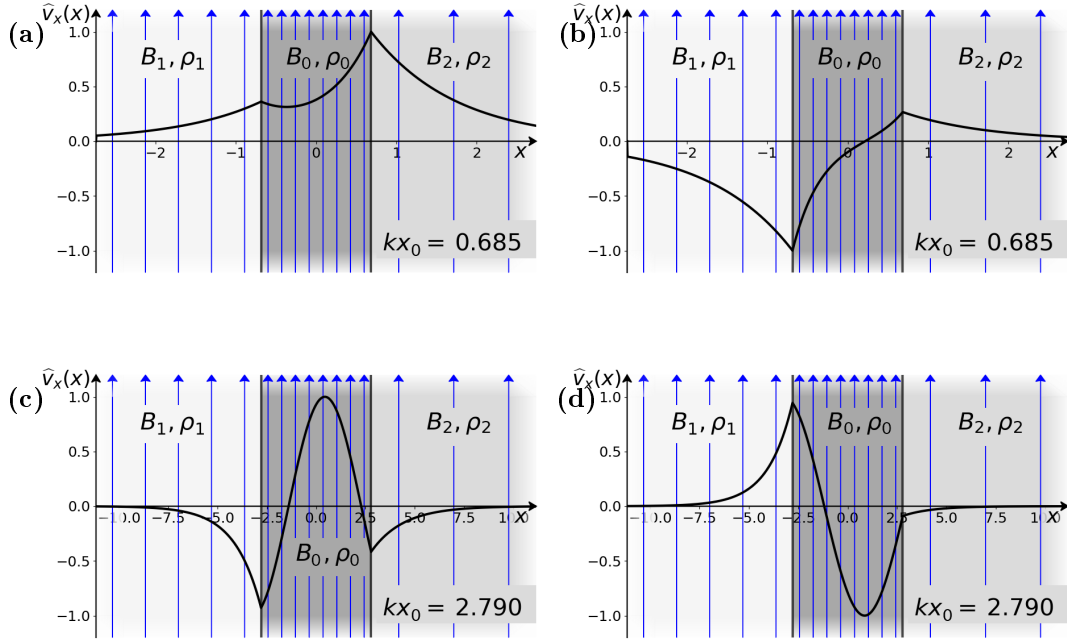


Figure 2.4: Distribution of the transverse velocity perturbation amplitude (\hat{v}_x) in a strongly magnetised slab and its rarefied asymmetric environment, plotted with solid black curves, as a function of the transverse spatial coordinate, x . Lighter gray shading represents lower background densities, while the blue arrows show the equilibrium magnetic fields, and darker grey shading corresponds to higher background densities. In Panel (a), a slow quasi-kink surface mode, in Panel (b), a slow quasi-sausage surface mode, in Panel (c), a fast quasi-kink body mode of order one, and in Panel (d), a fast quasi-sausage body mode of order one is presented. Panels (a) and (b) correspond to a thin slab ($kx_0 = 0.685$), while Panels (c) and (d) represent a wide slab ($kx_0 = 2.790$). These solutions to the dispersion relation (Equation 2.31) were obtained numerically, for a slab system characterized by $v_{A0} = 0.7c_0$, $v_{A1} = 0.2c_0$, $v_{A2} = 0.1c_0$, $c_1 = 2.2279c_0$, $c_2 = 1.8742c_0$, $\rho_1/\rho_0 = 0.28$, and $\rho_2/\rho_0 = 0.4$.

midpoint in the case of quasi-kink modes, too.

The presence of asymmetry affects the behaviour of both surface and body modes. The single minimum of the wave power of a surface mode across the slab will be found in the centre of a symmetric slab, but it will be displaced towards one side in the manner described above if the system includes any asymmetry (see Figures 2.4a and 2.4b). In the case of body modes, the differences may be more difficult to observe. The wave power of body modes is distributed in a spatially oscillatory manner within the slab (see also Figures 2.4c and 2.4d), and depending on their order, they may possess more than one zero location. The introduction of asymmetry in this case shifts the nodes and anti-nodes of the oscillations towards one side of the slab.

2.3 A mechanical analogy and quasi-symmetric oscillations

Allcock and Erdélyi (2017) introduced a mechanical analogy to magnetic slab sys-

tems in order to illustrate the fundamental behaviour of eigenmodes depending on the restoring forces present in the system. This analogy can also be further generalised to be applicable to slabs embedded in magnetic environments while also emphasizing the role that different restoring forces can play in shaping wave behaviour.

The analogous configuration in question is a coupled mechanical simple harmonic oscillation system, with the coupled springs representing the three plasma domains, and the small, massless plates suspended between them signal the position of the “slab” boundaries. For both externally magnetic and non-magnetic slab systems, the central domain can still be illustrated with the presence of a single spring, with spring constant k_0 . For an externally magnetic environment, specifically, the two environmental regions are represented with a pair of springs each, which are coupled in parallel on both sides of the central spring. In all panels of Figure 2.5, vertical dashed lines represent the equilibrium positions of the dark grey plates, blue springs symbolise forces related to the external magnetic fields, while red springs represent kinetic restoring forces. In the Figure, thicker springs indicate higher spring constants ($k_{i,j}$, where $i = 0, e, 1, 2$ and $j = 1, 2$). In such a geometry, the effective spring constant of either one of the external regions ($k_{e,j}$, for $j = 1, 2$) is the sum of the blue and red springs’ constants.

This system of coupled springs represents an analogy of the asymmetric slab system which is relatively easy to understand or even use for demonstration purposes. While in a coupled oscillator system, various springs can be chosen and a range of equilibrium positions for the plates can be accommodated, if a comparison to the slab system is to be made, pre-determined positions of slab boundaries can restrict the choice of spring lengths and spring constants.

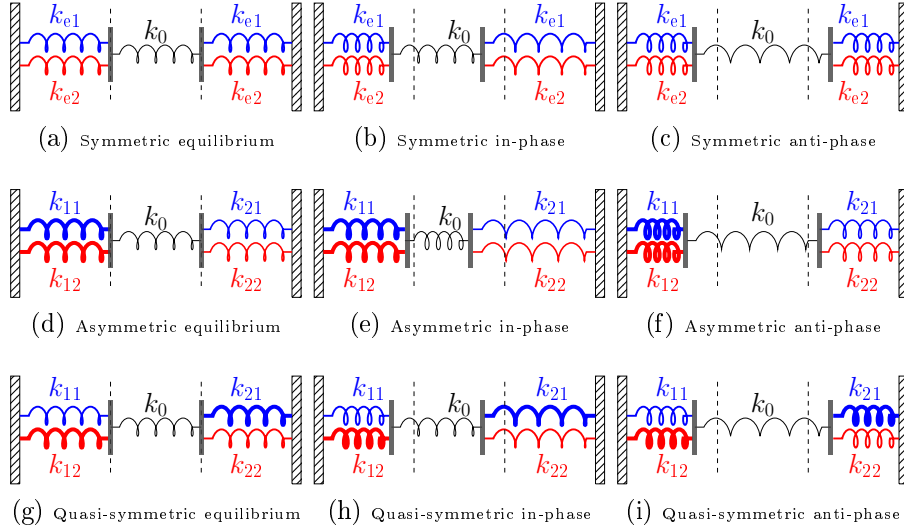


Figure 2.5: Illustration of a coupled mechanical oscillator system as an analogy to the asymmetric slab geometry. Thicker springs correspond to higher spring constants k_{ij} . Figures (a), (d) and (g) show the symmetric, asymmetric and quasi-symmetric spring systems in equilibrium. Figures (b) and (c) show the normal modes of a symmetric system. Figures (e) and (f) show the normal modes of an asymmetric system, while Figures (h) and (i) show the quasi-symmetric system. In each panel, the vertical dashed lines correspond to the positions of the gray plates at equilibrium.

If the spring constants k_{e1} and k_{e2} are equal on the left- and right-hand side, then the coupled mechanical oscillator is analogous to a magnetic slab embedded in a symmetric magnetic environment (studied in detail by Edwin and Roberts(1982)). This is the case illustrated Figures 2.5a-2.5c. In Figure 2.5a, the equilibrium state of the system is depicted, before any perturbations occur. Figure 2.5b shows the equivalent of a symmetric kink mode oscillation, with the plates indicating the slab boundaries displaced in the same direction, and the distance between them remaining unchanged. Finally, Figure 2.5c presents the mechanical analogue of a symmetric sausage mode, with the plates displaced in opposite directions, and the cross-section of the “slab”, which corresponds to the length of the central spring here, increasing and decreasing with time.

If the spring constants of the springs representing the magnetic and pressure forces are different on the two sides of the central region (Figure 2.5d), the coupled oscillator system corresponds to a magnetic slab embedded in an asymmetric magnetic environment. Then, the in-phase oscillations (Figure 2.5e) represent the quasi-kink modes, with the plates still being displaced in the same direction, but their distance (and so the cross-section of the slab it depicts) no longer being constant. Similarly, oscillations happening in anti-phase correspond to the quasi-sausage modes (Figure 2.5f), where the plates (or the slab boundaries) move in opposite directions, and the midpoint of the central spring (the central axis of the slab) is also displaced.

There is an interesting, but possibly rare phenomenon that may happen in asymmetric slab systems, the mechanical equivalent of which is presented in Figures 2.5g - 2.5i. Since there are two types of restoring forces in an asymmetric magnetic environment, it is possible to choose different spring constants in the mechanical system (corresponding to different magnetic field strengths and pressure gradients in a slab) in both external regions, but still obtain symmetric-looking oscillations in the system. The equilibrium state of this special system (Figure 2.5g) is very similar to the previously described equilibria. However, in this case, the springs have been chosen such that the equivalent spring constants of the two sides will be the same, that is, $k_{11} + k_{12} = k_{22} + k_{21}$. When this condition is fulfilled, in-phase oscillations of the system have the appearance of the symmetric kink mode (Figure 2.5h), and oscillations happening in anti-phase look like the symmetric sausage mode (Figure 2.5i). The mechanical example given here can be related back to slab systems in the solar atmosphere, where in some cases it may be possible to observe symmetric-looking oscillations in an asymmetric system. We call these oscillations ‘quasi-symmetric’ modes, and we discuss them in more detail in our Section 5.2.4.

2.4 Parametric solutions for the general case

The full dispersion relation of the asymmetric magnetic slab system (Equation 2.31) is a transcendental equation with a rich variety of solutions depending on the ordering of external and internal characteristic speeds, as well as the densities across the three regions of the plasma volume. In Chapter 3, we investigate several approximations of this equation, which can help us obtain analytical solutions for the angular frequencies and understand the behaviour of the waveguide in important limiting cases.

In the current section, however, we first provide an overview of possible eigen-

modes in a few cases chosen as illustrative examples, where we obtained numerical solutions to the dispersion relation. These solutions are displayed in the panels of Figure 2.6, with quasi-sausage (quasi-kink) modes plotted in blue (red), and hatching indicates bands of phase speed in which no trapped solutions exist. These dispersion diagrams depict the dependence of the phase speed (ω/k , or, normalised with a characteristic speed, $\omega/(kc_0)$) of trapped solutions on the dimensionless slab width parameter (kx_0).

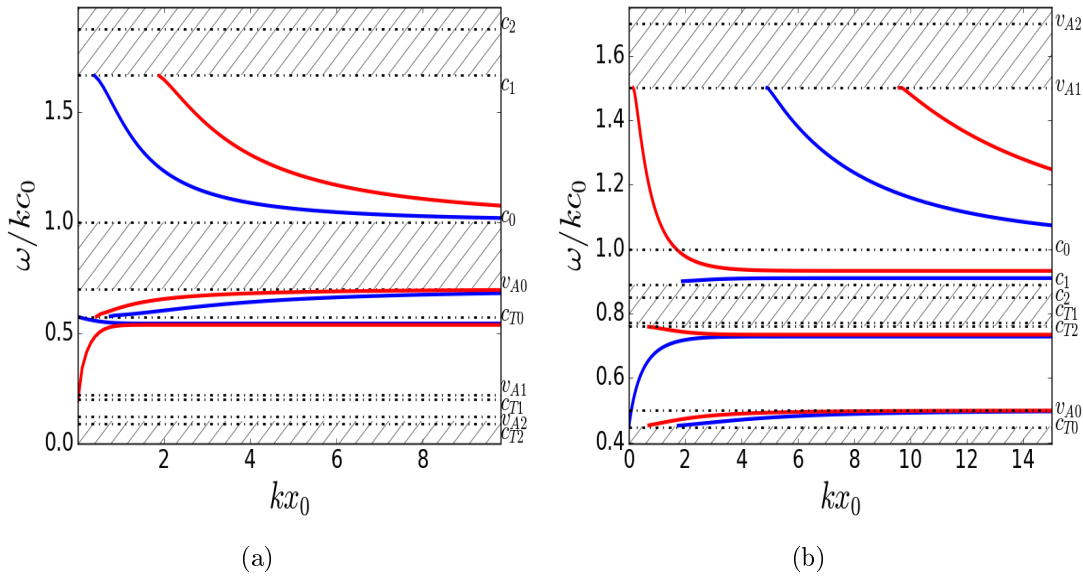


Figure 2.6: Diagnostic diagrams for the dispersion relation, Equation (2.31). Quasi-sausage (quasi-kink) modes are plotted in blue (red). **(a)** Slow and fast body modes, as well as slow surface mode waves can exist if the Alfvén speed of each domain is smaller than the corresponding sound speed. The characteristic speeds used in this case are: $v_{A0} = 0.7c_0$, $v_{A1} = 0.2c_0$, $v_{A2} = 0.1c_0$, $c_1 \approx 1.7c_0$, $c_2 \approx 1.9c_0$, with $\rho_1/\rho_0 = 0.5$, $\rho_2/\rho_0 = 0.4$. **(b)** Both fast and slow surface and body modes occur when the internal Alfvén speed is smaller than the internal sound speed, but the external Alfvén speeds are both higher than their corresponding sound speeds. The characteristic speed ordering used to obtain this figure is $v_{A0} = 0.5c_0$, $v_{A1} = 1.5c_0$, $v_{A2} = 1.7c_0$, $c_1 = 0.9c_0$, $c_2 = 0.85c_0$, $\rho_1/\rho_0 = 0.45$, $\rho_2/\rho_0 = 0.39$.

For the solutions in Figure 2.6a, the values $v_{A0} = 0.7c_0$, $v_{A1} = 0.2c_0$, $v_{A2} = 0.1c_0$, $c_1 \approx 1.7c_0$, $c_2 \approx 1.9c_0$, $\rho_1/\rho_0 = 0.5$, $\rho_2/\rho_0 = 0.4$ were chosen. It is important to observe here that all of the sound speeds are higher than the corresponding Alfvén speeds, therefore the plasma-*beta* parameter, defined as the ratio of gas to magnetic pressure, is high ($\beta > 1$) in all three regions. We might expect such a slab system to be found when the two environments sandwiching the slab have different temperatures, e.g. for waves propagating in the plume-interplume region.

With these chosen characteristic speeds, three types of trapped solutions exist. First, there is a pair of slow surface modes with phase speeds (v_{ph}) below the internal tube speed (c_{T0}). The rest of the solutions are body modes, occurring in two phase speed bands, with both bands containing an infinite number of harmonics. Here, and in later figures, we only plot a few of these body mode solutions for the sake of easy interpretation and visual clarity. In this high-*beta* case, the band of slow

body modes is located at phase speeds of $c_{T0} < v_{ph} < v_{A0}$, and that of fast body modes has $c_0 < v_{ph} < \min(c_1, c_2)$. At the upper limit, a cut-off can be observed in phase speeds. This is because we required that the waves must be evanescent far away from the slab, and in the hatched regions of the diagram (such as between $c_1 < v_{ph} < c_2$), this condition is violated and the waves become leaky.

In Figure 2.6b was prepared using $v_{A0} = 0.5c_0$, $v_{A1} = 1.5c_0$, $v_{A2} = 1.7c_0$, $c_1 = 0.9c_0$, $c_2 = 0.85c_0$, $\rho_1/\rho_0 = 0.45$, $\rho_2/\rho_0 = 0.39$. Thus, while the internal Alfvén speed is lower than the internal sound speed, the external Alfvén speeds both exceed their corresponding sound speeds. In this configuration, the slow surface waves exist as trapped oscillations for $v_{A0} < v_{ph} < c_{T2}$. The slow surface quasi-sausage mode experiences a change in character at intermediate slab widths. For high values of kx_0 , it exists as a surface wave, but for small kx_0 , it becomes a body wave. The slow surface quasi-kink mode also shows interesting behaviour, as it has a cut-off before it reaches phase speeds higher than c_{T2} for small values of kx_0 .

A pair of fast surface modes can also be found in this slab, in addition to the slow surface waves. In this phase speed region, the fast surface quasi-kink mode exists as a surface mode for high values of kx_0 , while for thinner slabs, it changes character and becomes a body mode. For the fast surface quasi-sausage mode, a cut-off can be observed at c_1 , below which phase speed, the wave would become leaky.

The body modes are still present in this mixed- β system, too, with the harmonics of the slow body modes found between $c_{T0} < v_{ph} < v_{A0}$, and the band of fast body modes located in the phase speed band of $c_0 < v_{ph} < v_{A1}$, once again experiencing a cut-off at the upper limit of the band.

These are, of course, only a couple of cases to illustrate the richness of the problem examined in this study. Further relevant cases of characteristic speed ordering and the corresponding solutions will be discussed in Chapters 3 and 4, together with their suggested applications to the features of the solar atmosphere.

2.4.1 The effect of varying magnetic field and density ratios

The solutions to the full dispersion relation (Equation 2.31) depend on a number of different parameters describing the plasma filling and the magnetic fields permeating the slab system. It is worthwhile to investigate the dependence of solutions on one of these parameters in particular, namely, the ratio of the two external densities to the internal density.

In Figure 2.7, exactly this dependence is plotted for a chosen set of characteristic speeds: $v_{A0} = 0.7c_0$, $v_{A1} = 0.2c_0$, $v_{A2} = 0.1c_0$, $c_2 = 1.8742c_0$. For each value of the dimensionless slab width, kx_0 , the density ratio ρ_1/ρ_0 of the left-hand-side domain to the inside of the slab is changed continuously, and c_1 changes along with this to keep the condition of pressure balance fulfilled. The other density ratio, that of the right-hand-side external region to the internal one, is held fixed at $\rho_2/\rho_0 = 0.4$ throughout. A particularly interesting phenomenon occurs at the density ratio indicated by the black bold line, where the phase speeds of the slow surface quasi-sausage (blue) and quasi-kink (red) modes perform a close approach and an avoided crossing.

Various physical processes can give rise to avoided crossings of eigenmodes, such as quantum mechanics, coupled spring oscillations, or photochemistry (Naqvi and Brown (1972); Devaquet (1975); Heiss and Sannino (1990); Novotny (2010)). In the context of MHD, they were first identified in dispersion diagrams of magneto-acoustic gravity waves in a plane stratified atmosphere by Abdelatif (1990), and

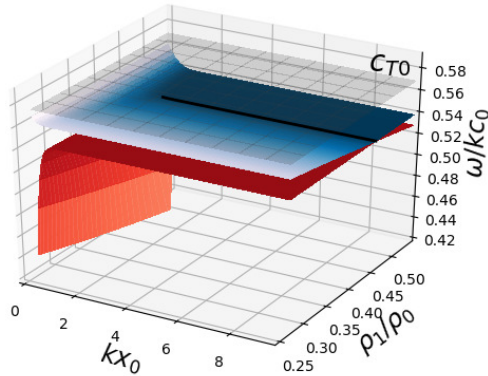


Figure 2.7: The dependence of the phase speeds of slow surface mode solutions of Equation (3.99) on the dimensionless slab width and left-hand-side density ratio in the incompressible limit. The blue surface shows the quasi-sausage mode, while the red one displays the quasi-kink mode. Here, $c_1 = 100.0$, $v_{A0} = 1.0$, $v_{A1} = 0.5$ and $v_{A2} = 0.7$ were used, while c_0 and c_2 were continuously changing in order to sustain total pressure balance between the domains. The black line indicates the values of the density ratio and the dimensionless slab width, for which the phase speeds of the quasi-sausage and quasi-kink modes perform a close approach and avoided crossing.

later also studied by e.g. Mather and Erdélyi (2016). Avoided crossings occur when constraints present in a physical system prevent the phase speeds of two supported wave modes from being equal. This is also accompanied by a transferral of properties between the modes.

For asymmetric slabs, Allcock and Erdélyi (2017) showed that avoided crossing can happen between the quasi-sausage and quasi-kink modes of a slab in a non-magnetic asymmetric environment with a variation of the density ratio similar to the one we performed to prepare Figure 2.7. In our example, the avoided crossing occurs between the slow surface modes of a slab, but the behaviour is not exclusive to slow modes. With the high- β speed ordering we chose to find the parametric solutions, however, fast surface modes would only exist as leaky oscillations, which leads us to keep our focus on the trapped slow surface modes.

As compared to the case of the slab in an asymmetric non-magnetic environment (Allcock and Erdélyi, 2017), an important difference is observed in our case. Namely, that in our slab, the closest approach of phase speeds during the avoided crossing does not occur at equal external densities. This is because of the inclusion of asymmetric external magnetic fields and the way we chose which parameters to change. While c_1 was varied alongside the corresponding density ratio, ρ_1/ρ_0 , the external Alfvén speed, v_{A1} , was kept constant. This requires that the external equilibrium magnetic field strength, B_1 , was also continuously changing throughout the process in a manner that kept v_{A1} at the same value. Consequently, reaching the equality of equal external densities ($\rho_1 = \rho_2$), on its own, does not mean that the entire slab system becomes symmetric, and the phase speeds of the quasi-sausage and quasi-kink modes may experience their closest approach at a different value of the changing density ratio, ρ_1/ρ_0 .

Since the inclusion of external magnetic asymmetry visibly plays such a significant role in determining the behaviour of waves and the parameters of their avoided crossings, we proceeded to investigate changes in both the density ratio, $R_1 = \rho_1/\rho_0$,

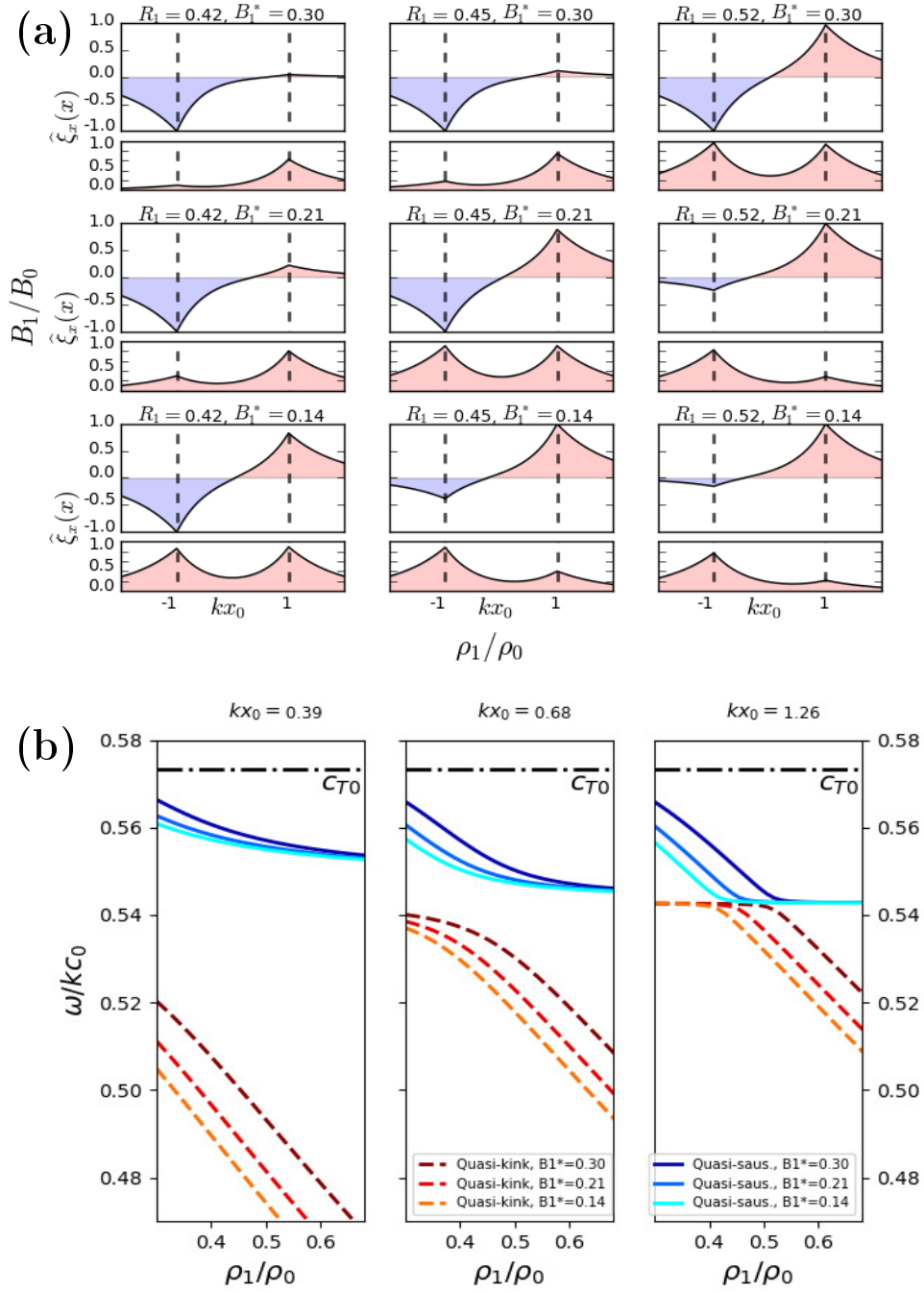


Figure 2.8: (a) The spatial variation of the transverse displacement perturbation ($\tilde{\xi}_x$) throughout the slab and its environment. The upper (lower) parts of the panel represent the quasi-sausage (quasi-kink) mode solutions. Negative amplitude regions are filled with blue, while positive ones are coloured red. In each column, the left-hand-side density ratio remains constant, while in each row, the ratio of the left-hand-side external magnetic field to the internal one ($B_1^* = B_1/B_0$) is kept at the same value. The right-hand-side density ratio is held fixed at $\rho_2/\rho_0 = 0.4$. The characteristic speeds used to obtain these plots are: $v_{A0} = 0.7c_0$, $v_{A1} = 0.2c_0$, $v_{A2} = 0.1c_0$, $c_2 = 1.8742c_0$, but c_1 varies to satisfy equilibrium pressure balance. Panel (b) displays phase speeds of solutions corresponding to different values of B_1^* , for specific fixed values of the non-dimensional slab width (kx_0).

and those in the ratio between the external equilibrium magnetic field strength to the internal one, $B_1^* = B_1/B_0$. In Figure 2.8a, we present the spatial variation of the transverse displacement perturbation ($\hat{\xi}_x$) across the slab for a few selected values of R_1 and B_1^* . The upper (lower) parts of each panel show the quasi-sausage (quasi-kink) mode solutions, with red shading indicating positive, and blue shading indicating negative values of $\hat{\xi}_x$. For all the panels, the second density ratio is kept the fixed value of $\rho_2/\rho_0 = 0.4$. The following characteristic speeds were used to solve the dispersion relation and calculate the amplitudes: $v_{A0} = 0.7c_0$, $v_{A2} = 0.1c_0$, $c_2 = 1.8742c_0$, and once again, c_1 was changed alongside the density ratio to keep equilibrium pressure balance. In the panels of each column, the left-side density ratio, R_1 is constant and has the same value. Similarly, in each panel of a row, the ratio of the left-hand-side external magnetic field to the internal magnetic field, B_1^* remains the same.

From Figure 2.8a, we can conclude that the behaviour of eigenmodes in a slab system incorporating external magnetic asymmetry is qualitatively similar to the case of an asymmetric slab embedded in a field-free environment. Overall, the left-hand-side external Alfvén speed, v_{A1} , decreases from the top left to the bottom right panel. As a result, different sources of avoided crossings are summarised in this Figure. The consecutive panels in each row of Figure 2.8a show that the amplitude of the quasi-sausage mode at the boundaries of the slab starts to change, and eventually, the highest amplitude shifts from the left side to the right, as a symmetric configuration is gradually approached. At the same time, the highest amplitude of the quasi-kink mode shows the opposite behaviour, as it migrates from the right to the left slab boundary, thus staying at the interface with the higher density ratio. Similarly, this maximum amplitude swap also occurs in each column as we move from the top to the bottom, this time, owing to the change in the magnetic field ratio. Finally, as both the density and magnetic field ratios come into play, an avoided crossing can be observed following the diagonal from the first, through the fifth, to the ninth panel.

In part b of Figure 2.8, we plot the dependence of phase speed solutions on the density ratio for a few fixed values of the dimensionless slab width, kx_0 . Continuous curves display quasi-sausage modes, while dashed lines indicate quasi-kink mode solutions. The different shades of blue and red show how changing the magnetic field ratio, B_1^* , changes the phase speeds of quasi-sausage and quasi-kink waves, respectively. It can easily be observed that (for the chosen set of characteristic speeds), there is a much closer approach of the phase speeds in wider slabs than in thinner ones. Furthermore, the variation in the magnetic field ratio visibly shifts where the closest approach of the phase speeds occurs during an avoided crossing, regardless of the fixed value of kx_0 .

2.5 Conclusion

In this Chapter, we introduced a further generalisation of the symmetric slab system described by Roberts (1981b) and Edwin and Roberts (1982) and the asymmetric slab system studied by Allcock and Erdélyi (2017). Namely, we studied the effect that incorporating asymmetric external magnetic fields into the model may have on the properties of magneto-acoustic waves guided by the slab system. This was accomplished by linearising the ideal MHD equations, and looking for plane-wave

solutions propagating along the slab. An ODE governing wave behaviour in each of the three regions of magnetised plasma was obtained, and by requiring the continuity of total pressure and velocity perturbations across the interfaces separating the slab from its environment, the full dispersion relation (Equation 2.31) of magneto-acoustic waves in an asymmetric magnetic slab was derived (Sections 2.2.1 and 2.2.2).

We have compared and confirmed our results with the previous studies of the symmetric slab in a magnetic environment and the asymmetric magnetic slab in a non-magnetic environment (Section 2.2.3). We found that there are fundamental differences between eigenmodes of slabs with symmetric or asymmetric surroundings, regardless of the presence or absence of external magnetic fields (Section 2.2.4). To better illustrate the characteristics of asymmetric eigenmodes, we have expanded upon the mechanical analogy of a slab system introduced by Allcock and Erdélyi (2017) (Section 2.3).

Finally, to illustrate the rich variety of solutions to the dispersion relation, we have found parametric solutions and described the guided modes in a pair of illustrative cases (Section 2.4). We studied the dependence of slow surface mode solutions, specifically, on the external-to-internal density and magnetic field ratios and provided a detailed description of avoided crossings occurring in a slab waveguide (Section 2.4.1).

We have found that the dispersion relation for a magnetic slab enclosed in an asymmetric magnetic environment does not decouple into two separate equations, irrespective of whether we include (Zsámberger et al., 2018) or neglect (Allcock and Erdélyi, 2017) external magnetic fields. Only with the assumption of weak asymmetry are decoupled equations for sausage and kink modes recovered. This is a significant difference from classical, symmetric slab systems, and it is reflected in the appearance of the eigenmodes as well.

Asymmetric eigenmodes are, therefore, waveforms with mixed properties, which we refer to as quasi-sausage and quasi-kink modes to distinguish them from the “purely” sausage or kink eigenmodes of a symmetric slab. Examples of this mixed character are that the quasi-sausage mode possesses an unperturbed magnetic surface at a location shifted away from the centre of the slab, and that the quasi-kink mode does not preserve the cross-section of the slab. These are both properties that we can utilise in developing tools for solar magneto-seismology.

Slab models provide a simple first approximation solar atmospheric waveguides, and they can be applied to a wide variety of structures, such as sunspot light bridges or coronal loop boundaries. In the following Chapters, we examine analytical approximations and numerical solutions of the dispersion relation in further detail, in order to explore the dependence of wave behaviour on the physical and geometric parameters of the slab system, and explore solar applications of the model.

Chapter 3

Approximations of the Dispersion Relation

Abstract

This Chapter explores various analytical approximations to the dispersion relation of the asymmetric magnetic slab model. First, solutions in the thin-slab and thick-slab limits are described. Then the effect of high- and low values of the plasma- β parameter is investigated. Finally, solutions are provided for the incompressible limit, and their dependence on density and magnetic asymmetries is described. This Chapter was based on the following publications: Section 3 of Zsámberger et al. (2018), Zsámberger and Erdélyi (2020) and Section 4.2 of Allcock et al. (2019). In more detail, the author of this thesis is primarily responsible for all of the referenced sections of these papers.

3.1 Chapter Introduction

In Chapter 2, we derived the general dispersion relation (Equation 2.31) for a magnetic slab embedded in an asymmetric magnetic environment, and we presented a few illustrative examples of numerical solutions to this transcendental equation. In the current Chapter, we focus on the analytical examination of this equation and of the behaviour of solutions in important limiting cases that may be applicable to a selection of solar and plasma-astrophysical structures. While discussing the analytical approximations we make, we also suggest a few examples of these possible applications of the asymmetric slab model for magneto-seismological studies. For ease of understanding, unless explicitly stated, we use the decoupled dispersion relation (Equation 2.39) as a starting point for our analysis. Therefore, the results obtained should only be applied to weakly asymmetric systems, i.e. where the difference between the two external densities, pressures, temperatures and magnetic field strengths is relatively small.

First, we consider the effect of the width of the slab compared to the wavelength of the studied oscillations. In Section 3.2, we obtain surface and body mode solutions for the case when the slab is relatively narrow, while in Section 3.3, the solutions are calculated for the opposite case, when the wavelength of the modes is small compared to the width of the slab. Section 3.3.3 provides a brief outlook on similar calculations performed for slabs with stronger asymmetry, using the full dispersion

relation.

Next, we move on to approximations based on plasma and magnetic field parameters, rather than geometry and wavelengths. In Section 3.4, we present analytical and numerical solutions for slab systems with low plasma- β values, and then for high- β slabs in Section 3.3. Section 3.5.3 provides solutions for configurations where stronger asymmetry is allowed, once again basing the calculations of the full dispersion relation. Finally, in Section 3.6, we study the approximation of incompressible plasma, which simplifies the solutions significantly, before we discuss our main results in Section 3.7.

3.2 Thin-slab approximation

When we apply the thin-slab approximation, we consider waves in slabs for which it is true that the wavelength, λ , of the waves is much greater than the width of the slab: $x_0/\lambda \approx kx_0 \ll 1$. This limit may have applications in both the photosphere (e.g. to sunspot light bridges and light walls (Yuan et al. (2014); Yang et al. (2016); Yang et al. (2017))), magnetic bright points (Utz et al. (2009); Liu et al. (2018)), and the corona (e.g. to prominences (Arregui et al., 2012)).

3.2.1 Surface modes

As discussed in the previous Chapters, surface waves are evanescent both outside and inside the slab, so they show the greatest perturbation amplitudes at the two interfaces separating the slab from its environment. Both quasi-sausage and quasi-kink surface eigenmodes are possible in an asymmetric magnetic slab, and in the following Subsections, we will look at these one by one.

Quasi-sausage surface modes

If the asymmetry is weak in the slab system, the dispersion relation can be decoupled into two separate equations describing sausage- and kink-type eigenmodes. The quasi-sausage surface modes which are governed by the component of Equation (2.39) containing the $\tanh(m_0x_0)$ function. As the wavenumber coefficient, m_0 is directly related to the z -component of the wavenumber vector, k , we apply the thin-slab approximation, in which $kx_0 \ll 1$, and suppose that in this limit, $m_0x_0 \ll 1$ is also true. Then it follows that $\tanh m_0x_0 \approx m_0x_0$, the hyperbolic tangent function can be approximated by its argument. Substituting this into Equation (2.39), we obtain the dispersion relation for quasi-sausage surface modes in a thin slab:

$$(k^2v_{A0}^2 - \omega^2) \left[\frac{\rho_0}{\rho_1} \frac{m_1}{(k^2v_{A1}^2 - \omega^2)} + \frac{\rho_0}{\rho_2} \frac{m_2}{(k^2v_{A2}^2 - \omega^2)} \right] + 2m_0^2x_0 = 0. \quad (3.1)$$

Both terms of this equation are proportional with $(k^2v_{A0}^2 - \omega^2)$, but the angular frequency $\omega^2 = k^2v_{A0}^2$ would be a trivial solution, which we do not consider here (for reasons explained in Chapter 2 and Zsámberger et al. (2018)).

A possible group of solutions that we do take into consideration is one where the phase speed of the waves approaches the cusp speed (but is not exactly equal to it): $\omega^2 \rightarrow k^2c_{T0}^2$. Substituting this assumed angular frequency into (3.1), after some

algebra, leads to

$$\omega^2 = k^2 c_{T0}^2 \left[1 + \frac{2(c_0^2 - c_{T0}^2)(v_{A1}^2 - c_{T0}^2)^{1/2}(v_{A2}^2 - c_{T0}^2)^{1/2} k x_0}{\rho_0 v_{A0}^2 c_0^2 R_v} \right],$$

where

$$R_v = \frac{1}{\rho_2} \frac{(v_{A1}^2 - c_{T0}^2)^{1/2}(c_2^2 - c_{T0}^2)^{1/2}}{(v_{A2}^2 + c_2^2)^{1/2}(c_{T2}^2 - c_{T0}^2)^{1/2}} + \frac{1}{\rho_1} \frac{(v_{A2}^2 - c_{T0}^2)^{1/2}(c_1^2 - c_{T0}^2)^{1/2}}{(v_{A1}^2 + c_1^2)^{1/2}(c_{T1}^2 - c_{T0}^2)^{1/2}}. \quad (3.2)$$

This is a slow quasi-sausage surface mode solution to the dispersion relation. As the slab becomes thinner, this solution approaches $\omega^2 \rightarrow k^2 c_{T0}^2$ from above as $k x_0 \rightarrow 0$. Without prescribing any specific ordering for the characteristic speeds in and outside the slab in advance, the following conditions for the existence of this mode can be found:

$$\sqrt{c_{T1}^2 - c_{T0}^2} > 0 \Rightarrow c_{T0}^2 < c_{T1}^2 \quad \text{and} \quad \sqrt{c_{T2}^2 - c_{T0}^2} > 0 \Rightarrow c_{T0}^2 < c_{T2}^2. \quad (3.3)$$

There are further possibilities for determining the relative magnitudes of the characteristic speeds, of course, but these will also affect the form of the approximate solution given in Equation (3.2). We have collected these speed orderings with their corresponding quasi-sausage surface mode solution below:

$$\begin{aligned} \omega^2 &= k^2 c_{T0}^2 \left[1 + \frac{2(c_0^2 - c_{T0}^2)(v_{A1}^2 - c_{T0}^2)^{1/2}(v_{A2}^2 - c_{T0}^2)^{1/2} k x_0}{\rho_0 v_{A0}^2 c_0^2 R_v} \right], \\ R_v &= \frac{1}{\rho_2} \frac{(v_{A1}^2 - c_{T0}^2)^{1/2}(c_2^2 - c_{T0}^2)^{1/2}}{(v_{A2}^2 + c_2^2)^{1/2}(c_{T0}^2 - c_{T2}^2)^{1/2}} + \frac{1}{\rho_1} \frac{(v_{A2}^2 - c_{T0}^2)^{1/2}(c_1^2 - c_{T0}^2)^{1/2}}{(v_{A1}^2 + c_1^2)^{1/2}(c_{T0}^2 - c_{T1}^2)^{1/2}}, \\ \text{for} \quad &c_1^2 < c_{T0}^2 < v_{A1}^2 \quad \text{and} \quad c_2^2 < c_{T0}^2 < v_{A2}^2; \end{aligned} \quad (3.4)$$

$$\begin{aligned} \omega^2 &= k^2 c_{T0}^2 \left[1 - \frac{2(c_0^2 - c_{T0}^2)(c_{T0}^2 - v_{A1}^2)^{1/2}(c_{T0}^2 - v_{A2}^2)^{1/2} k x_0}{\rho_0 v_{A0}^2 c_0^2 R_v} \right], \\ R_v &= \frac{1}{\rho_2} \frac{(c_{T0}^2 - v_{A1}^2)^{1/2}(c_2^2 - c_{T0}^2)^{1/2}}{(v_{A2}^2 + c_2^2)^{1/2}(c_{T0}^2 - c_{T2}^2)^{1/2}} + \frac{1}{\rho_1} \frac{(c_{T0}^2 - v_{A2}^2)^{1/2}(c_1^2 - c_{T0}^2)^{1/2}}{(v_{A1}^2 + c_1^2)^{1/2}(c_{T0}^2 - c_{T1}^2)^{1/2}} \\ \text{for} \quad &v_{A1}^2 < c_{T0}^2 < c_1^2 \quad \text{and} \quad v_{A2}^2 < c_{T0}^2 < c_2^2. \end{aligned} \quad (3.5)$$

By substituting $v_{A1}^2 = v_{A2}^2 = v_{Ae}^2$, $c_1^2 = c_2^2 = c_e^2$, $\rho_1 = \rho_2 = \rho_e$, all three cases (Equations 3.2, 3.5 and 3.6) can be reduced to the solutions obtained for the symmetric slab in a magnetic environment in Edwin and Roberts (1982), to Equations (16b, c, d), respectively.

Thanks to the rich possibilities provided by the plasma and magnetic asymmetries, further different orderings of characteristic speeds are possible, which give rise to the following solutions:

$$\begin{aligned} \omega^2 &= k^2 c_{T0}^2 \left[1 + \frac{2(c_0^2 - c_{T0}^2)(v_{A1}^2 - c_{T0}^2)^{1/2}(v_{A2}^2 - c_{T0}^2)^{1/2} k x_0}{\rho_0 v_{A0}^2 c_0^2 R_v} \right], \\ R_v &= \frac{1}{\rho_2} \frac{(v_{A1}^2 - c_{T0}^2)^{1/2}(c_2^2 - c_{T0}^2)^{1/2}}{(v_{A2}^2 + c_2^2)^{1/2}(c_{T0}^2 - c_{T2}^2)^{1/2}} + \frac{1}{\rho_1} \frac{(v_{A2}^2 - c_{T0}^2)^{1/2}(c_1^2 - c_{T0}^2)^{1/2}}{(v_{A1}^2 + c_1^2)^{1/2}(c_{T1}^2 - c_{T0}^2)^{1/2}}, \\ \text{for} \quad &c_{T0}^2 < c_{T1}^2 \quad \text{and} \quad c_2^2 < c_{T0}^2 < v_{A2}^2; \end{aligned} \quad (3.6)$$

$$\begin{aligned}\omega^2 &= k^2 c_{T0}^2 \left[1 + \frac{2(c_0^2 - c_{T0}^2)(v_{A1}^2 - c_{T0}^2)^{1/2}(c_{T0}^2 - v_{A2}^2)^{1/2} k x_0}{\rho_0 v_{A0}^2 c_0^2 R_v} \right], \\ R_v &= -\frac{1}{\rho_2} \frac{(v_{A1}^2 - c_{T0}^2)^{1/2}(c_2^2 - c_{T0}^2)^{1/2}}{(v_{A2}^2 + c_2^2)^{1/2}(c_{T0}^2 - c_{T2}^2)^{1/2}} + \frac{1}{\rho_1} \frac{(c_{T0}^2 - v_{A2}^2)^{1/2}(c_1^2 - c_{T0}^2)^{1/2}}{(v_{A1}^2 + c_1^2)^{1/2}(c_{T1}^2 - c_{T0}^2)^{1/2}}, \\ \text{for } c_{T0}^2 &< c_{T1}^2 \quad \text{and} \quad v_{A2}^2 < c_{T0}^2 < c_2^2;\end{aligned}\tag{3.7}$$

$$\begin{aligned}\omega^2 &= k^2 c_{T0}^2 \left[1 - \frac{2(c_0^2 - c_{T0}^2)(v_{A1}^2 - c_{T0}^2)^{1/2}(c_{T0}^2 - v_{A2}^2)^{1/2} k x_0}{\rho_0 v_{A0}^2 c_0^2 R_v} \right], \\ R_v &= \frac{1}{\rho_2} \frac{(v_{A1}^2 - c_{T0}^2)^{1/2}(c_2^2 - c_{T0}^2)^{1/2}}{(v_{A2}^2 + c_2^2)^{1/2}(c_{T0}^2 - c_{T2}^2)^{1/2}} - \frac{1}{\rho_1} \frac{(c_{T0}^2 - v_{A2}^2)^{1/2}(c_{T0}^2 - c_1^2)^{1/2}}{(v_{A1}^2 + c_1^2)^{1/2}(c_{T0}^2 - c_{T1}^2)^{1/2}}, \\ \text{for } c_1^2 &< c_{T0}^2 < v_{A1}^2 \quad \text{and} \quad v_{A2}^2 < c_{T0}^2 < c_2^2.\end{aligned}\tag{3.8}$$

$$\tag{3.9}$$

Equations (3.7), (3.8), and (3.9) can also be used to express the solutions in an asymmetric slab where the environmental regions are “swapped”, that is, the same conditions are met, but the $j = 1, 2$ indices of all the characteristic speeds and densities are swapped. An important difference from the first three possible solutions is, however, that in order to relate the latter three asymmetric modes to a symmetric equivalent, a “dominant” condition needs to be chosen. One could choose, for example, the minimum, maximum, or average of the two external parameters as the value of the corresponding external parameter in the symmetric case, and use this value to set the conditions and find the solutions. Such a treatment reveals that Equations (3.7) and (3.8) can be reduced to Equation (16b) of Edwin and Roberts (1982) if the dominant condition chosen is $c_{T0} < c_{Te}$. Alternately, Equation (3.7) reduces to Edwin and Roberts’s equation (16c) when selecting $c_e^2 < c_{T0}^2 < v_{Ae}^2$ for the condition to be met. Finally, Equation (3.8) reduces to Equation (16d) in Edwin and Roberts (1982) if the dominant condition is $v_{Ae}^2 < c_{T0}^2 < c_e^2$. Equation (3.9), however, does not have an equivalent examined in the symmetric case with either possible ordering of characteristic speeds.

Moving on from slow waves, a different type of quasi-sausage surface mode solution can also exist in a weakly asymmetric magnetic slab, which approaches one of the external sound speeds in the thin-slab limit. For example, if we take the approximation $\omega^2 \rightarrow k^2 c_2^2$, the solutions take the following form:

$$\begin{aligned}\omega^2 &= k^2 c_2^2 - \left[\frac{\rho_2}{\rho_0} \frac{2(c_{T2}^2 - c_2^2)^{1/2}(v_{A2}^4 - c_2^4)^{1/2}(c_0^2 - c_2^2)k^2 x_0}{(c_{T0}^2 - c_2^2)(c_0^2 + v_{A0}^2)} \right. \\ &\quad \left. + \frac{\rho_2}{\rho_1} \frac{(c_{T2}^2 - c_2^2)^{1/2}(v_{A2}^4 - c_2^4)^{1/2}(c_1^2 - c_2^2)^{1/2}}{(c_{T1}^2 - c_2^2)^{1/2}(v_{A1}^2 - c_2^2)^{1/2}(v_{A1}^2 + c_1^2)^{1/2}} \right]^2.\end{aligned}\tag{3.10}$$

The conditions of the existence of this trapped mode is that $c_2 < c_{T1}$ or $\min(c_1, v_{A1}) < c_2 < \max(c_1, v_{A1})$, since outside these limits, the waves would become leaky. As before, swapping all indices $j = 1, 2$ leads to the same type of solution.

A special case for this group of solutions is that of the isothermal external environment enclosing the slab. In this case, the external sound speeds are all equal:

$c_1^2 = c_2^2 = c_e^2$, and by substitution into Equation (3.10), the solutions simplify to

$$\begin{aligned} \omega^2 &= k^2 \left[c_e^2 + \frac{4(c_0^2 - c_e^2)^2 (kx_0)^2}{\rho_0^2 (v_{A0}^2 + c_0^2)^2 (c_{T0}^2 - c_e^2)^2 R_v^2} \right], \\ R_v^2 &= \left[\frac{1}{\rho_2 (v_{A1}^2 - c_e^2)^{1/2} (c_e^2 + v_{A2}^2)^{1/2} (c_{T2}^2 - c_e^2)^{1/2}} \right. \\ &\quad \left. + \frac{1}{\rho_1 (v_{A2}^2 - c_e^2)^{1/2} (c_e^2 + v_{A1}^2)^{1/2} (c_{T1}^2 - c_e^2)^{1/2}} \right]^2, \end{aligned} \quad (3.11)$$

for $v_{A1}, v_{A2} < c_e$ and $c_e < c_{T1}, c_{T2}$. If we now suppose that the environment is not only isothermal, but the Alfvén speeds are also the same ($v_{A1}^2 = v_{A2}^2 = v_{Ae}^2$), then $\rho_1 = \rho_2 = \rho_e$ must also be true. This corresponds to the case of the magnetic slab embedded in a symmetric, magnetic environment described by Edwin and Roberts (1982), and the solution given in Equation (3.11) will be the same as their Equation (16a). On the other hand, if the the external regions are non-magnetic, Equation (3.11) reduces to Equation (32) of Allcock and Erdélyi (2017).

Quasi-kink surface modes

In this Subsection, we investigate the quasi-kink surface mode solutions, which are governed by the $\coth(m_0 x_0)$ line of the decoupled dispersion relation (Equation 2.39). As before, we suppose that in a thin slab ($kx_0 \ll 1$), $m_0 x_0 \ll 1$, and then $\coth m_0 x_0 \approx (m_0 x_0)^{-1}$. If we substitute this approximation into Equation (2.39), the dispersion relation for quasi-kink modes becomes

$$\rho_0 x_0 (k^2 v_{A0}^2 - \omega^2) \left[\frac{m_1}{\rho_1 (k^2 v_{A1}^2 - \omega^2)} + \frac{m_2}{\rho_2 (k^2 v_{A2}^2 - \omega^2)} \right] + 2 = 0. \quad (3.12)$$

One type of quasi-kink modes might approach one of the external Alfvén speeds in a weakly asymmetric thin slab: $\omega^2 \rightarrow k^2 v_{A1}^2$. The angular frequency of these quasi-kink modes will be

$$\omega^2 = k^2 \left[v_{A1}^2 - \frac{\rho_0^2 \rho_2^2 (c_1^2 - v_{A1}^2) (v_{A0}^2 - v_{A1}^2)^2 (v_{A2}^2 - v_{A1}^2) (c_{T2}^2 - v_{A1}^2) (k^2 x_0)^2}{\rho_1^2 (c_{T1}^2 - v_{A1}^2) R_v^2} \right], \quad (3.13)$$

where

$$R_v = 2\rho_2 k (v_{A2}^2 - v_{A1}^2)^{1/2} (c_{T2}^2 - v_{A1}^2)^{1/2} (v_{A1}^2 + c_1^2)^{1/2} + \rho_0 (v_{A0}^2 - v_{A1}^2) (c_2^2 - v_{A1}^2)^{1/2} k^2 x_0.$$

For this mode to remain a trapped oscillation, the characteristic speeds have to be ordered as $v_{A1}^2 < c_{T2}^2$ or $\min(v_{A2}^2, c_2^2) < v_{A1}^2 < \max(v_{A2}^2, c_2^2)$. When the external Alfvén speeds are symmetric, $v_{A1}^2 = v_{A2}^2 = v_{Ae}^2$, the solution simplifies to

$$\omega^2 = k^2 v_{Ae}^2 \left[1 - \left(1 - \frac{v_{A0}^2}{v_{Ae}^2} \right)^2 \left(\frac{\rho_0 (kx_0)}{2} \right)^2 \left(\frac{1}{\rho_2} \sqrt{1 - \frac{c_2^2}{v_{Ae}^2}} + \frac{1}{\rho_1} \sqrt{1 - \frac{c_1^2}{v_{Ae}^2}} \right)^2 \right]. \quad (3.14)$$

In the case of an isothermal external environment, $c_1^2 = c_2^2 = c_e^2$. Then, as before, $\rho_1 = \rho_2 = \rho_e$ is also required, and Equation (3.14) reduces to the solution obtained for the slab in a symmetric magnetic environment (Equation (18a) of Edwin and Roberts 1982).

There is another type of kink mode solution in the symmetric slab, one that approaches the external cusp speed. An asymmetric equivalent for this mode can be found by substituting $\omega^2 \rightarrow k^2 c_{T1}^2$ into the thin-slab dispersion relation for quasi-kink modes (Equation 3.12). The angular frequency of this mode is

$$\omega^2 = k^2 \left[c_{T1}^2 - \frac{\rho_0^2 \rho_2^2}{\rho_1^2} \frac{R_{v1} (k^2 x_0)^2}{(v_{A1}^2 - c_{T1}^2)(c_1^2 + v_{A1}^2) R_{v2}^2} \right], \quad (3.15)$$

with

$$\begin{aligned} R_{v1} &= (c_1^2 - c_{T1}^2)(v_{A0}^2 - c_{T1}^2)^2(v_{A2}^2 - c_{T1}^2)(c_{T2}^2 - c_{T1}^2)(v_{A2}^2 + c_2^2), \\ R_{v2} &= 2\rho_2 k (v_{A2}^2 - c_{T1}^2)^{1/2} (c_{T2}^2 - c_{T1}^2)^{1/2} (v_{A2}^2 + c_2^2)^{1/2} + \rho_0 k^2 x_0 (v_{A0}^2 - c_{T1}^2)(c_2^2 - c_{T1}^2)^{1/2}. \end{aligned}$$

This solution exists as a trapped oscillation when the characteristic speeds fulfil the conditions $c_{T1}^2 < c_{T2}^2$ or $\min(v_{A2}^2, c_2^2) < c_{T1}^2 < \max(v_{A2}^2, c_2^2)$. When the two external tube speeds are equal, Equation (3.15) reduces to Equation (18b) of Edwin and Roberts (1982).

For Edwin and Roberts's (1982) Equation (19), which exists when v_{Ae}/v_{A0} is of the order of kx_0 , a generalised asymmetric version can also be found as:

$$\omega^2 = k^2 v_{A1}^2 \left[1 + \frac{\rho_0 \rho_2}{\rho_1} \frac{v_{A0}^2}{v_{A1}^2} \frac{v_{A2}^2 (kx_0)}{2\rho_2 v_{A2}^2 + \rho_0 v_{A0}^2 x_0} \right] \quad (3.16)$$

if $v_{A1} \ll v_{A2}$ is also satisfied. When $v_{A2} \ll v_{A1}$, the solution is

$$\omega^2 = k^2 v_{A1}^2 \left[1 + \frac{\rho_0 \rho_2}{\rho_1} \frac{v_{A0}^2}{v_{A1}^2} \frac{v_{A1}^2 (kx_0)}{\rho_0 v_{A0}^2 x_0 - 2\rho_2 v_{A1}^2} \right]. \quad (3.17)$$

When the external Alfvén speeds are symmetric ($v_{A1}^2 = v_{A2}^2 = v_{Ae}^2$), this approximation simplifies further to

$$\omega^2 = k^2 v_{Ae}^2 \left[1 + \frac{1}{R} \frac{v_{A0}^2}{v_{Ae}^2} (kx_0) \right], \quad (3.18)$$

where

$$R = \left[\frac{\rho_0}{2} \left(\frac{1}{\rho_1} + \frac{1}{\rho_1} \right) \right]^{-1} \quad (3.19)$$

is the measure of the density asymmetry introduced by Zsámberger et al. (2018).

Overall, we can conclude from the structure and possible simplifications of Equations (3.2)-(3.11) and (3.13)-(3.15) that the types of solutions in the thin-slab limit of an asymmetric magnetic slab is similar to those of the symmetric case. In general, the structure of Equations (3.2)-(3.15) also shows that surface waves guided by an asymmetric magnetic slab are sensitive to the relative magnitudes of the external

densities. We have investigated this dependence in detail in Section 2.4.1 when we described the avoided crossings of eigenmodes. It is important to keep in mind that although we are able to provide analytical approximations of the frequencies of the eigenmodes, wave dispersion in the asymmetric configuration is a complex phenomenon, and the validity of our approximations may have to be examined on a case-by-case basis. The external asymmetry can introduce new cut-off frequencies compared to the symmetric case, beyond which the waves become leaky.

3.2.2 Body modes

As a reminder, body waves are evanescent in the regions of the environment, however, they remain oscillatory within the slab. Before focusing on their analytical properties in the thin-slab limit, first, let us rewrite the full dispersion relation itself without the use of hyperbolic functions. As opposed to surface waves, where the parameter m_0^2 was positive, for body waves, $m_0^2 < 0$. Defining $n_0^2 := -m_0^2 > 0$, the full dispersion relation (Equation 2.31) becomes

$$\begin{aligned} & 2\frac{\rho_0}{\rho_1}m_1\frac{\rho_0}{\rho_2}m_2(k^2v_{A0}^2 - \omega^2)^2 - 2n_0^2(k^2v_{A1}^2 - \omega^2)(k^2v_{A2}^2 - \omega^2) + \\ & \rho_0n_0(k^2v_{A0}^2 - \omega^2)\left[\frac{m_1}{\rho_1}(k^2v_{A2}^2 - \omega^2) \right. \\ & \left. + \frac{m_2}{\rho_2}(k^2v_{A1}^2 - \omega^2)\right] [-\tan n_0x_0 + \cot n_0x_0] = 0. \end{aligned} \quad (3.20)$$

Similarly, we can express the decoupled dispersion relation (Equation 2.39) with the tangent and cotangent functions, too:

$$(k^2v_{A0}^2 - \omega^2)\left[\frac{\rho_0}{\rho_1}\frac{m_1}{(k^2v_{A1}^2 - \omega^2)} + \frac{\rho_0}{\rho_2}\frac{m_2}{(k^2v_{A2}^2 - \omega^2)}\right] + 2n_0\left(\frac{-\tan}{\cot}\right)\{n_0x_0\} = 0. \quad (3.21)$$

When looking for body mode solutions, we must make slightly different assumptions than in the case of surface modes. Namely, if we suppose that $m_0x_0 \rightarrow 0$ as the slab becomes thinner ($kx_0 \rightarrow 0$) will not provide a description of every possible wave mode (Roberts, 1981b). We require instead that m_0x_0 must remain bounded as $kx_0 \rightarrow 0$.

The dispersion relation for quasi-sausage body waves in a weakly asymmetric slab is given by the $\tan(n_0x_0)$ line of Equation (3.21). Using our new approach, here, the expression $n_0 \tan(n_0x_0)$ needs to remain finite. Therefore, n_0x_0 has to converge to the roots of $\tan(n_0x_0) = 0$, that is, $n_0x_0 = j\pi$ (for $j = 1, 2, 3 \dots$). Substituting $\omega^2 \approx k^2c_{T0}^2(1 + \nu(kx_0)^2)$ into the definition of n_0 , we find the following values for the parameter ν :

$$n_0^2x_0^2 = -m_0^2x_0^2 = \frac{(c_0^2 - c_{T0}^2)(v_{A0}^2 - c_{T0}^2)}{(c_0^2 + v_{A0}^2)c_{T0}^2\nu}. \quad (3.22)$$

From the condition on the values of $n_0^2x_0^2$, this expression also equals $j^2\pi^2$. Then Equation (3.22) can be rearranged to provide ν for every (integer) j as

$$\nu_j = \frac{(c_0^2 - c_{T0}^2)(v_{A0}^2 - c_{T0}^2)}{(c_0^2 + v_{A0}^2)c_{T0}^2j^2\pi^2}. \quad (3.23)$$

We can therefore conclude that there are countably many quasi-sausage body mode solutions. Each of these have a different number of nodes inside the slab, and so we will call them harmonics in the direction of structuring, or harmonics, in short. However, this type of description does not emphasize the influence of the external equilibrium asymmetry so far. There are two possibilities to consider the effects of the external magnetic asymmetry. For example, if either one of the external sound or Alfvén speeds is higher than c_{T0} , a cut-off frequency may be introduced, which prevents the phase speed from converging to the cusp speed in the limit of the thinnest slabs.

In the dispersion relation for body modes (3.21), all of the coefficients n_0^2, m_1^2, m_2^2 must have positive values. This means that there are three possibilities for the existence of slow body modes:

$$\begin{aligned} \max [c_{T0}, \min (c_1, v_{A1}), \min (c_2, v_{A2})] &< v_{ph} \\ &< \min [\min (c_0, v_{A0}), \max (c_1, v_{A1}), \max (c_2, v_{A2})], \end{aligned} \quad (3.24a)$$

$$\max [c_{T0}, \min (c_1, v_{A1})] < v_{ph} < \min [\min (c_0, v_{A0}), \max (c_1, v_{A1}), c_{T2}], \quad (3.24b)$$

$$c_{T0} < v_{ph} < \min [\min (c_0, v_{A0}), c_{T1}, c_{T2}]. \quad (3.24c)$$

A fourth type may also be described by swapping the $j = 1, 2$ indices in condition (3.24b), however, we will not look at this case in further detail, as it does not describe a qualitatively different type of body mode. The same will be true for the phase speed bands of fast body modes in the thin-slab limit, and bands of both slow and fast body waves in the wide-slab approximation.

Using these conditions we have just determined, one possibility to emphasize the role of magnetic asymmetry is to use Equation (3.22), and only accept the solutions while they fall within one of the phase speed bands determined in Equations (3.24a) - (3.24c). The second possible approach is to use an approximation which bounds the solutions to remain in the above-mentioned bands at all times. This method, however, can only serve as a general guideline for the shape of the solution curves, as in the extremes of the thin-slab limit, solutions can become leaky.

Following the second approach, we provide an approximate solution for all three cases, each of which converges either to the internal cusp speed, or to a value slightly offset from it:

$$\omega^2 \approx k^2 [c_{T0} + f]^2 [1 + \nu(kx_0)^2], \quad \text{where } \nu > 0. \quad (3.25)$$

The exact speed offset given by f depends on which band of body waves we consider, i.e.:

$$f = \max [c_{T0}, \min (c_1, v_{A1}), \min (c_2, v_{A2})] - c_{T0} \quad \text{for case (3.24a),} \quad (3.26a)$$

$$f = \max [c_{T0}, \min (c_1, v_{A1})] - c_{T0} \quad \text{for case (3.24b),} \quad (3.26b)$$

$$f = 0 \quad \text{for case (3.24c).} \quad (3.26c)$$

Substituting the suitable form of ω^2 into Equation (3.22) gives us the applicable expression for ν for every (integer) j :

$$\nu_j = \frac{[(c_{T0} + f)^2 - c_0^2][v_{A0}^2 - (c_{T0} + f)^2]}{(c_0^2 + v_{A0}^2)(c_{T0} + f)^2 \pi^2 j^2}. \quad (3.27)$$

Finally, we can substitute this into Equation (3.25) to find the approximate phase speed solutions for quasi-sausage body modes.

The corresponding slow quasi-kink mode solutions can be found using similar considerations, with the one important difference. For quasi-kink body modes, $n_0 \cot(n_0 x_0)$ has to remain finite, and so $n_0 x_0 \rightarrow (j - \frac{1}{2})\pi$ is required (for $j = 1, 2, 3 \dots$). Here, the values of the parameter ν_j are:

$$\nu_j = \frac{[(c_{T0} + f)^2 - c_0^2][v_{A0}^2 - (c_{T0} + f)^2]}{(c_0^2 + v_{A0}^2)(c_{T0} + f)^2 \pi^2 (j - \frac{1}{2})^2}. \quad (3.28)$$

Substituting these ν_j values back into Equation (3.25), we can derive an approximation for the phase speed of the slow quasi-kink body modes. Just like the quasi-sausage modes, these waves also tend to the limiting speed $c_{T0} + f$ from below as the slab becomes thinner.

When fast body modes exist, they behave similarly to the slow body modes in the thin-slab limit. Again, we have three potential bands of phase speed where fast body mode solutions may be found:

$$\begin{aligned} \max[\max(c_0, v_{A0}), \min(c_1, v_{A1}), \min(c_2, v_{A2})] < v_{ph} \\ < \min[\max(c_1, v_{A1}), \max(c_2, v_{A2})] \end{aligned} \quad (3.29a)$$

$$\max[\max(c_0, v_{A0}), \min(c_1, v_{A1})] < v_{ph} < \min[\max(c_1, v_{A1}), c_{T2}] \quad (3.29b)$$

$$\max(c_0, v_{A0}) < v_{ph} < \min(c_{T1}, c_{T2}). \quad (3.29c)$$

The magnitude of the plasma- β ($\beta = (2/\gamma)(c_0^2/v_{A0}^2)$) determines where the fast body mode phase speeds converge to in a thin slab. If we denote $\max(c_0^2, v_{A0}^2)$ as v_{\max}^2 and $\min(c_0^2, v_{A0}^2)$ as v_{\min}^2 . Then, the approximate solutions can be given in the form:

$$\omega^2 \approx k^2 [v_{\max} + f + u]^2 \left[1 + \frac{1}{\nu(kx_0)^2} \right], \quad \text{where } \nu > 0. \quad (3.30)$$

The exact values of the lower and upper speed boundary, f and u , depend on which band of solutions we investigate. For conditions (3.29a), ..., (3.29c), respectively, we have:

$$f = \max[v_{\max}, (\min(c_1, v_{A1}), \min(c_2, v_{A2}))] - v_{\max}, \quad (3.31a)$$

$$u = \min[\max(c_1, v_{A1}), \max(c_2, v_{A2})] - f - v_{\max},$$

$$f = \max[v_{\max}, (\min(c_1, v_{A1}))] - v_{\max}, \quad (3.31b)$$

$$u = \min[\max(c_1, v_{A1}), c_{T2}] - f - v_{\max},$$

$$f = 0, \quad (3.31c)$$

$$u = \min(c_{T1}, c_{T2}) - v_{\max}.$$

As before, for the quasi-sausage modes, $n_0 \tan(n_0 x_0)$ has to remain finite, so $n_0 x_0$ must converge to the roots of $\tan(n_0 x_0) = 0$. Substituting the prescribed form of ω^2 into $n_0 x_0 = j\pi$ (for $j = 1, 2, 3 \dots$) lets us determine the values of ν_j in each case:

$$\nu_j = \left\{ \frac{\pi^2 j^2 [v_{\min}^2 + v_{\max}^2][2fv_{\max} + 2uv_{\max} + (f + u)^2] + v_{\max}^4}{k^2 x_0^2 [(v_{\max} + f + u)^2 - v_{\min}^2][v_{\max} + f + u]^2} - \frac{2fv_{\max} + 2uv_{\max} + [f + u]^2}{[v_{\max} + f + u]^2} \right\}^{-1} \frac{1}{k^2 x_0^2}. \quad (3.32)$$

For the same characteristic speed ordering, the coefficients for the quasi-kink body modes have the form

$$\nu_j = \left\{ \frac{\pi^2 [j - \frac{1}{2}]^2 [v_{\min}^2 + v_{\max}^2] [2fv_{\max} + 2uv_{\max} + (f+u)^2] + v_{\max}^4}{k^2 x_0^2 [(v_{\max} + f + u)^2 - v_{\min}^2] [v_{\max} + f + u]^2} - \frac{2fv_{\max} + 2uv_{\max} + [f+u]^2}{[v_{\max} + f + u]^2} \right\}^{-1} \frac{1}{k^2 x_0^2}. \quad (3.33)$$

These coefficients can now be substituted into the body mode dispersion relation given by Equation (3.30) to find approximations for the angular frequencies of trapped body mode oscillations. All of this holds when the external sound speeds are greater than the external Alfvén speeds (so the plasma- β is high). If the opposite is true, and the plasma- β is low, then $\tan(n_0 x_0) \rightarrow \infty$ needs to be true for quasi-sausage modes, $\cot(n_0 x_0) \rightarrow \infty$ must hold for quasi-kink modes, and the coefficients j and $j - 1/2$ in the above expressions have to be modified accordingly.

Generally speaking, we can see that though the effect of density ratios ρ_0/ρ_1 and ρ_0/ρ_2 cannot be seen explicitly in the calculations performed for body waves, the density asymmetry still has an indirect influence on them through determining the values and relations of the characteristic speeds in the three plasma domains.

3.3 Wide-slab approximation

3.3.1 Surface modes

Wide asymmetric slabs in solar physics could represent a model of the global stratification of the atmosphere, e.g. the photosphere - interface region - corona system (see also Section 4.2). In a local context, the wide-slab limit can also serve as an approximation for high-frequency waves present in light bridges of sunspots or elongated magnetic bright points (MBPs) (see Sections 4.5 and 4.6).

For the wide-slab limit to be applicable, the width of the slab has to be much greater than the wavelength of oscillations considered: $kx_0 \gg 1$. Then $m_0 x_0 \gg 1$ also applies (see Roberts 1981b), and the full dispersion relation (2.31) becomes

$$\begin{aligned} & \frac{\rho_0}{\rho_1} m_1 \frac{\rho_0}{\rho_2} m_2 (k^2 v_{A0}^2 - \omega^2)^2 + m_0^2 (k^2 v_{A1}^2 - \omega^2) (k^2 v_{A2}^2 - \omega^2) \\ & + \rho_0 m_0 (k^2 v_{A0}^2 - \omega^2) \left[\frac{m_2}{\rho_2} (k^2 v_{A1}^2 - \omega^2) + \frac{m_1}{\rho_1} (k^2 v_{A2}^2 - \omega^2) \right] = 0. \end{aligned} \quad (3.34)$$

Since $m_0 x_0 \gg 1$, and therefore $\tanh m_0 x_0 \rightarrow 1$ and $\coth m_0 x_0 \rightarrow 1$ as well, the decoupled dispersion relation (2.39) takes the same form for both quasi-sausage and quasi-kink modes:

$$(k^2 v_{A0}^2 - \omega^2) \left[\frac{\rho_0}{\rho_1} \frac{m_1}{(k^2 v_{A1}^2 - \omega^2)} + \frac{\rho_0}{\rho_2} \frac{m_2}{(k^2 v_{A1}^2 - \omega^2)} \right] + 2m_0 = 0. \quad (3.35)$$

As the width of the slab increases, the waves at one interface affected by the conditions at the other boundary only to an ever smaller degree, essentially reducing the problem to a single interface system in the extreme wide slab case. This may be shown mathematically by taking the system of equations presented by the boundary

conditions, rearranging and substituting $\tanh m_0 x_0 = \coth m_0 x_0 = 1$ into them. This process leads to the result

$$\Lambda_j + \Lambda_0 = 0, \quad (3.36)$$

for $j = 1, 2$. Using the definitions of Λ_j from Equation (2.22), we can see that this expression is the dispersion relation of a single interface (see Roberts 1981a).

3.3.2 Body modes

Body modes in a wide slab can be handled in a similar manner to those in the thin-slab approximation, taking into account the limits and cut-offs introduced by the external density and magnetic asymmetry. In a non-magnetic asymmetric slab, the phase speed of slow body modes would converge to v_{\min} , but here, that approach might be subject to some offset, so the angular frequencies will have the form

$$\omega^2 = k^2 [v_{\min} - u]^2 \left[1 + \frac{\nu}{(kx_0)^2} \right], \quad (3.37)$$

where the exact value of u depends on the band of solutions. In case of (3.24a)-(3.24c)

$$u = v_{\min} - \min [\min (c_0, v_{A0}), \max (c_1, v_{A1}), \max (c_2, v_{A2})], \quad (3.38a)$$

$$u = v_{\min} - \min [\min (c_0, v_{A0}), \max (c_1, v_{A1}), c_{T2}], \quad (3.38b)$$

$$u = v_{\min} - \min [\min (c_0, v_{A0}), c_{T1}, c_{T2}], \quad (3.38c)$$

respectively. For the quasi-sausage mode solutions, to keep $n_0 \tan (n_0 x_0)$ bounded as $kx_0 \rightarrow \infty$, the condition can be set that $\tan (n_0 x_0) \rightarrow \pm \infty$, so that the argument $n_0 x_0 \rightarrow (j - \frac{1}{2})\pi$. This gives the ν_j parameters as

$$\nu_j = \pi^2 \left[j - \frac{1}{2} \right]^2 \frac{[v_{\min}^4 - (v_{\min}^2 + v_{\max}^2)(2uv_{\min} - u^2)]}{[v_{\max}^2 - (v_{\min} - u)^2][v_{\min} - u]^2}. \quad (3.39)$$

The slow quasi-kink body modes can be found using a similar process, but this time setting $n_0 x_0 \rightarrow j\pi$ so that $\cot (n_0 x_0) \rightarrow \pm \infty$. This yields

$$\nu_j = \pi^2 j^2 \frac{[v_{\min}^4 - (v_{\min}^2 + v_{\max}^2)(2uv_{\min} - u^2)]}{[v_{\max}^2 - (v_{\min} - u)^2][v_{\min} - u]^2}. \quad (3.40)$$

Substituting the expressions we have thus obtained for ν_j into Equation (3.37) lets us find the approximate frequencies of body modes in a low- β ($v_{A0} > c_0$) wide slab. In a high- β slab, the condition for the quasi-sausage modes is $\tan (n_0 x_0) \rightarrow 0$, and for quasi-sausage modes, it becomes $\cot (n_0 x_0) \rightarrow 0$, so any expressions that include j and $j - 1/2$ terms have to be adjusted accordingly.

We can repeat the same steps for the fast body waves in the wide slab, too. The phase speeds of these eigenmodes are assumed to tend towards the higher internal characteristic speed in the externally non-magnetic wide slab configuration. In the magnetically asymmetric slab system, the fast body wave frequencies are

$$\omega^2 = k^2 [v_{\max} + f]^2 \left[1 + \frac{1}{(kx_0)^2 \nu} \right], \quad (3.41)$$

where the value of f depends on the band of solutions in question. In case (3.29a), (3.29b) and (3.29c), the terms f are defined by Equations (3.31a), (3.31b) and (3.31c), respectively.

For quasi-sausage modes, the condition $n_0x_0 \rightarrow (j - \frac{1}{2})\pi$ has to be fulfilled, leading to

$$\nu_j = \left\{ \pi^2 \left[j - \frac{1}{2} \right]^2 \frac{[(v_{\min}^2 + v_{\max}^2)(2fv_{\max} + f^2) + v_{\max}^4]}{[(v_{\max} + f)^2 - v_{\min}^2][v_{\max} + f]^2} - \frac{[2fv_{\max} + f^2][kx_0]^2}{[v_{\max} + f]^2} \right\}^{-1}. \quad (3.42)$$

For the quasi-kink modes, this condition is $n_0x_0 \rightarrow j\pi$, so the coefficients and the frequencies are only slightly different:

$$\nu_j = \left\{ \pi^2 j^2 \frac{[(v_{\min}^2 + v_{\max}^2)(2fv_{\max} + f^2) + v_{\max}^4]}{[(v_{\max} + f)^2 - v_{\min}^2][v_{\max} + f]^2} - \frac{[2fv_{\max} + f^2][kx_0]^2}{[v_{\max} + f]^2} \right\}^{-1}. \quad (3.43)$$

Substituting the appropriate coefficient ν_j from Equations (3.42) and (3.43), into Equation (3.41) gives us the angular frequencies of the fast quasi-sausage and quasi-kink body modes in the wide-slab approximation. This holds true when $c_0 > v_{A0}$. In a low- β slab, however, the condition for quasi-sausage modes becomes $\tan(n_0x_0) \rightarrow 0$, while for quasi-kink modes, it is $\cot(n_0x_0) \rightarrow 0$, and the ν_j parameters have to be adjusted accordingly.

Similarly to what we have seen in the thin-slab approximation, the effect of the equilibrium density and magnetic asymmetries in the external environment on body modes is not obvious, and it only appears through the shifted band limits and cut-offs. From the approximate solutions found in this section, we may conclude that a magnetically asymmetric environment has greater effect on MHD surface waves than it does on body waves. Solar and astrophysical applications of the asymmetric slab model may be expected to have greater success for MHD surface waves observed in thin magnetic structures, since in wide slabs, the effects of asymmetry can be felt to a lesser degree at either of the two distant interfaces.

3.3.3 Thin- and wide-slab approximations based on the full dispersion relation

If we cannot reasonably assume that the asymmetry in the magnetic slab system is weak, then the full dispersion relation (Equation 2.31) should be used to describe any solutions. In the thin-slab approximation, both $\tanh(m_0x_0) \rightarrow m_0x_0$ and $\coth(m_0x_0) \rightarrow 1/(m_0x_0)$ can be used to repeat the analysis of the modes described in Sections 3.2 and 3.3.

With the above substitutions, for the slow quasi-sausage surface mode whose phase speed approaches c_{T0} in the limit of a thin slab ($\omega^2 \rightarrow k^2c_{T0}^2$), the following cubic equation can be obtained from the full dispersion relation:

$$U^3 + a_2U^2 + a_0 = 0, \quad (3.44)$$

where

$$\begin{aligned}
 a_2 &= 2 \frac{k^3 W_1 W_2 V A_0}{E}, & a_0 &= \frac{2k^5 v^3 A_0 A_1^2 A_2^2 R_1 R_2 x_0}{E} + V^3 A_0 k^4 x_0^2, \\
 A_0 &= \sqrt{(v_{A0}^2 - c_{T0}^2)}, & A_1 &= \sqrt{(v_{A1}^2 - c_{T0}^2)}, \\
 A_2 &= \sqrt{(v_{A2}^2 - c_{T0}^2)}, & E &= R_1 A_1^2 W_2 + R_2 A_2^2 W_1, \\
 R_1 &= \frac{\rho_1}{\rho_0}, & R_2 &= \frac{\rho_2}{\rho_0}, \\
 V &= \sqrt{\frac{(c_0^2 - c_{T0}^2)}{(v_{A0}^2 + c_0^2)}}, & W_1 &= \sqrt{\frac{(v_{A1}^2 - c_{T0}^2)(c_1^2 - c_{T0}^2)}{(v_{A1}^2 + c_1^2)(c_{T1}^2 - c_{T0}^2)}}, \\
 W_2 &= \sqrt{\frac{(v_{A2}^2 - c_{T0}^2)(c_2^2 - c_{T0}^2)}{(v_{A2}^2 + c_2^2)(c_{T2}^2 - c_{T0}^2)}}, & U &= \sqrt{k^2 c_{T0}^2 - \omega^2}.
 \end{aligned}$$

The (real) solutions are then given by

$$\omega^2 = k^2 c_{T0}^2 - \left(\frac{S}{6} + \frac{2a_2^2}{3S} - \frac{a_2}{3} \right)^2, \quad (3.45)$$

where

$$S = \left(-108a_0 - 8a_2^2 + 12\sqrt{12a_0a_2^3 + 81a_0^2} \right)^{1/3}.$$

In order to keep the solutions for the angular frequencies real, the same six characteristic speed orderings are possible which were detailed earlier, using the decoupled dispersion relation.

Applying a similar process, the approximation for the quasi-sausage surface mode with $\omega^2 \rightarrow k^2 c_2^2$ can be obtained from the full dispersion relation as:

$$\omega^2 = k^2 c_2^2 - \left(\frac{2k^2 x_0 R_1 R_2 A_1 A_2 V_0^2 + k^3 x_0^2 R_2 A_0^2 A_2 V_0^2 V_1 + k R_2 A_2 V_1}{2k x_0 A_0^2 V_1 W + k^2 x_0^2 R_1 A_0^2 A_1 V_0^2 W + R_1 A_1 W} \right)^2, \quad (3.46)$$

where

$$\begin{aligned}
 A_0 &= \sqrt{(v_{A0}^2 - c_2^2)}, & A_1 &= \sqrt{(v_{A1}^2 - c_2^2)}, \\
 A_2 &= \sqrt{(v_{A2}^2 - c_2^2)}, & W &= \sqrt{\frac{1}{(c_{T2}^2 - c_2^2)(c_2^2 + v_{A2}^2)}}, \\
 R_1 &= \frac{\rho_1}{\rho_0}, & R_2 &= \frac{\rho_2}{\rho_0}, \\
 V_0 &= \sqrt{\frac{(c_0^2 - c_2^2)}{(c_{T0}^2 - c_2^2)(v_{A0}^2 + c_0^2)}}, & V_1 &= \sqrt{\frac{(c_1^2 - c_2^2)}{(c_{T1}^2 - c_2^2)(v_{A1}^2 + c_1^2)}}.
 \end{aligned}$$

For the isothermal case, the dispersion relation for the quasi-sausage mode approaching $c_1 = c_2 = c_e$ simplifies to:

$$2A_0^2 W_1 W_2 x_0 U^2 + E (1 + A_0^2 V^2 k^2 x_0^2) U + 2R_1 R_2 v^2 A_1 A_2 x_0 = 0, \quad (3.47)$$

where

$$\begin{aligned}
 A_0 &= \sqrt{(v_{A0}^2 - c_e^2)}, & A_1 &= \sqrt{(v_{A1}^2 - c_e^2)}, \\
 A_2 &= \sqrt{(v_{A2}^2 - c_e^2)}, & E &= R_1 A_1 W_2 + R_2 A_2 W_1, \\
 R_1 &= \frac{\rho_1}{\rho_0}, & R_2 &= \frac{\rho_2}{\rho_0}, \\
 U &= \sqrt{k^2 c_e^2 - \omega^2}, & V &= \sqrt{\frac{(c_0^2 - c_e^2)}{(v_{A0}^2 + c_0^2)(c_{T0}^2 - c_e^2)}}, \\
 W_1 &= \sqrt{\frac{1}{(v_{A1}^2 + c_1^2)(c_{T1}^2 - c_e^2)}}, & W_2 &= \sqrt{\frac{1}{(v_{A2}^2 + c_2^2)(c_{T2}^2 - c_e^2)}}.
 \end{aligned}$$

For the quasi-kink surface mode approaching $\omega^2 \rightarrow k^2 v_{A1}^2$, the solutions are

$$\omega^2 = k^2 v_{A1}^2 - \left(\frac{2k^2 x_0 A_0^2 A_2 W_1 W_2 + k^3 x_0^2 R_2 A_0^2 A_2^2 V^2 W_1 + k R_2 A_2^2 W_1}{2k x_0 R_1 R_2 A_2^2 V^2 + k^2 x_0^2 R_1 A_0^2 A_2 V^2 W_2 + R_1 A_2 W_2} \right)^2, \quad (3.48)$$

where

$$\begin{aligned}
 A_0 &= \sqrt{(v_{A0}^2 - v_{A1}^2)}, & A_2 &= \sqrt{(v_{A2}^2 - v_{A1}^2)}, \\
 R_1 &= \frac{\rho_1}{\rho_0}, & R_2 &= \frac{\rho_2}{\rho_0}, \\
 W_1 &= \sqrt{\frac{(c_1^2 - v_{A1}^2)}{(c_{T1}^2 - v_{A1}^2)(c_1^2 + v_{A1}^2)}}, & W_2 &= \sqrt{\frac{(c_2^2 - v_{A1}^2)}{(c_{T2}^2 - v_{A1}^2)(v_{A2}^2 + c_2^2)}}, \\
 V &= \sqrt{\frac{(c_0^2 - v_{A1}^2)}{(c_{T0}^2 - v_{A1}^2)(v_{A0}^2 + c_0^2)}}.
 \end{aligned}$$

When the external Alfvén speeds are symmetric, and the phase speed of the mode approaches $v_{A1} = v_{A2} = v_{Ae}$, the solution for the quasi-kink mode simplifies to

$$2R_1 R_2 V^2 x_0^2 U^2 + E [k^2 V^2 A_0^2 x_0^2 + 1] U + 2W_1 W_2 A_0^2 k^2 x_0 = 0, \quad (3.49)$$

where

$$\begin{aligned}
 A_0 &= \sqrt{(v_{A0}^2 - v_{Ae}^2)}, & E &= R_1 W_2 + R_2 W_1, \\
 R_1 &= \frac{\rho_1}{\rho_0}, & R_2 &= \frac{\rho_2}{\rho_0}, \\
 U &= \sqrt{k^2 v_{Ae}^2 - \omega^2}, & V &= \sqrt{\frac{(c_0^2 - v_{Ae}^2)}{(v_{A0}^2 + c_0^2)(c_{T0}^2 - v_{Ae}^2)}}, \\
 W_1 &= \sqrt{\frac{(c_1^2 - v_{Ae}^2)}{(v_{Ae}^2 + c_1^2)(c_{T1}^2 - v_{Ae}^2)}}, & W_2 &= \sqrt{\frac{(c_2^2 - v_{Ae}^2)}{(v_{Ae}^2 + c_2^2)(c_{T2}^2 - v_{Ae}^2)}}.
 \end{aligned}$$

For the quasi-kink surface mode with its frequency $\omega^2 \rightarrow k^2 c_{T1}^2$, the solutions obtained from the full dispersion relation become

$$\omega^2 = k^2 c_{T1}^2 - \left(\frac{2k^2 x_0 A_0^2 W V_2 + k^3 x_0^2 R_2 A_0^2 A_2 V_0^2 W + k R_2 A_2 W}{2k x_0 R_1 R_2 A_1 A_2 V_0^2 + k^2 x_0^2 R_1 A_0^2 A_1 V_0^2 V_2 + R_1 A_1 V_2} \right)^2, \quad (3.50)$$

where

$$\begin{aligned}
 A_0 &= \sqrt{(v_{A0}^2 - c_{T1}^2)}, & A_1 &= \sqrt{(v_{A1}^2 - c_{T1}^2)}, \\
 A_2 &= \sqrt{(v_{A2}^2 - c_{T1}^2)}, & W &= \sqrt{\frac{(c_1^2 - c_{T1}^2)}{(c_1^2 + v_{A1}^2)}} \\
 R_1 &= \frac{\rho_1}{\rho_0}, & R_2 &= \frac{\rho_2}{\rho_0}, \\
 V_0 &= \sqrt{\frac{(c_0^2 - c_{T1}^2)}{(v_{A0}^2 + c_0^2)(c_{T0}^2 - c_{T1}^2)}}, & V_2 &= \sqrt{\frac{(c_2^2 - c_{T1}^2)}{(v_{A2}^2 + c_2^2)(c_{T2}^2 - c_{T1}^2)}}.
 \end{aligned}$$

For the derivation of body mode solutions, we once again use the same assumptions as we did in the previous Section, but we start our calculations from the full dispersion relation for body modes given by Equation (3.20). The angular frequency of slow body waves approaches the tube speed in a thin slab $\omega^2 \rightarrow k^2 c_{T0}^2$, or the appropriate cut-off frequency slightly offset from the tube speed (see the details after Equation 3.25) from above. For the expression $n_0(-\tan(n_0 x_0) + \cot(n_0 x_0))$ to remain bounded as $kx_0 \rightarrow 0$, $n_0 x_0$ should approach values that satisfy $(-\tan(n_0 x_0) + \cot(n_0 x_0)) = 0$. The roots of this equation are the multiples of $\pi/4$:

$$n_0 x_0 = \frac{2j-1}{4}\pi, \quad (3.51)$$

where $j = 1, 2, 3, \dots$. This condition is then used in Equation (3.25) to find the ν_j coefficients to be used in the appropriate approximation for ω^2 describing both quasi-sausage and quasi-kink modes.

In the limit of a wide slab, slow body modes are still described by the approximation given by Equation (3.37). The angular frequency of these waves approaches $\omega^2 \rightarrow k^2(\min(v_{A0}, c_0))^2$ (in some cases with a small offset due to cut-offs) from below. In a high- β slab, the same condition as in (3.51) can be set, while in a low- β plasma, then the ν_j parameters are determined from setting $(-\tan(n_0 x_0) + \cot(n_0 x_0)) \rightarrow \pm\infty$, and therefore

$$n_0 x_0 = \frac{j}{2}\pi. \quad (3.52)$$

Fast body waves in the thin-slab limit can be described by Equation (3.30). For finding the ν_j coefficients, the condition (3.51) applies in a low- β environment, and Equation (3.52) is valid in a high- β environment. In the wide-slab approximation, Equation (3.41) still describes fast body modes, and ν_j is determined from the condition (3.51) if $v_{A0} > c_0$, or from Equation (3.52) if $c_0 > v_{A0}$.

Overall, the same basic principles apply to the behaviour of the quasi-sausage and quasi-kink modes, whether we approximate them from the decoupled or the full dispersion relation. Expressions derived from the full dispersion relation may be applicable to a wider range of equilibrium asymmetries in the slab system, however, solutions calculated from the decoupled dispersion relation are generally simpler and provide an easier insight into how the waves behave near the extremes of the dimensionless slab width parameter.

3.4 Low- β approximation

In the current Section, we move on to setting constraints on the equilibrium plasma and magnetic parameters in each region of the slab system, while leaving the relative magnitudes of the slab width and wavenumber of the oscillations unrestricted. The parameter we use to categorise the different equilibrium configurations of the magnetised plasma domains is the plasma- β defined as the ratio between the gas and the magnetic pressure:

$$\beta_j = \frac{p_j}{p_{m,j}} = \frac{2}{\gamma} \frac{c_j^2}{v_{Aj}^2}, \quad (3.53)$$

for $j = 0, 1, 2$, where p_j is the gas- and $p_{m,j}$ is the magnetic pressure of region j .

In the low- β approximation ($\beta_j \ll 1$), the magnetic pressure dominates over the gas pressure in region j , and therefore $c_j/v_{Aj} \ll 1$. This particular approximation is analytically useful to simplify the dispersion relation, and it also has a significant range of solar applicability, since from about the mid-chromosphere upwards into the corona, the atmosphere of our Sun is considered to be a low- β environment.

3.4.1 Low plasma- β in all three domains

When the plasma- β is low, but non-zero, in each region of the asymmetric magnetic slab model, it is possible to express the coefficients m_0 , m_1 , m_2 in terms of β_0 , β_1 , β_2 , respectively:

$$m_j^2 = \frac{(k^2 \beta_i \gamma v_{Ai}^2 - 2\omega^2) (k^2 v_{Aj}^2 - \omega^2)}{(k^2 \beta_i \gamma v_{Ai}^4 - \beta_i \gamma v_{Aj}^2 \omega^2 - 2v_{Ai}^2 \omega^2)}, \quad \text{for } j = 0, 1, 2, \quad (3.54)$$

$$n_0^2 = \frac{(k^2 \beta_i \gamma v_{Ai}^2 - 2\omega^2) (\omega^2 - k^2 v_{Ai}^2)}{(k^2 \beta_i \gamma v_{Ai}^4 - \beta_i \gamma v_{Aj}^2 \omega^2 - 2v_{Ai}^2 \omega^2)}. \quad (3.55)$$

Using these forms of the wavenumber coefficients and assuming the plasma- β is small in all three domains, an expansion of the dispersion relation (Equation 2.39) about $(\beta_0, \beta_1, \beta_2) \approx (0, 0, 0)$ can be performed. Taking only zeroth- and first-order terms into consideration, the dispersion relation for surface waves in a low- β system takes the following form:

$$L_1 + L_2 + L_{0s} - \frac{\gamma}{4} \left\{ L_1 \beta_1 + L_2 \beta_2 + L_{0s} \beta_0 \pm \frac{2x_0 \beta_0}{v_{A0}^2} \left[1 - \left(\frac{\tanh^2}{\coth^2} \right) \{m_{0z} x_0\} \right] \right\} = 0, \quad (3.56)$$

where

$$L_j = \frac{\rho_0}{\rho_j} \frac{m_{jz}}{(k^2 v_{Aj}^2 - \omega^2)}, \quad \text{for } j = 1, 2, \quad (3.57)$$

$$L_{0s} = \frac{2m_{0z}}{(k^2 v_{A0}^2 - \omega^2)} \left(\frac{\tanh}{\coth} \right) \{m_{0z} x_0\}, \quad (3.58)$$

$$m_{iz} = \left(\frac{k^2 v_{Ai}^2 - \omega^2}{v_{Ai}^2} \right)^{1/2}, \quad \text{for } i = 0, 1, 2. \quad (3.59)$$

Here, the index 'z' denotes the form of the wavenumber coefficients obtained from Equations (3.54-3.55) when $\beta = 0$ in the given domain, and the index 's' indicates that the term L_{0s} is necessary for the description of surface waves. In Equation (3.56), the lines containing the tanh, coth functions describe quasi-sausage and quasi-kink surface modes, respectively. With a similar notation, the expansion of the dispersion relation for body modes becomes

$$L_1 + L_2 + L_{0b} - \frac{\gamma}{4} \left\{ L_1\beta_1 + L_2\beta_2 + \beta_0 \left[L_{0b} \mp \frac{1}{2} L_{0b}^2 x_0 (k^2 v_{A0}^2 - \omega^2) \mp \frac{2n_{0z}^2 x_0}{(k^2 v_{A0}^2 - \omega^2)} \right] \right\} = 0, \quad (3.60)$$

where

$$L_{0b} = \frac{2n_{0z}}{(k^2 v_{A0}^2 - \omega^2)} \begin{pmatrix} -\tan \\ \cot \end{pmatrix} \{n_{0z} x_0\}, \quad (3.61)$$

$$n_{0z} = \left(\frac{\omega^2 - k^2 v_{Ai}^2}{v_{Ai}^2} \right)^{1/2}. \quad (3.62)$$

Here, the index 'b' refers to the fact that the term L_{0b} is required for the description of body modes, and, again, the top upper line (with the tan function) describes quasi-sausage body modes, while the bottom line governs quasi-kink body modes.

Edwin and Roberts (1982) provided an analytical study and numerical results for the low- β limit in a magnetic, but symmetric environment of a magnetic slab slab, and their basic findings still hold true in an asymmetric slab system, too. In Figure 3.1, we provide numerical solutions of the dispersion relation in various low- β slab systems to illustrate the similarities and differences from the symmetric case. Blue (red) curves show quasi-sausage (quasi-kink) modes in all panels, and hatching represents regions in which no trapped modes are found.

Panel (a) of Figure (3.1) was prepared using $v_{A0} = 1.5c_0$, $v_{A1} = 4c_0$, $v_{A2} = 3c_0$, $c_1 = 0.5976c_0$, $c_2 = 0.6972c_0$, $\rho_1/\rho_0 = 0.21$, $\rho_2/\rho_0 = 0.36$ for the characteristic speeds and density ration. The relation between the internal and external characteristic speeds can be summarised as $c_j < c_0 < v_{A0} < v_{Aj}$ (where $j = 1, 2$). In this case, there are no surface modes, only body waves are trapped and guided by the slab. The slow body waves have phase speed $c_{T0} < v_{ph} < c_0$, while the fast body waves propagate with $v_{A0} < v_{ph} < v_{A2}$. This corresponds to the conditions outlined in case (3.24a) for the slow waves, and to those in case (3.29a) for the fast waves. Both the quasi-sausage and the quasi-kink modes are present, and have infinitely many harmonics (though as before, we only plot a few of these for visual clarity).

If the ordering of the sound speeds is different, so the slab is cooler than its environment, then $c_0 < c_j < v_{A0} < v_{Aj}$, similar results are obtained: both fast and slow waves are be present. This is illustrated in panel (b) of Figure (3.1), which was prepared specifically with $v_{A0} = 1.2c_0$, $v_{A1} = 3c_0$, $v_{A2} = 3.5c_0$, $c_1 = 1.5811c_0$, $c_2 = 1.6531c_0$, $\rho_1/\rho_0 = 0.22$, $\rho_2/\rho_0 = 0.17$. An interesting observation can be made about the solutions in this equilibrium configuration. While the slow body modes represent case (3.24c), there are two bands of fast body waves, corresponding to the conditions in (3.29a) for the band with higher phase speeds, and to (3.29c) for the slower band. A similar result was also presented by Edwin and Roberts (1982) for the symmetric case, illustrated in their Figure 7.

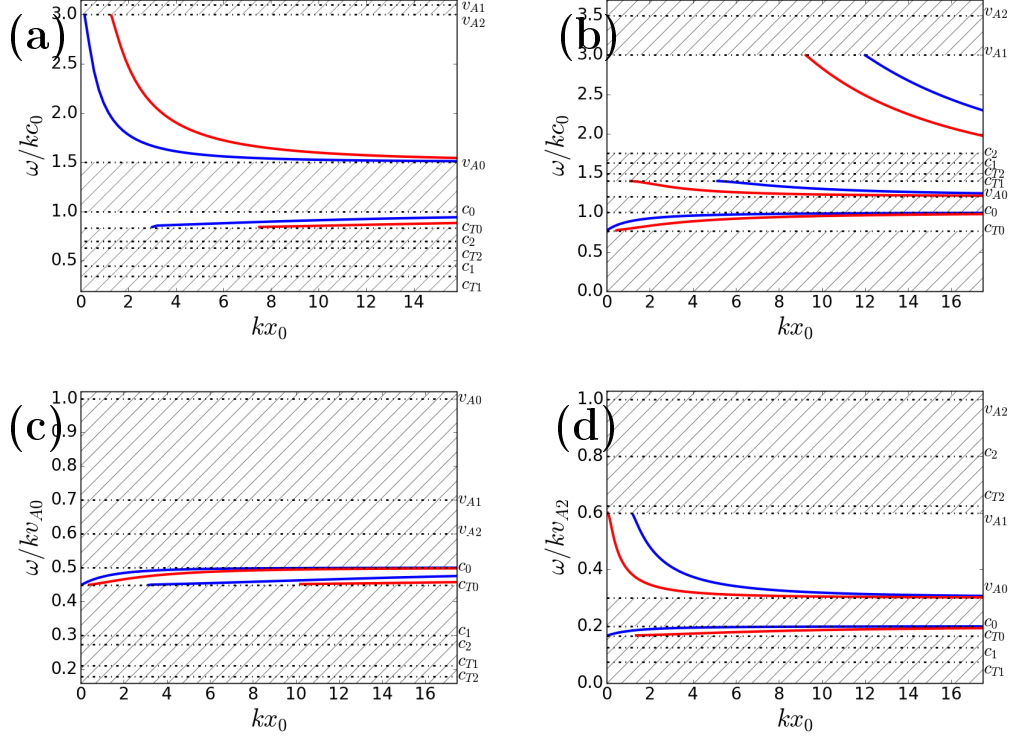


Figure 3.1: The phase speed (ω/k) of magnetoacoustic waves in various low- β situations characterised by typical choices of c_i , v_{Ai} , ρ_i . Blue (red) curves show quasi-sausage (quasi-kink) modes. Hatching represents regions in which no propagating modes are permitted. **(a)** Slow and fast mode body waves are seen when $v_{A0} = 1.5c_0$, $v_{A1} = 4c_0$, $v_{A2} = 3c_0$, $c_1 = 0.5976c_0$, $c_2 = 0.6972c_0$, $\rho_1/\rho_0 = 0.21$, $\rho_2/\rho_0 = 0.36$. **(b)** One band of slow-, and two bands of fast body modes appear when $v_{A0} = 1.2c_0$, $v_{A1} = 3c_0$, $v_{A2} = 3.5c_0$, $c_1 = 1.5811c_0$, $c_2 = 1.6531c_0$, $\rho_1/\rho_0 = 0.22$, $\rho_2/\rho_0 = 0.17$. **(c)** Only slow body modes can be found when $v_{A1} = 0.7v_{A0}$, $v_{A2} = 0.6v_{A0}$, $c_0 = 0.5v_{A0}$, $c_1 = 0.2504v_{A0}$, $c_2 = 0.2472v_{A0}$, $\rho_1/\rho_0 = 2.3$, $\rho_2/\rho_0 = 3.0$. **(d)** Even with more prominent asymmetry, one band of slow-, and one band of fast body modes exist when, e.g., $v_{A0} = 0.3v_{A2}$, $v_{A1} = 0.6v_{A2}$, $c_0 = 0.2v_{A2}$, $c_1 = 0.1v_{A2}$, $c_2 = 0.8v_{A2}$, $\rho_1/\rho_0 = 0.3710$, $\rho_2/\rho_0 = 0.0871$. In each panel, for the sake of clarity, only a couple of examples in each band of body modes are displayed.

If instead of the sound speeds, the Alfvén speeds are interchanged compared to the original ordering shown in panel (a), the solutions change considerably. Panel (c) of Figure (3.1) illustrates this case, with $v_{A1} = 0.7v_{A0}$, $v_{A2} = 0.6v_{A0}$, $c_0 = 0.5v_{A0}$, $c_1 = 0.2504v_{A0}$, $c_2 = 0.2472v_{A0}$, $\rho_1/\rho_0 = 2.3$, $\rho_2/\rho_0 = 3.0$. Here, the internal Alfvén speed is higher than both of the external Alfvén speeds, and, just like in a symmetric slab, only slow body mode solutions exist (described by the conditions in (3.24a)).

Panel (d) of Figure (3.1) was prepared using $v_{A0} = 0.3v_{A2}$, $v_{A1} = 0.6v_{A2}$, $c_0 = 0.2v_{A2}$, $c_1 = 0.1v_{A2}$, $c_2 = 0.8v_{A2}$, $\rho_1/\rho_0 = 0.3710$, $\rho_2/\rho_0 = 0.0871$. From this case, we find that even if the system is strongly asymmetric, making the internal sound speed fall between the external sound speeds, two bands of body mode solutions remain possible. The slow band corresponds to the conditions in (3.24b), with phase speeds between $c_{T0} < v_{ph} < c_0$. The fast body waves propagate with phase speeds in the range $v_{A0} < v_{ph} < v_{A1}$, corresponding to case (3.29b).

3.4.2 Zero- β limit

An extreme but often practical case of the low- β approximation is the zero- β limit. Here, the sound speeds are negligible compared to the Alfvén speeds: $c_1 \approx c_2 \approx c_0 \approx 0$, which can describe coronal plasma conditions using the MHD framework. This assumption further simplifies the dispersion relation from the low- β case. In the zero- β approximation, slow body waves are eliminated, and only the fast body waves remain possible, just like it was shown for the symmetric case by (Edwin and Roberts, 1982).

In the zero- β limit, the modified wavenumber coefficients are given by Equations (3.59) and (3.62), and the first-order terms of the expanded dispersion relation vanish, leading to

$$\begin{pmatrix} \tan \\ -\cot \end{pmatrix} \{n_{0z}x_0\} = \frac{1}{2} \frac{\rho_0 v_{A0}(k^2 v_{A0}^2 - \omega^2)^{1/2}}{\rho_1 v_{A1}(k^2 v_{A1}^2 - \omega^2)^{1/2}} + \frac{1}{2} \frac{\rho_0 v_{A0}(k^2 v_{A0}^2 - \omega^2)^{1/2}}{\rho_2 v_{A2}(k^2 v_{A2}^2 - \omega^2)^{1/2}}. \quad (3.63)$$

Equation (2.3) describes the requirement that total pressure balance must be upheld at both interfaces of the asymmetric slab system. Since the sound speeds are vanishingly small in the zero- β limit, Equation (2.3) simplifies to

$$\frac{\rho_j}{\rho_k} = \frac{v_{Ak}^2}{v_{Aj}^2}, \quad \text{where } j = 0, 1, 2; \quad k = 0, 1, 2; \quad j \neq k. \quad (3.64)$$

Using Equation (3.64), the dispersion relation further simplifies to

$$\begin{pmatrix} \tan \\ -\cot \end{pmatrix} \{n_{0z}x_0\} = -\frac{1}{2} \left(\frac{n_{0z}}{m_{1z}} + \frac{n_{0z}}{m_{2z}} \right). \quad (3.65)$$

In the fully symmetric case, this expression reduces to Equations (22) and (23) of Edwin and Roberts (1982).

In Equation (3.65), the wavenumber coefficients n_{0z} , m_{1z} and $m_{2z} > 0$, which is only true when $k^2 v_{A0}^2 < \omega^2 < \min(k^2 v_{A1}^2, k^2 v_{A2}^2)$. The role of asymmetry manifests in this selection for the lower value out of the two external Alfvén speeds. An alternate description of body waves in this band, e.g. in the wide-slab limit, can be provided by requiring the waves to approach $\omega^2 = k^2 v_{A,\min}^2 [\rho_{\min}/\rho_0] [1 + \nu/(kx_0)^2]$, where the index m denotes external equilibrium parameters on the side of the slab with the lower (external) Alfvén speed. We determine the coefficients ν_j through a process similar to the one we used while deriving the wide-slab approximation in the general case, leading to the expression

$$\omega^2 = k^2 v_{A,\min}^2 \frac{\rho_{\min}}{\rho_0} \left[1 + \frac{\pi^2 (j - \frac{1}{2})^2}{k^2 x_0^2} \right] \quad (3.66)$$

for quasi-sausage modes, and

$$\omega^2 = k^2 v_{A,\min}^2 \frac{\rho_{\min}}{\rho_0} \left[1 + \frac{\pi^2 j^2}{k^2 x_0^2} \right] \quad (3.67)$$

for quasi-kink modes. For given values of j , ω and k , Equations (3.66) and (3.67) determine a simple connection between the lower external Alfvén speed and the

external-to-internal density ratio on the same side, therefore, knowing one of them can provide an estimate of the other, thus serving a simple diagnostic purpose.

Overall, the description of eigenmodes in the low- and zero- β limits of the asymmetric slab model is formally analogous to that in the symmetric case. However, the difference in external equilibrium quantities adds some analytical complexity and can give rise to new phenomena. Perhaps the most important difference resulting from the added asymmetry is that, the fast body mode solution curves experience a cut-off in the thin-slab limit: with phase speed above the lower external Alfvén speed, the waves become leaky.

3.5 High- β approximation

In the high plasma- β approximation, magnetic pressure is dominated by plasma kinetic pressure. This is generally the case in the lower solar atmosphere, where various waveguides such as light bridges or MBPs can be modelled as slab systems, providing motivation for the further analytical and numerical examination of this possibility.

3.5.1 High plasma- β in all three domains

If the plasma- β is high, the Alfvén speeds are small compared to the corresponding sound speeds of each domain: $c_j/v_{Aj} \gg 1$ for $j = 0, 1, 2$. We can write the modified wavenumber coefficients as

$$m_j^2 = \frac{(k^2 c_i^2 - \omega^2)(2k^2 c_i^2 - \gamma \beta_j \omega^2)}{c_i^2(2k^2 c_i^2 - 2\omega^2 - \gamma \beta_j \omega^2)} \quad \text{for } j = 0, 1, 2, \quad (3.68)$$

$$n_0^2 = \frac{(\omega^2 - k^2 c_0^2)(2k^2 c_0^2 - \gamma \beta_0 \omega^2)}{c_0^2(2k^2 c_0^2 - 2\omega^2 - \gamma \beta_0 \omega^2)}. \quad (3.69)$$

In slabs that are characterised by high plasma- β values all throughout the system, we find a richer variety of modes than we did in the low- β case, as illustrated by Figure 3.2. Before we proceed to describe specific examples, we use the modified wavenumber coefficients, and expand the dispersion relation about $(1/\beta_0, 1/\beta_1, 1/\beta_2) \approx (0, 0, 0)$. Keeping only zeroth- and first-order terms then leads to the following expression:

$$\begin{aligned} H_1 + H_2 + H_{0s} + \frac{1}{\gamma \omega^2} \left\{ [2k^2 c_1^2 - \omega^2] \frac{H_1}{\beta_1} + [2k^2 c_2^2 - \omega^2] \frac{H_2}{\beta_2} \right. \\ \left. + [2k^2 c_0^2 - \omega^2] \frac{H_{0s}}{\beta_0} + \frac{2x_0 m_{0z}^2}{\beta_0} \left[1 - \left(\frac{\tanh^2}{\coth^2} \right) \{m_{0z} x_0\} \right] \right\} = 0 \end{aligned} \quad (3.70)$$

for surface waves, where

$$H_j = -\frac{\rho_0}{\rho_j} \frac{m_{jz}}{\omega^2}, \quad \text{for } j = 1, 2, \quad (3.71)$$

$$H_{0s} = -\frac{2m_{0z}}{\omega^2} \left(\frac{\tanh}{\coth} \right) \{m_{0z} x_0\}, \quad (3.72)$$

$$m_{iz} = \left(\frac{k^2 c_i^2 - \omega^2}{c_i^2} \right)^{1/2}, \quad \text{for } i = 0, 1, 2. \quad (3.73)$$

Adopting the same notation, the expansion of the dispersion relation for body waves becomes

$$H_1 + H_2 - H_{0b} + \frac{1}{\gamma\omega^2} \left\{ [2k^2c_1^2 - \omega^2] \frac{H_1}{\beta_1} + [2k^2c_2^2 - \omega^2] \frac{H_2}{\beta_2} - \frac{H_{0b}}{\beta_0} [2k^2c_0^2 - \omega^2] - \frac{2x_0n_{0z}^2}{\beta_0} \left[1 + \left(\frac{\tan^2}{\cot^2} \right) \{n_{0z}x_0\} \right] \right\} = 0, \quad (3.74)$$

where

$$H_{0b} = \frac{2n_{0z}}{\omega^2} \left(\frac{-\tan}{\cot} \right) \{n_{0z}x_0\}, \quad (3.75)$$

$$n_{0z} = \left(\frac{\omega^2 - k^2c_i^2}{c_i^2} \right)^{1/2}. \quad (3.76)$$

Examples of numerical solutions to the dispersion relation for high- β slabs enclosed in high- β environments are provided in Figure 3.2. As before, in each panel, only a few of the infinite harmonics of body modes in any given band are displayed. Blue (red) curves illustrate quasi-sausage (quasi-kink) modes, and no trapped oscillations exist in the hatched regions.

Panel (a) of Figure 3.2 was prepared using $v_{A0} = 0.7c_0$, $v_{A1} = 0.2c_0$, $v_{A2} = 0.1c_0$, $c_1 = 1.6683c_0$, $c_2 = 1.8742c_0$, $\rho_1/\rho_0 = 0.5$, $\rho_2/\rho_0 = 0.4$ for the characteristic speeds and density ratios. We find a band of fast body mode solutions (corresponding to case (3.29a)) with phase speed between the internal and external sound speeds, as well as a band of slow body modes between the internal cusp- and Alfvén speeds (fulfilling the conditions in (3.24a)). As opposed to the low- β limit, this system guides a pair of slow surface waves, too, propagating with phase speeds below the internal cusp speed.

Panel (b) of Figure 3.2 shows that interchanging the relative magnitudes of the internal and external Alfvén speeds ($v_{A0} = 0.6c_0$, $v_{A1} = 0.95c_0$, $v_{A2} = 0.9c_0$, $c_1 = 1.5c_0$, $c_2 = 1.4c_0$, $\rho_1/\rho_0 = 0.433$, $\rho_2/\rho_0 = 0.4934$) does not change the dispersion curves qualitatively. Besides the slow surface mode, there is still a band of fast body modes (corresponding to case (3.29a)), and a band of slow body modes (case (3.24c)).

As opposed to this, panel (c) of Figure 3.2 shows that if we swap the sound speeds instead ($v_{A1} = 0.4v_{A0}$, $v_{A2} = 0.3v_{A0}$, $c_0 = 1.4v_{A0}$, $c_1 = 1.15v_{A0}$, $c_2 = 1.1v_{A0}$, $\rho_1/\rho_0 = 1.9188$, $\rho_2/\rho_0 = 2.1738$), only the slow surface wave solutions and the band of slow body waves exist.

The splitting of body mode bands witnessed in symmetric slabs (Edwin and Roberts, 1982) remains possible in the high- β limit of an asymmetric slab, too, as evidenced by Figure 3.2d, prepared using the values of $v_{A0} = 0.2v_{A2}$, $v_{A1} = 0.7v_{A2}$, $c_0 = 0.5v_{A2}$, $c_1 = 1.1v_{A2}$, $c_2 = 1.8v_{A2}$, $\rho_1/\rho_0 = 0.1751$, $\rho_2/\rho_0 = 0.071$. We find a narrow band of slow body modes (fulfilling the conditions in (3.24c)), as well as slow surface modes. There are three bands of fast body modes present. The first one is confined between the internal sound speed and the lower one of the external cusp speeds (case (3.29c)). The second band corresponds to case (3.29b), being limited to phase speeds between $v_{A1} < v_{ph} < c_{T2}$. The third and final band of fast body modes realises case (3.29a) and occurs between $v_{A2} < v_{ph} < c_1$.

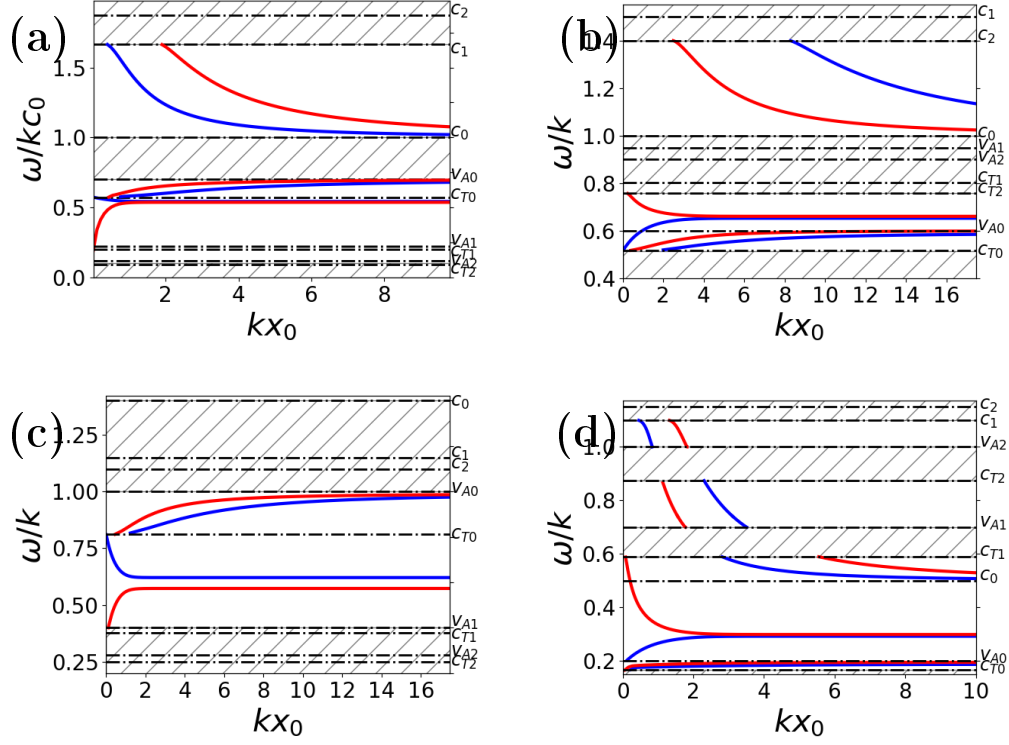


Figure 3.2: Solutions to the dispersion relation, similar to Figure 3.1, obtained for various high- β cases. **(a)** Slow and fast mode body waves, as well as slow surface waves are present when $v_{A0} = 0.7c_0$, $v_{A1} = 0.2c_0$, $v_{A2} = 0.1c_0$, $c_1 = 1.6683c_0$, $c_2 = 1.8742c_0$, $\rho_1/\rho_0 = 0.5$, $\rho_2/\rho_0 = 0.4$. **(b)** The same modes appear when $v_{A0} = 0.6c_0$, $v_{A1} = 0.95c_0$, $v_{A2} = 0.9c_0$, $c_1 = 1.5c_0$, $c_2 = 1.4c_0$, $\rho_1/\rho_0 = 0.433$, $\rho_2/\rho_0 = 0.4934$. **(c)** Only the slow surface and body modes can be observed when $v_{A1} = 0.4v_{A0}$, $v_{A2} = 0.3v_{A0}$, $c_0 = 1.4v_{A0}$, $c_1 = 1.15v_{A0}$, $c_2 = 1.1v_{A0}$, $\rho_1/\rho_0 = 1.9188$, $\rho_2/\rho_0 = 2.1738$. **(d)** Three bands of fast body modes, one band of slow body modes, and a pair of slow surface modes exist when $v_{A0} = 0.2v_{A2}$, $v_{A1} = 0.7v_{A2}$, $c_0 = 0.5v_{A2}$, $c_1 = 1.1v_{A2}$, $c_2 = 1.8v_{A2}$, $\rho_1/\rho_0 = 0.1751$, $\rho_2/\rho_0 = 0.071$. As before, in each panel, only a couple of examples in each band of body modes are displayed.

3.5.2 Infinite- β limit

In this extreme limiting case, magnetic forces are negligible as compared to kinetic ones, and so the approximation $v_{Ai} \approx 0$ for $i = 0, 1, 2$ can be applied. In this case, only fast body waves are present. The modified wavenumber coefficients simplify to the expressions in Equations (3.73) and (3.76), and the first-order terms vanish from the expansion. The pressure balance condition (2.3) simplifies as well, and it allows us to write the dispersion relation for body modes in the zero- β limit as

$$\begin{pmatrix} \tan \\ -\cot \end{pmatrix} \{n_0 x_0\} = \frac{1}{2} \left(\frac{m_1 c_1^2}{n_0 c_0^2} + \frac{m_2 c_2^2}{n_0 c_0^2} \right). \quad (3.77)$$

If the slab is fully symmetric, Equation (3.77) reduces to Equations (24) and (25) of Edwin and Roberts (1982). The conditions for the existence of these body modes, namely that n_{0z} , m_{1z} and $m_{2z} > 0$, are fulfilled only when $k^2 c_0^2 < \omega^2 < \min(k^2 c_1^2, k^2 c_2^2)$. Therefore, the band of fast body waves will be found between the

internal sound speed and the lower of the two external sound speeds. Introducing the notation $c_m = \min(c_1, c_2)$, the waves are expected to approach a sound speed as $\omega^2 = k^2 c_m^2 [\rho_m / \rho_0] [1 + \nu / (kx_0)^2]$. By using the alternate method described during the derivation of the general wide-slab approximations, the coefficients ν_j can be determined and used to obtain quasi-sausage body mode solutions in the following form:

$$\omega^2 = k^2 c_m^2 \frac{\rho_m}{\rho_0} \left[1 + \frac{\pi^2 (j - \frac{1}{2})^2}{k^2 x_0^2} \right], \quad (3.78)$$

while quasi-kink body modes behave as

$$\omega^2 = k^2 c_m^2 \frac{\rho_m}{\rho_0} \left[1 + \frac{\pi^2 j^2}{k^2 x_0^2} \right]. \quad (3.79)$$

A basic diagnostic purpose may be fulfilled by making these approximations. Namely, Equations (3.78) and (3.79) showcase a simple connection between the lower external sound speed, and the ratio of the same side's external density to the internal one for any given value of the wavenumber and angular frequency of a given order body mode. Thus, knowledge of one of these parameters can provide an estimate of the other.

Similarly to the low- β case, in the limits of high- and infinite plasma- β as well, the asymmetry shows its influence through a more complex dependence of the frequencies of eigenmodes on the set of external parameters in the system. The difference of external equilibrium parameters can shift the frequencies of surface-, as well as body waves, and it also introduces cut-off frequencies. As we have demonstrated, due to these, sometimes multiple, cut-offs, there can be more than one band of either fast or slow body modes. A further significant consequence of the asymmetry is that in the wide-slab limit, the phase speeds of surface modes will diverge (see Section 3.6 for details), leading to the phenomenon of avoided crossings that we described in Chapter 2.

3.5.3 Low- and high- β approximations based on the full dispersion relation

If we want to consider stronger asymmetries in the magnetic slab system, approximations in the various plasma- β limits can also be obtained from the full dispersion relation (Equation 2.31), using the modified wavenumber coefficients (3.55) and (3.54) for the low- β case. The following dependence on β_0 , β_1 and β_2 is found for a

low- β slab embedded in a low- β asymmetric environment:

$$\begin{aligned}
 & 2L_{0A} + 2m_{0z}^2 L_{0B} + m_{0z} L_{0C} \left\{ \tau_{0z} + \frac{1}{\tau_{0z}} \right\} \\
 & - \frac{1}{2} \left\{ m_{0z} L_{0C} \left[\tau_{0z} + \frac{1}{\tau_{0z}} \right] [k^2 v_{A0}^2 - \omega^2] - \frac{1}{2} \left[\tau_{0z}^2 + \frac{1}{\tau_{0z}^2} \right] [L_{0B} \right. \\
 & \left. + x_0 (k^2 v_{A0}^2 - \omega^2) L_{0C}] m_{0z}^2 + [L_{0B} + (k^2 v_{A0}^2 - \omega^2) x_0 L_{0C}] m_{0z}^2 \right\} \gamma \beta_0 \\
 & - \frac{1}{2} L_{0A} \gamma \{ \beta_1 + \beta_2 \} - \frac{1}{2} \gamma \rho_0 m_{0z} \{ k^2 v_{A0}^2 - \omega^2 \} \left\{ \beta_1 \frac{m_{1z}}{\rho_1} [k^2 v_{A2}^2 - \omega^2] \right. \\
 & \left. + \beta_2 \frac{m_{2z}}{\rho_2} [k^2 v_{A1}^2 - \omega^2] \right\} \left\{ \tau_{0z} + \frac{1}{\tau_{0z}} \right\} = 0, \tag{3.80}
 \end{aligned}$$

where

$$\begin{aligned}
 L_{0A} &= \frac{\rho_0^2}{\rho_1 \rho_2} m_{1z} m_{2z} (k^2 v_{A0}^2 - \omega^2), \\
 L_{0B} &= m_{0z}^2 (k^2 v_{A1}^2 - \omega^2) (k^2 v_{A2}^2 - \omega^2), \\
 L_{0C} &= \rho_0 m_{0z} \left[\frac{m_{1z}}{\rho_1} (k^2 v_{A2}^2 - \omega^2) + \frac{m_{2z}}{\rho_2} (k^2 v_{A1}^2 - \omega^2) \right], \\
 \tau_{0z} &= \tanh(m_{0z} x_0), \tag{3.81}
 \end{aligned}$$

and m_{jz} ($j = 0, 1, 2$) are defined in Equation (3.59). For body waves, using the expressions from Equations (3.62) and (3.81) and $T_{0z} = \tan(n_{0z} x_0)$, the expansion becomes

$$\begin{aligned}
 & 2L_{0A} - 2n_{0z}^2 L_{0B} - n_{0z} L_{0C} \left\{ \frac{1}{T_{0z}} - T_{0z} \right\} + \frac{1}{2} \left\{ \frac{1}{2} \left[\omega^2 \left(\frac{m_{1z}}{\rho_1} + \frac{m_{2z}}{\rho_2} \right) \right. \right. \\
 & \left. \left. - 1 \right] \left[\frac{1}{T_{0z}} - T_{0z} \right] [k^2 v_{A0}^2 - \omega^2] \rho_0 n_{0z} + \frac{1}{2} n_{0z} L_{0C} \left[T_{0z}^2 + \frac{1}{T_{0z}^2} \right] [k^2 v_{A0}^2 - \omega^2] \right. \\
 & \left. + n_{0z}^2 \left[x_0 (k^2 v_{A0}^2 - \omega^2) L_{0C} + 2L_{0B} \right] \right\} \gamma \beta_0 - \frac{1}{2} \gamma L_{0A} \{ k^2 v_{A0}^2 - \omega^2 \} \{ \beta_1 + \beta_2 \} \\
 & - \frac{1}{4} \gamma \rho_0 n_{0z} \left\{ \frac{1}{T_{0z}} - T_{0z} \right\} \{ k^2 v_{A0}^2 - \omega^2 \} \left\{ \beta_1 \frac{m_{1z}}{\rho_1} [k^2 v_{A2}^2 - \omega^2] \right. \\
 & \left. + \beta_2 \frac{m_{2z}}{\rho_2} [k^2 v_{A1}^2 - \omega^2] \right\} = 0. \tag{3.82}
 \end{aligned}$$

If the plasma- β is high in all three regions of the asymmetric slab system, after a similar process, the expansion of the dispersion relation becomes

$$\begin{aligned}
 & \left\{ 2H_{0A} + 2m_{0z}^2 + m_{0z} H_{0B} \left[\tau_{0z} + \frac{1}{\tau_{0z}} \right] \right\} \omega^4 - \frac{2}{\gamma} k^2 \omega^2 \left\{ \left[m_{0z} H_{0B} \left(\tau_{0z} + \frac{1}{\tau_{0z}} \right) \right. \right. \\
 & \left. \left. + 4H_{0A} \right] \frac{c_0^2}{\beta_0} + \rho_0 m_{0z} \left[\frac{c_2^2}{\beta_2} \frac{m_{1z}}{\rho_1} + \frac{c_1^2}{\beta_1} \frac{m_{2z}}{\rho_2} \right] + 2m_{0z}^2 \left[\frac{c_1^2}{\beta_1} + \frac{c_2^2}{\beta_2} \right] \right\} = 0, \tag{3.83}
 \end{aligned}$$

where

$$H_{0A} = \frac{\rho_0 \rho_0}{\rho_1 \rho_2} m_{1z} m_{2z}, \quad H_{0B} = \rho_0 \left(\frac{m_{1z}}{\rho_1} + \frac{m_{2z}}{\rho_2} \right), \quad (3.84)$$

and the m_{jz} ($j = 0, 1, 2$) coefficients are defined in Equation (3.73), while τ_{0z} is defined in Equation (3.81). Using the same factors, along with Equation (3.76), and the notation $T_{0z} = \tan(n_{0z}x_0)$, the dispersion relation for body waves in a high- β configuration can be expressed as

$$\begin{aligned} & \left(2H_{0A} - 2n_{0z}^2 - n_{0z}H_{0B} \left\{ T_{0z} - \frac{1}{T_{0z}} \right\} \right) \omega^4 \\ & + \frac{\omega^2}{\gamma} \left(\left\{ \left[n_{0z}H_{0B} \left(T_{0z}^2 + \frac{1}{T_{0z}^2} + 2 \right) + 2k^2c_0^2 \left(T_{0z} - \frac{1}{T_{0z}} \right) \right] \right. \right. \\ & \quad \left. \left. - 8H_{0A}k^2c_0^2 + 4\omega^2n_{0z}^2 \right\} \frac{1}{\beta_0} + 2k^2\rho_0n_{0z} \left\{ \frac{c_2^2}{\beta_2} \frac{m_{1z}}{\rho_1} + \frac{c_1^2}{\beta_1} \frac{m_{2z}}{\rho_2} \right\} \left\{ T_{0z} - \frac{1}{T_{0z}} \right\} \right. \\ & \quad \left. \left. + 4k^2n_{0z}^2 \left\{ \frac{c_1^2}{\beta_1} + \frac{c_2^2}{\beta_2} \right\} \right) = 0. \end{aligned} \quad (3.85)$$

3.6 The incompressible limit

Due to the highly complex nature of even the decoupled dispersion relation, analytical solutions can only be obtained in certain limiting cases. Perhaps the greatest simplification is brought in through the assumption of incompressible plasma filling the slab and its asymmetric environment. Then, the sound speeds tend to infinity, and $c_{Tj}^2 \rightarrow v_{Aj}^2$, and therefore $m_j \rightarrow k$, for $j = 0, 1, 2$. With these simplifications, the decoupled dispersion relation (Equation 2.39) reduces to:

$$\begin{aligned} & \left[2 \left(\frac{\tanh}{\coth} \right) \{kx_0\} + \frac{2}{R} \right] \omega^4 - k^2 \left[2(v_{A1}^2 + v_{A2}^2) \left(\frac{\tanh}{\coth} \right) \{kx_0\} \right. \\ & \quad \left. + \frac{\rho_0}{\rho_2}(v_{A0}^2 + v_{A1}^2) + \frac{\rho_0}{\rho_1}(v_{A0}^2 + v_{A2}^2) \right] \omega^2 \\ & \quad + k^4 \left[2v_{A1}^2v_{A2}^2 \left(\frac{\tanh}{\coth} \right) \{kx_0\} + \frac{\rho_0}{\rho_2}(v_{A0}^2v_{A1}^2) + \frac{\rho_0}{\rho_1}(v_{A0}^2v_{A2}^2) \right] = 0, \end{aligned} \quad (3.86)$$

which is a quadratic equation in ω^2 . Here, R is the measure of the density asymmetry:

$$R = \left[\frac{\rho_0}{2} \left(\frac{1}{\rho_1} + \frac{1}{\rho_2} \right) \right]^{-1}. \quad (3.87)$$

If $\rho_1 = \rho_2 = \rho_e$, then R reduces to just the ratio of the external to internal densities. The solutions of the Equation (3.86) are:

$$\omega^2 = \frac{-\mathcal{B} \pm \sqrt{\mathcal{B}^2 - 4\mathcal{A}\mathcal{C}}}{2\mathcal{A}}, \quad (3.88)$$

where

$$\mathcal{A} = \left[2 \left(\frac{\tanh}{\coth} \right) \{kx_0\} + \frac{2}{R} \right], \quad (3.89)$$

$$\mathcal{B} = -k^2 \left[2(v_{A1}^2 + v_{A2}^2) \left(\frac{\tanh}{\coth} \right) \{kx_0\} + \frac{\rho_0}{\rho_2} (v_{A0}^2 + v_{A1}^2) + \frac{\rho_0}{\rho_1} (v_{A0}^2 + v_{A2}^2) \right], \quad (3.90)$$

$$\mathcal{C} = k^4 \left[2v_{A1}^2 v_{A2}^2 \left(\frac{\tanh}{\coth} \right) \{kx_0\} + \frac{\rho_0}{\rho_2} v_{A0}^2 v_{A1}^2 + \frac{\rho_0}{\rho_1} v_{A0}^2 v_{A2}^2 \right]. \quad (3.91)$$

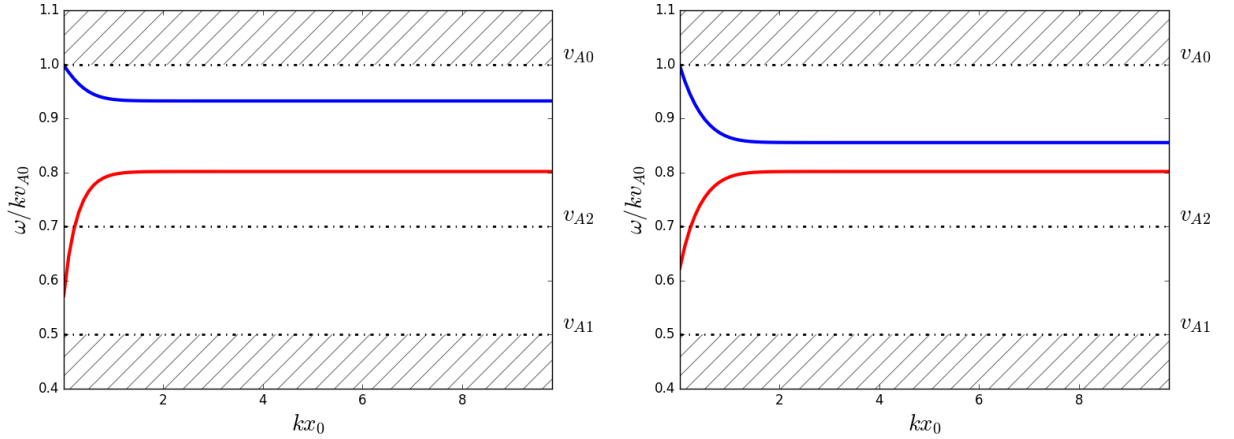


Figure 3.3: Solutions of Equation (3.88) for $R = 0.5$ (left panel) and $R = 1.0$ (right panel), showing the behaviour of magneto-acoustic waves in the limiting case of an incompressible plasma. The blue line indicates the quasi-sausage mode, while the red line shows the quasi-kink mode. Hatching denotes regions in which no modes occur. For the left panel $c_0 \approx 105$, $c_1 = 100$, $c_2 \approx 62$, $v_{A0} = 1.0$, $v_{A1} = 0.5$, $v_{A2} = 0.7$, $\rho_0/\rho_1 = 1.1$, $\rho_0/\rho_2 = 2.9$, while for the right panel $c_0 \approx 105$, $c_1 = 100$, $c_2 \approx 111$, $v_{A0} = 1.0$, $v_{A1} = 0.5$, $v_{A2} = 0.7$, $\rho_0/\rho_1 = 1.1$, $\rho_0/\rho_2 = 0.9$ were used.

If some symmetry is imposed on the system, and the external densities are equal $\rho_1 = \rho_2 = \rho_e$, while the external magnetic fields are still allowed to differ from one another, and introduce the notation

$$\mathcal{T} = \left(\frac{\tanh}{\coth} \right) \{kx_0\}, \quad (3.92)$$

$$\bar{R} = \frac{\rho_0}{\rho_e}, \quad (3.93)$$

then the solutions may be rewritten as:

$$\begin{aligned} \omega^2 = \frac{k^2}{2} \frac{1}{\mathcal{T} + \bar{R}} \left\{ 2 [v_{A1}^2 + v_{A2}^2] \mathcal{T} + \bar{R} [2v_{A0}^2 + v_{A1}^2 + v_{A2}^2] \right. \\ \left. \pm 4 \left[\mathcal{T}^2 (v_{A1}^2 - v_{A2}^2)^2 + 4\bar{R}\mathcal{T} (v_{A1}^2 - v_{A2}^2)^2 \right. \right. \\ \left. \left. + \bar{R}^2 \left(\{2v_{A0}^2 - v_{A1}^2\}^2 + \{2v_{A0}^2 - v_{A2}^2\}^2 - 4v_{A0}^2 \right) \right]^{1/2} \right\}. \quad (3.94) \end{aligned}$$

In the opposite case, if the densities are allowed to differ, but the external Alfvén speeds are equal ($v_{A1}^2 = v_{A2}^2 = v_{Ae}^2$), with the notation

$$\mathcal{D} = \frac{\rho_1 + \rho_2}{\rho_0}, \quad (3.95)$$

$$\mathcal{E} = \frac{\rho_1 \rho_2}{\rho_0^2}, \quad (3.96)$$

the solutions become

$$\begin{aligned} \omega^2 = \frac{k^2}{8} \frac{1}{\mathcal{E}\mathcal{T} + 2\mathcal{E}^2\mathcal{D}\rho_0^2} & \left\{ 4\mathcal{E}v_{Ae}^2\mathcal{T} + \frac{\mathcal{D}}{\rho_0}v_{A0}^2 + 2\mathcal{D}v_{Ae}^2 \right. \\ & \pm \left[\mathcal{D}^2v_{A0}^4 + \mathcal{D}^2v_{Ae}^4 - 2\mathcal{E}v_{Ae}^4 + 8\mathcal{T}\mathcal{D}\mathcal{E}v_{A0}^2v_{Ae}^2 + 8\mathcal{T}\mathcal{D}\mathcal{E}v_{Ae}^4 \right. \\ & \left. \left. + 2\mathcal{D}v_{A0}^2v_{Ae}^2 + 2\frac{\mathcal{E}}{\rho_0}v_{Ae}^4 - 8\mathcal{T}\mathcal{D}\mathcal{E}\rho_0v_{A0}^2v_{Ae}^2 - 32\mathcal{D}\mathcal{E}^3\rho_0^2v_{Ae}^4\mathcal{T} - 8\mathcal{D}^2\mathcal{E}^2v_{A0}^2v_{Ae}^2 \right]^{1/2} \right\}. \end{aligned} \quad (3.97)$$

In the case when the magnetic field strength (thus the Alfvén speed) is zero on both sides of the slab, the solutions simplify further to

$$\omega^2 = \frac{k^2}{8} \frac{1}{\mathcal{E}\mathcal{T} + 2\mathcal{E}^2\mathcal{D}\rho_0^2} \left\{ \frac{\mathcal{D}}{\rho_0}v_{A0}^2 \pm \mathcal{D}v_{A0}^2 \right\}. \quad (3.98)$$

If we allow stronger asymmetry to be present in the incompressible slab system, even the solutions to the full dispersion relation, Equation 2.31, can be expressed in a relatively concise form as

$$\begin{aligned} \omega^2 = \frac{k^2}{2\zeta + 4} & \{ v_{A0}^2\zeta + \theta + 2(v_{A1}^2 + v_{A2}^2) \\ & \pm [v_{A0}^4\zeta^2 + \theta^2 + (4 + 4v_{A0}^2 + 4\theta)(v_{A1}^2 + v_{A2}^2) - (2\zeta\theta + 8\theta)v_{A0}^2]^{1/2} \}, \end{aligned} \quad (3.99)$$

where

$$\zeta = \left(\frac{\rho_0}{\rho_1} + \frac{\rho_0}{\rho_2} \right) \left(\tau_0 + \frac{1}{\tau_0} \right) + \frac{2\rho_0^2}{\rho_1\rho_2}, \quad (3.100)$$

$$\theta = \left(\frac{\rho_0}{\rho_1}v_{A2}^2 + \frac{\rho_0}{\rho_2}v_{A1}^2 \right) \left(\tau_0 + \frac{1}{\tau_0} \right) + \frac{2\rho_0^2}{\rho_1\rho_2}v_{A0}^2, \quad (3.101)$$

$$\tau_0 = \tanh(kx_0). \quad (3.102)$$

In a magnetic slab embedded in an asymmetric non-magnetic environment, it was shown that the phase speeds of a surface modes diverge in the wide-slab limit (Allcock and Erdélyi, 2017). Parametric examinations show that the same is true for the slab embedded in an asymmetric magnetic environment: the incompressible modes tend towards distinct phase speeds as kx_0 increases. This phase speed limit is determined by the measure of density asymmetry, R , and the relative magnitudes of the Alfvén speeds. Figure 3.3 illustrates this effect, displaying the eigenmodes in an incompressible slab system with $R = 0.5$ (left panel) and $R = 1.0$ (right panel). The quasi-sausage (quasi-kink) mode is plotted in blue (red), and no trapped oscillations are found in the hatched regions. For the left panel $c_0 \approx 105$, $c_1 = 100$, $c_2 \approx 62$, $v_{A0} = 1.0$, $v_{A1} = 0.5$, $v_{A2} = 0.7$, $\rho_0/\rho_1 = 1.1$, $\rho_0/\rho_2 = 2.9$, while for the right

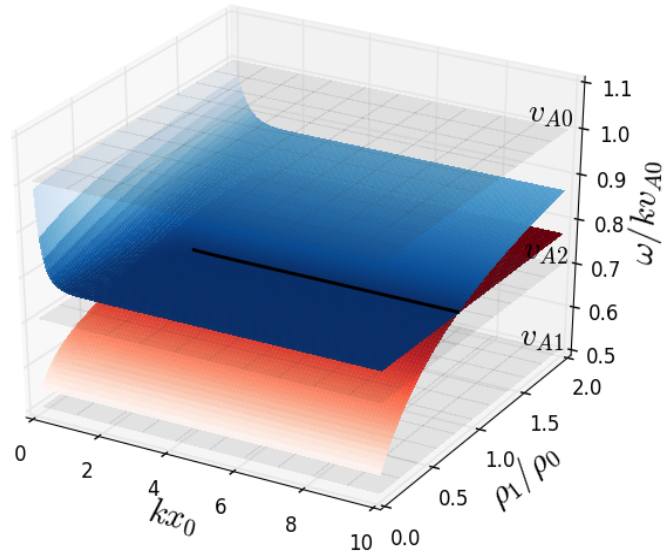


Figure 3.4: Slow surface mode solutions of Equation (3.99) in the incompressible limit, showing the dependence of the common phase speed limit on the density ratio ρ_1/ρ_0 . Blue indicates the quasi-sausage mode, while red applies to the quasi-kink mode. Here, $c_1 = 100.0$, $v_{A0} = 1.0$, $v_{A1} = 0.5$ and $v_{A2} = 0.7$ were used, while c_0 and c_2 were continuously changing in order to sustain total pressure balance between the domains. The black line indicates the values of the density ratio and the dimensionless slab width, for which the phase speeds of the quasi-sausage and quasi-kink modes perform a close approach and avoided crossing.

panel $c_0 \approx 105$, $c_1 = 100$, $c_2 \approx 111$, $v_{A0} = 1.0$, $v_{A1} = 0.5$, $v_{A2} = 0.7$, $\rho_0/\rho_1 = 1.1$, $\rho_0/\rho_2 = 0.9$ were used.

The difference in phase speed behaviour is further examined in Figures 3.4 and 3.5. Figure 3.4 shows the slow surface mode solutions of Equation (3.99) in the incompressible limit, displaying their dependence on both the slab width, kx_0 , and the density ratio, ρ_1/ρ_0 . For this figure, the characteristic speeds were set as $c_1 = 100.0$, $v_{A0} = 1.0$, $v_{A1} = 0.5$ and $v_{A2} = 0.7$, while c_0 and c_2 were continuously changing in order to maintain total pressure balance between all domains. The black line indicates the values of the density ratio and the dimensionless slab width, for which the phase speeds of the quasi-sausage (blue) and quasi-kink (red) modes perform a close approach and avoided crossing. (See this topic further discussed in Section 2.4.1). Figure 3.5 contains two-dimensional projections of Figure 3.4, demonstrating the effects of varying the slab width, kx_0 (panel a), and the density ratio ($R_1 = \rho_0/\rho_1$, panel b) on the phase speeds of incompressible eigenmodes of an asymmetric magnetic slab. Solid (dashed) lines represent quasi-sausage (quasi-kink) modes, and the different shades of blue and red indicate which pair of solutions exists for which value of the equilibrium parameters.

We can observe that when the external densities are identical, the smaller the Alfvén speed difference is, the closer the phase speeds of quasi-sausage and quasi-kink modes approach one another as $kx_0 \rightarrow \infty$. The magnitude of R , in this case, serves to determine what this common value is, with a lower R parameter increasing the gap between the common value and the internal Alfvén speed. Conversely, if the external Alfvén speeds are identical, then the changes in R drive the phase speeds

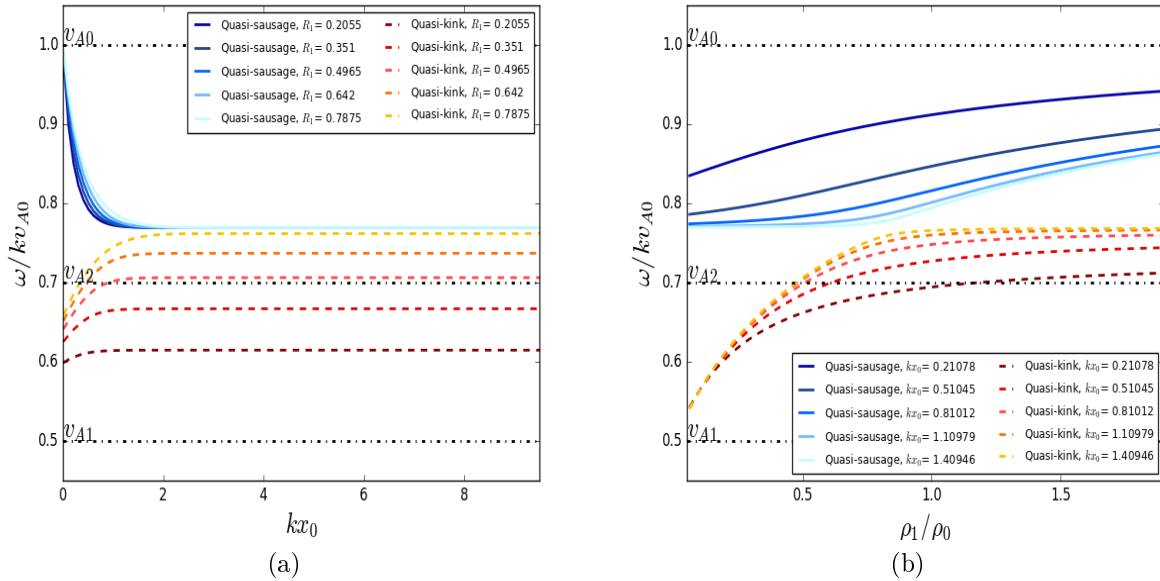


Figure 3.5: Two-dimensional projections of Figure 3.4 illustrating what the effects of varying the values of the equilibrium **(a)** slab width, kx_0 , and **(b)** density ratio ($R_1 = \rho_0/\rho_1$) are on the incompressible eigenmodes of an asymmetric magnetic slab. Solid (dashed) lines represent quasi-sausage (quasi-kink) modes, and colour coding indicates which pair of solutions is valid for which value of the equilibrium parameters.

towards ever closer approaches in the $kx_0 \rightarrow \infty$ limit. Then the two solutions grow further apart from one another again as R keeps changing.

This numerical analysis may serve some practical interest. For instance, kink oscillations in the linear long-wavelength approximation of coronal loop oscillations show nearly incompressible properties (Wang and Solanki (2004), Carter and Erdélyi (2007)). If we imagine the loop and its environment as a thin slab, and apply our findings, Figure 3.5 essentially contrasts wave dispersion in a rarefied medium to propagation in a dense, fat coronal loop. Another potential application of the incompressible limit lies in MBPs, which we will further detail in Section 4.6.

3.7 Conclusion

Wave propagation and dispersion in a magnetic slab embedded in plasma atmospheres of various structures (magnetic or free of field, uniform or asymmetric) is a rich and complex problem that has been studied for decades, and yet still offers new solutions and discoveries. In general, the associated dispersion relation for wave propagation is a transcendental equation, offering the description of a rich spectrum of normal modes.

In this Chapter, we have carried out a detailed analytical investigation of the dispersion relation of magneto-acoustic waves propagating in an asymmetric magnetic slab. With the aim of providing the theoretical background for future applications, in Section 3.2, 3.3 and 3.3.3, analytical expressions descriptive of wave behaviour were derived for slabs much thinner or wider than the characteristic length-scale

set by the wavelength of perturbations. We found that the introduction of external magnetic asymmetry results in important contributions to the dispersion of both surface- and body-mode waves, as well as in the appearance of cut-off frequencies, beyond which the waves become leaky. This results in the appearance of multiple bands of body modes, depending on the characteristic speed ordering.

In Sections 3.4-3.5.3, we explored how the ratio of plasma kinetic and magnetic pressures affects supported modes in the asymmetric slab system. Together with the incompressible limit investigated in Section 3.6, these approximations can serve as the basis of direct applications to solar physics, which we will explore in Chapter 4. In the current Chapter, we only explored purely high- or low- β systems, where all three regions of the configuration are either magnetically or kinetically dominated. The main difference between these two cases is that in a general high- β environment (which can represent photospheric conditions), a variety of both surface- and body mode solutions may be observed. In a low- β model (similar to upper chromospheric or coronal circumstances), only body waves were found to be present.

With these geometric and physical approximations, we have provided a set of mathematical tools which can be combined and applied to a number of asymmetric solar and astrophysical waveguides. Before we proceed with these studies, however, we must note that there are natural boundaries to the applicability of our model and its limiting cases. Beyond the requirements stemming from the initial assumptions we made when setting up our model and deriving our dispersion relation (such as the applicability of the ideal MHD equations), it must be examined on a case-by-case basis, whether a solar structure can be handled as a slab embedded in an asymmetric environment, taking into account the extent of local gradients in plasma and magnetic parameters. Using an asymmetric slab model to describe a solar structure should only be attempted in practice if the difference between the three regions is relatively big compared to the variation of background parameters within the three regions (which are essentially averaged out in this description). In short, the spatial scale of local gradients in the direction of structuring (i.e. the x -direction) should be comparable to the slab width.

Chapter 4

Solar Atmospheric Applications of the Asymmetric Magnetic Slab Model

Abstract

In this Chapter, we utilise the analytical approximations developed in Chapter 3, and apply them to various global and local structures of the solar atmosphere. We provide an overview of wave studies in each feature suggested for the applications of the slab model, and then we proceed to describe the types of solutions we can reasonably expect to observe in these solar atmospheric slabs. This Chapter was based on Section 3 of Zsámberger et al. (2018) and the paper Zsámberger and Erdélyi (2021), both of which contain the own results of the author of this thesis.

4.1 Chapter Introduction

In Chapter 3, we provided approximate solutions to the dispersion relation of the asymmetric magnetic slab system in various limiting cases of slab width and plasma- β values. The scope of applicability widens further if we combine these approaches and consider for example the thin or wide slab limits of various mixed plasma- β systems. In the current Chapter, we apply these approximations and also find numerical solutions for various slab models tailored to be analogues of solar atmospheric structures. We give a brief overview of wave detections in each of the structures suggested for application, and then we elaborate on what types of oscillations might be detected in them if they are considered as asymmetric magnetic slab systems.

The solar applications of our model can be divided into two main categories: the global stratification of the solar atmosphere, and local structures. The first global application we put forward involves the triad of the photosphere, the interface region, and the solar corona (Section 4.2). This model can be refined by focusing on the chromosphere - transition region - corona system, as we do in Section 4.2.1.

In the rest of the Chapter, we move on to local applications. The first one of these is the region of coronal hole boundaries and coronal plumes (Section 4.3). A further coronal application we present is that of prominences and their environment (Section 4.4). Then we shift our focus to the lower solar atmosphere, and proceed to study possible asymmetric waves in light bridges and light walls within sunspots

(Section 4.5). Finally, we investigate magnetic bright points of the solar photosphere first as incompressible, and then as compressible asymmetric waveguides in Section 4.6, before we discuss our main findings and expectations in Section 4.7.

4.2 From the photosphere to the corona with a global view

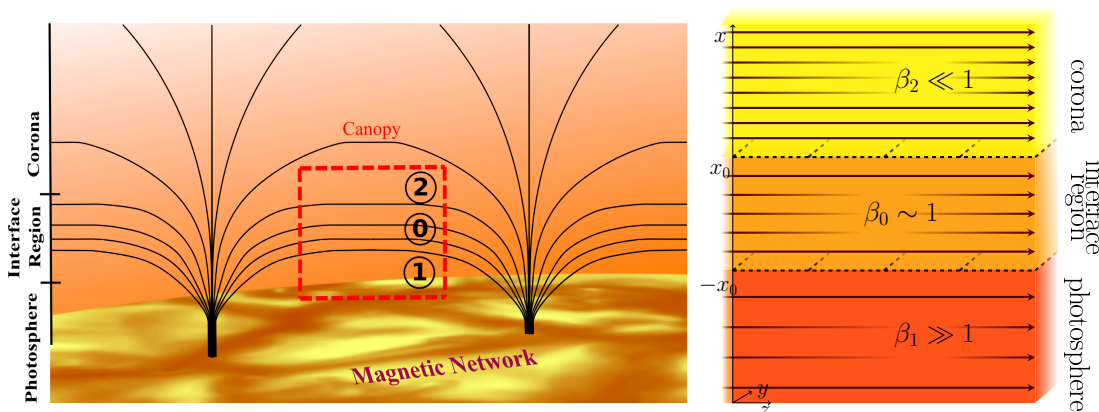


Figure 4.1: The layers of the solar atmosphere modelled as an asymmetric slab configuration. The illustration on the left puts this suggested application in the context of the magnetic fields and network elements of the solar atmosphere, and the dashed red box is used to highlight where exactly the slab is placed in this model. For the sake of clarity, we included the same numbering of the regions that is used in the simplified slab model on the right-hand side: the number and index 1 denotes the photosphere, 0 shows the interface region, while 2 indicates the corona. Compared to the original model, the coordinate system was rotated by 90° , therefore, now, the black arrows on the right illustrate the horizontal magnetic fields, $B_0\hat{z}$, $B_1\hat{z}$ and $B_2\hat{z}$. As before, the dashed black lines denote the boundaries of the slab. The illustration on the left was prepared using Figure 5 of Bushby (2008).

When it comes to the global applications to the solar atmosphere that we suggest, we first have to consider two potentially important limitations in our model, namely, the absence of curvature and of gravitational effects. If the gravitational scale height and the radius of curvature are both much larger than the investigated characteristic length scales, only then can we (as a first approximation) ignore the effects of gravity and the spherical nature of the solar atmosphere, which are both necessary for our Cartesian slab model. With these constraints in place, we can construct a model for a slice of the solar atmosphere from a series of horizontal segments separated by plane-parallel layers. Accordingly, we also rotate the coordinate system of our slab model, to reflect the fact that structuring is now present in the vertical (radial) direction.

The first possibility for a global application of the slab model is the three-region system of the photosphere, the interface region, and the corona. Here, we define the interface region as the magnetic slab, made up of the chromosphere and the narrow transition region. The slab is enclosed in an asymmetric magnetic environment: by the photosphere below and the corona above, as visualised in Figure 4.1. The right-hand-side panel of this Figure provides a simplified sketch of the (rotated) slab model, while the left-hand-side panel places our proposed slab model in the

context of the magnetic fields and network elements of the solar atmosphere. The dashed red box highlights where the slab is placed in this application. For the sake of clarity, we used the same numbering of the three regions in both the left and right panels of the figure: the number and index 1 denotes the photosphere, 0 indicates the interface region, while 2 shows the corona. As mentioned above, compared to our previous depictions of the asymmetric slab model, the coordinate system was rotated by 90° , therefore, now, the black arrows on the right illustrate the horizontal magnetic fields, $B_0\hat{z}$, $B_1\hat{z}$ and $B_2\hat{z}$; while the dashed black lines are the horizontal boundaries between the photosphere and the interface region, and the interface region and the corona, respectively. The panel on the left was originally prepared using Figure 5 of Bushby (2008), and the whole Figure was included in Zsámberger and Erdélyi (2021).

As we mentioned in our Introduction, the thin layer of dense plasma that makes up the photosphere is the lowest layer of the solar atmosphere. Above this layer, the chromosphere is composed of a rarer and optically more transparent plasma. The outermost layer of the solar atmosphere is the corona, which is rarer still and reaches temperatures of millions of degrees. This is about three orders of magnitude higher than the visible surface of our star, as we discussed in Chapter 1, together with the coronal heating problem.

The ubiquitous magnetic fields permeating the solar plasma are both one of the most likely candidates to supply the energy required for maintaining the extremely hot coronal temperatures, and, at the same time, they turn the entire atmosphere into a highly complex, coupled system. The large, concentrated magnetic fields weaving through the layers of the solar atmosphere can serve as excellent waveguides for local and global oscillations (e.g. Erdélyi, 2006a; Wedemeyer-Böhm et al., 2012).

The largest source of wave energy is the sub-photospheric convection, which can also excite MHD waves. Largely incompressible (transversal kink and Alfvén) waves can travel up from these areas and manifest as oscillations in the chromospheric fine structure (Morton et al., 2012). Consequently, several kinds of waves have been observed in chromospheric flux tubes, such as torsional Alfvén, fast sausage and kink modes (Jess et al., 2009). Observations of spicules led to identifying MHD waves with sufficient energy to drive the solar wind (De Pontieu et al. (2004); De Pontieu et al. (2005); Zaqrashvili and Erdélyi (2009); McIntosh et al. (2011); Komm et al. (2015)). Since the start of the SOHO and TRACE missions, a rich selection of coronal waves and oscillations have been documented and studied, for example global Moreton waves, propagating and standing waves in loops, and compressible waves in plumes and coronal loops alike (see e.g. Nakariakov and Verwichte (2005); Banerjee et al. (2007); De Pontieu et al. (2007b); Erdélyi and Fedun (2007); Jess et al. (2009); Taroyan and Erdélyi (2009); McIntosh et al. (2011); Morton et al. (2012); Morton et al. (2013)).

This specific application to the main layers of the solar atmosphere can be viewed as a simple, broad-strokes representation of stratification present due to gravity. With how rich these atmospheric layers are in wave phenomena, and how prominent the differences between their thermodynamic and magnetic parameters can be, we can reasonably expect to see detections of asymmetrically distributed wave power in their waveguides, providing the motivation for proceeding with the application of our asymmetric slab model. Before we discuss the wave modes we might expect to see, let us briefly return to the constraints of the model.

As we have stated, for a waveguide system constructed out of plane-parallel layers to be applicable, the curvature over the segment of the solar atmosphere we include in the model should be small. A simple estimation of the limits posed by this requirement can be made if we suppose that e.g. 1-10° of curvature is allowed and negligible. Then, considering the solar radius, the length of the slab in the z -direction can be up to $\Delta z \approx [700 - 7000]$ Mm. The cross-section of the slab (that is, the slab width in the x -direction), Δx will be the height range encompassed by the chromosphere (some 2000 km) and the transition region (a few hundred kilometres (Priest (2014), p. 31), so in total we can have a slab with width approximately in the range of $\Delta x = [2.1 - 2.5]$ Mm. For the slab to be reasonably considered infinite in the z -direction (or at least very large compared to the wavelength of the observable waves), like we have done when setting up our model, we require that the typical wavelength of oscillations we want to observe should not be larger than a tenth of the horizontal extent (Δz) of the solar atmospheric segment considered. This means that $\lambda_{max} = [70 - 700]$ Mm. The corresponding minimum wavenumbers should then be in the range $k_{min} \in [(2\pi)/700, (2\pi)/70]$ 1/Mm. With these acceptable range of values, the dimensionless slab width is at least $k_{min}x_0 = k_{min}(0.5\Delta x) \in [0.0094, 0.1122]$. This entire range of kx_0 values is much smaller than one, therefore, in this approximation, the photosphere-interface region-corona system corresponds to a very thin asymmetric magnetic slab. Analytical and numerical results obtained for wide slabs could be realistic only if we restrict our investigation to even smaller acceptable curvatures, that is, a segment of the solar atmosphere one or a few orders of magnitude smaller than we have allowed in this estimation so far.

We also have to consider the typical plasma- β values of the layers of the solar atmosphere in question, before we move on to analytical and numerical solutions. The photosphere is generally characterised by high plasma- β values, while the corona is a low- β environment. In-between them, the slab (the interface region) can be assigned a value of $\beta \leq 1$. This last assumption requires us to examine the case when the plasma- β is close to unity in the slab.

For simplicity, in this step, one can choose to transform the dispersion relation to only contain either Alfvén or sound speeds. Here, the choice was made to express the sound speeds of each domain in terms of the corresponding Alfvén speed and plasma- β parameter. Then, these expressions for the sound speeds are substituted into the decoupled dispersion relation. For a configuration with $\beta = 1$ all throughout, the equations take a simpler form and the full dispersion relation (Equation 2.31) reduces to

$$2 \frac{\rho_0 v_{A0} m_1^* \rho_0 v_{A0} m_2^*}{\rho_1 v_{A1} m_0^* \rho_2 v_{A2} m_0^*} + 2 + \left[\frac{\rho_0 v_{A0} m_1^*}{\rho_1 v_{A1} m_0^*} + \frac{\rho_0 v_{A0} m_2^*}{\rho_2 v_{A2} m_0^*} \right] \left[\tau_0 + \frac{1}{\tau_0} \right] = 0 \quad (4.1)$$

for surface waves, and

$$2 \frac{\rho_0 v_{A0} m_1^* \rho_0 v_{A0} m_2^*}{\rho_1 v_{A1} n_0^* \rho_2 v_{A2} n_0^*} - 2 - \left[\frac{\rho_0 v_{A0} m_1^*}{\rho_1 v_{A1} n_0^*} + \frac{\rho_0 v_{A0} m_2^*}{\rho_2 v_{A2} n_0^*} \right] \left[T_0 - \frac{1}{T_0} \right] = 0 \quad (4.2)$$

for body modes, where we used the notation

$$\begin{aligned}
 T_0 &= \tan(n_0 x_0), \\
 n_0^{*2} &= \frac{(2\omega^2 - k^2 \gamma v_{A0}^2)}{(k^2 v_{A0}^2 - \omega^2)(k^2 \gamma v_{A0}^2 - \gamma \omega^2 - 2\omega^2)}, \\
 m_j^{*2} &= \frac{(k^2 \gamma v_{Aj}^2 - 2\omega^2)}{(k^2 v_{Aj}^2 - \omega^2)(k^2 \gamma v_{Aj}^2 - \gamma \omega^2 - 2\omega^2)} \quad \text{for } j = 0, 1, 2. \quad (4.3)
 \end{aligned}$$

Using the same notation, the decoupled dispersion relation (Equation 2.39) becomes

$$\frac{\rho_0 v_{A0} m_1^*}{\rho_1 v_{A1} m_0^*} + \frac{\rho_0 v_{A0} m_2^*}{\rho_2 v_{A2} m_0^*} + 2 \left(\frac{\tanh}{\coth} \right) \{m_0 x_0\} = 0 \quad (4.4)$$

for surface modes, and

$$\frac{\rho_0 v_{A0} m_1^*}{\rho_1 v_{A1} m_0^*} + \frac{\rho_0 v_{A0} m_2^*}{\rho_2 v_{A2} m_0^*} - 2 \left(\frac{\tan}{-\cot} \right) \{n_0 x_0\} = 0 \quad (4.5)$$

for body waves.

We can now combine this additional calculation with the results from low- and high- β approximations detailed in Chapter 3. The photosphere – interface region – corona system can be constructed as a mixed- β asymmetric magnetic slab model, in which the wavenumber coefficient for the inside of the slab is

$$n_0^2 = -m_0^2 = \frac{(k^2 \gamma v_{A0}^2 - 2\omega^2)(\omega^2 - k^2 v_{A0}^2)}{v_{A0}^2 (k^2 \gamma v_{A0}^2 - \gamma \omega^2 - 2\omega^2)}. \quad (4.6)$$

Substituting this into the dispersion relation (2.39), and (for clarity and ease of calculations) using the results from the zero- and infinite- β approximations, we obtain the following relation describing the dispersion of surface waves in the atmospheric segment considered:

$$\begin{aligned}
 &- 2 \frac{\sqrt{k^2 \gamma v_{A0}^2 - (\gamma + 2)\omega^2} \sqrt{k^2 v_{A0}^2 - \omega^2} \rho_0 v_{A0}}{\sqrt{k^2 \gamma v_{A0}^2 - 2\omega^2}} \left[-\frac{1}{\rho_1} \frac{\sqrt{k^2 c_1^2 - \omega^2}}{c_1 \omega^2} + \right. \\
 &\quad \left. \frac{1}{\rho_2} \frac{1}{\sqrt{k^2 v_{A2}^2 - \omega^2} v_{A2}} \right] = \left(\frac{\tanh}{\coth} \right) \{m_0 x_0\}, \quad (4.7)
 \end{aligned}$$

Similarly, the dispersion of body modes in this slab system is governed by the equation

$$\begin{aligned}
 &- 2 \frac{\sqrt{k^2 \gamma v_{A0}^2 - (\gamma + 2)\omega^2} \sqrt{k^2 v_{A0}^2 - \omega^2} \rho_0 v_{A0}}{\sqrt{k^2 \gamma v_{A0}^2 - 2\omega^2}} \left[-\frac{1}{\rho_1} \frac{\sqrt{k^2 c_1^2 - \omega^2}}{c_1 \omega^2} + \right. \\
 &\quad \left. \frac{1}{\rho_2} \frac{1}{\sqrt{k^2 v_{A2}^2 - \omega^2} v_{A2}} \right] = \left(\frac{\tan}{-\cot} \right) \{n_0 x_0\}. \quad (4.8)
 \end{aligned}$$

In addition to the simple analytical approximations we provided, Figure 4.2 displays exact numerical solutions to the full dispersion relation, which were found by choosing values for the characteristic speeds descriptive of the plasma and magnetic

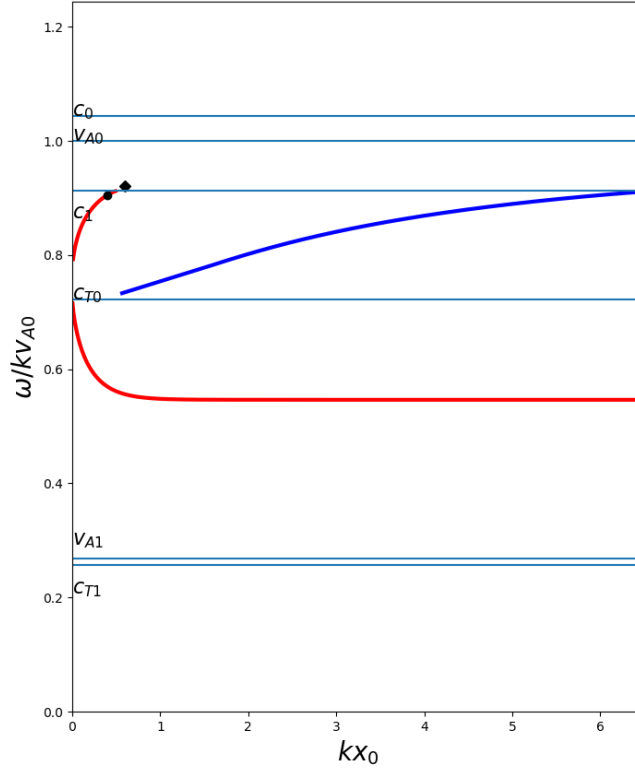


Figure 4.2: The phase speed of magnetoacoustic waves as a function of kx_0 in the photosphere-interface region-corona system. Blue (red) lines denote sausage (kink) modes. The diagram was produced by setting $c_0 = 1.044v_{A0}$, $c_1 = 0.783v_{A0}$, $c_2 = 13.1v_{A0}$, $v_{A1} = 0.267v_{A0}$, $v_{A2} = 130.6v_{A0}$ for the characteristic velocities in the three domains. The density ratios between the three regions were set to be $\rho_1/\rho_0 = 2.1503$ and $\rho_2/\rho_0 = 0.0001$. The black circle (diamond) denotes a trapped (leaky) solution, for which the transverse velocity perturbation throughout the slab system is displayed on the left (right) side of Figure 4.3.

field parameters in the photosphere – interface region – corona system based on the available literature (Hurlburt et al. (2002); Solanki et al. (2006); De Pontieu et al. (2007a); Sobotka et al. (2013); Nisticò et al. (2017)), and determining the density ratios so that total pressure balance is maintained. The photospheric parameters we chose were $v_{A1} = 2.05$ km/s, $c_1 = 6$ km/s, the interface region was characterised by a low average value of $v_{A0} = 7.66$ km/s and $c_0 = 8$ km/s, while the corona was described by $v_{A2} = 1000$ km/s and $c_2 = 100$ km/s. This fixed the density ratios as $\rho_1/\rho_0 = 2.1503$ and $\rho_2/\rho_0 = 0.0001$. Figure 4.2 displays these speeds as well as the phase speeds normalised by the internal Alfvén speed, leading to $c_0 = 1.044v_{A0}$, $c_1 = 0.783v_{A0}$, $c_2 = 13.1v_{A0}$, $v_{A1} = 0.267v_{A0}$, $v_{A2} = 130.6v_{A0}$. Blue (red) lines denote quasi-sausage (quasi-kink) modes. The black circle (diamond) indicates a trapped (leaky) solution, for which the transverse velocity perturbation throughout the slab system is displayed on the left (right) side of Figure 4.3.

In the diagram of Figure 4.2, we can identify a slow surface sausage mode, which

exists if $\omega^2 < \min(k^2 v_{A0}^2, (\gamma/2)k^2 v_{A0}^2, (\gamma/(\gamma+2))k^2 v_{A0}^2, k^2 c_1^2, k^2 v_{A2}^2)$. Additionally, slow body waves can be found in this slab, too, propagating with angular frequencies $k^2(\gamma/(\gamma+2))v_{A0}^2 < \omega^2 < \min(k^2 v_{A0}^2, (\gamma/2)k^2 v_{A0}^2, k^2 c_1^2, k^2 v_{A2}^2)$. At frequencies higher than this upper limit, the waves become leaky due to the asymmetry, and we do not show them in our diagram.

This particular case shows that in an asymmetric system, waves can become leaky towards one of the environmental regions, while they could still remain trapped with respect to the other, if the characteristic speeds are ordered appropriately. For example, the solution marked by the black circle in Figure 4.2 is a trapped oscillation with respect to both boundaries. For illustration, we also show the distribution of its transverse velocity perturbation in the left-hand-side of Figure 4.3. However, the solution indicated by the black diamond symbol in Figure 4.2 is already in the regime of leaky oscillations. Its transverse velocity perturbation across the slab is shown in the right-hand-side panel of Figure 4.3. This plot clearly shows that leakage happens only towards “region 1” (of constant density ρ_1), which corresponds to the photosphere in our rotated slab system. This would suggest that energy transport happens downwards from the interface region via one-sided leaky oscillations. Before overinterpreting this result, we should remember that we have modelled the photosphere as a layer of constant density, while a more realistic approach would have been to take the internal stratification of the photospheric plasma into consideration. The entire depth of the photosphere should only be viewed as a region of uniform density that extends to infinity, if all substantial changes in the amplitudes of the displacement and velocity eigenfunctions occur within the narrow slice of it that can actually be considered uniform, that is, over a distance that is shorter than the local gravitational scale-height. This is not the case in our example. In the right-hand-side panel of Figure 4.3, the transverse velocity perturbation amplitude drops off over a distance considerably longer than the width of the slab, which we have estimated earlier as $\Delta x \in [2.1, 2.5]\text{Mm}$. This means that even one slab width would represent a vertical distance longer than the photospheric gravitational scale height. Therefore, in reality, the internal density stratification of the photosphere would alter the velocity and displacement perturbation amplitudes, which would, in turn, lead to the oscillations being once again evanescent far away from the lower interface.

This case serves as a reminder that before we accept all the results derived from the simple first approximation of handling the solar atmospheric layers as an asymmetric Cartesian magnetic slab system, the fulfilment of all modelling conditions, including the transverse spatial distribution of the eigenfunctions, should be examined on a case-by-case basis, taking into account the slab heights and widths, densities and characteristic speeds we have allowed and used.

4.2.1 The transition region

While we still consider global slab-like structures, it is possible to go into finer detail of the overall atmospheric structure and include the transition region as a separate layer, serving as the “magnetic slab” this time. In practice, the transition region is a highly dynamic irregular volume encompassing all the plasma that has transition region temperatures at any given moment, thus consisting of spicular jets, explosive events, or thin layers near the base of coronal loops. The width of the transition region is estimated between a few hundred to a few thousand kilome-

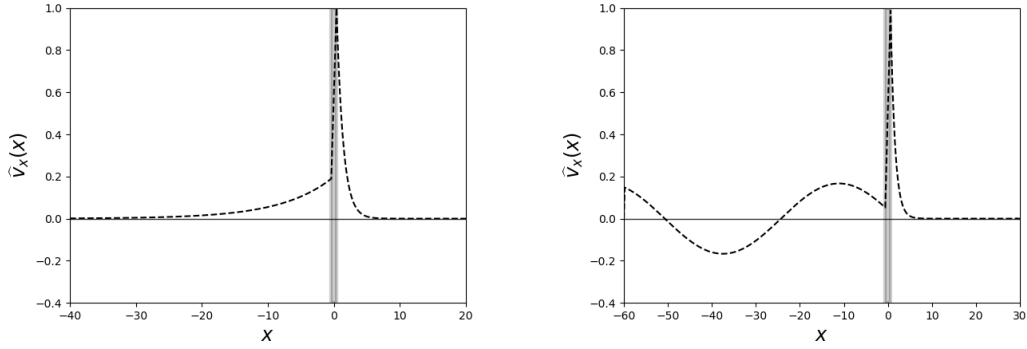


Figure 4.3: The amplitude of the transverse velocity perturbation of a trapped and a leaky solution in the photosphere - interface region - corona system. The wavenumber and phase speed values representing the trapped (leaky) solution are denoted with a black circle (diamond) symbol in Figure 4.2.

tres, and its base may be located at various heights depending on the underlying structures (Mariska, 1986; Priest, 2014). Observations and simulations have found that upward-propagating magneto-acoustic waves can be guided through the transition region plasma and contribute to the energy requirement of coronal heating (Banerjee et al. (2007); Scullion et al. (2010); McIntosh et al. (2011); Priest (2014); Arregui (2015)). Strong, optically thin extreme ultraviolet (EUV) emission generated at higher transition region temperatures might function as an indicator of such up- or downwards-propagating perturbations at the footpoints of coronal loops (De Pontieu and Erdélyi, 2006).

Figure 4.4 illustrates our new slab system. Similarly to Figure 4.1, the left-hand side of Figure fig:pcc provides the location of the slab in the context of the magnetic fields and network elements of the atmosphere, with the dashed red box delineating the volume we consider in our model. The right-hand-side Figure fig:pcc displays a simplified sketch of the asymmetric magnetic slab model used here, which has also been rotated by 90° , like in the photospheric case. The layers numbers and indices in this application have the following interpretation: index 1 identifies the chromosphere, 0, the transition region, and 2 denotes the corona. The illustration on the left was prepared using Figure 5 of Hansteen and Carlsson (2009) and the whole figure has been incorporated from Zsámberger and Erdélyi (2021).

As we consider slightly different layers of the atmosphere than in the previous Section, we have to establish the limits of the applicability of our model anew. As before, keeping the curvature negligible means that the horizontal extent of the slab system must be no greater than $\Delta z \in [700, 7000]$ Mm. Now, however, the cross-section of the slab, Δx , corresponds to the width of the transition region itself, making it much smaller than in the previous application: $\Delta x = [0.1 - 0.5]$ Mm. We keep the condition that the length of the slab in the direction of the magnetic field lines should be at least ten times as large as the wavelengths of the waves we would expect to study, which means that $\lambda_{max} = [70 - 700]$ Mm. Accordingly, the minimum wavenumbers required are between $k_{min} \in [(2\pi)/700, (2\pi)/70]$ 1/Mm. Overall, the dimensionless slab width in the case of the transition region application has to be at least $k_{min}x_0 = k_{min}(0.5\Delta x) = \pi/7 \in [0.001, 0.05]$. These minimum values are tiny

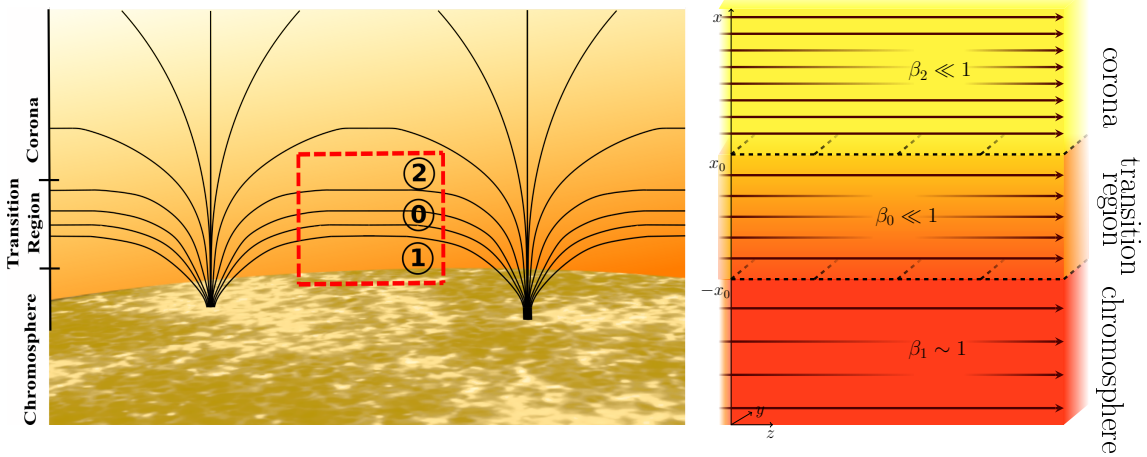


Figure 4.4: The upper layers of the solar atmosphere modelled as an asymmetric slab configuration. Like in Figure 4.1, the image on the left places this suggested application in the context of the magnetic fields and network elements of the atmosphere, and the dashed red box is used to indicate the position of the slab, illustrated in detail on the right. The different layers have the same numbering on both sides: index 1 identifies the chromosphere, 0 stands for the transition region, and 2 denotes the corona. Compared to the original mathematical model, the coordinate system is now rotated by 90° , therefore the black arrows illustrate the horizontal magnetic fields, $B_0 \hat{z}$, $B_1 \hat{z}$ and $B_2 \hat{z}$; the dashed black lines outline the boundaries of the slab. The illustration on the left was prepared using Figure 5 of Hansteen and Carlsson (2009).

even compared to the ones in the photosphere - interface region - corona system. Consequently, the chromosphere - transition region - corona system corresponds to very thin slabs, too. The findings for wide slabs become applicable if the typical wavelengths are a few orders of magnitude smaller than those defined here as λ_{max} .

Our new slab system therefore consist of the magnetic slab of the transition region, which is considered as a low- β region. The slab is bounded on one side by the chromosphere, where the plasma- β is taken to be approximately unity. The second region of the asymmetric environment is the corona, which is filled with low- β magnetised plasma, just like the slab itself. Using our results for low and intermediate plasma- β values from Sections 3.4 and 4.2, the dispersion relation for the transition region slab system becomes

$$\begin{aligned}
 & -\sqrt{k^2 v_{A0}^2 - \omega^2} v_{A0} \rho_0 \left[\frac{\sqrt{k^2 \gamma v_{A1}^2 - 2\omega^2}}{\sqrt{k^2 \gamma v_{A1}^2 - (\gamma + 2)\omega^2} \sqrt{k^2 v_{A1}^2 - \omega^2} v_{A1} \rho_1} \right. \\
 & \quad \left. + \frac{1}{\sqrt{k^2 v_{A2}^2 - \omega^2} v_{A2} \rho_2} \right] = 2 \begin{pmatrix} \tanh \\ \coth \end{pmatrix} \{m_0 x_0\} \quad (4.9)
 \end{aligned}$$

for surface waves, and

$$\begin{aligned}
 & -\sqrt{k^2 v_{A0}^2 - \omega^2} v_{A0} \rho_0 \left[\frac{\sqrt{k^2 \gamma v_{A1}^2 - 2\omega^2}}{\sqrt{k^2 \gamma v_{A1}^2 - (\gamma + 2)\omega^2} \sqrt{k^2 v_{A1}^2 - \omega^2} v_{A1} \rho_1} \right. \\
 & \quad \left. + \frac{1}{\sqrt{k^2 v_{A2}^2 - \omega^2} v_{A2} \rho_2} \right] = 2 \begin{pmatrix} \tan \\ -\cot \end{pmatrix} \{n_0 x_0\} \quad (4.10)
 \end{aligned}$$

for body waves. Here,

$$n_0^2 = -m_0^2 = \frac{(k^2 \beta_0 \gamma v_{A0}^2 - 2\omega^2)(\omega^2 - k^2 v_{A0}^2)}{(k^2 \beta_0 \gamma v_{A0}^4 - \beta_0 \gamma v_{A0}^2 \omega^2 - 2v_{A0}^2 \omega^2)}. \quad (4.11)$$

$$(4.12)$$

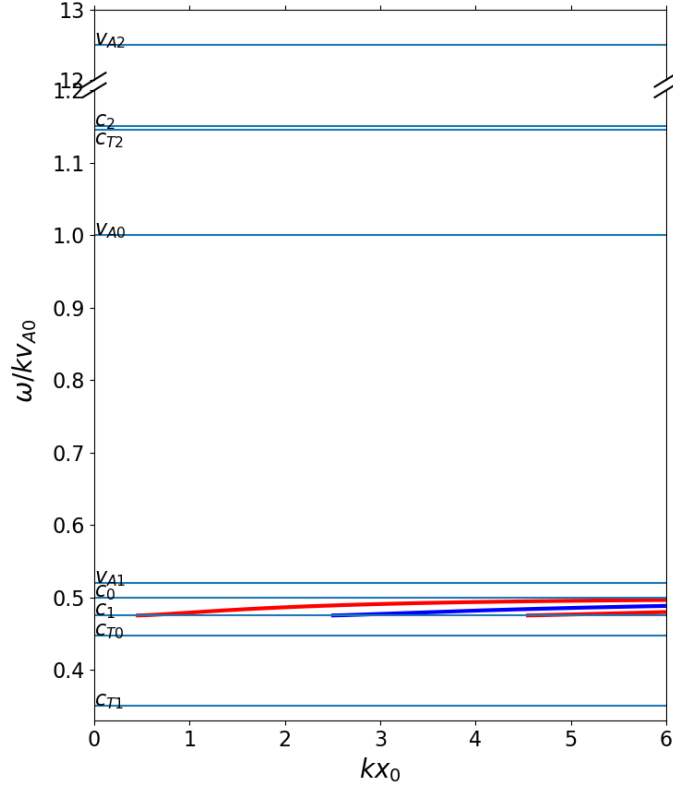


Figure 4.5: The phase speed of magnetoacoustic waves as a function of kx_0 in a the chromosphere - transition region - corona system. The diagram was produced by setting $c_0 = 0.5v_{A0}$, $c_1 = 0.475v_{A0}$, $c_2 = 1.15v_{A0}$, $v_{A1} = 0.52v_{A0}$, $v_{A2} = 12.5v_{A0}$ for the characteristic speeds in the three domains, and density ratios of $\rho_1/\rho_0 = 2.402291$ and $\rho_2/\rho_0 = 0.008236$.

Numerical solutions for the modes supported by the transition region slab system are shown in Figure 4.5. Based on the estimates available in the literature (Hurlburt et al. (2002); Solanki et al. (2006); De Pontieu et al. (2007a); Jiang et al. (2011); Sobotka et al. (2013); Kleint et al. (2014); Nisticò et al. (2017)), we set the characteristic speeds in the chromosphere to $c_1 = 37.2$ km/s and $v_{A1} = 41.6$ km/s, in the transition region to $c_0 = 40$ km/s and $v_{A0} = 80$ km/s, and in the corona to $c_2 = 92$ km/s and $v_{A2} = 1000$ km/s, with $\rho_1/\rho_0 = 2.402291$ and $\rho_2/\rho_0 = 0.008236$ to ensure pressure balance. Again, in the figure itself, the phase speeds and characteristic speeds are normalised by the internal Alfvén speed, so $c_0 = 0.5v_{A0}$, $c_1 = 0.475v_{A0}$, $c_2 = 1.15v_{A0}$, $v_{A1} = 0.52v_{A0}$, $v_{A2} = 12.5v_{A0}$. With such strongly asymmetric characteristic speeds in the three regions, only a thin band of body mode solutions was

found. The phase speed of these modes is slower than the internal (transition region) sound speed, c_0 , but faster than the chromospheric sound speed, c_1 , and it approaches the internal sound speed in the wide-slab limit.

4.3 Coronal hole boundaries

In this Section, we move away from global applications towards more localised features in the solar atmosphere. The first such application of the asymmetric slab model we put forward is that of the environment of coronal plumes. They are one of the most notable structures in the higher atmosphere at times of low solar activity. These cool, dense features appear as bright, predominantly radial rays (hence their alternate name of coronal rays) observable in visible and extreme ultraviolet (EUV) light. Their linear shape follows the magnetic field lines present, and they can remain quiescent for days, making them a suitable candidate for setting up an equilibrium background area for a slab model. Plumes arise from network flux concentrations, and their contrast reduces with distance from the Sun (DeForest and Gurman, 1998; Ofman et al., 2000).

Theory, observations and simulations all show that plumes can serve as effective solar atmospheric waveguides. Slow, compressible magneto-acoustic waves have been observed in polar plumes in the EUV range by SOHO’s EIT (Extreme ultraviolet Imaging Telescope) instrument. They have been captured well in two-dimensional simulations, and described with models of varying complexity. Even with one-dimensional linear models, it was possible to establish the growing amplitude of perturbations while moving away from the solar surface. EUV brightening events similar to polar plumes, as well as perturbations originating from them have also been observed on the solar disk (at the footpoints of long, weak, quasi-open loops) (Berghmans and Clette, 1999; Ofman et al., 1999). Indirect evidence of the presence of fast magneto-acoustic and Alfvén waves in plumes has been found, and (cylindrical) models have been developed for each of these oscillations. More recently, transverse MHD waves with multiple, superimposed oscillations of various periods and amplitudes have been found in plumes, likely originating from the lower solar atmosphere. Observing high-amplitude, compressive waves propagating outwards in these structures is important, as they may provide a contribution to the necessary heating in the coronal hole region (Newkirk and Harvey (1968); DeForest and Gurman (1998); Berghmans and Clette (1999); Ofman et al. (1999); Ofman et al. (2000); Nakariakov (2006); Thurgood et al. (2014)).

The simple geometry and long-lasting nature of plumes makes them ideal features for theoretical MHD studies (Nakariakov, 2006). If we now apply our asymmetric Cartesian model, the slab will be defined as an interplume region, and the asymmetric environment is comprised of a plume on one side of the slab, and a quiet Sun region on the other. Figure 4.6 depicts the environment of coronal plumes as an asymmetric slab system, in the corona (left) and as a sketch (on the right). The two panels follow identical numbering and indexing conventions, with 1 denoting a coronal hole region, 0 the coronal hole boundary / interplume region, and 2 the quiet Sun. The illustration on the left was prepared using Figure 1 of Poletto (2015), and the whole Figure has been adapted from Zsámberger and Erdélyi (2021).

The extent of polar plumes as coherent structures is not very clear (see e.g. in Poletto (2015)), but based on the requirement of a constant density we can estimate

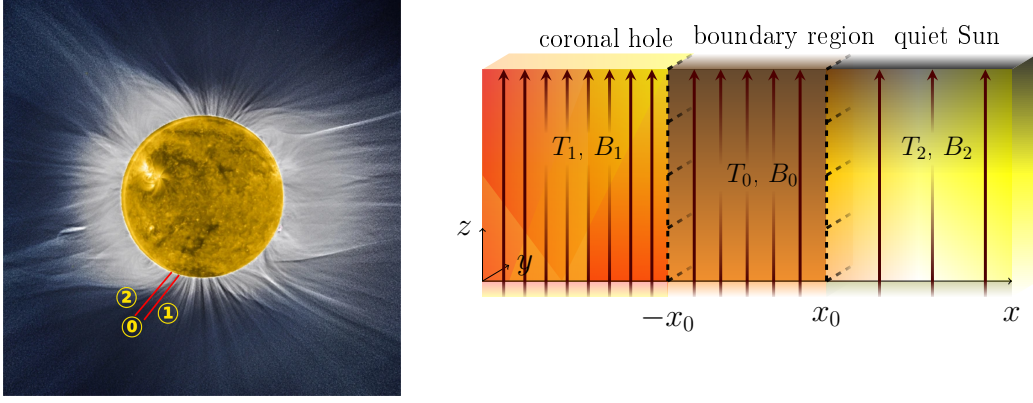


Figure 4.6: Polar plumes modelled as an asymmetric slab configuration. On the left, the red lines show the boundaries of the slab in the context of the solar atmosphere. The numbering of the three regions is identical on the left- and right-hand-side images, with 1 denoting a coronal hole region, 0 the coronal hole boundary region, and 2 the quiet Sun. On the right, as before, the dark red arrows illustrate the vertical magnetic fields, $B_0 \hat{z}$, $B_1 \hat{z}$ and $B_2 \hat{z}$; and the dashed black lines denote the boundaries of the slab. The illustration on the left was prepared using Figure 1 of Poletto (2015).

their height as at least $\Delta z = 70$ Mm. In simulations, the width of plumes at the base of the corona was found to be $\Delta x \in [20 - 28]$ Mm (Raouafi et al., 2007). To allow any waves to be studied to complete at least ten full oscillations along the slab of length $\Delta z = 70$ Mm, we find that the maximum allowable wavelength is $\lambda_{max} = 7$ Mm. The minimum wavenumber calculated from this condition is $k_{min} = (2\pi)/7$ 1/Mm. These estimation lead us to dimensionless slab widths of at least $k_{min}x_0 = k_{min}(0.5\Delta x) = 4\pi/7 \in [5, 7]$, which are all significantly larger than one, and therefore correspond to wide slabs. Results obtained for thin slabs below should then only be accepted if the plume / boundary layer is shown to be much narrower or if it stays a coherent structure much further out in the solar atmosphere in the z -direction, allowing for larger maximal wavelengths to be included.

When it comes to the plasma and magnetic parameters in the model, we take plumes to be regions filled with low- β plasma. Since the plasma- β in the corona is generally low as well, all three regions in our model, including the inter-plume and the quiet sun area, will be characterised by low plasma- β values. Therefore, in the analytically convenient limit of the zero- β approximation, the dispersion relation becomes

$$\begin{aligned} & \sqrt{k^2 v_{A0}^2 - \omega^2} v_{A0} \left[\frac{\rho_0}{\rho_1} \frac{1}{\sqrt{k^2 v_{A1}^2 - \omega^2}} + \frac{\rho_0}{\rho_2} \frac{1}{\sqrt{k^2 v_{A2}^2 - \omega^2}} \right] \\ & = -2 \left(\frac{\tanh}{\coth} \right) \{m_0 x_0\}, \end{aligned} \quad (4.13)$$

for surface waves, and

$$\begin{aligned} & \sqrt{\omega^2 - k^2 v_{A0}^2} v_{A0} \left[\frac{\rho_0}{\rho_1} \frac{1}{\sqrt{k^2 v_{A1}^2 - \omega^2} v_{A1}} + \frac{\rho_0}{\rho_2} \frac{1}{\sqrt{k^2 v_{A2}^2 - \omega^2} v_{A2}} \right] \\ & = 2 \begin{pmatrix} \tan \\ -\cot \end{pmatrix} \{n_0 x_0\}, \end{aligned} \quad (4.14)$$

for body waves. Here,

$$n_0^2 = -m_0^2 = \frac{(k^2 \beta_0 \gamma v_{A0}^2 - 2\omega^2) (\omega^2 - k^2 v_{A0}^2)}{(k^2 \beta_0 \gamma v_{A0}^4 - \beta_0 \gamma v_{A0}^2 \omega^2 - 2v_{A0}^2 \omega^2)}. \quad (4.15)$$

Since we considered a uniformly zero- β system, in the plume-interplume region-quiet Sun configuration, only body modes can exist. This is also confirmed by numerical results shown in Figure 4.7. We chose the characteristic speeds as $c_0 = 152$ km/s, $c_1 = 144$ km/s, $c_2 = 496$ km/s, $v_{A0} = 800.0$ km/s, $v_{A1} = 1280$ km/s, $v_{A2} = 1040$ km/s and density ratios of $\rho_1/\rho_0 = 0.407429$ and $\rho_2/\rho_0 = 0.513077$. Normalised with the internal Alfvén speed, the values depicted are $c_0 = 0.19v_{A0}$, $c_1 = 0.18v_{A0}$, $c_2 = 0.62v_{A0}$, $v_{A1} = 1.6v_{A0}$, $v_{A2} = 1.3v_{A0}$. With these defining parameters, we find a band of slow body modes with phase speeds approaching c_{T0} in a thin slab and c_0 in a wide slab. Fast body modes also exist, and their phase speed tends to v_{A0} if the coronal hole boundary region is wide compared to the wavelength of the perturbations. In thinner slabs, they approach the lower external Alfvén speed, v_{A2} , beyond which they become leaky.

4.4 Prominences

Another localised coronal application of the asymmetric magnetic slab model can be found in prominences. These elongated features can be found both in- and outside active regions on the solar limb (they are called filaments when seen on-disc). They are essentially cooler, denser clouds of plasma in a hotter, rarer coronal environment. They are found in a mainly horizontal magnetic field above polarity-inversion lines, and they hang suspended tens of thousands of kilometres above the photosphere. They show a fine structure out of numerous horizontal threads outlining the magnetic structures in which they reside.

Prominence oscillations are a well-studied problem. Both cylindrical and slab models have been constructed to interpret them, and much like in observational studies, it was found that prominences can support a wide variety of waves with a range of different periods (from about 30 s to 6 h) and amplitudes. Short period oscillations may owe their existence to photospheric or chromospheric oscillations transmitted by upwards-propagating kink or Alfvén waves. Large-amplitude velocity oscillations (> 20 km/s) have been found in transverse and longitudinal directions, which ultimately stem from excitation by flares. Vertically polarised oscillatory motions have been documented in prominences and subsequently been interpreted as transverse waves on the horizontal magnetic field lines (Joarder and Roberts (1992a); Joarder and Roberts (1992b); Joarder and Roberts (1993); Banerjee et al. (2007); Erdélyi and Fedun (2007); Arregui and Ballester (2011); Wang (2011); Arregui et al. (2012)).

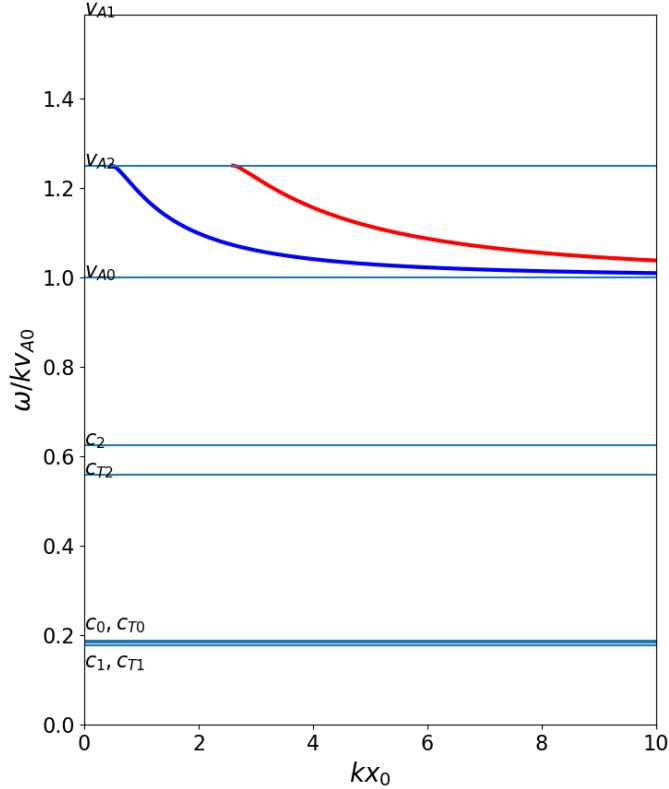


Figure 4.7: The phase speed (ω/k) of magnetoacoustic waves that occur in a low-beta situation. Blue lines show sausage modes, while red lines indicate kink modes. The figure illustrates the case when $c_0 = 0.19v_{A0}$, $c_1 = 0.18v_{A0}$, $c_2 = 0.62v_{A0}$, $v_{A1} = 1.6v_{A0}$, $v_{A2} = 1.3v_{A0}$ are the characteristic speeds in the three domains, and the ratios of the external densities to the internal one are $\rho_1/\rho_0 = 0.407429$ and $\rho_2/\rho_0 = 0.513077$.

Figure 4.8 illustrates how the asymmetric slab model may be applied to prominences in the solar corona. The picture on the left shows the orientation and position of the slab in the solar atmosphere using an SDO 304 Å observation from July 20, 2013. The dashed yellow box indicates the volume we suggest for modelling the prominence system, and the dotted yellow lines delimit the slab (prominence) boundaries. In both the left- and right-hand-side images, the index 1 denotes the coronal region beneath the prominence, 2 the one above the prominence, while 0 corresponds to the prominence itself. On the right, once again, the coordinate system was rotated by 90° , as it was in the photospheric and transition region cases.

The prominence viewed as a magnetic slab will have a length of $\Delta z \in [60, 600]$ Mm along the magnetic field lines, and a width of $\Delta x \in [3 - 10]$ Mm across (see Priest (2014) p. 79). Allowing a sufficient number of full oscillations for the guided waves in the prominence system, we determine the maximum acceptable wavelength as $\lambda_{max} \in [6, 60]$ Mm, and the minimum wavenumber as $k_{min}\pi/3 \in [0.1, 1]$ 1/Mm. These wavenumbers and physical sizes yield dimensionless slab widths of at least $k_{min}x_0 = k_{min}(0.5\Delta x) \in [0.157, 5.236]$, which means that the results might be ap-

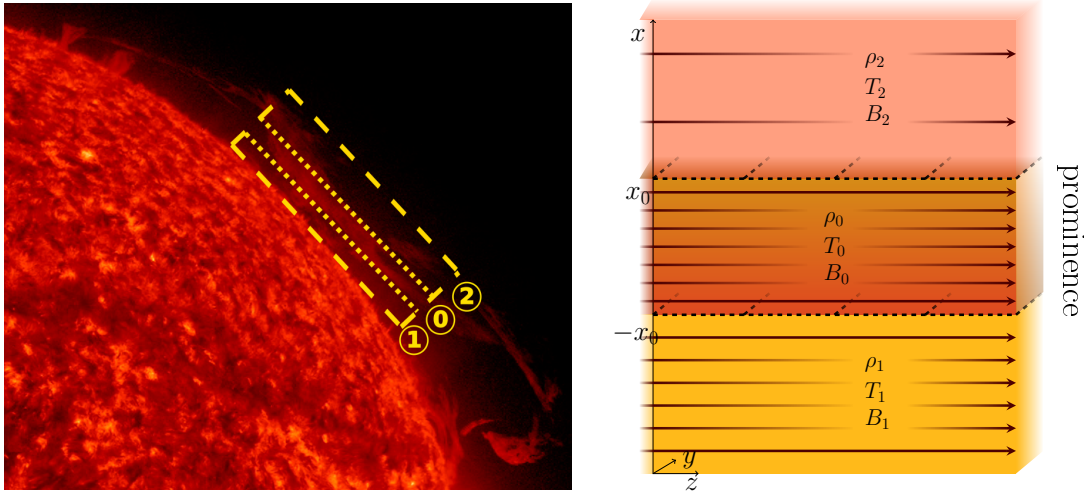


Figure 4.8: Stratification around a solar prominence viewed as an asymmetric slab configuration. The picture on the left shows the orientation and position of the slab in the context of the solar atmosphere using an SDO 304 Å observation from July 20, 2013. The dashed yellow box shows the region of space suggested for modelling, and the dotted yellow lines delimit the slab boundaries. In both the left- and right-hand-side images, the index 1 denotes the coronal region beneath the prominence, 2 the one above the prominence, while 0 stand for the volume of the prominence itself. On the right, once again, the coordinate system was rotated by 90°, therefore now the dark red arrows illustrate the horizontal magnetic fields, $B_0\hat{z}$, $B_1\hat{z}$ and $B_2\hat{z}$; while the dashed black lines still denote the boundaries of the slab.

plicable in both thin and wide slabs depending on the actual dimensions of the prominence within the ranges given by the literature. Based on this, a horizontally very long (large Δz and therefore large allowed λ), but vertically not very tall (small Δx) prominence can be considered as a thin slab. In the opposite case, a horizontally short but vertically tall prominence will qualify as a wide slab.

When applying the asymmetric magnetic slab model to the prominence and its environment, the prominence acts as a slab of relatively cold plasma, which is much denser and is permeated by a stronger magnetic field than either coronal region in its environment. The region below the prominence is filled with a rarefied but warmer plasma woven through by a weaker magnetic field than the prominence itself. Finally, above the prominence, the environment is filled with plasma that is much less dense, but much hotter than the prominence, permeated by a much weaker magnetic field. In this situation, the prominence can be handled as a low- β slab placed in low- β coronal plasma, in which case the dispersion relation takes the same form as in the previous Section (at the discussion of plumes).

Numerical solutions of the dispersion relation for a prominence and its environment modelled as an asymmetric slab system are plotted in Figure 4.9. Here, we consider the prominence slab to be filled with material similar to the chromospheric plasma, and we note that a low plasma- β is necessary for its stability (Hillier and van Ballegoijen, 2013). We chose the following characteristic speeds for our analysis: $c_0 = 8$ km/s, $c_1 = 239.3$ km/s, $c_2 = 195.6$ km/s, $v_{A0} = 87.6$ km/s, $v_{A1} = 957$ km/s, $v_{A2} = 958$ km/s (or, normalised with the internal Alfvén speed, $c_0 = 0.09v_{A0}$, $c_1 = 2.73v_{A0}$, $c_2 = 2.23v_{A0}$, $v_{A1} = 10.92v_{A0}$, $v_{A2} = 10.94v_{A0}$), with density ratios

being $\rho_1/\rho_0 = 0.007872$ and $\rho_2/\rho_0 = 0.008043$. The plasma- β is very low in this slab system, which has the consequence that only body mode solutions are found. Their phase speeds tend to v_{A1} , the lower of the two external Alfvén speeds, in a thin slab, above which speed they become leaky. If the slab is wide, their phase speed approaches the internal Alfvén speed of the prominence slab. In-between these two limiting values, the body waves are located in three bands of trapped oscillations: $v_{A0} < v_{ph} < c_{T2}$, $c_{T2} < v_{ph} < c_2$, and $c_{T1} < v_{ph} < c_1$; while in the phase speed bands of $c_{T2} < v_{ph} < c_2$, and $c_{T1} < v_{ph} < c_1$, they would be leaky modes.

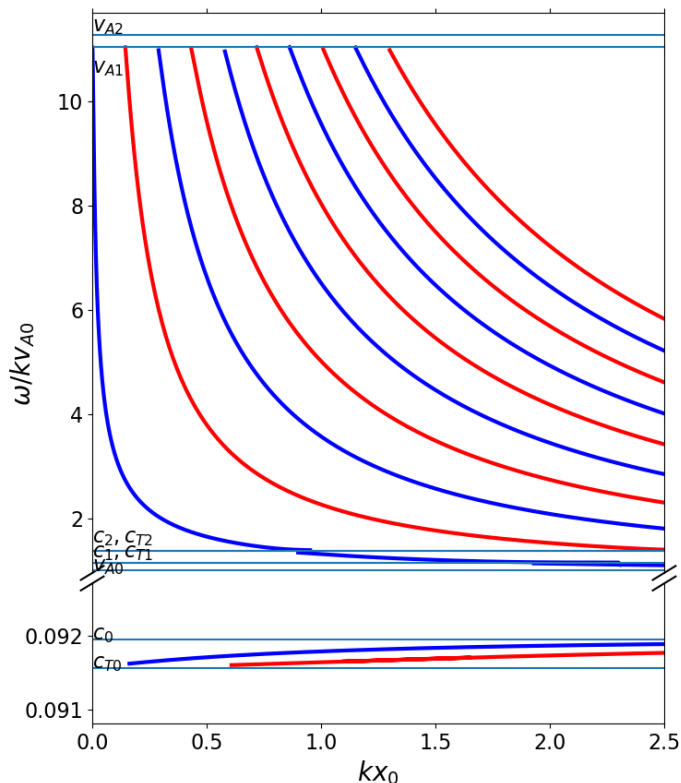


Figure 4.9: Phase speeds of magnetoacoustic waves in a prominence examined as a low-beta slab. In the examined configuration $c_0 = 0.09v_{A0}$, $c_1 = 2.73v_{A0}$, $c_2 = 2.23v_{A0}$, $v_{A1} = 10.92v_{A0}$, $v_{A2} = 10.94v_{A0}$, $\rho_1/\rho_0 = 0.007872$ and $\rho_2/\rho_0 = 0.008043$. The phase speed range between v_{A0} and c_2 contains multiple bans of leaky modes, where solutions are not plotted, and therefore the first fast body mode solution appearing in this figure appears as a line broken into three parts.

4.5 Light bridges

We propose two further applications for the asymmetric magnetic slab system, with both of them being structure occurring in the lower solar atmosphere. The first such application can be found in light bridges inside sunspot umbrae, which are themselves known to be important MHD waveguides.

Sunspots are relatively cool and dark areas on the solar surface, which appear due to a concentration of magnetic flux that is able to suppress convection. They are comprised of two main parts: the warmer and less dim penumbra (6000 K) surrounds the “coldest” central region called the umbra (4500 K). Not only the temperature, but also the ambient magnetic field of these two areas is fundamentally different. In the umbra, the field lines run vertically (radially) for the most part, while in the penumbra, the field lines are highly inclined (Borrero and Ichimoto, 2011).

Both short- and long-period oscillations have been detected in sunspots. The long-period oscillations appear on timescales of tens of minutes to hours or days, and they are particularly difficult to observe, requiring good observing conditions that remain stable for a long while (Khomenko and Collados, 2015). Among the short-period waves, 3- and 5-minute oscillations are of particular significance. 5-minute oscillations are present in the sunspot umbra, with their amplitudes slightly reduced compared to the quiet-Sun photosphere. The chromosphere above the umbra is dominated by 3-minute oscillations, which is either due to reflection or the presence of a chromospheric resonance cavity that traps slow magneto-acoustic waves. Contrary to previous expectations these waves are capable of reaching even the corona. In addition to the umbral oscillations, running penumbral waves propagating upwards along the inclined field lines have also been observed (Priest (2014); Banerjee et al. (2007); Khomenko and Collados (2015)).

Thanks to high-resolution observations, we now know that sunspots have a complex fine structure related to convective motions. This fine structure includes e.g. penumbral filaments, umbral dots, and light bridges. The latter appear as elongated bright areas or bands embedded in the umbra, and often they can fully split the umbra into two separate cores. The magnetic field in light bridges is weaker than in the rest of the umbra, and the field lines are more inclined with respect to the local normal. Interestingly, the magnetic field strength above light bridges increases with height, while the inclination of the field lines decreases. In the chromosphere, the light bridges can show up as brightly as the magnetic plage surrounding a sunspot (Borrero and Ichimoto, 2011; Sobotka et al., 2013).

Light bridges themselves are slowly evolving phenomena, covering a range of various widths throughout their existence. Their cross-section may be anywhere between sub-arcsecond and several arcseconds, with their brightnesses distributed between photospheric intensity and the brightness of umbral dots. Light bridges may show a granular, filamentary, or mixed structure, which is determined by the inclination of the local magnetic field. Additionally, some light bridges show an elongated dark lane in their centre (Sobotka et al., 2013). Light bridges are usually formed in young or in decaying sunspots or pores, where they form a region of partially restored convection between two umbral cores. However, the formation of light bridges does not always lead to a permanent division of the sunspot: especially narrower light bridges may disappear within a few days (Vazquez (1973); Sobotka et al. (2013); Yuan and Walsh (2016)).

In the lower layers of light bridges, atmospheric conditions are qualitatively similar to the interior of quiet-Sun or plage granules. Granular light bridges are characterised by very weak magnetic fields, while narrower light bridges may contain as strong as hecto-Gauss fields (Lagg et al., 2014). Simulations show the presence of upflows in the central parts of light bridges, and downflows at their lateral edges. They can create a favourable environment for magnetic reconnection, which can

then give rise to blobs, brightenings and jets reaching into the chromosphere, or even the transition region above light bridges (Bharti, 2015).

Wave phenomena have been studied not only in sunspots, but specifically in light bridges, too. The 5-minute oscillations were found to be more prominent, while the 3-minute oscillations were suppressed (Yuan et al., 2014). Apart from these, Yuan and Walsh (2016) detected anomalous, sub-minute oscillations and jet activities at a granular light bridge, which was distributed in an asymmetric spatial pattern. Further oscillations were identified in light walls, which are ensembles of oscillating bright features rooted in light bridges, reaching up as high as the chromosphere or the transition region. The height oscillations were first observed by Yang et al. (2015), who also gave light walls their names. The oscillations were connected to a leakage of p -modes from below the photosphere. Light walls were found to be strongly affected by external events such as the impact of material after a flare (Yang et al., 2016). They could also be observed independently of light bridges along the umbral-penumbral boundary of a sunspot (Hou et al., 2016).

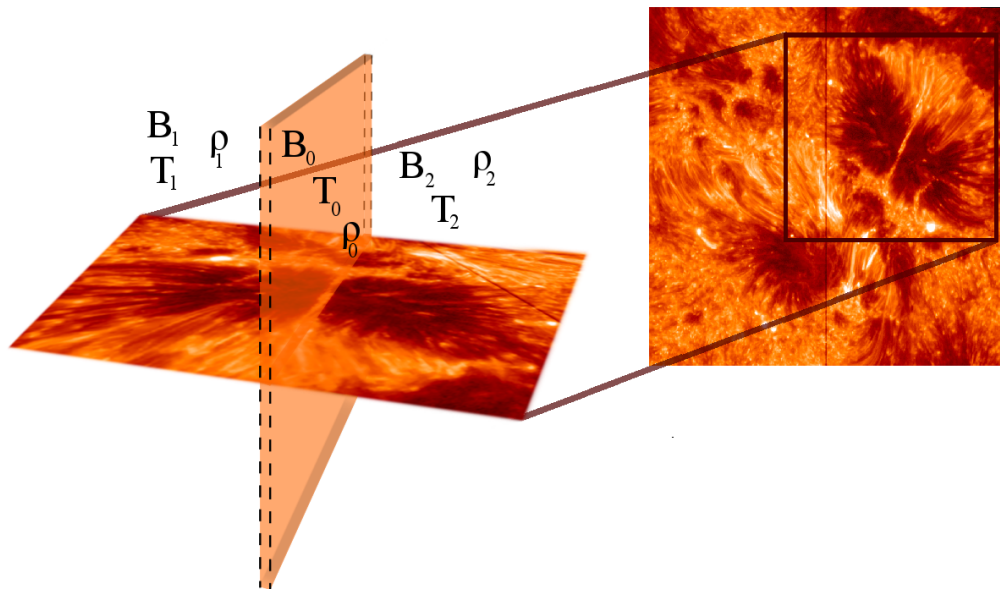


Figure 4.10: A light bridge examined as an asymmetric slab. The bright region of the light bridge between the two umbral blobs (or cores) is the slab itself, while physical parameters (density, temperature, magnetic field strength) on either side of it in the umbrae are slightly different from one another. The original picture (in the top right corner) used for the graphic is a slit-jaw image observed by the Interface Region Imaging Spectrograph (IRIS) in 1400 \AA , on 2014 July 3.

With their location and the asymmetric oscillations detected in them, light bridges readily lend themselves to a new application of the asymmetric slab model. The light bridge is sandwiched between two umbral cores, sometimes separating them completely. Especially in these cases, the plasma and magnetic environment on either side of the bridge may differ from the other side significantly, which is also supported by the observations that the umbral cores separated may have the same, but also the opposite magnetic polarities (Yang et al., 2015). In this first approximation model, we shall neglect the flows that may be present in light bridges, and we focus on waves that have large enough wavenumbers for us to handle the light

bridge as if it was infinitely long in the y - and z -directions. The asymmetric slab model of a light bridge is illustrated in Figure (4.10). The bright region formed by the light bridge between the two umbral blobs (or cores) serves as the slab itself, while physical parameters (density, temperature, magnetic field strength) on either side of the bridge may differ from one another in the two umbral regions. The original picture (in the top right corner) used for the graphic is a slit-jaw image observed by the Interface Region Imaging Spectrograph (IRIS) in 1400 Å, on 2014 July 3, and the source of the edited figure is Zsámberger and Erdélyi (2021).

If we take a typical light bridge with a width of 1", which corresponds to about $\Delta x = 700$ km on the solar surface, we have a possible length in the z -direction of the magnitude $\Delta z = 3500$ -7000 km of length, since light bridges can be 5-10 times as long as they are wide. As in our model, this is the direction of wave propagation, this extent of the light bridge must be much greater than the wavelength of oscillations, so that from the perspective of the waves, the slab acts as though it were infinite in the z -direction. As before, we require that the waves should complete at least 10 periods of oscillation over this distance, which means a maximum wavelength of $\lambda_{max} = 350 - 700$ km and a minimum wavenumber in the range of $k_{min} \in [(2\pi)/700, (2\pi)/350]$ 1/km. With these parameters, the dimensionless slab width is at least $k_{min}x_0 = k_{min}(0.5\Delta x) \in [\pi, 2\pi]$. These values are only slightly greater than one, but, considering that we have carried out this estimation for the maximum wavelengths permitted in a relatively narrow light bridge, kx_0 will likely take mostly larger values than this, so light bridges could be confidently approximated as examples of wide slabs.

In addition to the model geometry, we also have some relevant information about the properties of the plasma and the magnetic field in and around a light bridge. As light bridges are considered more similar to quiet Sun areas than to umbral cores, we adopt quiet Sun values for the characteristic speeds in a light bridge. According to Sobotka et al. (2013), the sound speed in the middle photosphere is 7 km/s in the quiet Sun, and 6 km/s in the umbra. Characteristic speeds are further narrowed down by Liu et al. (2016), who provide estimates of Alfvén speeds as 10-20 km/s in the umbra, and the fact that we expect the plasma- β to be somewhere between 0.02-1 (see Figure 16 in Borrero and Ichimoto, 2011). We found even fewer constraints for the plasma- β inside the light bridge itself (see e.g. Figure 14 of Felipe et al., 2016). Therefore, we decided to provide analytical and numerical results for a few possible combinations of plasma- β values in- and outside the asymmetric slab system of two umbral cores and a light bridge.

As opposed to the photosphere in general, the plasma- β is low in the magnetic flux concentration of the umbra (Borrero and Ichimoto, 2011). Therefore, in all of the alternatives we examine, the two external regions in the slab model form a low- β environment, with differences between pressure, temperature and magnetic field strength values between the two umbral cores, since they are separated by the light bridge. In the light bridge itself, the magnetic field is weaker, and the interior of the slab more closely resembles the quiet Sun photosphere, which is why, in our first model, we assume the internal plasma- β to be high.

Using the dispersion relations derived separately for low- and high- β cases in Chapter 3, we can now construct a dispersion relation for a high- β slab enclosed between two low- β domains (with the plasma- β changing discontinuously across the

two interfaces at $-x_0$ and x_0) as

$$\frac{c_0\omega^2}{\sqrt{k^2c_0^2 - \omega^2}} \left[\frac{\rho_0}{\rho_1} \frac{1}{\sqrt{k^2v_{A1}^2 - \omega^2}} + \frac{\rho_0}{\rho_2} \frac{1}{\sqrt{k^2v_{A2}^2 - \omega^2}} \right] = 2 \begin{pmatrix} \tanh \\ \coth \end{pmatrix} \{m_0x_0\} \quad (4.16)$$

for surface waves. For body waves, this can be re-written as

$$\frac{c_0\omega^2}{\sqrt{k^2c_0^2 - \omega^2}} \left[\frac{\rho_0}{\rho_1} \frac{1}{\sqrt{k^2v_{A1}^2 - \omega^2}} + \frac{\rho_0}{\rho_2} \frac{1}{\sqrt{k^2v_{A2}^2 - \omega^2}} \right] = 2 \begin{pmatrix} \tan \\ -\cot \end{pmatrix} \{n_0x_0\}, \quad (4.17)$$

where

$$n_0^2 = -m_0^2 = \frac{(\omega^2 - k^2c_0^2)(2\beta_0k^2c_0^2 - \gamma\omega^2)}{c_0^2(2\beta_0k^2c_0^2 - (\gamma + 2\beta_0)\omega^2)}.$$

Figure 4.11 provides numerical solutions for four possible cases of characteristic speed and density ordering in light bridges and their environment. Figure 4.11(a) shows the case described above, when the plasma- β is high inside the slab, but low in both external regions. Based on the available literature, the characteristic speeds were chosen to be $v_{A0} = 1.0$ km/s, $v_{A1} = 35$ km/s, $v_{A2} = 14$ km/s, $c_0 = 7$ km/s, $c_1 = 5.5$ km/s, $c_2 = 6.5$ km/s (or, normalised by the internal Alfvén speed, $v_{A1} = 35v_{A0}$, $v_{A2} = 14v_{A0}$, $c_0 = 7v_{A0}$, $c_1 = 5.5v_{A0}$, $c_2 = 6.5v_{A0}$), which required density ratios of $\rho_1/\rho_0 = 0.046122$ and $\rho_2/\rho_0 = 0.242400$. With this ordering, a several types of trapped oscillations might be observed. A phase speed band with infinite harmonics of slow body modes exists between c_{T0} and v_{A0} . A slow quasi-sausage surface mode is present, with phase speed approaching c_{T0} in the thin slab. The phase speed of the corresponding slow surface quasi-kink mode approaches c_{T1} at moderately small dimensionless slab widths. Another pair of surface modes can be present in narrow bands of higher phase speed values. Between c_2 and v_{A2} , a fast quasi-kink mode can be seen, which starts as a body mode in a thin slab and changes its character to that of a surface mode at intermediate values of the slab width. A band of fast body modes propagate phase speeds between $c_0 < v_{ph} < v_{A2}$.

A second possibility is that we still assume the plasma- β to be high inside the light bridge and low on its one side, but we focus on the unique case when $\beta_2 = 1$ in the other umbral core region. The dispersion relation for this system becomes

$$\frac{c_0\omega^2}{\sqrt{k^2c_0^2 - \omega^2}} \left[\frac{\rho_0}{\rho_1} \frac{1}{\sqrt{k^2v_{A1}^2 - \omega^2}} + \frac{\rho_0}{\rho_2} \frac{\sqrt{k^2\gamma v_{A2}^2 - 2\omega^2}}{\sqrt{k^2\gamma v_{A2}^2 - (\gamma + 2)\omega^2} \sqrt{k^2v_{A2}^2 - \omega^2}} \right] = 2 \begin{pmatrix} \tanh \\ \coth \end{pmatrix} \{m_0x_0\} \quad (4.18)$$

for surface waves, and

$$\frac{c_0\omega^2}{\sqrt{k^2c_0^2 - \omega^2}} \left[\frac{\rho_0}{\rho_1} \frac{1}{\sqrt{k^2v_{A1}^2 - \omega^2}} + \frac{\rho_0}{\rho_2} \frac{\sqrt{k^2\gamma v_{A2}^2 - 2\omega^2}}{\sqrt{k^2\gamma v_{A2}^2 - (\gamma + 2)\omega^2} \sqrt{k^2v_{A2}^2 - \omega^2}} \right] = 2 \begin{pmatrix} \tan \\ -\cot \end{pmatrix} \{n_0x_0\}, \quad (4.19)$$

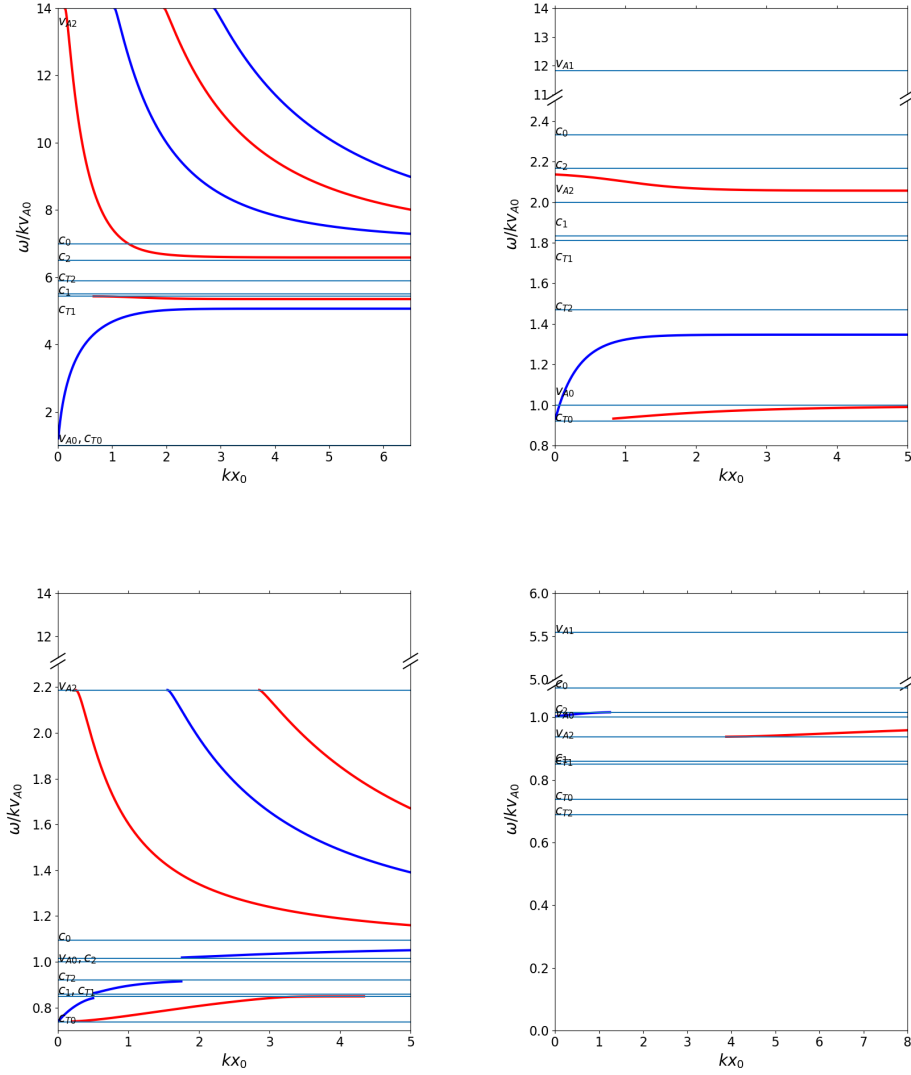


Figure 4.11: The phase speed (ω/k) of magnetoacoustic waves that may be supported by light bridges under various possible characteristic speed orderings suggested by observations. **(a)** $v_{A1} = 35v_{A0}$, $v_{A2} = 14v_{A0}$, $c_0 = 7v_{A0}$, $c_1 = 5.5v_{A0}$, $c_2 = 6.5v_{A0}$, $\rho_1/\rho_0 = 0.046122$ and $\rho_2/\rho_0 = 0.242400$. **(b)** $v_{A1} = 11.83v_{A0}$, $v_{A2} = 2v_{A0}$, $c_0 = 2.33v_{A0}$, $c_1 = 1.83v_{A0}$, $c_2 = 2.17v_{A0}$, $\rho_1/\rho_0 = 0.076943$ and $\rho_2/\rho_0 = 1.150634$. **(c)** $v_{A1} = 5.55v_{A0}$, $v_{A2} = 2.19v_{A0}$, $c_0 = 1.093v_{A0}$, $c_1 = 0.86v_{A0}$, $c_2 = 1.02v_{A0}$, $\rho_1/\rho_0 = 0.076943$ and $\rho_2/\rho_0 = 0.404378$. **(d)** $v_{A1} = 5.55v_{A0}$, $v_{A2} = 0.94v_{A0}$, $c_0 = 1.09v_{A0}$, $c_1 = 0.86v_{A0}$, $c_2 = 1.02v_{A0}$, $\rho_1/\rho_0 = 0.076943$ and $\rho_2/\rho_0 = 1.150634$.

for body waves, where

$$n_0^2 = -m_0^2 = \frac{(\omega^2 - k^2 c_0^2)}{c_0^2}.$$

Figure 4.11(b) was obtained for this special case when the plasma- β is still high inside the light bridge, low on one side, and one on the other side, with the following characteristic speeds: $v_{A0} = 3$ km/s, $v_{A1} = 35.5$ km/s, $v_{A2} = 6$ km/s, $c_0 = 7$ km/s,

$c_1 = 5.5$ km/s, $c_2 = 6.5$ km/s (or, normalised with the internal Alfvén speed for the plot, $v_{A1} = 11.83v_{A0}$, $v_{A2} = 2v_{A0}$, $c_0 = 2.33v_{A0}$, $c_1 = 1.83v_{A0}$, $c_2 = 2.17v_{A0}$). The density ratios required to maintain total pressure balance are $\rho_1/\rho_0 = 0.076943$ and $\rho_2/\rho_0 = 1.150634$. The slow body modes are still present, as before, but the fast body modes are missing, and we only have an additional pair of surface mode solutions as trapped oscillations in the rest of the phase speed domain.

Next, we study the case when the umbral cores still form an asymmetric low- β environment, but the while the plasma- β inside the slab is fixed at unity. The dispersion relation for surface waves in this configuration is

$$-\frac{\sqrt{k^2\gamma v_{A0}^2 - (\gamma + 2)\omega^2}\sqrt{k^2v_{A0}^2 - \omega^2}\rho_0v_{A0}}{\sqrt{k^2\gamma v_{A0}^2 - 2\omega^2}} \left[\frac{1}{\rho_1} \frac{1}{\sqrt{k^2v_{A1}^2 - \omega^2}v_{A1}} + \frac{1}{\rho_2} \frac{1}{\sqrt{k^2v_{A2}^2 - \omega^2}v_{A2}} \right] = 2 \left(\frac{\tanh}{\coth} \right) \{m_0x_0\}. \quad (4.20)$$

For body waves, the dispersion relation becomes

$$-\frac{\sqrt{k^2\gamma v_{A0}^2 - (\gamma + 2)\omega^2}\sqrt{k^2v_{A0}^2 - \omega^2}\rho_0v_{A0}}{\sqrt{k^2\gamma v_{A0}^2 - 2\omega^2}} \left[\frac{1}{\rho_1} \frac{1}{\sqrt{k^2v_{A1}^2 - \omega^2}v_{A1}} + \frac{1}{\rho_2} \frac{1}{\sqrt{k^2v_{A2}^2 - \omega^2}v_{A2}} \right] = 2 \left(\frac{\tan}{-\cot} \right) \{n_0x_0\}, \quad (4.21)$$

where

$$n_0^2 = -m_0^2 = \frac{(2 + \gamma)(k^2\gamma v_{A0}^2 - 2\omega^2)(\omega^2 - k^2v_{A0}^2)}{2(1 + \gamma)v_{A0}^2(k^2\gamma v_{A0}^2 - \gamma\omega^2 - 2\omega^2)}.$$

Figure 4.11(c) displays possible solutions when the plasma- β in the light bridge is one, and the surrounding umbral cores are both low- β regions. For this case, the characteristic speeds were chosen as $v_{A0} = 6.4$ km/s, $v_{A1} = 35.5$ km/s, $v_{A2} = 14$ km/s, $c_0 = 7$ km/s, $c_1 = 5.5$ km/s, $c_2 = 6.5$ km/s (or $v_{A1} = 5.55v_{A0}$, $v_{A2} = 2.19v_{A0}$, $c_0 = 1.093v_{A0}$, $c_1 = 0.86v_{A0}$, $c_2 = 1.02v_{A0}$ after normalisation), leading to density ratios of $\rho_1/\rho_0 = 0.076943$ and $\rho_2/\rho_0 = 0.404378$. This slab system possesses a band of slow body mode solutions with phase speeds between c_{T0} and v_{A0} , surface modes between c_2 and c_0 , and fast body modes propagating faster than the internal sound speed but slower than the lowest external Alfvén speed, v_{A2} .

Finally, we turn our attention to the possibility that the plasma- β is low in the first umbral core, but it might be one in the other environmental region, as well as inside the slab, while this second umbral core and the bridge itself are still characterised by different sound and Alfvén speeds. In this case, the surface wave dispersion relation simplifies to

$$-\frac{\sqrt{k^2\gamma v_{A0}^2 - (\gamma + 2)\omega^2}\sqrt{k^2v_{A0}^2 - \omega^2}\rho_0v_{A0}}{\sqrt{k^2\gamma v_{A0}^2 - 2\omega^2}} \left[\frac{1}{\rho_1} \frac{1}{\sqrt{k^2v_{A1}^2 - \omega^2}v_{A1}} + \frac{\rho_0}{\rho_2} \frac{\sqrt{k^2\gamma v_{A2}^2 - 2\omega^2}}{\sqrt{k^2\gamma v_{A2}^2 - (\gamma + 2)\omega^2}\sqrt{k^2v_{A2}^2 - \omega^2}v_{A2}} \right] = 2 \left(\frac{\tanh}{\coth} \right) \{m_0x_0\}. \quad (4.22)$$

For body waves, the dispersion relation is

$$\begin{aligned}
& - \frac{\sqrt{k^2\gamma v_{A0}^2 - (\gamma + 2)\omega^2} \sqrt{k^2 v_{A0}^2 - \omega^2} \rho_0 v_{A0}}{\sqrt{k^2\gamma v_{A0}^2 - 2\omega^2}} \left[\frac{1}{\rho_1} \frac{1}{\sqrt{k^2 v_{A1}^2 - \omega^2} v_{A1}} \right. \\
& \left. + \frac{\rho_0}{\rho_2} \frac{\sqrt{k^2\gamma v_{A2}^2 - 2\omega^2}}{\sqrt{k^2\gamma v_{A2}^2 - (\gamma + 2)\omega^2} \sqrt{k^2 v_{A2}^2 - \omega^2} v_{A2}} \right] = 2 \begin{pmatrix} \tan \\ -\cot \end{pmatrix} \{n_0 x_0\}, \quad (4.23)
\end{aligned}$$

where

$$n_0^2 = -m_0^2 = \frac{(2 + \gamma)(k^2\gamma v_{A0}^2 - 2\omega^2)(\omega^2 - k^2 v_{A0}^2)}{2(1 + \gamma)v_{A0}^2(k^2\gamma v_{A0}^2 - \gamma\omega^2 - 2\omega^2)}.$$

Figure 4.11(d) shows the solutions in this last case, where only one band of body modes was found (with phase speeds $v_{A2} < v_{ph} < v_{A0}$ for trapped oscillations), as well as a surface mode that tends to v_{A0} in the thin slab but already becomes leaky at speeds above c_2 . These solutions were obtained by choosing $v_{A0} = 6.4$ km/s, $v_{A1} = 35.5$ km/s, $v_{A2} = 6$ km/s, $c_0 = 7$ km/s, $c_1 = 5.5$ km/s, $c_2 = 6.5$ km/s ($v_{A1} = 5.55v_{A0}$, $v_{A2} = 0.94v_{A0}$, $c_0 = 1.09v_{A0}$, $c_1 = 0.86v_{A0}$, $c_2 = 1.02v_{A0}$ after normalisation) and density ratios of $\rho_1/\rho_0 = 0.076943$ and $\rho_2/\rho_0 = 1.150634$.

4.6 Magnetic bright points

The last feature of the lower solar atmosphere that we suggest for the applications of the asymmetric magnetic slab model is that of magnetic bright points (MBPs) of the solar photosphere. MBPs are small concentrations of intense magnetic field with strength of the order of kilogauss. They are located in the dark intergranular lanes formed from convective downflow and appear as brighter regions because of two reasons. Firstly, their lower plasma pressure allows observers to glance deeper into the photosphere, and secondly, their interior is further heated by their environment (Roupe van der Voort et al. (2005); Crockett et al. (2010); Keys et al. (2013)).

MBPs are often treated as cylindrical flux tubes, although in reality, their appearance can vary greatly. They often possess strongly elongated or irregular shapes, especially near pores (Berger et al., 1995; Bovelet and Wiehr, 2003). This opens up the possibility to treat an MBP locally as a magnetic slab. Furthermore, as they are wedged in-between two neighbouring granular cells, conditions on either side of an MBP may be different from one another, which makes them excellent candidates for applying the asymmetric slab model. Figure 4.12 illustrates such a configuration. The bright region at the centre is the slab itself, while physical parameters (density, temperature, magnetic field strength) on either side of it in the intergranular lane are assumed to be slightly different from one another. The original sketch is based on Figure 11 of (Liu et al., 2018), showing TiO 7058 Å observations taken by the New Vacuum Solar Telescope, and the source of the completed figure is Zsámberger and Erdélyi (2021).

Shapes and size distributions of MBPs have been the subject of extensive studies. Measuring with the Swedish Vacuum Solar Telescope on La Palma, Berger et al. (1995) found a lognormal size distribution of MBPs with a modal value of 220 km (0."30) and an average of 250 km (0."35). Using the Dutch Open Telescope, a similar result (dominant diameter of 220 ± 25 km) was obtained by Bovelet and Wiehr

(2003), who also noted that only in about two thirds of cases do isolated MBPs have circular shapes, with the remaining bright points being elongated or irregular. Later observations with the 1m Swedish Solar Telescope (SST) established lower dominant diameter values of $160 \pm 20\text{km}$ (Wiehr et al. (2004); Crockett et al. (2010)). Sánchez Almeida et al. (2004) applied two-Gaussian fits to MBPs on images taken by the SST and found major axis lengths of up to 350km, while minor axes peaked around 135km (reaching the spatial resolution of the observations) and mostly stayed below 200km. Solanki et al. (2010) stated that the sizes of MBPs may be close to the $0.''15$ spatial resolution limit of the balloon-borne SUNRISE observatory ($\approx 60\text{-}100\text{km}$). The lower limit on the size of MBPs seems to lie at a 100-km diameter, where radiative pressure stops the convective collapse of the tube (Venkatakrisnan, 1986), or, if interaction with acoustic waves keeps splitting up the larger flux tubes, somewhere between 40-60km, according to Ryutova (1996).

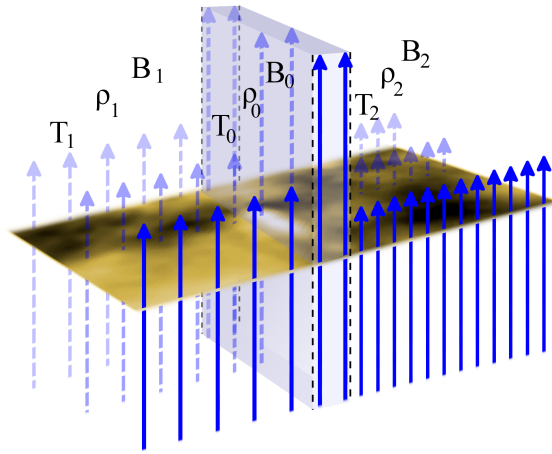


Figure 4.12: An elongated MBP can be considered as an asymmetric magnetic slab. The bright region at the centre itself is the slab, while physical parameters (density, temperature, magnetic field strength) on either side of it in the intergranular lane are slightly different from one another. The illustration was prepared using Figure 11 of (Liu et al., 2018), showing TiO 7058 Å observations taken by the New Vacuum Solar Telescope.

Treating an MBP as a magnetic slab requires that its finite major axis should be much longer than the wavelengths of supported modes. If we take a large elongated MBP with 1000km length (major axis) and require that the waves should be able to complete at least 10 periods of oscillation in the slab, then the maximum allowable wavelength is $\lambda = 100\text{km}$, with the minimum required wavenumber being $k = 2\pi \cdot 10^{-1}\text{km}^{-1}$. The characteristic speeds in the photosphere are $c_s \approx 10\text{kms}^{-1}$ for the sound speed, and $v_A \approx 8.25\text{kms}^{-1}$ for the Alfvén speed (Kohl and Crammer, 2013; Mullan, 2009). As these values determine the phase speed trapped waves guided by the MBP system, and we have just given an estimate of the wavenumber, it follows that the frequency of waves we might examine in this asymmetric slab system is around $\omega = 2\pi \cdot [0.0825, 0.1]\text{Hz}$. These are quite high-frequency oscillations. A non-magnetic analogue to the observational problems they raise can be found in high-frequency acoustic waves, which could play an important part in chromospheric heating.

High-frequency acoustic waves are readily excited by convective motions, how-

ever, they are difficult to observe due to the smearing effect of seeing (in ground-based observations) and the weakening of the signal by the width of the response function (in both space- and ground-based observations), see e.g. Fossum and Carlsson (2004; 2005). There is no consensus on the wave power found in these high-frequency oscillations. Based on the analysis of TRACE and later Hinode data, Fossum and Carlsson (2004; 2005), as well as Carlsson et al. (2007) deduced that most of the energy flux should be carried into the chromosphere by waves of frequency 5-40 mHz. These, however, seem to be unable to balance out radiative losses. The results have been subject to criticism due to 2D and 3D hydrodynamic simulations generating a greater acoustic energy flux than expected by Fossum and Carlsson (2005). Furthermore, a direct comparison of theoretical models with TRACE observations can only be done cautiously. On length scales shorter than the limited spatial resolution of the instrument, small pockets of hotter material can be embedded in a relatively cold environment (Cuntz et al., 2007; Wedemeyer-Böhm et al., 2007).

Detecting and identifying waves in MBPs might pose similar problems of requiring extremely high spatial and temporal resolution. Such precise measurements should now be possible with the recently completed Daniel K. Inouye Solar Telescope (DKIST). This 4-meter diameter Gregorian telescope in Haleakala, Maui, Hawaii, is the largest ground-based solar observatory, and its ≤ 30 Hz frame rates and $\approx 0.''03$ spatial resolution (19km on the Sun) (Tritschler et al., 2015) should be sufficient to resolve oscillations within MBPs.

As a simple first application of the asymmetric slab model to MBPs, we can consider it as an incompressible slab. Depending on the wavelength of oscillations investigated, an MBP may be approximated as either a thin or a wide slab. Using the estimation of $\lambda \approx 100$ km from before and taking into account that the width ($2x_0$) of an MBP may be only a few hundred kilometres, it turns out that $kx_0 \ll 1$. Therefore, the MBP can be considered a thin slab for these waves and $\tanh(kx_0) \approx kx_0$ can be used to simplify the equation providing solutions for the incompressible limit (Equation 3.99). Then the angular frequency of possible modes becomes

$$\begin{aligned} \omega^2 = & \frac{k^2}{2} \frac{1}{\rho_0(\rho_1^{-1} + \rho_2^{-1}) + 2\rho_0^2\rho_1^{-1}\rho_2^{-1} + 2} \{v_{A0}^2\rho_0(\rho_1^{-1} + \rho_2^{-1})K \\ & + 4v_{A0}^2\rho_0^2\rho_1^{-1}\rho_2^{-1} + R_E K + 2[v_{A1}^2 + v_{A2}^2] \pm [(v_{A0}^2\rho_0(\rho_1^{-1} + \rho_2^{-1})K - KR_E)^2 \\ & + 2v_{A0}^2(\rho_0^2\rho_1^{-1}\rho_2^{-1}KR_E - 4R_E K - 8\rho_0^2\rho_1^{-1}\rho_2^{-1}v_{A0}^2) \\ & + (4 + 4v_{A0}^2 + 4R_E K + 8\rho_0^2\rho_1^{-1}\rho_2^{-1}v_{A0}^2)(v_{A1}^2 + v_{A2}^2)]^{1/2}\}, \end{aligned} \quad (4.24)$$

where

$$R_E = \frac{\rho_0}{\rho_1}v_{A2}^2 + \frac{\rho_0}{\rho_2}v_{A1}^2, \quad (4.25)$$

$$K = kx_0 + \frac{1}{kx_0}. \quad (4.26)$$

For larger wavenumbers, the MBP could act like a wide slab ($1 \ll kx_0$), and then

using the approximation $\tanh(kx_0) \approx 1$, Equation (3.99) simplifies to

$$\begin{aligned} \omega^2 = & \frac{k^2}{2} \frac{1}{\rho_0(\rho_1^{-1} + \rho_2^{-1}) + \rho_0^2 \rho_1^{-1} \rho_2^{-1} + 1} \{v_{A0}^2 \rho_0 (\rho_1^{-1} + \rho_2^{-1}) + 2v_{A0}^2 \rho_0^2 \rho_1^{-1} \rho_2^{-1} \\ & + R_E + [v_{A1}^2 + v_{A2}^2] \pm [(v_{A0}^2 \rho_0 (\rho_1^{-1} + \rho_2^{-1}) - R_E)^2 + (1 + v_{A0}^2 + 2R_E \\ & + 2\rho_0^2 \rho_1^{-1} \rho_2^{-1} v_{A0}^2)(v_{A1}^2 + v_{A2}^2)]^{1/2}\}. \end{aligned} \quad (4.27)$$

For a more in-depth investigation, we now re-introduce compressibility into the MBP slab, and we consider the intergranular lanes to be regions with high but slightly different plasma- β values. We choose characteristic speeds of the magnitude the photosphere is known for: $c_{sj} \approx 10\text{kms}^{-1}$ for the sound speeds, and $v_{Aj} \approx 8\text{kms}^{-1}$ for the Alfvén speeds, for $j = 1, 2$ (Mullan (2009); Kohl and Crammer (2013)). However, to the best of our knowledge, the available literature does not provide strong constraints on the plasma- β values in an MBP. Therefore, we briefly examine all three possibilities.

If the internal plasma- β is large, the MBP and its environment are described as an asymmetric slab system with high plasma- β all throughout its regions. We discussed this approximation in detail in Section 3.5.

If the internal plasma- β is exactly one, the decoupled dispersion relation becomes

$$\begin{aligned} & \frac{\sqrt{k^2 \gamma v_{A0}^2 - (\gamma + 2) \omega^2} \sqrt{k^2 v_{A0}^2 - \omega^2} \rho_0 v_{A0}}{\omega^2 \sqrt{k^2 \gamma v_{A0}^2 - 2\omega^2}} \left[\frac{\sqrt{k^2 c_1^2 - \omega^2}}{c_1 \rho_1} + \frac{\sqrt{k^2 c_2^2 - \omega^2}}{c_2 \rho_2} \right] \\ & = 2 \left(\frac{\tanh}{\coth} \right) \{m_0 x_0\} \end{aligned} \quad (4.28)$$

for surface waves, and

$$\begin{aligned} & \frac{\sqrt{k^2 \gamma v_{A0}^2 - (\gamma + 2) \omega^2} \sqrt{k^2 v_{A0}^2 - \omega^2} \rho_0 v_{A0}}{\omega^2 \sqrt{k^2 \gamma v_{A0}^2 - 2\omega^2}} \left[\frac{\sqrt{k^2 c_1^2 - \omega^2}}{c_1 \rho_1} + \frac{\sqrt{k^2 c_2^2 - \omega^2}}{c_2 \rho_2} \right] \\ & = 2 \left(\frac{\tan}{-\cot} \right) \{n_0 x_0\} \end{aligned} \quad (4.29)$$

for body waves. Here, the wavenumber coefficients are

$$n_0^2 = -m_0^2 = \frac{(2 + \gamma)(k^2 \gamma v_{A0}^2 - 2\omega^2)(\omega^2 - k^2 v_{A0}^2)}{2(1 + \gamma)v_{A0}^2(k^2 \gamma v_{A0}^2 - \gamma \omega^2 - 2\omega^2)}.$$

Lastly, if the internal plasma- β is low due to the strong concentration of magnetic fields in the MBP, the wavenumber coefficients are

$$n_0^2 = -m_0^2 = \frac{(\omega^2 - k^2 v_{A0}^2)}{v_{A0}^2}. \quad (4.30)$$

The decoupled dispersion relation becomes

$$\frac{\sqrt{k^2 v_{A0}^2 - \omega^2} v_{A0} \rho_0}{\omega^2} \left[\frac{\sqrt{k^2 c_1^2 - \omega^2}}{c_1 \rho_1} + \frac{\sqrt{k^2 c_2^2 - \omega^2}}{c_2 \rho_2} \right] = 2 \left(\frac{\tanh}{\coth} \right) \{m_0 x_0\} \quad (4.31)$$

for surface waves, and

$$\frac{\sqrt{k^2 v_{A0}^2 - \omega^2} v_{A0} \rho_0}{\omega^2} \left[\frac{\sqrt{k^2 c_1^2 - \omega^2}}{c_1 \rho_1} + \frac{\sqrt{k^2 c_2^2 - \omega^2}}{c_2 \rho_2} \right] = 2 \begin{pmatrix} \tan \\ -\cot \end{pmatrix} \{n_0 x_0\} \quad (4.32)$$

for body waves.

In addition to the analytical approximations above, we also prepared numerical solutions for all three characteristic cases identified. However, the solutions themselves are rather similar, as can be seen from the panels of Figure 4.13. Panel (a) of Figure 4.13 was obtained by approximating the MBP as a high- β slab embedded in an asymmetric high- β environment, with $v_{A0} = 10\text{km/s}$, $v_{A1} = 2.05\text{km/s}$, $v_{A2} = 3\text{km/s}$, $c_0 = 11\text{km/s}$, $c_1 = 7\text{km/s}$, $c_2 = 8\text{km/s}$ and density ratios $\rho_1/\rho_0 = 4.329987$ and $\rho_2/\rho_0 = 3.179487$ to ensure pressure balance. Panel (b) of Figure 4.13 displays the case when the internal plasma- β parameter is exactly one, while the photospheric environment of the MBP is still treated as a pair of asymmetric high- β layers. The characteristic speeds and density ratios used to obtain these solutions were $v_{A0} = 12.05\text{km/s}$, $v_{A1} = 2.05\text{km/s}$, $v_{A2} = 3\text{km/s}$, $c_0 = 11\text{km/s}$, $c_1 = 7\text{km/s}$, $c_2 = 8\text{km/s}$, with the density ratios $\rho_1/\rho_0 = 4.609381$ and $\rho_2/\rho_0 = 3.384645$. Last but not least, panel (c) of Figure 4.13 shows the solutions in the case of a low- β slab in an asymmetric high- β environment. The values of characteristic speeds used to obtain the solutions here were $v_{A0} = 15\text{km/s}$, $v_{A1} = 2.05\text{km/s}$, $v_{A2} = 3\text{km/s}$, $c_0 = 11\text{km/s}$, $c_1 = 7\text{km/s}$, $c_2 = 8\text{km/s}$ (or, after normalisation, $v_{A1} = 0.14v_{A0}$, $v_{A2} = 0.2v_{A0}$, $c_0 = 0.73v_{A0}$, $c_1 = 0.47v_{A0}$, $c_2 = 0.53v_{A0}$), with the density ratios $\rho_1/\rho_0 = 5.875957$ and $\rho_2/\rho_0 = 4.314685$ to ensure pressure balance. Comparing these three cases, it becomes easy to see that with well-constrained photospheric background parameters, the choice of internal plasma- β for an MBP does not fundamentally change the types of supported modes. In all three cases, due to the ordering of characteristic speeds, only a pair of surface mode solutions are found to be supported by the MBP slab systems as trapped oscillations, as any wave with a phase speed above c_1 would be leaky. The only effect that changing the internal plasma- β of the MBP slab has with the selected values is that it changes the frequencies of the supported surface modes for a given slab with, as well as the exact positions of the cut-offs on the graphs. In each case, these cut-offs occur in thin slabs once at an external sound speed (c_1), above which oscillations become leaky. Another band of leaky modes is present between the Alfvén- and tube speeds on the other side (v_{A2} , c_{T2}) in all three cases, but the waves can exist as trapped oscillations between $v_{A1} < v_{ph} < c_{T2}$ and $v_{A2} < v_{ph} < c_1$.

4.7 Conclusion

The continuing development of observational capabilities in solar physics also motivates further research into the theory of MHD wave propagation in various waveguides of the solar atmosphere. In the previous Chapters, we have derived the dispersion relation for the asymmetric magnetic slab, and we provided approximate solutions to this highly complex equation in various physically significant limiting cases. In the current Chapter, we proceeded to utilise these approximations in examining specific slab-like waveguides of the solar atmosphere.

As the solar atmosphere is structured both by gravity and by inhomogeneous magnetic fields, both magnetic and density asymmetries can be present in solar

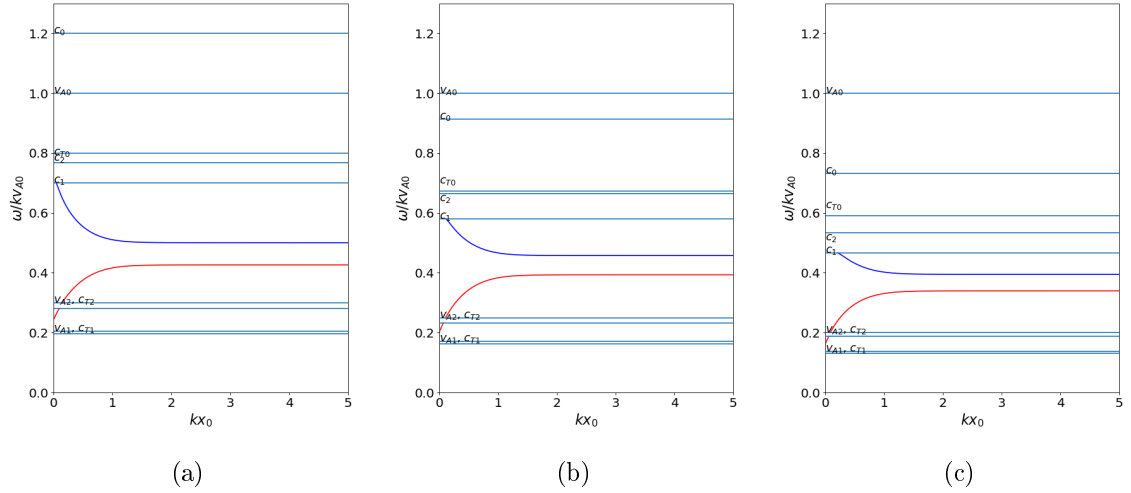


Figure 4.13: Numerical solutions for the phase speed (ω/k) of magnetoacoustic waves supported by an elongated MBP in a high- β asymmetric magnetic environment. Solutions in panel **(a)** were obtained using characteristic speeds and density ratios of $v_{A1} = 0.205v_{A0}$, $v_{A2} = 0.3v_{A0}$, $c_0 = 1.2v_{A0}$, $c_1 = 0.7v_{A0}$, $c_2 = 0.8v_{A0}$, $\rho_1/\rho_0 = 4.329987$ and $\rho_2/\rho_0 = 3.179487$, in which case the MBP itself is a high- β slab as well. Panel **(b)** shows solutions obtained in a slab system characterised by $v_{A1} = 0.170v_{A0}$, $v_{A2} = 0.249v_{A0}$, $c_0 = 0.913v_{A0}$, $c_1 = 0.581v_{A0}$, $c_2 = 0.663v_{A0}$, $\rho_1/\rho_0 = 4.609381$ and $\rho_2/\rho_0 = 3.384645$, in which case the MBP itself is described by a plasma- β value of one. Finally, panel **(c)** shows trapped solutions when $v_{A1} = 0.0137v_{A0}$, $v_{A2} = 0.2v_{A0}$, $c_0 = 0.733v_{A0}$, $c_1 = 0.47v_{A0}$, $c_2 = 0.53v_{A0}$, $\rho_1/\rho_0 = 5.875957$ and $\rho_2/\rho_0 = 4.314685$, and therefore the MBP itself is a low- β slab.

features on both small and large scales. By applying the asymmetric magnetic slab model, we essentially consider these waveguides as a series of internally homogeneous parallel layer. This can be a valuable starting point in understanding the influence of asymmetries on the behaviour of eigenmodes of these systems, however, the model can and should still be improved in the future. For example, we have ignored gravity when building our model out of internally homogeneous regions. This can be considered a simplistic version of gravitational stratification, if the slab is positioned appropriately, as we have done in e.g. Sections 4.2, 4.2.1 and 4.4. This is, of course, not an exact description, and (as it happened in Section 4.2), it may require us to check the validity of our results on a case-by-case basis.

Keeping these limitations in mind, throughout the Chapter, we investigated various solar applications of the asymmetric slab system. We started from applications to the global stratification of the solar atmosphere in Section 4.2, in which we constructed a slab from the photosphere, the interface region, and the solar corona. We discussed some already known wave detections in these regions, defined the limits of our model's applicability, and provided analytical and numerical results about the expected wave modes based on known physical parameters of the three regions.

In Section 4.2.1, we constructed a new slab from the chromosphere, the transition region and the solar corona, in order to better resolve the change from the high- β lower solar atmosphere to the low- β corona, and to avoid the limitations on

the model's applicability introduced by the small scale height in the photosphere. Next, we moved on to more localised applications in the solar corona. We discussed asymmetric slabs at coronal hole boundaries in Section 4.3, and in the environment of prominence in Section 4.4. Both of these could be treated as low- β slabs, although the difference in expected characteristic speeds and densities meant that we found significant differences between trapped oscillations of the two environments. It must be noted that even when we are investigating localised structures, if these have a large vertical sizes, such as coronal plumes do, we must pay attention to the limits that local gravitational scale-heights may pose. Rather than over-interpreting our findings, the vertical extent of the waveguide we selected must be compared against the typical scale-height of stratification.

In the last two Sections, we focused on lower atmospheric structures that can be approximated as asymmetric magnetic slabs. In Section 4.5, we described light bridges and summarised a few important results known about waves guided by them and by sunspots in general. We constructed an asymmetric magnetic slab system from two umbral cores separated by a light bridge, and investigated what kinds of eigenmodes we can expect to find depending on the plasma- β values inside the light bridge. Last, but not least, in Section 4.6, we applied the model of an asymmetric magnetic slab to a magnetic bright point and its environment of an intergranular lane. We provided an estimate for the parameters of waves we might expect to detect in MBPs with the new generation of solar telescopes. We gave an analytical description and numerical solutions for eigenmodes in both the incompressible limit of an asymmetric slab centred on an MBP, and in a compressible MBP slab with various values of internal plasma- β .

Chapter 5

Solar Magneto-Seismology of an Asymmetric Magnetic Slab

Abstract

This Chapter further generalises the amplitude ratio and minimum perturbation shift methods developed for the purposes of solar magneto-seismology by Allcock and Erdélyi (2018) and applied to an externally non-magnetic asymmetric slab system. Here, we investigate the effect of including an external magnetic asymmetry on these spatial seismology techniques and provide estimates of an unknown Alfvén speed in the slab waveguide. Further, we also revisit the concept of quasi-symmetric oscillations introduced in Chapter 2 and provide a clearer definition of such modes of oscillations, as well as describe a simple seismological use for these special waves. A paper (Zsámberger and Erdélyi (2022)) on the solar magneto-seismology paper of asymmetric magnetic slabs has been submitted to the *Astrophysical Journal* based on this Chapter.

5.1 Chapter Introduction

The atmosphere of our Sun is a complex plasma environment finely structured by its ubiquitous magnetic fields. In understanding and measuring the properties of this rich variety of solar waveguides, the constantly evolving methods of solar magneto-seismology provide a useful and versatile toolkit.

In this Chapter, we further generalise and develop the SMS methods described in Allcock and Erdélyi (2018), by applying them to the problem of wave propagation in an asymmetric magnetic slab. Similarly to the case of the externally field-free asymmetric slab, the eigenmodes of an asymmetric magnetic slab also possess mixed characteristics of the traditional kink and sausage modes. We have described the important differences between symmetric and asymmetric eigenmodes in Chapter 2, where we also highlighted some special attributes of the latter which we can utilise in the current Chapter to provide diagnostic tools for solar waveguides.

In Section 5.2, we focus on the distributions of the transverse velocity amplitudes of eigenmodes across the slab. More specifically, make use of the fact that their amplitudes at the two slab boundaries are asymmetric, and that the ratio of these amplitudes depends of the physical and geometric parameters of the slab waveguide. We provide an analytical description the amplitude ratios of quasi-sausage

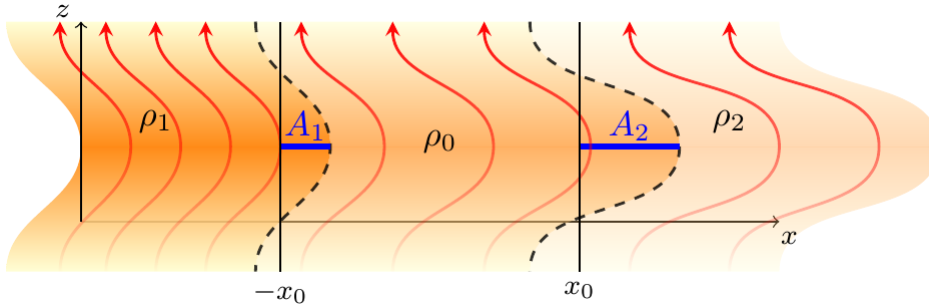


Figure 5.1: Illustration of the principle of the amplitude ratio method: the ratio of transverse displacement (or velocity) amplitudes at the two boundaries of the slab, A_1 and A_2 , is calculated and measured.

and quasi-kink modes in the general case, as well as various limits of slab width and plasma- β values. We also compare these approximations with results obtained for numerical solutions of the general dispersion relation. In addition, we carry on with investigating the behaviour of so-called quasi-symmetric modes, which we first described in a mechanical analogy to the slab system in Section 2.3. In Section 5.3, we generalise the minimum perturbation shift method described by Allcock and Erdélyi (2018) to magnetically asymmetric slabs. This diagnostic tool is based on another unique attribute of the asymmetric eigenmodes, namely, that due to the difference of equilibrium parameters in their environment, the minimally perturbed surface they possess will be offset from the centre of the slab. Just like the ratio of velocity amplitudes, this offset value is also dependant on the characteristic speeds and densities in the slab system, as well as the parameters of the observable oscillations.

5.2 Amplitude ratios

By generalising the amplitude ratio method described in Allcock and Erdélyi (2018), this Section aims to derive an expression describing the ratio of the transverse displacement or velocity amplitudes on the two boundaries of an asymmetric magnetic slab. As we will show, this ratio depends on the parameters of an observed oscillation in the slab waveguide, as well as on the physical and geometric attributes of the waveguide itself. The expression for the amplitude ratio is then utilised to estimate background parameters of the system. Figure 5.1 demonstrates the principle of the amplitude ratio method for a quasi-kink mode of a perturbed asymmetric magnetic slab waveguide.

The process through which we derive the amplitude ratio is formally similar to the method described in Allcock and Erdélyi (2018) and Allcock et al. (2019), however, both density and magnetic asymmetry are incorporated into the quantities we define (such as m_j , Λ_j , for $j = 0, 1, 2$), which will become clear in the final result.

In Section 2.2.2, it was shown that the x component of the velocity perturbation of trapped magneto-acoustic modes propagating along a magnetic slab embedded in an asymmetric magnetic environment has the form of $v_{I,x}(\mathbf{x}, t) = \hat{v}_x(x)e^{i(kz - \omega t)}$, where $\hat{v}_x(x)$ is the transverse velocity amplitude given by a combination of the

hyperbolic functions in each region of the slab system, namely:

$$\hat{v}_x(x) = \begin{cases} A (\cosh m_1 x + \sinh m_1 x), & x < -x_0, \\ B \cosh m_0 x + C \sinh m_0 x, & |x| < x_0, \\ D (\cosh m_2 x - \sinh m_2 x), & x_0 < x, \end{cases} \quad (5.1)$$

with A , B , C , and D being arbitrary constants. These constants can be determined (within one degree of freedom) by satisfying the four boundary conditions imposing the continuity of total pressure and velocity perturbations at the two interfaces separating the slab from its asymmetric environment. From the application of these boundary conditions, we obtained a system of four coupled, linear, homogeneous algebraic equations summarised as

$$\begin{bmatrix} C_1 - S_1 & -C_0 & S_0 & 0 \\ 0 & C_0 & S_0 & S_2 - C_2 \\ -\Lambda_1 (C_1 - S_1) & -\Lambda_0 S_0 & \Lambda_0 C_0 & 0 \\ 0 & \Lambda_0 S_0 & \Lambda_0 C_0 & -\Lambda_2 (S_2 - C_2) \end{bmatrix} \begin{bmatrix} A \\ B \\ C \\ D \end{bmatrix} = \begin{bmatrix} 0 \\ 0 \\ 0 \\ 0 \end{bmatrix}.$$

As a reminder, here,

$$\begin{aligned} C_j &= \cosh(m_j x_j), \\ S_j &= \sinh(m_j x_j), \text{ and} \\ \Lambda_j &= -\frac{i\rho_j k^2 v_{Aj}^2 - \omega^2}{\omega m_j} \quad (\text{for } j = 0, 1, 2). \end{aligned} \quad (5.2)$$

In Chapter 2, we obtained the dispersion relation (Equation 2.30) for the asymmetric magnetic slab system by ensuring that the determinant of this matrix was zero. Satisfying the dispersion relation then allows one degree of freedom to be gained in the system of Equations derived from the boundary conditions. This means that we may choose one of the constants, B or C as arbitrary. Depending on this choice, we will deal with either the quasi-sausage or the quasi-kink eigenmodes of the system.

5.2.1 Quasi-sausage modes

For quasi-sausage modes, we let the constant C to be arbitrary, which allows us to determine the other three coefficients as

$$A = \frac{1}{C_1 - S_1} (BC_0 - CS_0), \quad (5.3)$$

$$D = \frac{1}{C_2 - S_2} (BC_0 + CS_0), \quad (5.4)$$

$$B = \frac{\Lambda_0 C_0 + \Lambda_1 S_0}{\Lambda_0 S_0 + \Lambda_1 C_0} C, \quad (5.5)$$

$$B = -\frac{\Lambda_0 C_0 + \Lambda_2 S_0}{\Lambda_0 S_0 + \Lambda_2 C_0} C. \quad (5.6)$$

The second expression for B can be found by using the dispersion relation (Equation 2.30), which we re-state here for ease of understanding:

$$2(\Lambda_0^2 + \Lambda_1 \Lambda_2) + \Lambda_0 (\Lambda_1 + \Lambda_2) \left[\tau_0 + \frac{1}{\tau_0} \right] = 0, \quad (5.7)$$

where

$$\tau_0 = \tanh(m_0 x_0). \quad (5.8)$$

If we substitute Equation (5.5) into Equation (5.1) describing the transverse velocity amplitudes and take the values at the two interfaces, we get

$$\hat{v}_x(-x_0) = BC_0 - CS_0 = \frac{\Lambda_0}{\Lambda_0 + \Lambda_1(1/\tau_0)} \frac{1}{S_0} C, \text{ and} \quad (5.9)$$

$$\hat{v}_x(x_0) = BC_0 + CS_0 = \frac{\Lambda_0(\tau_0 + 1/\tau_0) + 2\Lambda_1}{\Lambda_0 + \Lambda_1(1/\tau_0)} C_0 C. \quad (5.10)$$

Similarly, if we substitute Equation (5.6) instead, the result is

$$\hat{v}_x(-x_0) = BC_0 - CS_0 = -\frac{\Lambda_0(\tau_0 + 1/\tau_0) + 2\Lambda_2}{\Lambda_0 + \Lambda_2(1/\tau_0)} C_0 C, \text{ and} \quad (5.11)$$

$$\hat{v}_x(x_0) = BC_0 + CS_0 = -\frac{\Lambda_0}{\Lambda_0 + \Lambda_2(1/\tau_0)} \frac{1}{S_0} C. \quad (5.12)$$

The two forms of the velocity perturbation amplitudes at the slab boundaries are equivalent. They express the magnitude as well as the direction of the transverse velocity perturbation, therefore they can be considered a signed amplitude, with positive values expressing perturbations in the positive x -direction, and vice versa.

We adopt the following definition of the amplitude ratio from Allcock and Erdélyi (2018):

$$R_A := \frac{\hat{\xi}_x(x_0)}{\hat{\xi}_x(-x_0)}, \quad (5.13)$$

which compares the displacement perturbation amplitude (defined as $\hat{\xi}_x(x) = i\hat{v}_x(x)/\omega$) at the right-hand-side interface to the amplitude at the left-hand-side interface. An equivalent definition can be given using the velocity perturbations as

$$R_A := \frac{\hat{v}_x(x_0)}{\hat{v}_x(-x_0)}. \quad (5.14)$$

We substitute the simpler expressions for the velocity amplitudes at the boundaries, Equations (5.9) and (5.12) for quasi-sausage modes into the definition of the amplitude ratio (Equation 5.14), which yields

$$R_A = -\frac{\Lambda_0 + \Lambda_1 \frac{1}{\tau_0}}{\Lambda_0 + \Lambda_2 \frac{1}{\tau_0}}, \quad (5.15)$$

or equivalently

$$R_A = -\frac{\rho_1 m_2 \left[\frac{\rho_0}{\rho_1} m_1 (k^2 v_{A0}^2 - \omega^2) + m_0 (k^2 v_{A1}^2 - \omega^2) \frac{1}{\tau_0} \right]}{\rho_2 m_1 \left[\frac{\rho_0}{\rho_2} m_2 (k^2 v_{A0}^2 - \omega^2) + m_0 (k^2 v_{A2}^2 - \omega^2) \frac{1}{\tau_0} \right]}. \quad (5.16)$$

The amplitude ratio is negative, as in quasi-sausage modes, the displacement perturbations at the two boundaries of the slab happen in opposite directions. If the configuration is symmetric (and so the characteristic speeds and densities on the two sides are equal), this ratio reduces to $R_A = -1$, as expected, meaning that in the sausage modes of the symmetric slab system, the two boundaries oscillate exactly in anti-phase.

Quasi-sausage amplitude ratio in the thin slab approximation

Since the amplitude ratio is a measurable quantity, our main aim is to use it to determine a background parameter of the asymmetric waveguide we derived it for. This background parameter should be one that is not easy to observe directly, such as a magnetic field strength or Alfvén speed in the system. In order to provide an analytical approximation for one of these, we must restrict ourselves to various limiting cases of either slab width or plasma- β parameters.

In the thin slab limit, the wavelength of the oscillations is much longer than the width of the slab, that is, $kx_0 \ll 1$, and therefore $m_0x_0 \ll 1$. Then, the coth function can be approximated by the reciprocal of its argument in Equation (5.16), so the amplitude ratio can be approximated as

$$R_A = -\frac{\rho_1 m_2 \left[\frac{\rho_0}{\rho_1} m_1 x_0 (k^2 v_{A0}^2 - \omega^2) + (k^2 v_{A1}^2 - \omega^2) \right]}{\rho_2 m_1 \left[\frac{\rho_0}{\rho_2} m_2 x_0 (k^2 v_{A0}^2 - \omega^2) + (k^2 v_{A2}^2 - \omega^2) \right]}. \quad (5.17)$$

This makes it possible for us to express the internal Alfvén speed in the slab as a function of the external characteristic speeds, the densities, as well as the amplitude ratios, wavenumbers and angular frequencies:

$$v_{A0}^2 = \frac{\omega^2}{k^2} \left[1 - \frac{\rho_1 m_2 (k^2 v_{A1}^2 - \omega^2) + R_A \rho_2 m_1 (k^2 v_{A2}^2 - \omega^2)}{\omega^2 x_0 m_1 m_2 \rho_0 (1 + R_A)} \right]. \quad (5.18)$$

Most quantities on the right-hand-side are known or can be expressed as a function of other measurable quantities themselves. The right-hand-side, in the end, depends on two wave parameters (wavenumber and angular frequency), the background temperatures, and the Alfvén speed on one side of the slab. The dependence on the second external Alfvén speed can be eliminated using the condition of total pressure balance. Therefore, if we have previous information on one of the external Alfvén speeds, measure the temperature throughout the configuration, and detect oscillations in it, we can estimate the internal Alfvén speed, thus the strength of the magnetic field inside the slab.

To complement this analysis, we also conduct a numerical investigation of the amplitude ratios of quasi-sausage modes in an asymmetric magnetic slab. First of all, we present numerical solutions of the full dispersion relation (Equation 2.31) in Figure 5.2. The characteristic speeds of the three plasma regions were chosen as $v_{A0} = 1$, $c_0 = 1.4$, $v_{A1} = 0.19$, $c_1 = 1.2$, $\rho_1/\rho_0 = 1.9$, $v_{A2} = 0.18$, $c_2 = 1.09$, $\rho_2/\rho_0 = 2.28$, with the density asymmetry parameter defined in Equation (5.34), $\delta = 0.2$, and the magnetic asymmetry parameter defined in Equation (5.35), $\epsilon = 0.1$. Body mode solutions can exist between the internal tube- and Alfvén speeds, but here we focus on the pair of slow surface modes propagating with phase speeds lower than c_{T0} . The quasi-sausage mode is plotted in blue, while the quasi-kink mode is displayed in red. Taking the wavenumbers and the corresponding angular frequencies (or phase speeds) of these solutions, we can now calculate the amplitude ratio for the quasi-sausage waves. (Note that in an observational example, we could take these wave parameters from the observations, and the amplitude ratios could be calculated without having to find numerical solutions to the dispersion relation.)

The amplitude ratio (Equation 5.16) of slow quasi-sausage surface modes as a function of the slab width is then plotted in Figure 5.3, alongside its thin slab

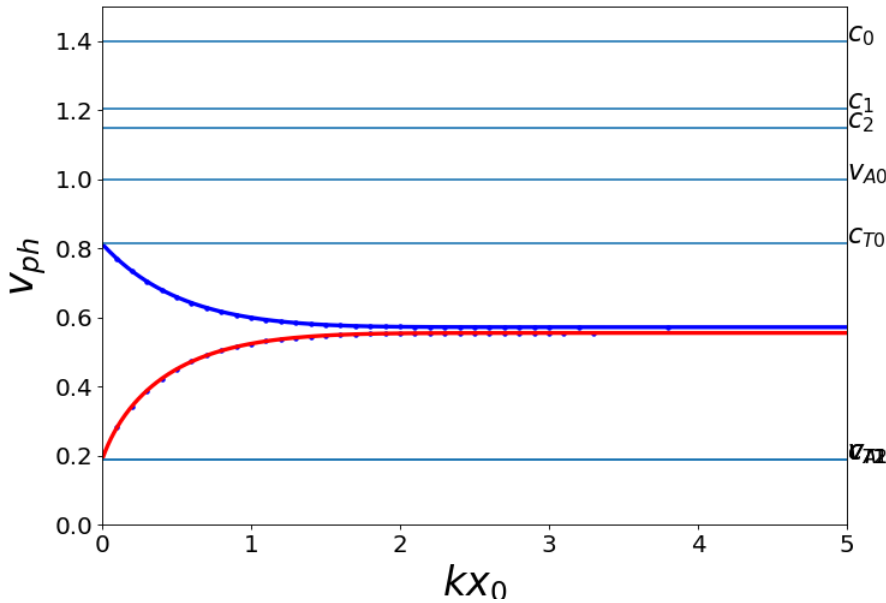


Figure 5.2: Trapped surface mode solutions in an asymmetric slab with $v_{A0} = 1$, $c_0 = 1.4$, $v_{A1} = 0.19$, $c_1 = 1.2$, $\rho_1/\rho_0 = 1.9$, $v_{A2} = 0.18$, $c_2 = 1.09$, $\rho_2/\rho_0 = 2.28$. The blue (red) line displays the quasi-sausage (quasi-kink) surface mode, with other types of solutions not displayed in the figure.

approximation (Equation (5.17)). The exact amplitude ratio is shown by the blue curve, while the approximation is displayed with the red points. Up to dimensionless slab width parameters of about 1, the thin-slab approximation of the ratio works relatively well, showing little deviation from the exact values. For wider slabs (or longer wavelengths), however, the differences between the estimate and the exact solution become significant. This is to be expected, as we applied the condition $kx_0 \ll 1$ to obtain our thin-slab amplitude ratio.

5.2.2 Quasi-kink modes

Firstly, we repeat the steps of the derivation process we followed for quasi-sausage modes in Section 5.2.1. We start by stating that for quasi-kink modes, it is the constant B which we choose arbitrarily, and we can express the rest of the coefficients as

$$A = \frac{1}{C_1 - S_1}(BC_0 - CS_0), \quad (5.19)$$

$$D = \frac{1}{C_2 - S_2}(BC_0 + CS_0), \quad (5.20)$$

$$C = \frac{\Lambda_0 S_0 + \Lambda_1 C_0}{\Lambda_0 C_0 + \Lambda_1 S_0} B, \quad (5.21)$$

$$C = -\frac{\Lambda_0 S_0 + \Lambda_2 C_0}{\Lambda_0 C_0 + \Lambda_2 S_0} B. \quad (5.22)$$

The second expression for C was found using the dispersion relation for the asymmetric magnetic slab system, Equation 5.7). If we now substitute Equation (5.21)

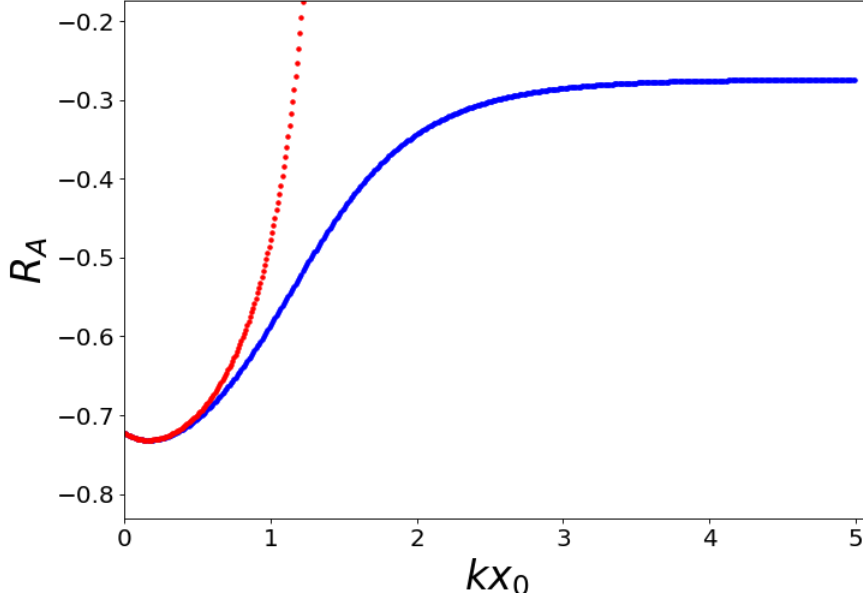


Figure 5.3: Amplitude ratios of the quasi-sausage mode as a function of kx_0 . The exact amplitude ratio is plotted with blue, the approximation with red, using the same background parameters as Figure 5.2. For small slab widths, as expected, the approximation follows the exact solutions closely, but for wide slabs, the difference between the two grows quickly.

into Equation (5.1) describing the transverse velocity amplitudes and take the values at the two interfaces, we get

$$\hat{v}_x(-x_0) = BC_0 - CS_0 = \frac{\Lambda_0}{\Lambda_0 + \Lambda_1\tau_0} \frac{1}{C_0} B, \text{ and} \quad (5.23)$$

$$\hat{v}_x(x_0) = BC_0 + CS_0 = \frac{\Lambda_0(\tau_0 + 1/\tau_0) + 2\Lambda_1}{\Lambda_0 + \Lambda_1\tau_0} S_0 B. \quad (5.24)$$

Similarly, if we use Equation (5.22) instead, the result for the perturbed velocity amplitudes at the slab boundaries becomes

$$\hat{v}_x(-x_0) = BC_0 - CS_0 = \frac{\Lambda_0(\tau_0 + 1/\tau_0) + 2\Lambda_2}{\Lambda_0 + \Lambda_2\tau_0} S_0 B, \text{ and} \quad (5.25)$$

$$\hat{v}_x(x_0) = BC_0 + CS_0 = \frac{\Lambda_0}{\Lambda_0 + \Lambda_2\tau_0} \frac{1}{C_0} B. \quad (5.26)$$

Once again, the two forms of the velocity perturbation amplitudes at the interfaces are equivalent. and can be used to calculate the signed amplitude ratio, R_A as

$$R_A = \frac{\Lambda_0 + \Lambda_1\tau_0}{\Lambda_0 + \Lambda_2\tau_0}, \quad (5.27)$$

or expressed with the characteristic speeds,

$$R_A = \frac{\rho_1 m_2 \frac{\rho_0}{\rho_1} m_1 (k^2 v_{A0}^2 - \omega^2) + m_0 (k^2 v_{A1}^2 - \omega^2) \tau_0}{\rho_2 m_1 \frac{\rho_0}{\rho_2} m_2 (k^2 v_{A0}^2 - \omega^2) + m_0 (k^2 v_{A2}^2 - \omega^2) \tau_0}. \quad (5.28)$$

The amplitude ratio for quasi-kink modes is positive, since the displacement perturbation at the two boundaries of the slab happen in the same direction. In a symmetric slab, as expected, this ratio reduces to $R_A = 1$, showing that the symmetric kink oscillations happen exactly in phase at the boundaries of the slab.

Quasi-kink amplitude ratio in the thin slab approximation

In the thin slab limit, where the width of the slab is much smaller than the wavelength of the oscillations ($kx_0 \ll 1$), the $\tanh m_0 x_0$ function can be approximated with its argument, and Equation (5.28) becomes

$$R_A = \frac{\rho_1 m_2 \left[\frac{\rho_0}{\rho_1} m_1 (k^2 v_{A0}^2 - \omega^2) + (k^2 v_{A1}^2 - \omega^2) m_0^2 x_0 \right]}{\rho_2 m_1 \left[\frac{\rho_0}{\rho_2} m_2 (k^2 v_{A0}^2 - \omega^2) + (k^2 v_{A2}^2 - \omega^2) m_0^2 x_0 \right]}. \quad (5.29)$$

This equation, too, can be rearranged to give an estimate of the internal Alfvén speed in relation measurable quantities of the asymmetric slab system and the waves it guides:

$$v_{A0}^2 = \frac{c_0^2 \omega^2}{k^2 c_0^2 - \omega^2} + \frac{m_1 \rho_2 R_A (k^2 v_{A2}^2 - \omega^2) - m_2 \rho_1 (k^2 v_{A1}^2 - \omega^2)}{m_1 m_2 \rho_0 (1 - R_A)} x_0. \quad (5.30)$$

Similarly to the case of quasi-sausage modes, this expression can be used to estimate the internal Alfvén speed of oscillating solar structures as a function of only one of the external Alfvén speeds, if we express the second external Alfvén speed in terms of the other equilibrium parameters of its region using the condition of total pressure balance.

Such a formula makes it possible not only to estimate the Alfvén speed itself, but also to gauge how big an effect the assumption of symmetry versus asymmetry in the slab model might have on the estimate. If we define Equation (5.30) as the asymmetric Alfvén speed (squared), v_{AS}^2 , then we can also define the symmetric Alfvén speed, v_S^2 in the following manner. Let us assume that the only source of the asymmetry in the slab system is the external density difference (δ). Then, as $\delta \rightarrow 0$, it is also true that $\rho_2 \rightarrow \rho_1$, $c_2 \rightarrow c_1$, $v_{A2} \rightarrow v_{A1}$, and $m_2 \rightarrow m_1$. This allows us to simplify some terms in Equation (5.30), which gives us the symmetric Alfvén speed as:

$$v_S^2 = \frac{c_0^2 \omega^2}{k^2 c_0^2 - \omega^2} + \frac{\rho_1 (k^2 v_{A1}^2 - \omega^2) (1 - R_A)}{\rho_0 m_1 (1 - R_A)} x_0. \quad (5.31)$$

Taking difference of Equation (5.30) and (5.31) then gives us the relative error we can expect in the estimation of the Alfvén speed due to the assumption that a slab system in the solar atmosphere is symmetric, while in reality it is asymmetric:

$$\begin{aligned} v_D^2 &= \frac{v_{AS}^2 - v_S^2}{v_S^2} \\ &= \frac{(m_1 \rho_2 R_A [k^2 v_{A2}^2 - \omega^2] - m_2 \rho_1 R_A [k^2 v_{A1}^2 - \omega^2] [R_A - 2]) (k^2 c_0^2 - \omega^2) x_0}{m_2 (c_0^2 \omega^2 \rho_0 + \rho_1 [k^2 v_{A1}^2 - \omega^2] [k^2 c_0^2 - \omega^2] x_0) (1 - R_A)}. \end{aligned} \quad (5.32)$$

Amplitude ratio in the wide slab approximation

In the limit of a wide slab, the amplitude ratios of quasi-sausage and quasi-kink modes can be handled together. Now, the typical wavelength of oscillations is far shorter than the width of the slab. Therefore, $kx_0 \gg 1$, and therefore $m_0x_0 \gg 1$. Then, both the tanh and coth functions take a value of approximately one, and the expression for the amplitude ratio becomes

$$R_A = \mp \frac{\frac{\rho_0}{\rho_1} m_1 (k^2 v_{A0}^2 - \omega^2) + m_0 (k^2 v_{A1}^2 - \omega^2)}{\frac{\rho_0}{\rho_2} m_2 (k^2 v_{A0}^2 - \omega^2) + m_0 (k^2 v_{A2}^2 - \omega^2)}, \quad (5.33)$$

where the negative sign corresponds to quasi-sausage modes, while the positive one describes quasi-kink waves.

5.2.3 Approximation of amplitude ratios in a weakly asymmetric slab

If we want to examine the dependence of the amplitude ratios on the density and magnetic field asymmetries in detail, we can define the following small quantities from the ratios of the external background parameters:

$$\delta = \frac{\rho_2}{\rho_1} - 1, \quad \text{and} \quad (5.34)$$

$$\varepsilon = \frac{B_2^2}{B_1^2} - 1. \quad (5.35)$$

In the following subsections, we conduct an analytical study using these parameters, and we also show a collection of numerical results on how the amplitude ratios of the eigenmodes depend on these two sources of background asymmetry.

Quasi-sausage modes

If we assume that both the density- and the magnetic asymmetries are weak in the slab system, then both δ and ε are small parameters, and we can expand the characteristic speeds on the right-hand-side of the slab in terms of δ and ε as

$$\begin{aligned} v_{A2}^2 &= v_{A1}^2 (1 + \varepsilon - \delta), \\ c_2^2 &= c_1^2 - \frac{\gamma}{2} v_{A1}^2 \varepsilon - \delta c_1^2, \\ c_{T2}^2 &= \frac{1}{c_1^2 + v_{A1}^2} \left\{ c_1^2 + \left(c_1^2 - \frac{\gamma}{2} v_{A1}^2 - \frac{c_1^2 [1 - \frac{\gamma}{2}] v_{A1}^2}{c_1^2 + v_{A1}^2} \right) \varepsilon - c_1^2 \delta \right\} \end{aligned} \quad (5.36)$$

Here, we also used the condition of total pressure balance (Equation 2.2), and we only kept first order terms. Using the expressions thus obtained for the characteristic speeds, we can rewrite m_2 as

$$|m_2| = |m_1| + S (A\varepsilon + B\delta), \quad (5.37)$$

where

$$\begin{aligned}
 A &= v_{A1}^2 [m_1^2 - k^2] \left[\frac{\gamma}{2} \{k^2 v_{A1}^2 - \omega^2\} - \{k^2 c_1^2 - \omega^2\} \right], \\
 B &= \omega^2 \left(2\omega^2 - \left[\{k^2 + m_1^2\} \{c_1^2 + v_{A1}^2\} \right] \right), \\
 S &= \frac{1}{2\sqrt{m_1^2(k^2 c_{T1}^2 - \omega^2)(c_1^2 + v_{A1}^2)}}.
 \end{aligned} \tag{5.38}$$

Therefore, the amplitude ratio for quasi-sausage modes in the thin-slab approximation in terms of ε and δ is

$$R_A = -\frac{G}{L} \left(\pm 1 + \left[P - \left\{ \pm \frac{N}{L} \right\} \right] \varepsilon + \left[Q - \left\{ \pm \frac{M}{L} \right\} \right] \delta \right) \tag{5.39}$$

where

$$\begin{aligned}
 G &= \rho_0 m_1 x_0 [k^2 v_{A0}^2 - \omega^2] + \rho_1 [k^2 v_{A1}^2 - \omega^2], \\
 L &= \rho_0 x_0 \sqrt{m_1^2 [k^2 v_{A0}^2 - \omega^2] + \rho_1 [k^2 v_{A1}^2 - \omega^2]}, \\
 M &= SB \rho_0 x_0 [k^2 v_{A0}^2 - \omega^2] - \rho_1 [k^2 v_{A1}^2 + \omega^2], \\
 N &= SA \rho_0 x_0 [k^2 v_{A0}^2 - \omega^2] + \rho_1 k^2 v_{A1}^2, \\
 P &= \frac{SA}{m_1}, \\
 Q &= \frac{SB}{m_1};
 \end{aligned} \tag{5.40}$$

To further extend the investigation of the different asymmetric effects on the amplitude ratios of the eigenmodes, we include a few illustrative numerical results, too. The top panels of Figures 5.4 and 5.5 show the dependence of the quasi-sausage amplitude ratio on δ for different two different (fixed) values of the dimensionless slab width and the same fixed value of the magnetic asymmetry parameter, ε . The exact amplitude ratio is plotted with the bright blue line, while its thin-slab approximation is shown by the dark blue dots. The bottom panels of both figures show the difference between the exact and approximate amplitude ratios (ΔR_A) which is negligibly small even for slabs of intermediate width. An interactive (video) version of this figure is also available as supplementary material SM-S1, showing how the difference between the exact and approximate expressions for the amplitude ration changes as a function of δ as the slab width is slowly increased to intermediate values.

From our analytical and complimentary numerical results, we can conclude that both the slab width and the density asymmetry have a significant effect on the amplitude ratio. Moreover, the thin slab approximation holds up very well for the changing values of delta, even as far up as $\delta = 3$, which would mean a rather high density asymmetry (ρ_2 is four times as large as ρ_1). However, all of this is only true for slab width values up to about $kx_0 = 0.7$, which is where the amplitude ratio obtained from the thin slab approximation visibly starts to differ from the actual value.

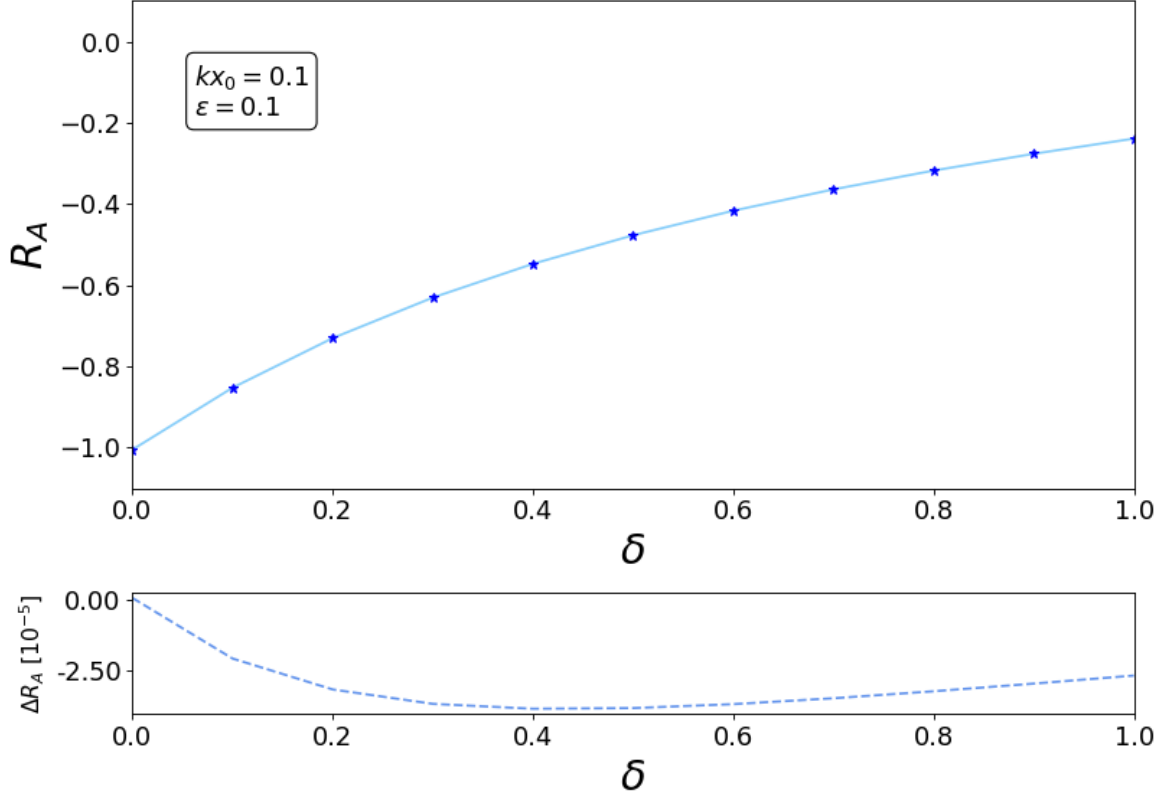


Figure 5.4: Dependence of the amplitude ratio on δ , for $\epsilon = 0.1$ and $kx_0 = 0.1$, for the quasi-sausage mode.

Quasi-kink modes

Through a similar process, we can express the amplitude ratio for quasi-kink modes in terms of the density and magnetic asymmetries (to first order) in the following form:

$$R_A = \frac{T}{U} \left(\pm + \left[P - \pm \frac{V}{U} \right] \epsilon + \left[Q - \pm \frac{W}{U} \right] \delta \right) \quad (5.41)$$

where

$$\begin{aligned} T &= \rho_0 m_1 [k^2 v_{A0}^2 - \omega^2] + \rho_1 [k^2 v_{A1}^2 - \omega^2] m_0^2 x_0, \\ U &= \rho_0 \sqrt{m_1^2} [k^2 v_{A0}^2 - \omega^2] + \rho_1 m_0^2 x_0 [k^2 v_{A1}^2 - \omega^2], \\ V &= SA \rho_0 [k^2 v_{A0}^2 - \omega^2] + \rho_1 m_0^2 x_0 k^2 v_{A1}^2, \\ W &= SB \rho_0 [k^2 v_{A0}^2 - \omega^2] + \rho_1 m_0^2 x_0 [k^2 v_{A1}^2 + \omega^2], \end{aligned} \quad (5.42)$$

Similarly to Figures 5.4 and 5.5, the dependence of the amplitude ratio of the quasi-kink modes on the density asymmetry δ is displayed in Figures 5.6 and 5.7, for the same characteristic speeds as before, and $kx_0 = 0.1$ and $kx_0 = 0.5$, respectively. For the chosen values of background parameters, at least, from small up to intermediate slab widths, the difference between the dependence of the amplitude ratio on the density asymmetry calculated from the exact general formula and the thin slab

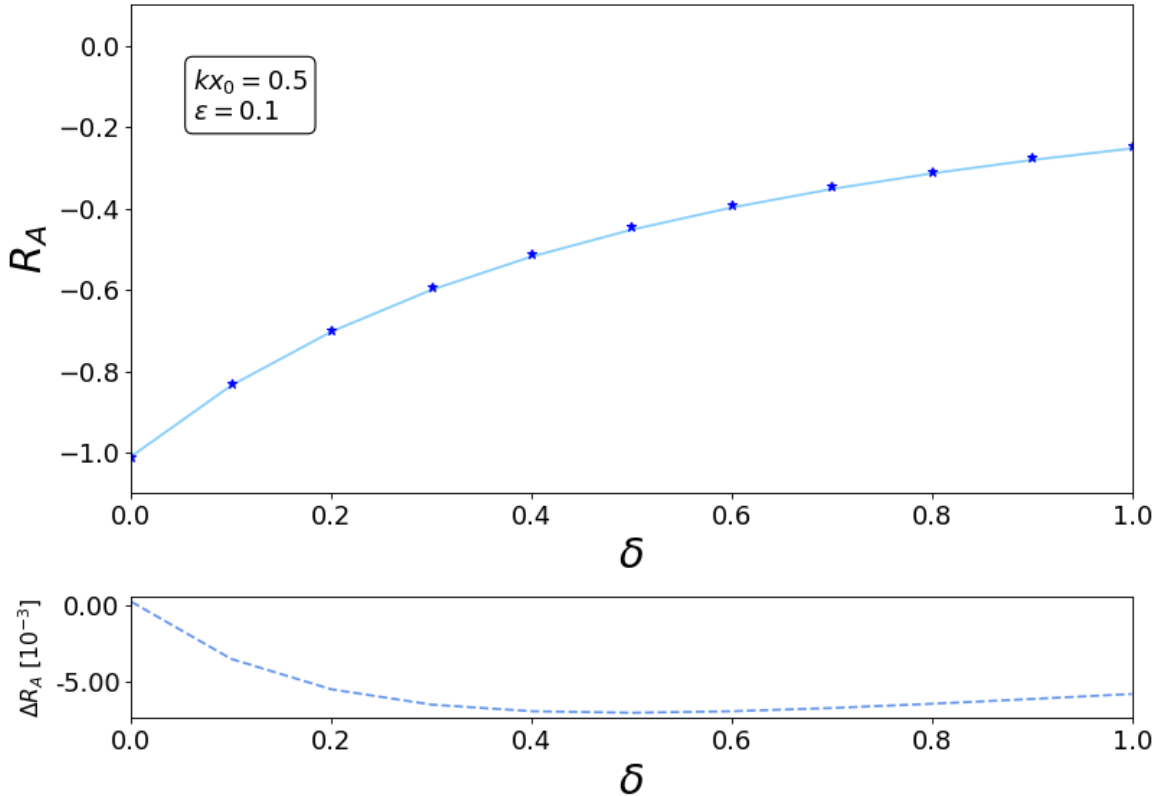


Figure 5.5: Dependence of the amplitude ratio on δ , for $\epsilon = 0.5$ and $kx_0 = 0.5$, for the quasi-sausage mode.

approximation is still relatively small. An interactive version of this figure, showing the influence of the changing slab width on the amplitude ratios is also available as supplementary material SM-S2. Along with the difference, the density-dependence itself also displays a much stronger effect on the magnitude of the amplitude ratio for higher values of the slab width.

5.2.4 Quasi-symmetric modes

When we described the mechanical analogy for the asymmetric slab system in Section 2.3, we found the coupled mechanical oscillator system may have a mode of oscillation that is generated by an asymmetric background, but appears symmetric at the boundaries.

Similarly, thanks to the presence of competing pressure gradient and magnetic forces on either side of the slab, it is possible that an asymmetric magnetic slab will show so-called quasi-symmetric oscillations, which have equal transverse displacement amplitude on each boundary of the slab. This means that $\hat{v}_x(-x_0) = -\hat{v}_x(x_0)$ for quasi-sausage modes and $\hat{v}_x(-x_0) = \hat{v}_x(x_0)$ for quasi-kink modes. Although at first glance, they appear to be "pure" sausage or kink modes, these quasi-symmetric oscillations may have different perturbation penetration depth in the external regions, and different spatial distribution of wave power within the slab.

In order to find an analytical relation to identify the set of asymmetric parameters that imitates a symmetric system, we require that the structures of the symmetric (Equation 5.43) and decoupled asymmetric (Equation 5.44) dispersion relations have

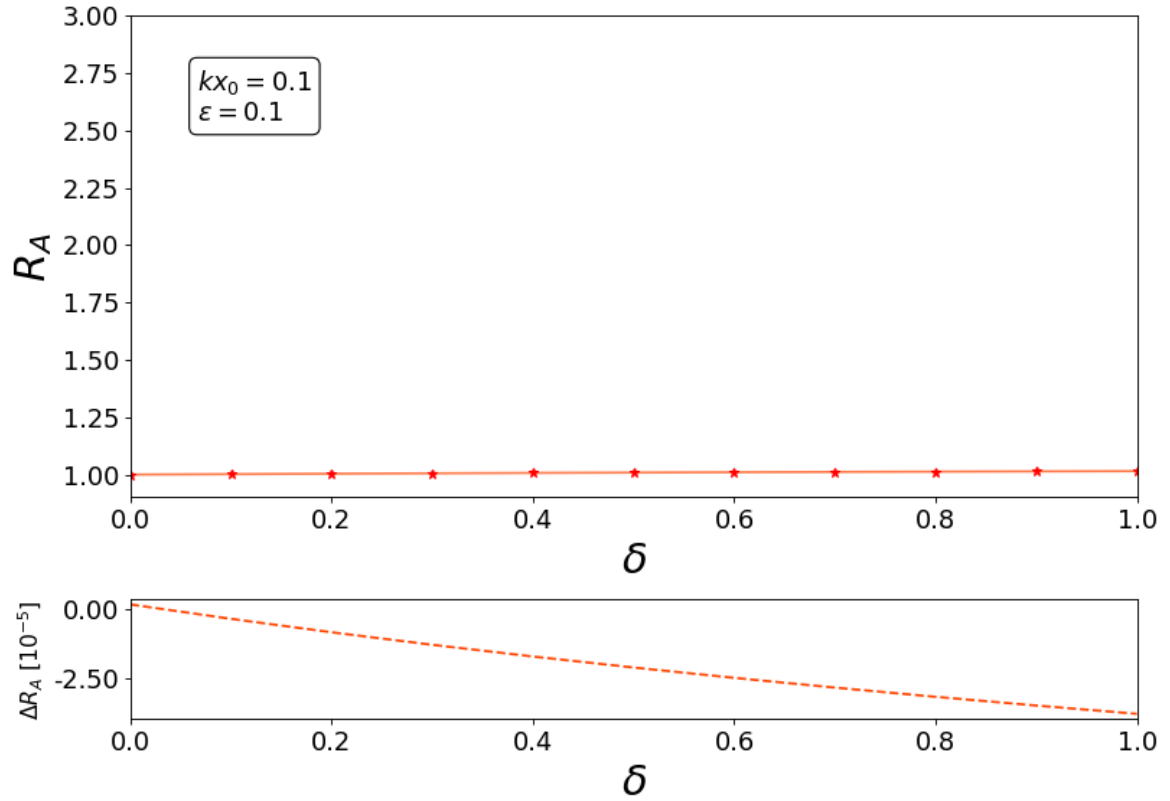


Figure 5.6: Dependence of the amplitude ratio on δ , for $\epsilon = 0.1$ and $kx_0 = 0.1$. for the quasi-kink mode.

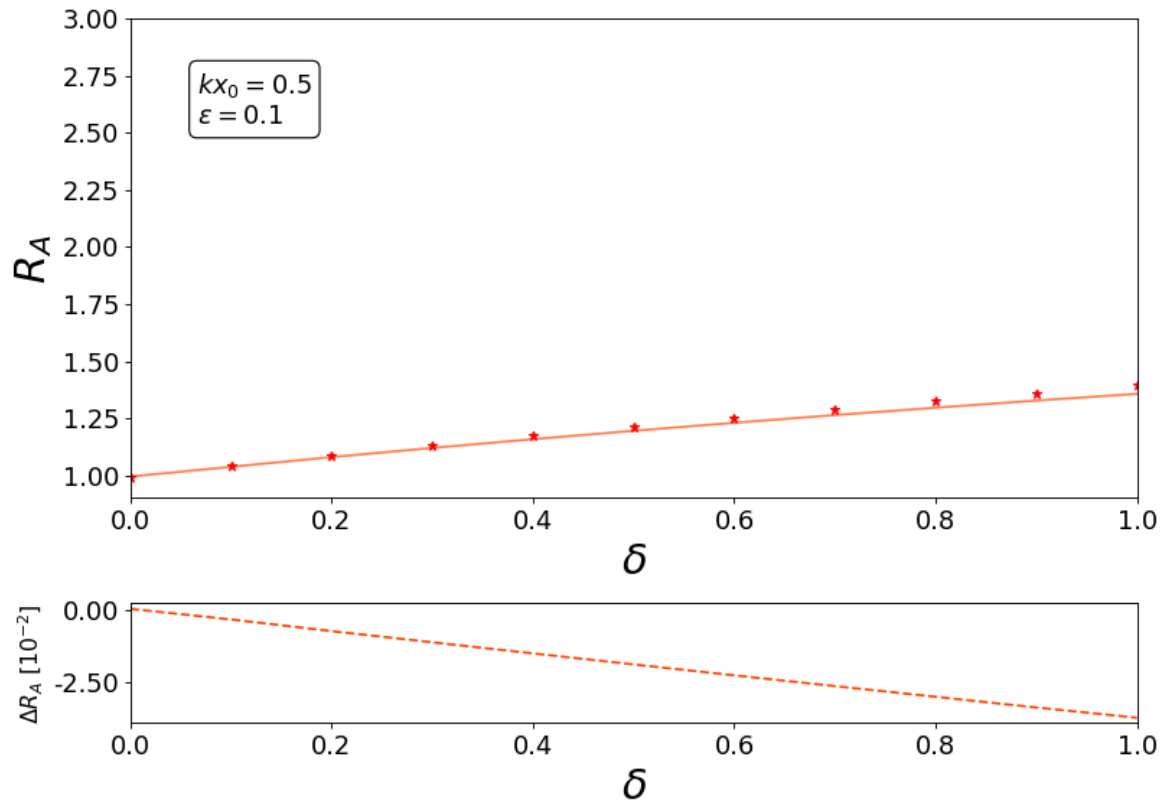


Figure 5.7: Dependence of the amplitude ratio on δ , for $\epsilon = 0.1$ and $kx_0 = 0.5$. for the quasi-kink mode.

to be the same:

$$\frac{\rho_0}{\rho_e} \frac{m_e}{(k^2 v_{Ae}^2 - \omega^2)} = -\frac{m_0}{(k^2 v_{A0}^2 - \omega^2)} \left(\frac{\tanh}{\coth} \right) \{m_0 x_0\}, \quad (5.43)$$

$$\frac{1}{2} \left[\frac{\rho_0}{\rho_1} \frac{m_1}{(k^2 v_{A1}^2 - \omega^2)} + \frac{\rho_0}{\rho_2} \frac{m_2}{(k^2 v_{A2}^2 - \omega^2)} \right] = -\frac{m_0}{(k^2 v_{A0}^2 - \omega^2)} \left(\frac{\tanh}{\coth} \right) \{m_0 x_0\}. \quad (5.44)$$

Here, quantities with index e refer to the symmetric system that the appropriate choice of asymmetric parameters is equivalent to. Since the right-hand sides in the two equations of (5.43 and eq:compare2) are the same, the left-hand sides should also be equal:

$$\frac{\rho_0}{\rho_e} \frac{m_e}{(k^2 v_{Ae}^2 - \omega^2)} = \frac{1}{2} \left[\frac{\rho_0}{\rho_1} \frac{m_1}{(k^2 v_{A1}^2 - \omega^2)} + \frac{\rho_0}{\rho_2} \frac{m_2}{(k^2 v_{A2}^2 - \omega^2)} \right]. \quad (5.45)$$

To ensure this equality, we require that the two terms on the right themselves should be equal:

$$\frac{\rho_0}{\rho_1} \frac{m_1}{(k^2 v_{A1}^2 - \omega^2)} = \frac{\rho_0}{\rho_2} \frac{m_2}{(k^2 v_{A2}^2 - \omega^2)} \quad (5.46)$$

This is a necessary and sufficient condition on the magnetic and plasma parameters in the external regions that result in quasi-symmetric eigenmodes of an asymmetric magnetic slab for a given set of wave parameters. To show that Equation (5.46) is a necessary condition, we first consider the case of quasi-sausage modes supported by an asymmetric magnetic slab. We use the requirement of equal but opposite amplitudes at the two interfaces for quasi-symmetric modes and state it in terms of the transverse velocity perturbation given by Equation (5.1), where we substitute the form of the coefficient B , from Equation (5.5).

$$\widehat{v}_x(-x_0) = -\widehat{v}_x(x_0), \quad (5.47)$$

$$\implies \left(\frac{\Lambda_0 C_0 + \Lambda_1 S_0}{\Lambda_0 S_0 + \Lambda_1 C_0} \right) C_0 - S_0 = - \left(\frac{\Lambda_0 C_0 + \Lambda_1 S_0}{\Lambda_0 S_0 + \Lambda_1 C_0} \right) C_0 - S_0, \quad (5.48)$$

$$\implies \Lambda_0 C_0 + \Lambda_1 S_0 = 0. \quad (5.49)$$

Similarly, taking the second expression for B (Equation 5.6), it may be shown that

$$\Lambda_0 C_0 + \Lambda_2 S_0 = 0. \quad (5.50)$$

Therefore, $\Lambda_1 = \Lambda_2$, which, after substituting in the appropriate expressions, is equivalent to Equation (5.46).

For symmetric-looking quasi-kink modes, we require that the velocity perturbation amplitudes from Equation (5.1) should be equal on the two slab boundaries. Substituting the first form of C from Equation (5.5) gives us

$$\widehat{v}_x(-x_0) = \widehat{v}_x(x_0), \quad (5.51)$$

$$\implies \left(C_0 - \frac{\Lambda_0 S_0 + \Lambda_1 C_0}{\Lambda_0 C_0 + \Lambda_1 S_0} \right) S_0 = \left(C_0 + \frac{\Lambda_0 S_0 + \Lambda_1 C_0}{\Lambda_0 C_0 + \Lambda_1 S_0} \right) S_0, \quad (5.52)$$

$$\implies \Lambda_0 S_0 + \Lambda_1 C_0 = 0, \quad (5.53)$$

while substituting C from Equation (5.22) leads to

$$\Lambda_0 S_0 + \Lambda_2 C_0 = 0. \quad (5.54)$$

Similarly to the case of quasi-sausage modes, this implies that $\Lambda_1 = \Lambda_2$ for quasi-symmetric quasi-kink modes, too, which is the concise form of Equation (5.46). To show that this equation is also a sufficient condition for the existence of quasi-symmetric modes, we consider an asymmetric magnetic slab with equilibrium parameters that satisfy this formula. Then the transverse velocity perturbation solution for quasi-sausage modes reduces to

$$\widehat{v}_x(x) = \begin{cases} A(\cosh m_1 x + \sinh m_1 x) & \text{if } x < -x_0, \\ C \sinh m_0 x & \text{if } |x| \leq x_0, \\ D(\cosh m_2 x - \sinh m_2 x) & \text{if } x > x_0, \end{cases} \quad (5.55)$$

with

$$A = \frac{-CS_0}{C_1 - S_1}, \quad D = \frac{CS_0}{C_2 - S_2}, \quad C \text{ is arbitrary.} \quad (5.56)$$

Here, the solution within the slab, $|x| \leq x_0$, is simply an odd function of x , and therefore has the property $\widehat{v}_x(-x_0) = -\widehat{v}_x(x_0)$, showing that Equation (5.46) is a sufficient condition. For quasi-kink modes the corresponding expressions simplify to

$$\widehat{v}_x(x) = \begin{cases} A(\cosh m_1 x + \sinh m_1 x) & \text{if } x < -x_0, \\ B \cosh m_0 x & \text{if } |x| \leq x_0, \\ D(\cosh m_2 x - \sinh m_2 x) & \text{if } x > x_0, \end{cases} \quad (5.57)$$

where

$$A = \frac{BC_0}{C_1 - S_1}, \quad D = \frac{BC_0}{C_2 - S_2}, \quad B \text{ is arbitrary.} \quad (5.58)$$

With these parameters, the solution inside the slab is an even function of the x -coordinate, concluding the proof that Equation (5.46) is a necessary and sufficient condition for the existence of quasi-symmetric modes in a magnetic slab, for both quasi-sausage and quasi-kink type oscillations.

So far, we have required that the magnitudes of the transverse velocity perturbation on the two interfaces should be equal for quasi-symmetric modes. If we further specify that the eigenfunction is fully symmetric, and so the penetration depth of perturbations in the external plasma has to be equal on either side of the slab, then the external parameters must also be equal, and the entire slab system is symmetric.

It is noteworthy that the condition (5.46) for quasi-symmetric oscillations of an asymmetric magnetic slab provides a relation between the external parameters on the two sides of the slab. This connection can be restated using Equation (2.3) in the following form:

$$\frac{(k^2 v_{A2}^2 - \omega^2) m_1}{(k^2 v_{A1}^2 - \omega^2) m_2} = \frac{\rho_1}{\rho_2} = \frac{c_2^2 + \frac{\gamma}{2} v_{A2}^2}{c_1^2 + \frac{\gamma}{2} v_{A1}^2}. \quad (5.59)$$

For the purposes of magneto-seismology, this means that if quasi-symmetric oscillations with a given angular frequency and wavenumber are detected, one of the external characteristic speeds can be determined as a function of the other three.

This, of course, means that (using the expressions of characteristic speeds), one unknown external magnetic field strength, density, pressure (or temperature) can also be determined as a function of the other five such quantities.

We can confirm this relationship between the external plasma and magnetic parameters using the definition of amplitude ratios as well. We start by considering the concise form of the decoupled dispersion relation for quasi-sausage (quasi-kink) modes, which is

$$\Lambda_0(\Lambda_1 + \Lambda_2) + 2\Lambda_1\Lambda_2 \left(\frac{\tanh \{m_0 x_0\}}{\coth \{m_0 x_0\}} \right) = 0. \quad (5.60)$$

By rearranging this equation, we obtain the following relation:

$$-\frac{\Lambda_1}{\Lambda_2} = \frac{\Lambda_0 + \Lambda_1 \left(\frac{\tanh \{m_0 x_0\}}{\coth \{m_0 x_0\}} \right)}{\Lambda_0 + \Lambda_2 \left(\frac{\tanh \{m_0 x_0\}}{\coth \{m_0 x_0\}} \right)}, \quad (5.61)$$

If we compare this with the amplitude ratio for quasi-sausage (Equation 5.15) and quasi-kink modes (Equation 5.27), we see that the right-hand side of Equation (5.61) is also the expression for the amplitude ratio of the two types of eigenmodes. To be more exact,

$$R_{A,saus} = -\frac{\Lambda_0 + \Lambda_1 \coth \{m_0 x_0\}}{\Lambda_0 + \Lambda_2 \coth \{m_0 x_0\}} = \frac{\Lambda_1}{\Lambda_2}, \text{ and} \quad (5.62)$$

$$R_{A,kink} = \frac{\Lambda_0 + \Lambda_1 \tanh \{m_0 x_0\}}{\Lambda_0 + \Lambda_2 \tanh \{m_0 x_0\}} = -\frac{\Lambda_1}{\Lambda_2}, \quad (5.63)$$

or, in short,

$$R_A = \pm \frac{\Lambda_1}{\Lambda_2} = \pm \frac{\rho_1 m_2 (k^2 v_{A1}^2 - \omega^2)}{\rho_2 m_1 (k^2 v_{A2}^2 - \omega^2)}, \quad (5.64)$$

where the positive sign corresponds to quasi-sausage modes, and the negative sign to quasi-kink modes. We also know that for the quasi-symmetric modes, the amplitudes of both the quasi-sausage and the quasi-kink waves will have the same magnitude at the two interfaces. Therefore, the amplitude ratios are $R_A = -1$ for these quasi-sausage modes, and $R_A = 1$ for the quasi-kink ones. Using this information, Equation (5.64) becomes

$$\frac{m_1 \rho_2}{m_2 \rho_1} = \frac{(k^2 v_{A1}^2 - \omega^2)}{(k^2 v_{A2}^2 - \omega^2)}, \quad (5.65)$$

which is exactly the condition we rearranged to obtain Equation (5.59) connecting the external parameters of an asymmetric slab system that supports quasi-symmetric oscillations.

5.3 Minimum perturbation shift

The second spatial magneto-seismology technique we describe here is one that describes the shift in the position of minimum wave power away from the centre of an asymmetric slab. As mentioned in Chapter 2, the position of the minimally perturbed surface for a symmetric sausage or kink mode lies at exactly the central axis

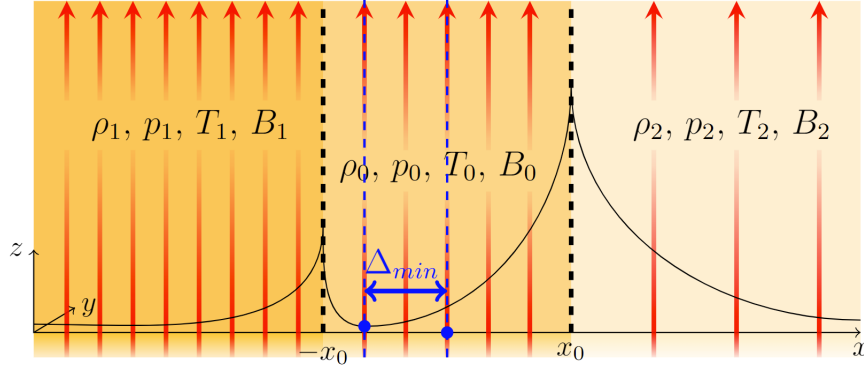


Figure 5.8: The principle of the minimum perturbation shift method. Figure courtesy of Allcock and Erdélyi (2018).

of the slab ($x = 0$). We define the minimum perturbation shift, Δ_{min} as the offset of the minimum wave power from the centre of the slab, as illustrated for a quasi-kink mode in Figure 5.8. The method of the minimum perturbation shift is exclusive to surface modes, which, as we have seen in Chapter 3, are significantly more sensitive to the external plasma parameters than body modes.

Body modes show a shift in the position of their nodes and anti-nodes under the effect of external asymmetries, however, this is expected to be a much smaller and therefore less easily observable quantity (see also Allcock and Erdélyi (2018)).

5.3.1 Quasi-sausage modes

For a symmetric slab system, the sausage modes leave the surface in the centre of the slab unperturbed. When density and/or magnetic asymmetry is introduced into the environment, the position of this surface is shifted away from the middle to a new x -coordinate can be found simply by setting the transverse velocity perturbation amplitude,

$$\hat{v}_x(x) = B \cosh m_0 x + C \sinh m_0 x = 0, \quad (5.66)$$

from which x can be expressed as

$$x = \frac{1}{m_0} \tanh^{-1} \left\{ -\frac{B}{C} \right\}, \quad (5.67)$$

where $|x| \leq x_0$. Using the equations describing the continuity of velocity and total pressure perturbations at the boundaries of the slab, the coefficient B can be expressed in two different forms described in Equations (5.5) and (5.6). Substituting this into Equation (5.67), the x -coordinate of the minimally perturbed surface, Δ_{min} becomes

$$\begin{aligned} \Delta_{min} &= \frac{1}{m_0} \tanh^{-1} \left\{ -\frac{\Lambda_0 C_0 + \Lambda_1 S_0}{\Lambda_0 S_0 + \Lambda_1 C_0} \right\} \\ &= \frac{1}{m_0} \tanh^{-1} \left\{ -\frac{\frac{\rho_0}{\rho_1} m_1 [k^2 v_{A0}^2 - \omega^2] + m_0 [k^2 v_{A1}^2 - \omega^2] \tau_0}{\frac{\rho_0}{\rho_1} m_1 [k^2 v_{A0}^2 - \omega^2] \tau_0 + m_0 [k^2 v_{A1}^2 - \omega^2]} \right\} \end{aligned} \quad (5.68)$$

In the thin-slab approximation, as we have stated before, $kx_0 \ll 1$, and so $m_0 x_0 \ll 1$. Then it is also true that the minimum perturbation shift is $\Delta_{min} < x_0$

and therefore $m_0\Delta_{min} \ll 1$. In this case, the hyperbolic tangent can be approximated by its argument, and Equation (5.68) can be rearranged to provide another estimate for the internal Alfvén speed as a function of the slab width, the minimum perturbation shift, the external parameters on one side of the slab, as well as the internal density and sound speed:

$$v_{A0}^2 = \frac{(k^2c_0^2 - \omega^2)x_0\Delta_{min} + c_0^2}{(k^2c_0^2 - \omega^2)(k^2x_0\Delta_{min} + 1)}\omega^2 - \frac{(x_0 + \Delta_{min})(k^2v_{A1}^2 - \omega^2)}{\rho_0/\rho_1m_1(k^2x_0\Delta_{min} + 1)}. \quad (5.69)$$

The minimum perturbation shift is ill-defined in the wide-slab limit, when $kx_0 \gg 1$, when the two interfaces oscillate basically independently of one another at their own eigenfrequency (see also Allcock and Erdélyi (2018)).

5.3.2 Quasi-kink modes

Symmetric kink modes are characterised by causing zero perturbation along the central surface of the slab, too. Asymmetric quasi-kink modes, on the other hand, only possess a surface of minimum perturbation (where the transverse velocity perturbation is smallest, but not necessarily zero), which is, again, shifted from the centre of the slab. The x -coordinate of this least perturbed surface can be determined by finding where the derivative of the transverse velocity perturbation is zero:

$$\frac{d\hat{v}_x(x)}{dx} = m_0 (B \sinh m_0x + C \cosh m_0x) = 0. \quad (5.70)$$

From this, the required x -coordinate can be expressed as

$$x = \frac{1}{m_0} \tanh^{-1} -\frac{C}{B} = \frac{1}{m_0} \coth^{-1} -\frac{B}{C}. \quad (5.71)$$

Now substituting the form of the C coefficients from Equations (5.21) and (5.22) into this expression give us the x -coordinate of the minimally perturbed surface, Δ_{min} as

$$\begin{aligned} \Delta_{min} &= \frac{1}{m_0} \coth^{-1} \left\{ -\frac{\Lambda_0C_0 + \Lambda_1S_0}{\Lambda_0S_0 + \Lambda_1C_0} \right\} \\ &= \frac{1}{m_0} \coth^{-1} \left\{ -\frac{\frac{\rho_0}{\rho_1}m_1 [k^2v_{A0}^2 - \omega^2] + m_0 [k^2v_{A1}^2 - \omega^2] \tau_0}{\frac{\rho_0}{\rho_1}m_1 [k^2v_{A0}^2 - \omega^2] \tau_0 + m_0 [k^2v_{A1}^2 - \omega^2]} \right\}. \end{aligned} \quad (5.72)$$

Applying the thin-slab approximation allows us to provide an estimate for the internal Alfvén speed in the case of the quasi-kink modes, too, following a similar reasoning as we used to obtain Equation (5.69) for quasi-sausage modes. Here, the internal Alfvén speed can be approximated as

$$v_{A0}^2 = \frac{-B \pm \sqrt{B^2 - 4AC}}{2A}, \quad (5.73)$$

where

$$\begin{aligned} A &= (k^2c_0^2 - \omega^2) \frac{\rho_0}{\rho_1} k^2 m_1 \Delta_{min}, \\ B &= (k^2c_0^2 - \omega^2) \left([k^2v_{A1}^2 - \omega^2] \left[\frac{\rho_0}{\rho_1} m_1 x_0 + 1 + k^2 \Delta_{min} x_0 \right] - \frac{\rho_0}{\rho_1} \omega^2 m_1 \Delta_{min} \right), \\ C &= (k^2v_{A1}^2 - \omega^2) \left(\left[\frac{\rho_0}{\rho_1} m_1 x_0 + 1 \right] c_0^2 + (k^2c_0^2 - \omega^2) \Delta_{min} x_0 \omega^2 \right). \end{aligned} \quad (5.74)$$

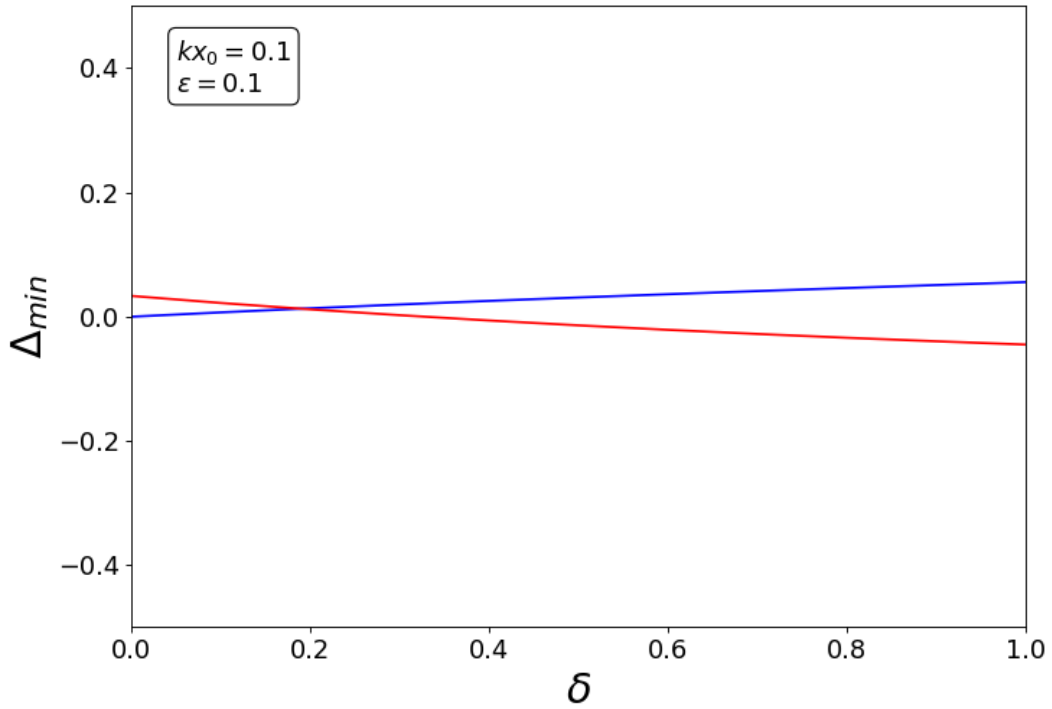


Figure 5.9: Dependence of the minimum perturbation shift of the quasi-sausage (blue) and quasi-kink mode (red) on δ , for $\epsilon = 0.1$ and $kx_0 = 0.1$.

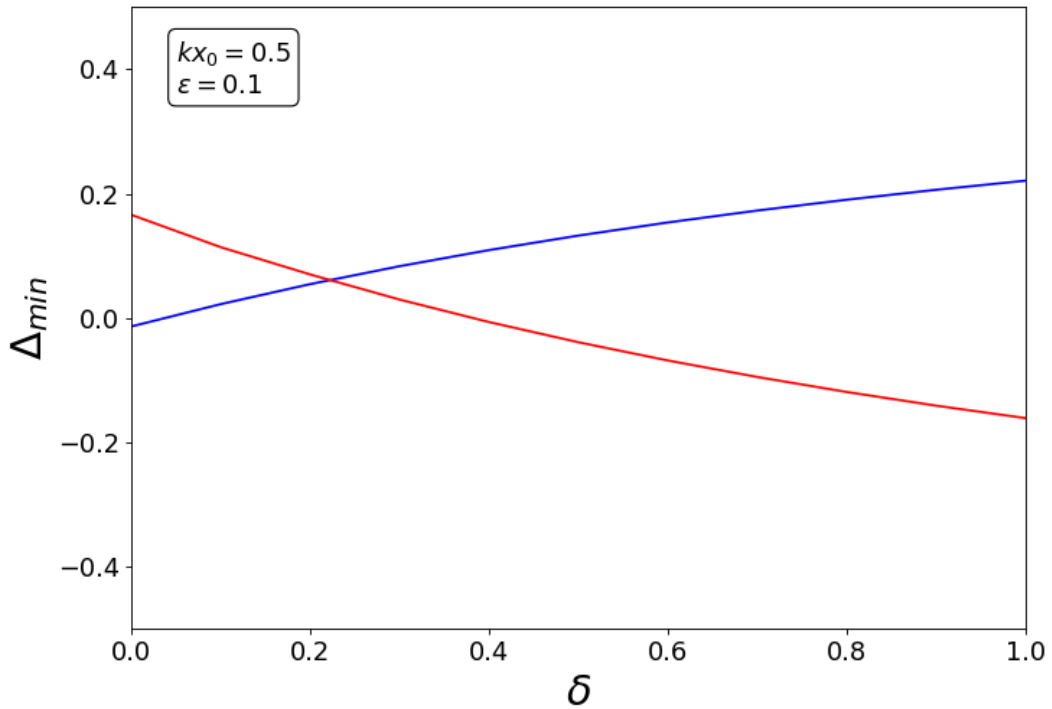


Figure 5.10: Dependence of the minimum perturbation shift of the quasi-sausage (blue) and quasi-kink mode (red) on δ , for $\epsilon = 0.1$ and $kx_0 = 0.5$.

The dependence of the minimum perturbation shift of the eigenmodes of an asymmetric magnetic slab system on the density asymmetry, δ , for a given fixed value of the magnetic asymmetry parameter, ε , and two different values of the dimensionless slab width, kx_0 , is displayed in Figures 5.9 and 5.10, for the same characteristic speeds as all other figures in this Chapter. Of course, this is only an illustrative example of the perturbation shift method, and the solutions might behave differently for an alternative characteristic speed ordering, which was beyond the scope of the current investigation.

5.3.3 The incompressible limit

One last approximation which is interesting to investigate is that of the system being filled with incompressible plasma. In this case, the sound speeds are unbounded, so that $m_j = k$, for $j=0, 1, 2$. Then the minimum perturbation shift for quasi-sausage (top) and quasi-kink modes (bottom) can be expressed as

$$\Delta_{min} = \frac{1}{k} \left(\frac{\tanh^{-1}}{\coth^{-1}} \right) \left\{ -\frac{\frac{\rho_0}{\rho_1} [v_{A0}^2 - \omega^2] + [k^2 v_{A1}^2 - \omega^2] \tanh[kx_0]}{\frac{\rho_0}{\rho_1} [v_{A0}^2 - \omega^2] \tanh[kx_0] + [k^2 v_{A1}^2 - \omega^2]} \right\}. \quad (5.75)$$

This can be rearranged to provide a relatively simple estimate for the internal Alfvén speed in terms of an external Alfvén speed and density ratio, as well as measurable wave and geometric parameters of the slab system:

$$v_{A0}^2 = \frac{\omega^2}{k^2} \left(1 - \frac{\rho_1 [k^2 v_{A1}^2 - \omega^2]}{\rho_0 \omega^2} \left(\frac{\tanh}{\coth} \right) \{ k [x_0 + \Delta_{min}] \} \right) \quad (5.76)$$

5.4 Conclusion

In this chapter, we provided an overview of solar magneto-seismologic tools developed for asymmetric slab systems which rely on the change in character occurring in the eigenmodes supported by a waveguide that is under the effect of its asymmetric environment. Both of the methods described here belong under the wider umbrella of spatial magneto-seismology, which, as opposed to temporal seismology methods, has had a shorter history and a recent “golden age” thanks to the rapidly increasing observational capabilities of solar telescopes.

We have provided a derivation for two SMS techniques introduced by Allcock and Erdélyi (2018) for an asymmetric magnetic slab placed in a non-magnetic environment, and we have generalised them to the case of a magnetic slab enclosed in an asymmetric magnetic environment. Section 5.2 describes the amplitude ratio method, which relies on the fact that the ratio of oscillation amplitudes at the two boundaries of the slab deviates from unity for general asymmetric eigenmodes. We provided an exact formula for the amplitude ratios of both quasi-sausage and quasi-kink modes, and then we proceeded to include some analytical approximations of these in order to make inversion possible and derive estimates for the Alfvén speed within the slab in terms of the rest of the equilibrium background parameters, as well as the frequencies and wavenumbers of oscillations.

We revisited the concept of quasi-symmetric oscillations introduced earlier in the mechanical analogy to an asymmetric slab system (see Section 2.3). We defined

these as perturbations of an asymmetric slab system that show symmetric oscillation amplitudes at the slab boundaries but may have different penetration depths in the asymmetric external media. We obtained a necessary and sufficient condition for the existence of quasi-symmetric modes and used it to describe a simple relation between the external plasma and magnetic parameters, which allows us to determine one external parameter in terms of the other three.

Finally, in Section 5.3, we generalised the minimum perturbation shift method to asymmetric slab systems including external magnetic asymmetry next to the density asymmetry. This allowed us to express new estimates for the Alfvén speed within the slab in the analytical limit of a thin or an incompressible slab. All of the Alfvén speed estimates we provided show dependence on an asymmetric spatial parameter of waves (either the amplitude ratio or the minimum perturbation shift), the wavenumber and frequency of the eigenmodes, the geometric extent of the slab, and at least one external density and Alfvén speed. It is often the case that multiple plasma or magnetic parameters of a solar atmospheric structure are unknown. However, if we use wave parameters measured in a solar atmospheric structure, we only have to provide an estimate for some of the unknown external parameters in order to use our formulae. If, however, we want to apply them to all possible eigenmodes supported by a given asymmetric slab system, an implicit dependence on the remaining external parameters also has to be taken into account when we solve the dispersion relation to obtain the angular frequencies and wavenumbers of trapped oscillations.

Chapter 6

Standing Waves in an Asymmetric Slab

Abstract

This Chapter describes standing waves in an asymmetric non-magnetic, and then in an asymmetric magnetic environment. The necessary boundary conditions for the existence of standing waves in both cases are studied, and then the appropriate dispersion relations are obtained. This is motivated by a solar magneto-seismological aim: once we find analytical solutions to the dispersion relation of standing waves, the frequencies and amplitudes of their different harmonics can be compared. These are measurable quantities in a solar context, and together with the rest of the waveguide parameters, they provide enough information to use our theoretical results to solve an inverse problem and estimate an unknown parameter of a solar waveguide. This Chapter is based on the results obtained in Oxley et al. (2020a) and Oxley et al. (2020b), which are two papers written as the result of a summer student project in the SURE scheme at the University of Sheffield, and the extended cooperation following the project. Calculations were performed and mutually checked by the co-authors in both papers. William Oxley was primarily responsible for the 2D-figures published in these papers and used as illustrations in this Chapter, while Noemi Zsámberger worked on the 3D-plots and their interactive versions available in the supplementary material. Furthermore, the author of this thesis was responsible for the Appendix of Oxley et al. (2020a) on the Rayleigh-Ritz theorem, which is included as Section 6.4 of this Chapter.

6.1 Chapter Introduction

We have described in the previous Chapters how MHD waves can provide us with a tool to diagnose solar atmospheric structures, and in Chapter 5 specifically, we provided tools to perform solar magneto-seismological studies. There, we focused on propagating waves in asymmetric magnetic slabs, in a non-magnetic external region (Allcock and Erdélyi, 2017) and with a magnetic external region (based on e.g. Zsámberger et al. (2018)). However observations have discovered a large range of standing waves in MHD waveguides (de Moortel, 2009), too. A review by Taroyan and Erdélyi (2009), as well as studies by Wang et al. (2007) and Wang (2011) discuss SMS applications of standing waves in the context of coronal loops included.

Standing waves in other solar features have also been examined. For example, prominence oscillations are a prime candidate both for the detection of standing waves and for the application of a Cartesian waveguide model (Oliver 2009; Arregui et al. 2012).

Motivated by these and further solar applications, the aim of the current Chapter is to build on the results of previous studies on propagating waves in asymmetric waveguides, and now focus on standing waves, along with the new SMS techniques they may be used to develop. In order to describe standing waves in an asymmetric slab system, we introduce a line-tying boundary condition, allowing the waves propagating in the slab to be reflected from these new boundaries, leading to interference and to the formation of standing waves.

In Section 6.2, we describe the equilibrium configuration and the boundary conditions for standing waves in an asymmetric slab embedded in a non-magnetic environment. Through a similar process to that followed in Allcock and Erdélyi (2017), we derive the dispersion relation for the harmonics of magneto-acoustic waves in the asymmetric slab waveguide. Next, we introduce the thin slab and weak asymmetry assumptions in order to make analytical progress. In Sections 6.3.1 and 6.3.2, we then calculate the frequencies and amplitudes of the harmonics of standing waves present in the system, to then proceed to introduce their ratios for purposes of magneto-seismology. In Section 6.3.3, the results are supplemented by numerical solutions for a chosen set of characteristic speeds and densities.

Next, in Section 6.5, the main steps of this process are repeated for a magnetic slab embedded in an asymmetric magnetic environment, so that our results may be further generalised. We apply similar boundary conditions as before to obtain the standing wave dispersion relation. Before we proceed, we restrict our investigation to isothermal plasmas and weak asymmetries. After these preparations, we obtain the expressions for the frequencies and amplitudes of the standing harmonics in Sections 6.5.4 and 6.5.5, in order to use their differences to infer values for an internal or external magnetic field strength in the system. We conclude the Chapter with a short discussion of the results.

6.2 The Slab in a Non-Magnetic Environment

We consider an asymmetric magnetic slab waveguide like the one set up by Allcock and Erdélyi (2017): a three-dimensional, inviscid, static, ideal plasma split into three regions in the x direction. This equilibrium configuration is shown in Figure 6.1, with all boundaries of the slab indicated by dashed lines. The slab has a finite width in the x -direction of $2x_0$, and a finite length of L in the z -direction (while it is still unbounded in the y -direction). The equilibrium magnetic field is given by $B(x)\hat{e}_z$, where

$$B(x) = \begin{cases} B_0 & \text{if } |x| \leq x_0 , \\ 0 & \text{if } |x| > x_0 , \end{cases} \quad (6.1)$$

and B_0 is constant. The equilibrium pressure, temperature and density are denoted p_j , T_j and ρ_j , respectively, with the index $j = 0$ inside the slab, $j = 1$ to the left, and $j = 2$ to the right of the slab. (A partial exception to this is the Alfvén speed inside the slab, which we simply denote by v_A in this subsection, as the external

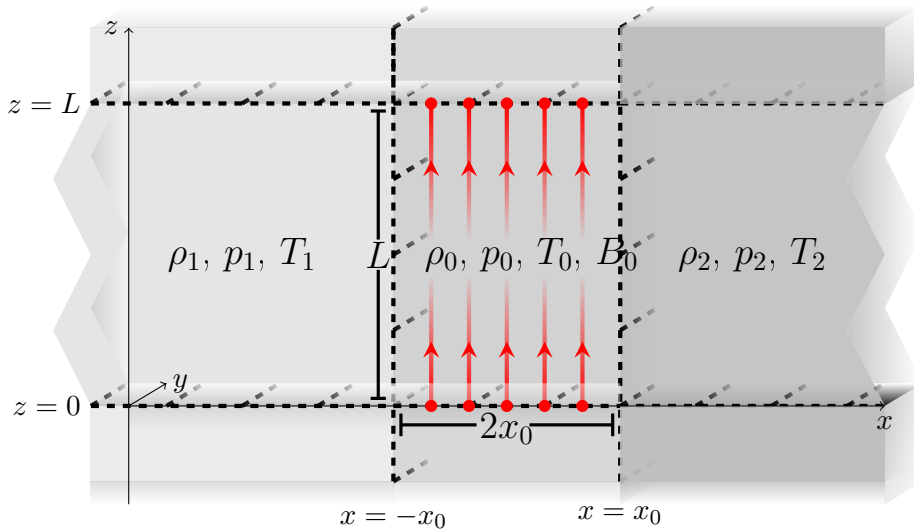


Figure 6.1: The equilibrium state inside ($|x| \leq x_0$) and outside of the magnetic slab ($x < -x_0$ and $x > x_0$), with the magnetic field lines indicated in red. The source of the Figure is: Oxley et al. (2020a).

Alfvén speeds are both zero.) As we would like to analyse the effect of asymmetry on standing waves first, we neglect the effects of gravity in this derivation.

In order to describe standing waves in this asymmetric waveguide, we have to set out some boundary conditions in the directions of structuring. In the x -direction, pressure balance must be maintained across the interfaces at $x = \pm x_0$:

$$p_1 = p_0 + \frac{B_0^2}{2\mu_0} = p_2. \quad (6.3)$$

This expression may be transformed to provide a relationship between the external sound speeds and densities:

$$c_1^2 \rho_1 = c_2^2 \rho_2. \quad (6.4)$$

In the z -direction, we must use different boundary conditions. Here, the aim is to allow the propagating waves supported by the slab system to be reflected at the endpoints (top and bottom boundaries in our illustration), causing them to interfere and form standing waves. Accordingly, we apply line-tying boundary conditions at $z = 0, L$. The conditions relevant to our study are that the x -component of the velocity perturbation, v_x , and the z -component of the magnetic field perturbation, b_z , are zero at $z = 0, L$. Additionally, we can also impose that the total pressure perturbation is also zero at $z = 0, L$. In summary:

$$\begin{aligned} v_x(z = 0) &= v_x(z = L) = 0, \\ b_z(z = 0) &= b_z(z = L) = 0, \\ p_T(z = 0) &= p_T(z = L) = 0. \end{aligned} \quad (6.5)$$

6.3 Derivation of the Dispersion Relation

The first steps of the process of deriving the dispersion relation for standing waves in an asymmetric slab are formally analogous to the derivation carried out by Allcock

and Erdélyi (2017), which is why we only highlight the differences in this subsection. The ideal MHD equations are linearised about a basic state, and plane-wave solutions are sought. To satisfy the line-tying boundary condition given by Equation (6.5), these now take the form

$$v_x = \hat{v}_x(x)e^{-i\omega t} \sin(kz), \quad v_z = \hat{v}_z(x)e^{-i\omega t} f(z), \quad p_T = \hat{p}_T(x)e^{-i\omega t} \sin(kz), \quad (6.6)$$

where f is an arbitrary function to be determined. The line-tying boundary conditions ($v_x(z=0) = v_x(z=L) = 0$) also provide a condition on k :

$$k = \frac{n\pi}{L}, \quad n \in \mathbb{Z}^+, \quad (6.7)$$

where $k = 0$ is excluded to ensure we consider non-trivial solutions. From the linearised momentum equation and the line-tying conditions, we find that the form of the arbitrary function as $f(z) = Q \cos(kz)$, for an arbitrary constant Q . The constant Q can be absorbed into, say, the $\hat{v}_z(x)$ velocity amplitude, and so we can simply take $f(z) = \cos(kz)$.

We proceed with substituting the now complete expressions for v_x and v_z into the linearised MHD equations, which leads us to formally the same governing equation that Allcock and Erdélyi (2017) found for propagating waves:

$$\frac{d^2 \hat{v}_x}{dx^2} - m_0^2 \hat{v}_x = 0, \quad \text{where} \quad m_0^2 = \frac{(k^2 c_0^2 - \omega^2)(k^2 v_A^2 - \omega^2)}{(k^2 c_T^2 - \omega^2)(c_0^2 + v_A^2)}, \quad c_T^2 = \frac{c_0^2 v_A^2}{c_0^2 + v_A^2}, \quad (6.8)$$

however, here, k can only take the values prescribed by Equation (6.7). The ODE (6.8) is valid inside the slab, while in the environmental regions,

$$\frac{d^2 \hat{v}_x}{dx^2} - m_j^2 \hat{v}_x = 0, \quad \text{with} \quad m_j^2 = k^2 - \frac{\omega^2}{c_j^2}, \quad \text{for} \quad j = 1, 2. \quad (6.9)$$

Matching solutions for Equations (6.8) and (6.9) and ensuring that the pressure and velocity continuity conditions are fulfilled, we recover formally the same dispersion relation which Allcock and Erdélyi (2017) provided for propagating waves in an asymmetric slab embedded in a non-magnetic environment:

$$\begin{aligned} & \omega^4 m_0^2 + \frac{\rho_0}{\rho_1} m_1 \frac{\rho_0}{\rho_2} m_2 (k^2 v_A^2 - \omega^2)^2 \\ & - \frac{1}{2} m_0 \omega^2 (k^2 v_A^2 - \omega^2) \left(\frac{\rho_0}{\rho_1} m_1 + \frac{\rho_0}{\rho_2} m_2 \right) (\tanh(m_0 x_0) + \coth(m_0 x_0)) = 0, \end{aligned} \quad (6.10)$$

but, as before, our wavenumbers k must fulfil the line-tying requirements.

As explained in the previous Chapters, asymmetric magnetic slab systems can support quasi-kink and quasi-sausage, slow or fast, surface or body modes. In this Chapter, we focus only on surface modes ($m_0^2 > 0$), as they are more sensitive to the effects of the external asymmetry. Furthermore, in the system we consider, only slow surface waves exist in the general case for any wavenumber (see also Allcock and Erdélyi (2017)).

With these restrictions in mind, we now simplify the dispersion relation using the thin slab and weak asymmetry assumptions. We introduce the notation

$$\varepsilon = \frac{x_0}{L}, \quad \text{and} \quad \rho_2 = \rho_1(1 + \delta), \quad \text{where} \quad \delta = \frac{\rho_2 - \rho_1}{\rho_1} > 0, \quad (6.11)$$

meaning we have taken $\rho_1 < \rho_2$. This can be done without a loss of generality, as a simple swap of all indices 1 and 2 would allow us to apply the results to a slab system where the right-hand-side density is the greater one.

The assumption of weak asymmetry assumption corresponds to $\delta \ll 1$, and we can use this to recover the form of the decoupled dispersion relation, Equation (22) from Allcock and Erdélyi (2017). Explicitly using the δ notation and neglecting second-order terms in the decoupled dispersion relation yields

$$(k^2 v_A^2 - \omega^2) \frac{\rho_0}{\rho_1} m_1 \left(2 - \delta \left[1 + \frac{\omega^2}{2(k^2 c_1^2 - \omega^2)} \right] \right) \approx 2\omega^2 m_0 \left(\frac{\tanh}{\coth} \right) (m_0 x_0). \quad (6.12)$$

In order to make further analytical progress, we study waves in the thin-slab limit, which corresponds to $\varepsilon \ll 1$. We use this to simplify Equation (6.10), by keeping only the leading terms in ε . Additionally, due to the line-tying boundary condition and Equation (6.7), $kx_0 = n\pi\varepsilon$, and therefore kx_0 can also be treated as a small quantity. With these considerations, the dispersion relation becomes

$$\begin{aligned} \omega^4 m_0^3 L \varepsilon + m_0 L \varepsilon \frac{\rho_0}{\rho_1} m_1 \frac{\rho_0}{\rho_2} m_2 (k^2 v_A^2 - \omega^2)^2 \\ - \frac{1}{2} m_0 \omega^2 (k^2 v_A^2 - \omega^2) \left(\frac{\rho_0}{\rho_1} m_1 + \frac{\rho_0}{\rho_2} m_2 \right) \approx 0. \end{aligned} \quad (6.13)$$

Based on numerical solutions found by Allcock and Erdélyi (2017), we assume that there is a slow quasi-sausage surface wave with $\omega^2 \approx k^2 c_T^2$. By substituting $\omega^2 \approx k^2 c_T^2 (1 - \alpha\varepsilon)$, we find the angular frequency of the standing wave harmonics (to leading order in ε) as

$$\omega_n^2 \approx \frac{n^2 \pi^2 c_T^2}{L^2} \left[1 - \varepsilon \frac{2n\pi c_0^4 c_1 \rho_1}{\rho_0 (c_0^2 + v_A^2)^2} \left(\frac{1 + \delta}{(1 + \delta)(c_1^2 - c_T^2)^{\frac{1}{2}} + (c_1^2 - c_T^2(1 + \delta))^{\frac{1}{2}}} \right) \right], \quad (6.14)$$

where we have used $k = n\pi/L$.

Based on Allcock and Erdélyi (2017) for propagating waves, we further assume that a slow quasi-kink surface wave with $\omega^2 \rightarrow 0$ exists as $\varepsilon \rightarrow 0$. Now using $\omega^2 \approx \beta\varepsilon$ and $k = n\pi/L$, we obtain the angular frequency of these standing quasi-kink mode harmonics as

$$\omega_n^2 \approx \varepsilon \frac{\rho_0 n^3 \pi^3 v_A^2}{L^2 \rho_1 (1 + \delta/2)}. \quad (6.15)$$

Figures 6.2 - 6.16 contain diagrams of the phase speed (ω_n/k) of the fundamental mode and the first harmonic, for both a range of ε and a range of δ , for a set of background parameters chosen for illustrative purposes only. Specific solar applications

would require further study and different characteristic speed ordering, although using e.g. prominence parameters, the pair of slow surface waves would still exist and show qualitatively the same behaviour in the thin- and wide-slab limits, even though the exact angular frequencies would of course be different.

Both Figures use a blue surface to depict the quasi-sausage waves (given by Equation 6.14), and a red one to show the quasi-kink waves (given by Equation 6.15). The equilibrium parameters used to prepare these Figures are: $c_0 = 5.00$, $v_A = 3.16$, $c_T = 2.67$, $c_1 = 4.71$, and $\rho_1/\rho_0 = 1.50$. Rotating animations of the 3D plots are available online as part of the publication Oxley et al. (2020a) and as supplementary material SM-A1 and SM-A2, respectively.

In these plots, we have the restriction that ε should be small (by assumption), but we have taken a large range of δ to show more general results. Cutoffs in the frequencies appear because some combinations of ε and δ yield an expression with $\omega^2 < 0$. Numerical solutions of the full dispersion relation in Allcock and Erdélyi (2017) show that the slab width-dependent eigenfrequencies of the two modes should not intersect. However, our Figure 6.16 shows an intersection for small values of ε , which make us conclude that there is a restriction on the valid ranges of ε and δ for which our approximation may be used. An interesting feature observable in these Figures is that the intersection occurs for narrower slabs in the case of the first harmonics than in that of the fundamental modes. This is due to the structure of the approximate solutions, which contain a cubic dependence on the harmonic mode number (n), making the phase speeds of the first harmonics change faster than those of the fundamental modes.

We also conduct a brief numerical investigation of the phase speeds of eigenmodes for a fixed slab width, contained in Figure 6.16. It appears from these diagrams that the phase speeds of the quasi-kink modes are less sensitive to changes in the asymmetry parameter δ than quasi-sausage modes, especially in the case of the first harmonics.

6.3.1 Frequencies of the Standing Harmonic Modes

In the following part of the Section, we keep both the thin slab and weak asymmetry approximations in place ($\varepsilon \ll 1$ and $\delta \ll 1$). We further assume that $\varepsilon, \delta \gg \varepsilon^2, \varepsilon\delta, \delta^2$. We use the decoupled dispersion relation to obtain analytical expressions for the frequencies and amplitudes of the standing modes, which requires us to keep ignoring any terms of order δ^2 .

After calculating the eigenfrequencies themselves, we also construct the ratio of the first harmonic to the fundamental mode, and the relative frequency difference due to the asymmetry. To highlight the influence of asymmetry on the standing oscillations, all three of these quantities can be compared with the corresponding counterpart where the system is symmetric. The study is motivated by the fact that the frequency ratio is a measurable quantity, which, once observations with the required resolution are available, allow this method to be utilised in SMS studies.

Eigenfrequencies of Quasi-sausage Modes

Using Equation (6.12) in the limit $\varepsilon \ll 1$, the dispersion relation for the quasi-sausage modes becomes

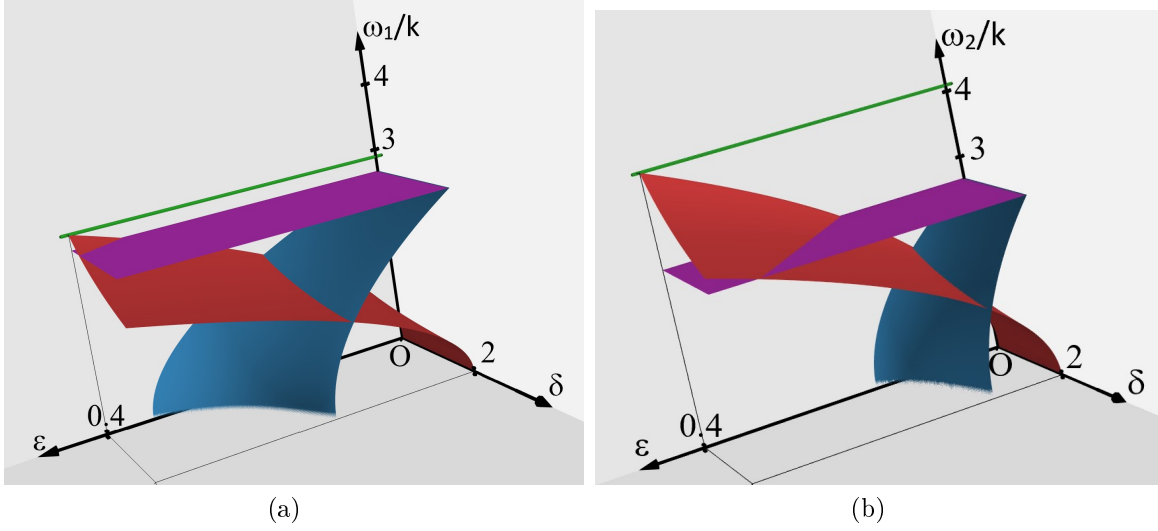


Figure 6.2: The phase speed for the fundamental mode ($n = 1$, panel (a)) and the first harmonic ($n = 2$, displayed in panel (b)) as a function of ϵ ranging from 0 to 0.4, and δ ranging from 0 to 2. The purple plane represents the value of c_T , and the green line illustrates the maximum plotted value, which is $\omega_1/k \approx 2.89$ in panel (a), and $\omega_2/k \approx 4.09$ in panel (b), by joining it to the vertical axis. The source of the Figure is: Oxley et al. (2020a).

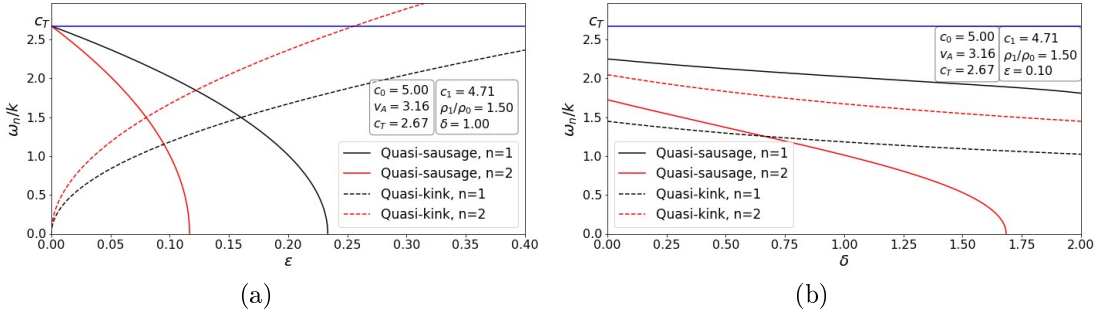


Figure 6.3: The phase speed for the fundamental mode ($n = 1$) and the first harmonic ($n = 2$) of the quasi-sausage waves (given by Equation 6.14) and the quasi-kink waves (given by Equation 6.15), **(a)** as a function of ϵ , with $\delta = 1$ fixed, and **(b)** as a function of δ , with $\epsilon = 0.1$ fixed. The source of the Figure is: Oxley et al. (2020a).

$$(k^2 v_A^2 - \omega^2) \left(\frac{\rho_0}{\rho_1} m_1 + \frac{\rho_0}{\rho_2} m_2 \right) \approx 2\omega^2 m_0^2 x_0 \left(1 - \frac{m_0^2 x_0^2}{3} \right). \quad (6.16)$$

Supposing that $\omega^2 \neq k^2 v_A^2$, we cancel a factor of $(k^2 v_A^2 - \omega^2)$ and use $\epsilon = x_0/L$ to get

$$\frac{\rho_0}{\rho_1} m_1 + \frac{\rho_0}{\rho_2} m_2 \approx 2\omega^2 \frac{(k^2 c_0^2 - \omega^2)}{(k^2 c_T^2 - \omega^2)(c_0^2 + v_A^2)} L \epsilon \left(1 - \frac{m_0^2 L^2 \epsilon^2}{3} \right). \quad (6.17)$$

Using the notation

$$\Pi = \frac{c_0^4 c_1 \rho_1}{\rho_0 (c_1^2 - c_T^2)^{\frac{1}{2}} (c_0^2 + v_A^2)^2}, \quad (6.18)$$

there is a solution of Equation (6.17) of the form

$$\begin{aligned} \omega_n^2 \approx & \frac{n^2 \pi^2 c_T^2}{L^2} \left[1 - \varepsilon n \pi \Pi \right. \\ & - \varepsilon^2 n^2 \pi^2 \left\{ \frac{\Pi^2 (c_0^2 + v_A^2)}{2c_0^4 (c_1^2 - c_T^2)} (4c_T^2 c_1^2 - 3c_T^4 + c_0^2 c_T^2 - 2c_0^2 c_1^2) - \frac{c_T^2}{3(c_0^2 + v_A^2)} \right\} \\ & \left. - \varepsilon \delta \frac{n \pi \Pi (2c_1^2 - c_T^2)}{4(c_1^2 - c_T^2)} \right]. \end{aligned} \quad (6.19)$$

Equation (6.19) is the frequency of the slow quasi-sausage mode in a thin and weakly asymmetric slab. This expression gives the eigenfrequency as approximately $k^2 c_T^2$, as expected, with additional terms due to the changing slab width and density asymmetry. The leading correction term is of order ε , and there is no density asymmetry factor present until second order in the small quantities.

A visualisation of the fundamental mode and the first harmonic for the standing quasi-sausage wave solution is provided in Figures 6.4 and 6.5. A diagram of the phase speed of the fundamental mode and the first harmonic are displayed in Figure 6.6. The phase speeds of the quasi-sausage and quasi-kink modes are included in the same figure.

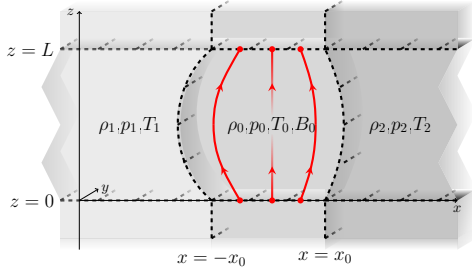


Figure 6.4: Illustration of a fundamental standing quasi-sausage mode oscillation in the asymmetric magnetic slab. The source of the Figure is: Oxley et al. (2020a).

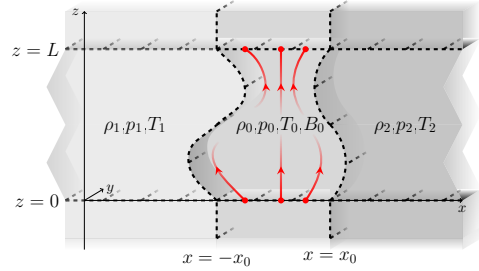


Figure 6.5: Same as Figure 6.4 but for the first harmonic. The source of the Figure is: Oxley et al. (2020a).

In Figure 6.6, the phase speed shows a quadratic dependence on the slab width parameter ε . As $\varepsilon \rightarrow 0$, the phase speeds of the quasi-sausage and quasi-kink solutions tend towards roughly the tube speed and zero, respectively, as expected. Panel (b) of Figure 6.6 shows that the phase speed does not change much as δ is changed, which we expected to see for two reasons. Firstly, due to the ranges of the small parameters we chose ($\delta \ll \varepsilon$), and secondly, because the density dependence only appeared in the solutions in second order terms.

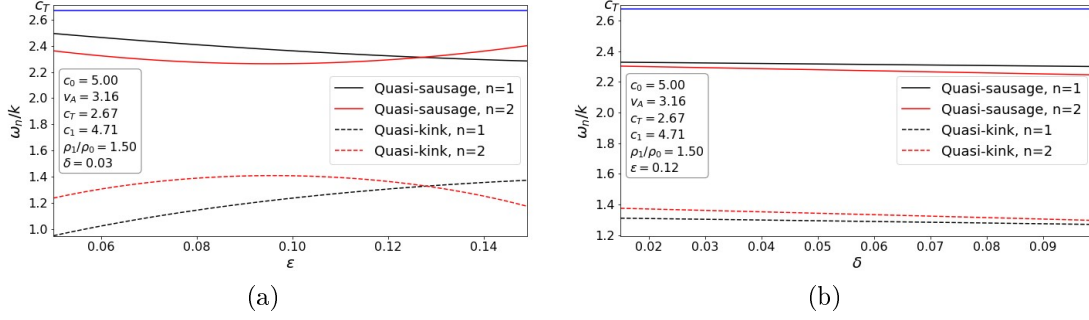


Figure 6.6: The phase speed for the fundamental mode ($n = 1$) and the first harmonic ($n = 2$) of the quasi-sausage waves (given by Equation 6.19) and the quasi-kink waves (given by Equation 6.24), **(a)** as a function of ε , with $\delta = 0.03$ fixed and **(b)** as a function of δ , with $\varepsilon = 0.12$ fixed. The source of the Figure is: Oxley et al. (2020a).

Frequency Ratio of the First Harmonic to the Fundamental Quasi-sausage Mode

We can use Equation (6.19) to construct the frequency ratio of the first harmonic to the fundamental mode as

$$\frac{\omega_2}{\omega_1} \approx 2 \left[1 - \varepsilon \frac{\pi \Pi}{2} - \varepsilon^2 \pi^2 \left[\frac{\Pi^2 (c_0^2 + v_A^2)}{8(c_1^2 - c_T^2)c_0^4} (19c_T^2 c_1^2 - 13c_T^4 + c_0^2 c_T^2 - 7c_0^2 c_1^2) - \frac{c_T^2}{2(c_0^2 + v_A^2)} \right] - \varepsilon \delta \frac{\pi \Pi (2c_1^2 - c_T^2)}{8(c_1^2 - c_T^2)} \right]. \quad (6.20)$$

We include plots of the frequency ratio for a range of ε and of δ , in Figure 6.7. The quasi-sausage and quasi-kink modes are included in the same figure. Figure 6.7 shows that the quasi-kink frequency ratio is more sensitive to changes in ε than its quasi-sausage counterpart. Pane (b) of Figure 6.7 shows no dependence of quasi-kink ratio on δ up to the order of terms we have included, whereas the quasi-sausage ratio shows a linear dependence on δ .

Relative Frequency Difference of Quasi-sausage Modes due to Asymmetry

We introduce the notation $\omega_{n,a}$ and $\omega_{n,s}$ for the eigenfrequencies of the mode n in the asymmetric and symmetric case, respectively. Using Equation (6.19) gives us $\omega_{n,a}^2$ directly, and substituting in $\delta = 0$ for the symmetric case gives $\omega_{n,s}^2$. Using Taylor expansions, we calculate the relative change in frequency due to the asymmetry, for the quasi-sausage waves as:

$$d_{\omega,S} = \left| \frac{\omega_{n,a} - \omega_{n,s}}{\omega_{n,s}} \right| \approx \varepsilon \delta \frac{n \pi \Pi (2c_1^2 - c_T^2)}{8(c_1^2 - c_T^2)}. \quad (6.21)$$

The dependence of the frequency difference of quasi-sausage and quasi-kink modes due to asymmetry on ε and δ is shown in Figure 6.8. Figure 6.8 shows that the frequency difference for the quasi-kink modes does not depend on ε , whereas the quasi-sausage modes show a linear dependence on ε , with an increase in the

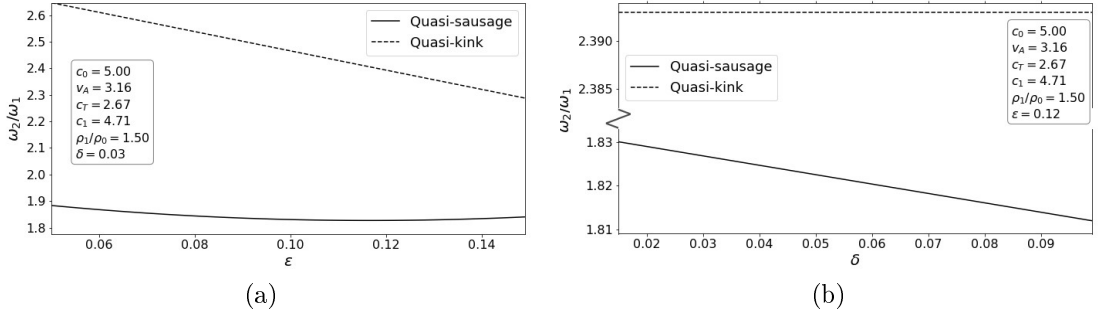


Figure 6.7: The ratio of the frequencies of the first harmonic to the fundamental mode of the quasi-sausage waves (given by Equation 6.20) and the quasi-kink waves (given by Equation 6.25), **(a)** as a function of ε , with $\delta = 0.03$ fixed, and **(b)** as a function of δ , with $\varepsilon = 0.12$ fixed. The source of the Figure is: Oxley et al. (2020a).

slope with increasing n . Panel (b) of Figure 6.8 shows that both the quasi-sausage and quasi-kink modes have a linear dependence on δ . Interestingly, the frequency difference for the quasi-kink modes does not depend on n , while increasing n results in increased slopes for the quasi-sausage modes.

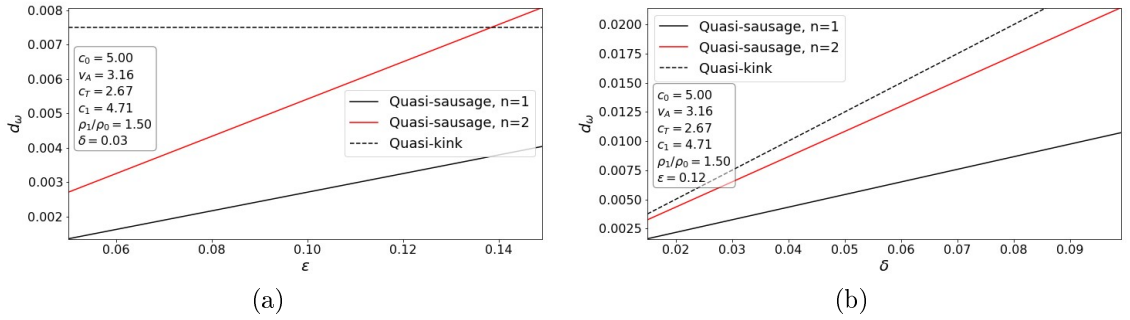


Figure 6.8: The frequency difference due to asymmetry of the fundamental mode ($n = 1$) and the first harmonic ($n = 2$) quasi-sausage waves (given by Equation 6.21) and the quasi-kink waves (given by Equation 6.26), **(a)** as a function of ε , with $\delta = 0.03$ fixed, and **(b)** as a function of δ , with $\varepsilon = 0.12$ fixed. The source of the Figure is: Oxley et al. (2020a).

Eigenfrequencies of Quasi-kink Modes in the Thin Slab and Weak Asymmetry Approximations

The decoupled dispersion relation (Equation 6.12) for quasi-kink modes in the thin-slab limit ($\varepsilon \ll 1$) becomes

$$(k^2 v_A^2 - \omega^2) \left(\frac{\rho_0}{\rho_1} m_1 + \frac{\rho_0}{\rho_2} m_2 \right) \approx 2 \frac{\omega^2}{x_0}. \quad (6.22)$$

After substituting $\varepsilon = \frac{x_0}{L}$ into this relation and rearranging, we obtain

$$L\varepsilon (k^2 v_A^2 - \omega^2) \left(\frac{\rho_0}{\rho_1} m_1 + \frac{\rho_0}{\rho_2} m_2 \right) \approx 2\omega^2. \quad (6.23)$$

In the thin-slab and weak asymmetry approximations, a slow quasi-kink surface mode solution to Equation (6.23) exists with angular frequency

$$\omega_n^2 \approx \varepsilon \frac{\rho_0 n^3 \pi^3 v_A^2}{2L^2 \rho_1} \left(2 - (n\pi\varepsilon) \frac{\rho_0}{\rho_1} \left(2 + \frac{v_A^2}{c_1^2} \right) - \delta \right). \quad (6.24)$$

This eigenfrequency tends towards zero as the slab becomes thinner, as all terms are proportional to ε . However, no δ -dependence appears up to second order in the small quantities. Figures 6.9 and 6.10 illustrate the fundamental mode and the first harmonic of the standing quasi-kink waves, respectively. Plots of the phase speeds corresponding to the frequencies given in Equation (6.24) have already been provided in Figure 6.6 in the section on quasi-sausage modes.

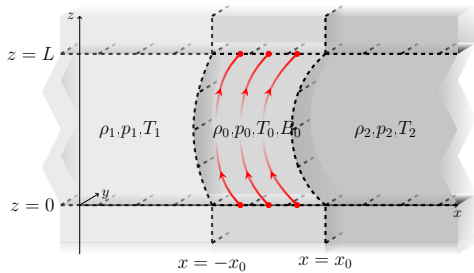


Figure 6.9: Illustration of a fundamental standing quasi-kink mode oscillation in the asymmetric magnetic slab. The source of the Figure is: Oxley et al. (2020a).

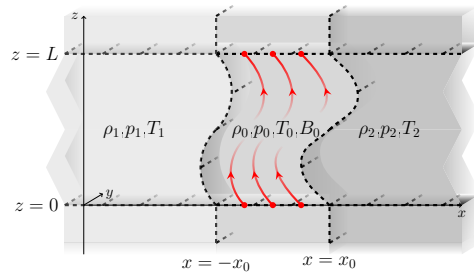


Figure 6.10: Same as Figure 6.9 but for the first harmonic. The source of the Figure is: Oxley et al. (2020a).

Frequency Ratio of the First Harmonic to the Fundamental Quasi-kink Mode

Using the frequencies from Equation (6.24), we construct the frequency ratio of the first harmonic to the fundamental mode as

$$\frac{\omega_2}{\omega_1} \approx 2\sqrt{2} \left(1 - \varepsilon \frac{\pi \rho_0}{4\rho_1} \left(2 + \frac{v_A^2}{c_1^2} \right) \right), \quad (6.25)$$

which has been plotted along with its quasi-sausage counterpart in Figure 6.7.

Relative Frequency Difference of Quasi-kink Modes due to Asymmetry

Again, we introduce $\omega_{n,a}$ and $\omega_{n,s}$ to denote the frequency in the asymmetric and symmetric case, respectively. Equation (6.24) gives us $\omega_{n,a}^2$ directly, and substituting in $\delta = 0$ gives $\omega_{n,s}^2$ for the symmetric case. With these considerations, the relative change in frequency due to the asymmetry for the quasi-kink waves becomes (to first order):

$$d_{\omega,K} = \left| \frac{\omega_{n,a} - \omega_{n,s}}{\omega_{n,s}} \right| \approx \frac{\delta}{4}. \quad (6.26)$$

Diagrams of this frequency difference have been included in Figure 6.8 and, together with the discussion on quasi-sausage modes.

6.3.2 Amplitudes of the Standing Harmonic Modes

Beyond the frequencies, the amplitudes of the eigenoscillations can also provide useful information about the standing harmonic modes, as well as about the effects of asymmetry. In this subsection, we define and (to leading order in ε and δ) calculate the following quantities in order to prepare tool of SMS applications:

- the relative difference in amplitude between the two sides of the slab (denoted $R_{S,1}$ for the quasi-sausage and $R_{K,1}$ for the quasi-kink modes),
- the relative amplitude difference compared to the symmetric slab (denoted $R_{S,2}$ for the quasi-sausage and $R_{K,2}$ for the quasi-kink modes).

Similarly to the process we followed in the part about frequency differences, for this subsection, we introduce the notation $\hat{v}_{x,a}$ for the velocity perturbation in the asymmetric case, and $\hat{v}_{x,s}$ for the velocity perturbation in the symmetric case. We will use the displacement perturbation $\hat{\xi}_x(x) = i\hat{v}_x(x)/\omega$, to define $\hat{\xi}_{x,a}$ and $\hat{\xi}_{x,s}$ analogously to the velocity perturbations.

Relative Amplitude Difference Between the Two Sides of the Slab for Quasi-sausage Modes

For the quasi-sausage modes, $\hat{v}_x(x_0)$ and $\hat{v}_x(-x_0)$ (as well as $\hat{\xi}_x(x_0)$ and $\hat{\xi}_x(-x_0)$) will have opposite signs, so the quantity we are interested in is

$$R_{S,1} = \left| \frac{\hat{\xi}_x(x_0) + \hat{\xi}_x(-x_0)}{\hat{\xi}_x(-x_0)} \right| = \left| \frac{\hat{v}_x(x_0) + \hat{v}_x(-x_0)}{\hat{v}_x(-x_0)} \right|, \quad (6.27)$$

which reduces to zero in the symmetric case. Substituting in the appropriate velocity perturbations at the slab boundaries, for the asymmetric case, we obtain

$$R_{S,1} = \left| \frac{m_0\omega^2(\rho_2m_1 - \rho_1m_2)}{m_0m_1\omega^2\rho_2 + \rho_0m_2m_1(\omega^2 - k^2v_A^2)\tanh(m_0x_0)} \right|. \quad (6.28)$$

From here, using Taylor expansions and the eigenfrequency given by Equation (6.19), we find that the amplitude difference is

$$R_{S,1} \approx \delta \frac{2c_1^2 - c_T^2}{2(c_1^2 - c_T^2)}. \quad (6.29)$$

The relative amplitude difference between the two sides of the slab is shown as a function of ε and δ in Figure 6.11. Once again, the same figures display the quasi-sausage and quasi-kink modes. From Figure 6.11, we can see that the quasi-sausage amplitude difference between the two sides of the slab does not depend on ε , while the quasi-kink amplitude difference follows a quadratic dependence. Panel (b) of Figure 6.11 shows that for both the quasi-sausage and quasi-kink modes, the amplitude difference between the two sides of the slab has a linear relationship with δ .

From Equation (6.29), we can obtain an approximation for the internal Alfvén speed of the slab as

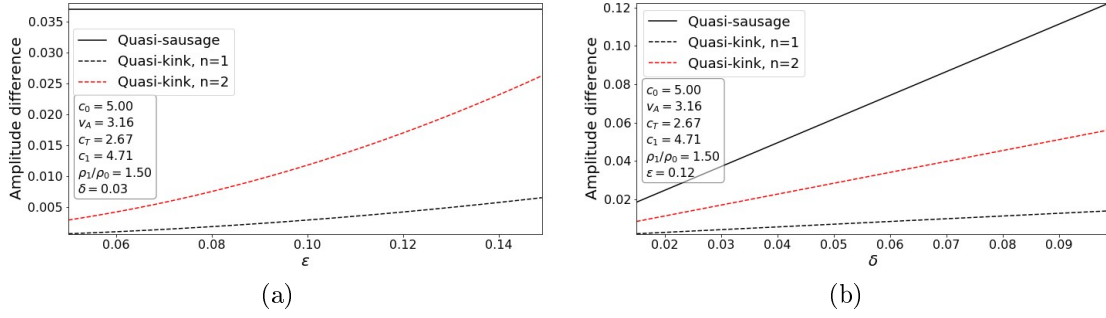


Figure 6.11: The amplitude difference between the two sides of the slab for the quasi-sausage waves (given by Equation 6.29) and both the fundamental mode ($n = 1$) and the first harmonic ($n = 2$) quasi-kink waves (given by Equation 6.35), **(a)** as a function of ε , with $\delta = 0.03$ fixed, and **(b)** as a function of δ , with $\varepsilon = 0.12$ fixed. The source of the Figure is: Oxley et al. (2020a).

$$v_A^2 \approx \frac{2(R_{S,1} - \delta)c_1^2 c_0^2}{c_0^2(2R_{S,1} - \delta) - 2c_1^2(R_{S,1} - \delta)}. \quad (6.30)$$

As the Alfvén speed is directly related to the magnetic field strength, observing the amplitude difference $R_{S,1}$ and measuring the densities and sound speeds in the slab system will allow us to use this result to determine an approximate value of the magnetic field strength B_0 , which might not be possible to do through direct measurements.

Relative Amplitude Difference Compared to the Symmetric Slab for Quasi-sausage Modes

The quasi-sausage mode has its maximum amplitude on the side of the slab with smaller external density (Allcock and Erdélyi, 2017), and as in our study, $\rho_1 < \rho_2$, this happens at $x = -x_0$ (also shown in Figures 6.4 and 6.5). We can then express $R_{S,2}$ as

$$R_{S,2} = \left| \frac{\hat{\xi}_{x,a}(-x_0) - \hat{\xi}_{x,s}(-x_0)}{\hat{\xi}_{x,s}(-x_0)} \right| = \left| \frac{\hat{v}_{x,a}(-x_0) - \hat{v}_{x,s}(-x_0)}{\hat{v}_{x,s}(-x_0)} \right|. \quad (6.31)$$

Through substitutions similar to the ones applied in the previous subsection, we can calculate this quantity as

$$R_{S,2} \approx \delta \frac{2c_1^2 - c_T^2}{4(c_1^2 - c_T^2)}. \quad (6.32)$$

$R_{S,2}$ gives us the relative amplitude difference compared to the symmetric slab for quasi-sausage modes. As we will see, this result largely agrees to the one obtained for quasi-kink modes, with the only difference being a factor of two.

Relative Amplitude Difference Between the Two Sides of the Slab for Quasi-kink Modes

For the quasi-kink modes, $\hat{v}_x(x_0)$ and $\hat{v}_x(-x_0)$ will have the same sign, so the relative amplitude difference can be calculated as

$$R_{K,1} = \left| \frac{\hat{\xi}_x(x_0) - \hat{\xi}_x(-x_0)}{\hat{\xi}_x(-x_0)} \right| = \left| \frac{\hat{v}_x(x_0) - \hat{v}_x(-x_0)}{\hat{v}_x(-x_0)} \right|. \quad (6.33)$$

This can also be written as

$$R_{K,1} = \left| \frac{m_0 \omega^2 (\rho_2 m_1 - \rho_1 m_2) \tanh(m_0 x_0)}{\rho_0 m_2 m_1 (k^2 v_A^2 - \omega^2) - \omega^2 \rho_2 m_1 m_0 \tanh(m_0 x_0)} \right|. \quad (6.34)$$

Using Taylor expansions, substituting $k = n\pi/L$ and $\varepsilon = x_0/L$, as well as the frequency given by Equation (6.24), we find

$$R_{K,1} \approx \delta \varepsilon^2 n^2 \pi^2. \quad (6.35)$$

This quantity has been plotted in Figure 6.11 along with its quasi-sausage counterpart.

Relative Amplitude Difference of Quasi-Kink Modes Compared to the Symmetric Slab

The maximum amplitude for the quasi-kink mode falls on the side of the slab with larger external density (Allcock and Erdélyi, 2017). We have $\rho_1 < \rho_2$, so this happens at $x = x_0$ (as shown in Figures 6.9 and 6.10). We can then write down an equation for the relative amplitude difference, $R_{K,2}$:

$$R_{K,2} = \left| \frac{\hat{\xi}_{x,a}(x_0) - \hat{\xi}_{x,s}(x_0)}{\hat{\xi}_{x,s}(x_0)} \right| = \left| \frac{\hat{v}_{x,a}(x_0) - \hat{v}_{x,s}(x_0)}{\hat{v}_{x,s}(x_0)} \right|. \quad (6.36)$$

In terms of the small parameters ε and δ , this becomes

$$R_{K,2} \approx \delta \varepsilon^2 \frac{n^2 \pi^2}{2}. \quad (6.37)$$

This is the relative amplitude difference of quasi-kink modes compared to the symmetric slab, which is qualitatively very similar to the result obtained for quasi-sausage modes.

6.3.3 Numerical Solutions of the Dispersion Relation

Although we had to restrict our investigation to weakly asymmetric thin slabs in the interest of analytical tractability, in the current subsection, we provide numerical solutions to the full dispersion relation for standing waves for a wider range of parameters. We proceed to compare these results to those obtained from our analytical approximations in order to determine what ranges of the small parameters ε and δ can be considered small enough for the analytical solutions to give accurate results

The phase speeds of the quasi-sausage and quasi-kink fundamental modes are shown in Figure 6.12. We used the following equilibrium parameters to obtain these results: $c_0 = 5.00$, $v_A = 3.16$, $c_T = 2.67$, $c_1 = 4.71$, and $\rho_1/\rho_0 = 1.50$. Rotating animations of the 3D plots are available online as part of the publication Oxley et al. (2020a) and as supplementary material SM-C1 and SM-C2, respectively.

In Figure 6.12, the lighter blue coloured (bottom) surface is calculated using Equation (6.14), while the darker blue coloured (top) surface comes from using numerical methods to solve the asymmetric dispersion relation given by Equation (6.10). Similarly, in panel (b) of Figure 6.12, the light red (top) surface is created by using Equation (6.15), while the darker red (bottom) surface stems from numerically solving the dispersion relation given by Equation (6.10).

For the quasi-sausage mode, the decreasing of either δ or ε decreases the size of the gap between the two (approximate and exact solutions) surfaces. Consequently, if we aim to satisfy $\delta \ll \varepsilon$ (which we used for the illustrations in the analytical frequency calculations), we are justified in taking a combination of ε and δ where $0.01 < \delta < 0.1$ and ε is as large as $\varepsilon \approx 0.19$. For these limits, we allowed a maximum percentage difference between the values of the two surfaces of approximately 20%. This was calculated by taking the difference between the values on the two surfaces, and dividing by the value on the larger surface.

For the quasi-kink mode, decreasing δ increases the size of the gap between the two surfaces. However, decreasing ε decreases the size of the gap between the two surfaces. If we again aim to satisfy $\delta \ll \varepsilon$, then we can take $0.01 < \delta < 0.1$ and ε as large as $\varepsilon \approx 0.19$. Within these ranges, our analytical results provide good accuracy for the fundamental modes. Although the solution surfaces would be qualitatively similar for the first harmonics, the limits of the small parameters corresponding to the same percentage difference might be different.

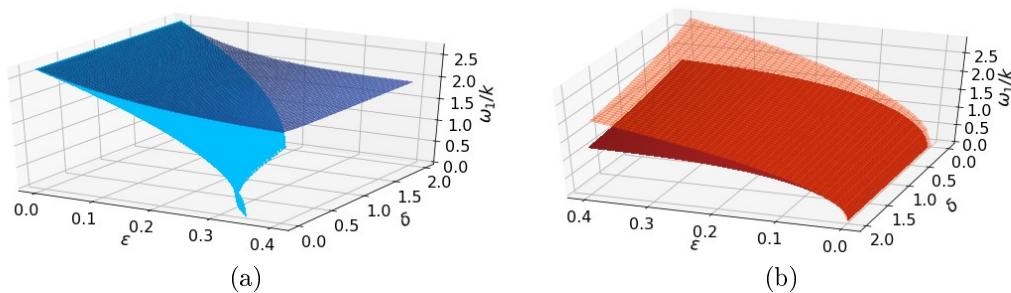


Figure 6.12: (a) The phase speed for the fundamental mode ($n = 1$) of the quasi-sausage waves as a function of ε and δ . Panel (b) displays the same, but for the quasi-kink mode. The source of the Figure is: Oxley et al. (2020a).

6.4 The Rayleigh-Ritz Technique

We defined the frequency difference due to asymmetry, and the amplitude difference compared to the symmetric slab with the aim of making a comparison between the eigenfrequencies and the eigenfunctions of the slab system. The Rayleigh-Ritz Technique predicts that eigenvalues will be less sensitive to perturbations in a system than eigenvectors. By considering the asymmetry as a perturbation to the symmetric slab model, accordingly, we expect the frequency difference due to asymmetry (eigenfrequencies) to have a higher order sensitivity when compared with the amplitude difference due to asymmetry (eigenfunctions).

This subsection reiterates the summary of the Rayleigh-Ritz technique provided in the Appendix of Oxley et al. (2020a). Following the definitions and the derivation

set out in Chapter 27 of Schnack (2009), we introduce $\boldsymbol{\xi}_i, i = 0, 1, 2, \dots$ as the eigenvectors of the ideal linear MHD force operator, $F\{\boldsymbol{\xi}_i\}$, which therefore satisfy the equation $F\{\boldsymbol{\xi}_i\} = -\rho_0\omega_i^2\boldsymbol{\xi}_i$. The eigenvalues $\omega_i^2, i = 0, 1, 2, \dots$ are ordered such that $\omega_0 < \omega_1 < \omega_2 \dots$ i.e., ω_0 could be the sausage or kink eigenfrequency of a symmetric slab MHD waveguide.

If the eigenvector $\boldsymbol{\xi}_0$ is known, the corresponding eigenfrequency can be determined from the kinetic energy, K_0 , and the change in potential energy, δW_0 , of the system that results from the displacement $\boldsymbol{\xi}_0$ as

$$\omega_0^2 = \frac{\delta W_0\{\boldsymbol{\xi}_0^*, \boldsymbol{\xi}_0\}}{K_0\{\boldsymbol{\xi}_0^*, \boldsymbol{\xi}_0\}}, \quad (6.38)$$

Here, the following quantities were introduced:

$$\begin{aligned} K_0\{\boldsymbol{\xi}_0^*, \boldsymbol{\xi}_0\} &= \frac{1}{2} \int \rho_0 \boldsymbol{\xi}_0^* \cdot \boldsymbol{\xi}_0 dV, \\ \delta W_0\{\boldsymbol{\xi}_0^*, \boldsymbol{\xi}_0\} &= -\frac{1}{2} \int \boldsymbol{\xi}_0^* \cdot F\{\boldsymbol{\xi}_0\} dV = \omega_0^2 K_0\{\boldsymbol{\xi}_0^*, \boldsymbol{\xi}_0\}, \end{aligned} \quad (6.39)$$

and * denotes the complex conjugate (see also Equations (22.7), (22.21), and (25.12)-(25.16) in Schnack (2009)).

If we perturb $\boldsymbol{\xi}_0$, by introducing a (weakly) asymmetric environment in the slab MHD waveguide, we can write the perturbed eigenvector $\boldsymbol{\xi}$ as

$$\boldsymbol{\xi} = \boldsymbol{\xi}_0 + \delta\boldsymbol{\xi}, \quad (6.40)$$

where $\delta\boldsymbol{\xi}$ is the change caused by the linear perturbation. By definition, the perturbation $\delta\boldsymbol{\xi}$ is orthogonal to (i.e., has no projection along) the unperturbed eigenvector $\boldsymbol{\xi}_0$ (it contains all the parts of $\boldsymbol{\xi}$ that differ from $\boldsymbol{\xi}_0$), so that we can write

$$\boldsymbol{\xi} = \boldsymbol{\xi}_0 + \sum_{i=1}^{\infty} a_i \boldsymbol{\xi}_i, \quad (6.41)$$

where $i = 0$ has been excluded from the summation. We now want to estimate the perturbed eigenvalue, taking into account the energy contribution of the added asymmetry. We may calculate this as

$$\omega^2 = \frac{\delta W\{\boldsymbol{\xi}_0^* + \delta\boldsymbol{\xi}^*, \boldsymbol{\xi}_0 + \delta\boldsymbol{\xi}\}}{K\{\boldsymbol{\xi}_0^* + \delta\boldsymbol{\xi}^*, \boldsymbol{\xi}_0 + \delta\boldsymbol{\xi}\}}. \quad (6.42)$$

We expand the new kinetic and potential energies corresponding to the perturbed state as

$$\begin{aligned} \delta W\{\boldsymbol{\xi}_0^* + \delta\boldsymbol{\xi}^*, \boldsymbol{\xi}_0 + \delta\boldsymbol{\xi}\} &= \delta W\{\boldsymbol{\xi}_0^*, \boldsymbol{\xi}_0\} + \delta W\{\boldsymbol{\xi}_0^*, \delta\boldsymbol{\xi}\} \\ &\quad + \delta W\{\delta\boldsymbol{\xi}^*, \boldsymbol{\xi}_0\} + \delta W\{\delta\boldsymbol{\xi}^*, \delta\boldsymbol{\xi}\}, \end{aligned} \quad (6.43)$$

and

$$\begin{aligned} K\{\boldsymbol{\xi}_0^* + \delta\boldsymbol{\xi}^*, \boldsymbol{\xi}_0 + \delta\boldsymbol{\xi}\} &= K\{\boldsymbol{\xi}_0^*, \boldsymbol{\xi}_0\} + K\{\boldsymbol{\xi}_0^*, \delta\boldsymbol{\xi}\} \\ &\quad + K\{\delta\boldsymbol{\xi}^*, \boldsymbol{\xi}_0\} + K\{\delta\boldsymbol{\xi}^*, \delta\boldsymbol{\xi}\}. \end{aligned} \quad (6.44)$$

The second and third terms on the right-hand-side of Equation (6.43) are equal to one another due to the self-adjoint nature of F . Furthermore, they are both equal to zero because of the orthogonality of the eigenvectors. Similar considerations can be made for Equation (6.44). Applying the definitions from Equations (6.39) to the rest of the terms of Equations (6.43) and (6.44), we obtain

$$\begin{aligned}\delta W\{\boldsymbol{\xi}_0^* + \delta\boldsymbol{\xi}^*, \boldsymbol{\xi}_0 + \delta\boldsymbol{\xi}\} &= \delta W_0 + \frac{1}{2}\rho_0 \sum_{i=1}^{\infty} |a_i|^2 \omega_i^2, \\ K\{\boldsymbol{\xi}_0^* + \delta\boldsymbol{\xi}^*, \boldsymbol{\xi}_0 + \delta\boldsymbol{\xi}\} &= K_0 + \frac{1}{2}\rho_0 \sum_{i=1}^{\infty} |a_i|^2,\end{aligned}\quad (6.45)$$

where, by Equations (6.39), $K_0 = \rho_0/2$.

Substituting these results into Equation (6.42), the denominator can be expanded if the perturbation to the system due to asymmetry ($\delta\boldsymbol{\xi}$) is small. Then, an estimate of the eigenvalue ω^2 as a result of linear perturbation is

$$\omega^2 \sim \omega_0^2 + \sum_{i=1}^{\infty} |a_i|^2 (\omega_i^2 - \omega_0^2), \quad (6.46)$$

where ω_0^2 is the actual eigenvalue (i.e. sausage or kink frequency) of the unperturbed (symmetric) system associated with $\boldsymbol{\xi}_0$. Here, the summation is the contribution to the eigenvalue of the unperturbed (symmetric) waveguide system caused by the introduction of asymmetry. The following properties can be observed:

1) Even though the perturbation $\delta\boldsymbol{\xi}$ in our estimate of the eigenvector is $O(a_i)$ (see Equation (6.41)), the perturbation in the estimate of the eigenvalue is $O(|a_i|^2) \ll O(a_i)$. Therefore, the perturbation in the eigenvalue caused by the introduced asymmetry is much smaller than the perturbation in the eigenvector. As an example, say, a 10% linear perturbation introduced by asymmetry in the eigenvector $\boldsymbol{\xi}_0$ results in only a 1% perturbation in the estimate of the waveguide's eigenfrequency ω^2 .

2) It is worth noting that the introduction of the waveguide asymmetry cannot result in an instability given that $\omega_0^2 < \omega_i^2$.

For the quasi-sausage modes, comparing Equations (6.21) and (6.32), we see that they fulfil the expectations stemming from the Rayleigh-Ritz Technique. The frequency difference due to asymmetry is proportional to $\varepsilon\delta$, and the amplitude difference due to asymmetry is proportional to δ .

However, the quasi-kink mode does not seem to obey the same rule, as Equations (6.26) and (6.37) show that the frequency difference due to asymmetry is proportional to δ , but the amplitude difference due to asymmetry is proportional to $\varepsilon^2\delta$. This is a consequence of the factor of ε that is present in all terms of the frequency of the standing harmonic modes, meaning that there is no constant term and we cannot expect to obtain the result suggested by the Rayleigh-Ritz Technique for the quasi-kink modes.

6.5 The Slab in a Magnetic Environment

In the current Section, we generalise the results from Section 6.2 though the reintroduction of asymmetric magnetic fields in the environment of the slab, making

this model of standing waves more applicable to features of the solar atmosphere in which the external magnetic fields may not be neglected (such as prominences or further coronal waveguides).

6.5.1 The Equilibrium Magnetic Slab

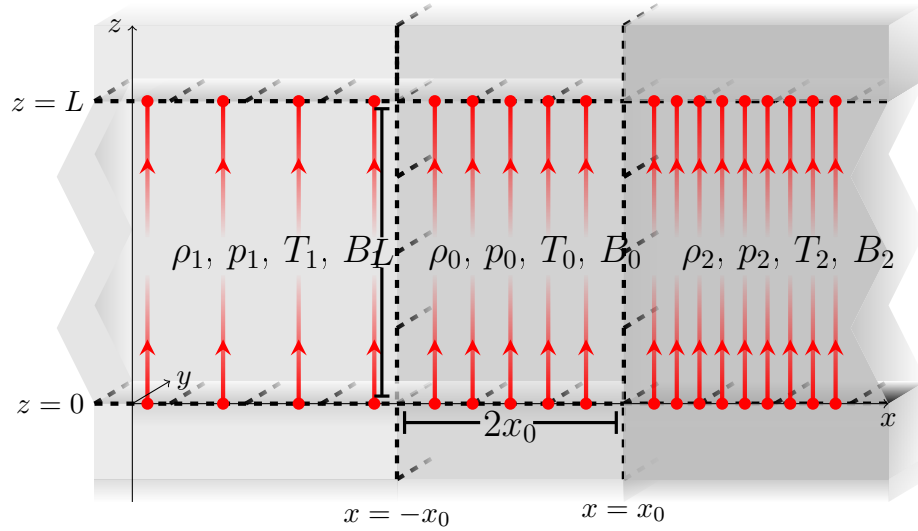


Figure 6.13: Visualisation of the equilibrium state inside ($|x| \leq x_0$) and outside of the magnetic slab ($x < -x_0$ and $x > x_0$), where the magnetic field is indicated by the red lines. The source of the Figure is: Oxley et al. (2020b).

As before, we consider a 3-dimensional, inviscid, static, ideal plasma split into three regions in the x -direction, with the equilibrium configuration shown in Figure 6.13. We assume that the slab is unbounded in the y -direction. The equilibrium magnetic field is given by $B(x)\hat{e}_z$, where

$$B(x) = \begin{cases} B_1 & \text{if } x < -x_0, \\ B_0 & \text{if } -x_0 \leq x \leq x_0, \\ B_2 & \text{if } x > x_0, \end{cases} \quad (6.47)$$

$$B_0 \quad \text{if } -x_0 \leq x \leq x_0, \quad (6.48)$$

$$B_2 \quad \text{if } x > x_0, \quad (6.49)$$

and B_j , for $j = 0, 1, 2$, are constant. Here, p_j , T_j and ρ_j can also be different for each region of the slab system ($j = 0, 1, 2$).

6.5.2 Boundary Conditions

We apply the same principles as we did in Section 6.2 to determine the boundary conditions at each interface. The criteria on the horizontal structuring is still the requirement of total pressure balance across the interfaces at $x = \pm x_0$. This condition has the same form now as did in Chapter 6.2, where propagating waves in a similar configuration were examined. Total pressure balance is therefore maintained if

$$p_1 + \frac{B_1^2}{2\mu_0} = p_0 + \frac{B_0^2}{2\mu_0} = p_2 + \frac{B_2^2}{2\mu_0}. \quad (6.50)$$

In the vertical direction, we still assume line-tying, which gives us the boundary conditions to be applied at $z = 0, L$:

$$\begin{aligned}
 v_x(z=0) &= v_x(z=L) = 0, \\
 b_z(z=0) &= b_z(z=L) = 0, \\
 p_T(z=0) &= p_T(z=L) = 0,
 \end{aligned} \tag{6.51}$$

where v_x and b_z are the x -component of the velocity perturbation and the z -component of the magnetic field perturbation, respectively. From the physical assumption of line-tying, meaning that the plasma does not move at $z = 0, L$, the condition on v_x follows trivially. The 'frozen-in' property of the field lines in ideal MHD implies that the magnetic flux through an arbitrary flux bundle must remain constant. Since there is no motion at $z = 0, L$ (by the assumption of line-tying), the cross sectional area of a flux bundle does not change. Therefore, the z -component of the magnetic field strength remains constant, leading us to deduce the condition on b_z stated above. The condition on p_T is acquired simply because a non-zero pressure perturbation would cause a force, and consequently cause motion as well.

6.5.3 Derivation of the Dispersion Relation

The process of deriving the dispersion relation is formally analogous to the method we followed in Section 6.2. We refrain from repeating all steps (they are included in Oxley et al. (2020b)), and merely state the conclusion that all three regions ($j = 0, 1, 2$) of plasma are governed by the same form of ODE, namely

$$\frac{d^2 \hat{v}_x}{dx^2} - m_j^2 \hat{v}_x = 0, \quad \text{where} \quad m_j^2 = \frac{(k^2 c_j^2 - \omega^2)(k^2 v_{Aj}^2 - \omega^2)}{(k^2 c_{Tj}^2 - \omega^2)(c_j^2 + v_{Aj}^2)}, \quad c_{Tj}^2 = \frac{c_j^2 v_{Aj}^2}{c_j^2 + v_{Aj}^2},$$

and due to the line-tying conditions

$$k = \frac{n\pi}{L}, \quad n \in \mathbb{Z}^+, \tag{6.52}$$

with $k = 0$ excluded to avoid trivial solutions. In the following, we assume that $m_0^2 > 0$ to examine surface waves only, and $m_1^2, m_2^2 > 0$ so that the solutions are evanescent outside of the slab.

Applying the conditions of the continuity of p_T and v_x across both $x = \pm x_0$ gives us the dispersion relation for MHD waves in a slab embedded in an asymmetric magnetic environment (with the details given in Zsámberger et al. (2018) and in Chapter 2):

$$\begin{aligned}
 2m_0^2(k^2 v_{A1}^2 - \omega^2)(k^2 v_{A2}^2 - \omega^2) &+ 2\frac{\rho_0}{\rho_1} m_1 \frac{\rho_0}{\rho_2} m_2 (k^2 v_{A0}^2 - \omega^2)^2 \\
 &+ m_0 (k^2 v_{A0}^2 - \omega^2) \left(\frac{\rho_0}{\rho_1} m_1 (k^2 v_{A2}^2 - \omega^2) \right. \\
 &\left. + \frac{\rho_0}{\rho_2} m_2 (k^2 v_{A1}^2 - \omega^2) \right) (\tanh(m_0 x_0) + \coth(m_0 x_0)) = 0.
 \end{aligned} \tag{6.53}$$

$$\tag{6.54}$$

We now assume that the external regions are isothermal in order to emphasize the effects of the magnetic asymmetry. The assumption results in the following relations:

$$T_1 = T_2, \quad c_1 = c_2. \quad (6.55)$$

As before, the thin slab and weak asymmetry approximations will be used. Let us introduce the notation

$$\varepsilon = \frac{x_0}{L}, \quad \text{and} \quad v_{A2}^2 = v_{A1}^2(1 + \zeta), \quad (6.56)$$

where $\zeta > 0$ is taken, meaning $v_{A2} > v_{A1}$. The quantity ε represents the ratio of the slab's half-width to its height, and ζ represents the asymmetry in the external Alfvén speeds. This asymmetry can be obtained through the presence asymmetry in density, magnetic field strength, or both of these.

The weak asymmetry assumption corresponds to $\zeta \ll 1$, which we then use to simplify the dispersion relation and obtain as follows:

$$(k^2 v_{A0}^2 - \omega^2) \left(\frac{\rho_0 m_1}{\rho_1 (k^2 v_{A1}^2 - \omega^2)} + \frac{\rho_0 m_2}{\rho_2 (k^2 v_{A2}^2 - \omega^2)} \right) + 2m_0 \left(\frac{\tanh}{\coth} \right) (m_0 x_0) \approx 0, \quad (6.57)$$

where ζ is not explicitly written, however, it is within the quantities ρ_2 , m_2 and v_{A2} implicitly.

This is formally the same relation as the decoupled dispersion relation from Chapter 2, but in the current case, we have $c_1 = c_2$ and $k = n\pi/L$.

Thin Slab Approximation

The thin slab approximation is expressed by $\varepsilon \ll 1$, which further simplifies the dispersion relation (Equation 6.57). For quasi-sausage modes, this gives us

$$(k^2 v_{A0}^2 - \omega^2) \left(\frac{\rho_0 m_1}{\rho_1 (k^2 v_{A1}^2 - \omega^2)} + \frac{\rho_0 m_2}{\rho_2 (k^2 v_{A2}^2 - \omega^2)} \right) + 2m_0^2 x_0 \left(1 - \frac{m_0^2 x_0^2}{3} \right) \approx 0, \quad (6.58)$$

and for the quasi-kink oscillations,

$$(k^2 v_{A0}^2 - \omega^2) \left(\frac{\rho_0 m_1}{\rho_1 (k^2 v_{A1}^2 - \omega^2)} + \frac{\rho_0 m_2}{\rho_2 (k^2 v_{A2}^2 - \omega^2)} \right) + \frac{2}{x_0} \approx 0. \quad (6.59)$$

In the following, $O(\zeta) \sim O(\varepsilon)$ will be taken in order to use Equations (6.58) and (6.59) to derive the frequencies and keep second-order terms of size $\varepsilon\zeta$ and ε^2 . Terms of size ζ^2 are ignored, just as they were in deriving the decoupled dispersion relations for the quasi-sausage and -kink modes.

6.5.4 Eigenfrequencies of Standing Harmonic Modes

Here, we calculate the eigenfrequencies of the waves in an asymmetric magnetised slab system analytically, following a similar method to Section 6.2, and using the quantisation of k given in Equation (6.52), to express the frequencies of the standing harmonic modes as ω_n .

Quasi-sausage Modes

Ignoring the trivial solution $\omega = kv_{A0}$, we simplify Equation (6.58) and obtain the following solutions for the quasi-sausage mode frequencies:

$$\omega_n^2 \approx \frac{n^2 \pi^2 c_{T0}^2}{L^2} \left\{ 1 + \varepsilon n \pi \bar{\Pi} + \varepsilon^2 n^2 \pi^2 \left[\bar{\Pi}^2 c_{T0}^2 \left(\frac{1}{2(c_1^2 - c_{T0}^2)} - \frac{1}{2(c_{T1}^2 - c_{T0}^2)} - \frac{1}{2(v_{A1}^2 - c_{T0}^2)} - \frac{1}{(c_0^2 - c_{T0}^2)} \right) + \frac{c_{T0}^2}{3(c_0^2 + v_{A0}^2)} \right] + \varepsilon \zeta \frac{n \pi \bar{\Pi}}{4} \left[\frac{v_{A1}^2}{v_{A1}^2 - c_{T0}^2} \left(1 + \frac{(c_1^2 - c_{T0}^2)(v_{A1}^2 - c_{T0}^2)}{(c_{T1}^2 - c_{T0}^2)(c_1^2 + v_{A1}^2)} \right) - \frac{2v_{A1}^2 \gamma}{2c_1^2 + v_{A1}^2 \gamma} \right] \right\}, \quad (6.60)$$

where

$$\bar{\Pi} = - \frac{\rho_1 c_0^2 (c_{T0}^2 - v_{A1}^2)^{1/2} (c_{T0}^2 - c_{T1}^2)^{1/2} (c_1^2 + v_{A1}^2)^{1/2}}{\rho_0 v_{A0}^2 (c_1^2 - c_{T0}^2)^{1/2} (c_0^2 + v_{A0}^2)}. \quad (6.61)$$

This solution is valid when $v_{A1} < c_{T0} < c_1$, to ensure that $m_j^2 > 0$ for $j = 0, 1, 2$. Although the form in which we present the solutions suggests the ordering $c_1 < c_{T0} < v_{A1}$ could be valid. However, the quantity $\bar{\Pi}$ has been simplified using the ordering $v_{A1} < c_{T0} < c_1$, and by deriving the more general form of this quantity, it is observed that the ordering $c_1 < c_{T0} < v_{A1}$ would result in a solution violating the condition $m_j^2 > 0$ for $j = 0, 1, 2$ is not satisfied.

This solution given is analogous to Equation (16d) in Edwin and Roberts (1982). While it is possible to derive analogues of Equations (16b, c) under speed orderings similar to the ones presented there, those solutions describe a surface wave, which, in a thin slab, changes its character to that of a body wave. Since we exclude body modes from our analysis, we only investigate solutions that have the character of surface waves in both wide and thin slabs, and therefore satisfy $m_j^2 > 0$ for $j = 0, 1, 2$.

A comparison to the magnetic slab embedded in a non-magnetic asymmetric environment from the previous Section can also be made. If we set $B_1 = B_2 = 0$ and consequently $v_{A1} = v_{A2} = 0$, then $\bar{\Pi}$ reduces $-\bar{\Pi}$ from the section on the non-magnetic environment. The terms of order 1, ε and ε^2 in Equation (6.60) will each be equal to the corresponding terms of the same order for the non-magnetic case. However, there is no direct correspondence between the $\varepsilon \zeta$ terms of the magnetic and the $\varepsilon \delta$ terms on the non-magnetic case.

Using Equation (6.60), the frequency ratio for quasi-sausage modes is

$$\frac{\omega_2}{\omega_1} \approx 2 \left\{ 1 + \varepsilon \frac{\pi \bar{\Pi}}{2} + \varepsilon^2 \pi^2 \left[\frac{\bar{\Pi}}{8} \left(\frac{6c_{T0}^2}{c_1^2 - c_{T0}^2} - \frac{6c_{T0}^2}{c_{T1}^2 - c_{T0}^2} - \frac{6c_{T0}^2}{v_{A1}^2 - c_{T0}^2} - \frac{12c_{T0}^2}{c_0^2 - c_{T0}^2} - 5 \right) + \frac{c_{T0}^2}{2(c_0^2 + v_{A0}^2)} \right] \right. \quad (6.62)$$

$$\left. + \varepsilon \zeta \frac{\pi \bar{\Pi}}{8} \left[\frac{v_{A1}^2}{v_{A1}^2 - c_{T0}^2} (1 + \frac{(c_1^2 - c_{T0}^2)(v_{A1}^2 - c_{T0}^2)}{(c_{T1}^2 - c_{T0}^2)(c_1^2 + v_{A1}^2)}) - \frac{2v_{A1}^2 \gamma}{2c_1^2 + v_{A1}^2 \gamma} \right] \right\}. \quad (6.63)$$

$$(6.64)$$

In the magnetically asymmetric case, there is another solution to Equation (6.58), which takes the form

$$\omega_n^2 \approx \frac{n^2 \pi^2 c_1^2}{L^2} \left\{ 1 + \varepsilon^2 n^2 \pi^2 \tilde{\Pi} + \varepsilon^2 \zeta \frac{n^2 \pi^2 \tilde{\Pi} v_{A1}^2}{2} \left[\frac{1}{v_{A1}^2 - c_1^2} - \frac{2\gamma}{2c_1^2 + \gamma v_{A1}^2} \right] \right\}, \quad (6.65)$$

where

$$\tilde{\Pi} = \frac{\rho_1^2 c_1^2 (c_0^2 - c_1^2)^2 (v_{A1}^2 - c_1^2)}{\rho_0^2 (c_{T0}^2 - c_1^2)^2 (c_0^2 + v_{A0}^2)^2}. \quad (6.66)$$

A solution with this frequency can only exist in the thinnest slabs due to the condition that the external plasma is isothermal. When it exists, the frequency ratio for the harmonics of this mode is

$$\frac{\omega_2}{\omega_1} \approx 2 \left\{ 1 + \varepsilon^2 \frac{3\pi^2 \tilde{\Pi}}{2} + \varepsilon^2 \zeta \frac{3\pi^2 \tilde{\Pi} v_{A1}^2}{4} \left[\frac{1}{v_{A1}^2 - c_1^2} - \frac{2\gamma}{2c_1^2 + \gamma v_{A1}^2} \right] \right\}. \quad (6.67)$$

In Figures 6.14 and 6.15, we provide illustrations of the fundamental and first harmonic modes of quasi-sausage standing waves in the asymmetric magnetic configuration. Then in Figures ?? and ??, we plot the dependence of the frequency ratio of the first harmonic to the fundamental mode on the slab width and asymmetry parameters. For both solutions, we see a quadratic-like relation to ε as expected, whereas only a weaker, linear relationship with ζ is observed. The reason for this is that ζ only appears as a second-order quantity in Equation (6.64), and as a third-order quantity in Equation (6.67). I

Quasi-kink Modes

First, let us define the kink speed, v_k in terms of the asymmetry parameter as

$$v_k^2 = \frac{\rho_1 v_{A1}^2 + \rho_2 v_{A2}^2}{\rho_1 + \rho_2} \approx v_{A1}^2 \left(1 + \frac{\zeta}{2} \right), \quad (6.68)$$

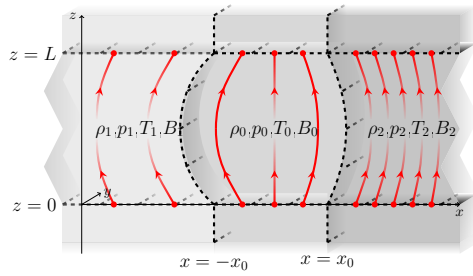


Figure 6.14: Illustration of a fundamental standing quasi-sausage mode oscillation in the magnetic slab embedded in a magnetically asymmetric environment. The source of the Figure is: Oxley et al. (2020b).

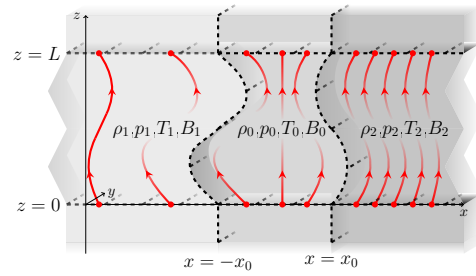


Figure 6.15: Same as Figure 6.14 but for the first harmonic. The source of the Figure is: Oxley et al. (2020b).

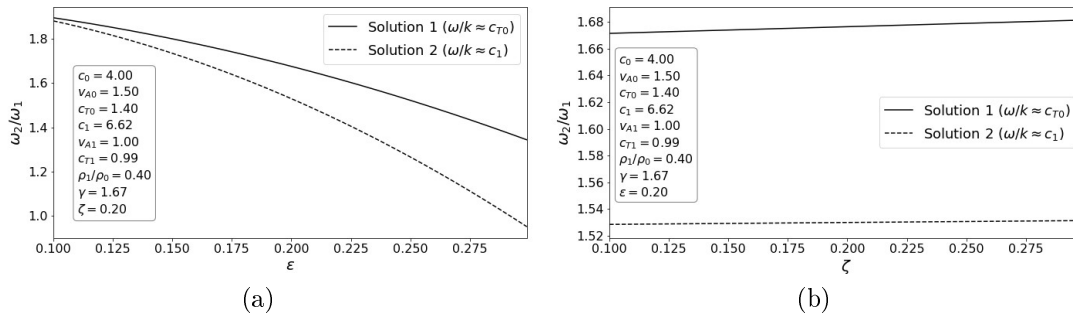


Figure 6.16: The ratio of the frequencies of the first harmonic to the fundamental mode of the quasi-sausage waves (Solution 1 given by Equation (6.64) and Solution 2 by Equation 6.67), **(a)** as a function of ε , with $\zeta = 0.2$ fixed, and **(b)** as a function of ζ , with $\varepsilon = 0.2$ fixed. The source of the Figure is: Oxley et al. (2020b).

where the approximation is written using Equation (6.56) and keeping only first-order terms in ζ . In terms of this characteristic speed, there is a solution to Equation (6.59), with $\omega^2 = k^2 v_k^2 (1 + \alpha_1)$, where $\alpha_1 \sim O(\varepsilon^2)$. It would be possible to make a similar expansion about both $k^2 v_{A1}^2$ or $k^2 v_{A2}^2$, as they both differ from $k^2 v_k^2$ by only a factor of $\zeta/2$ to first-order. However, using the kink speed here is a more natural choice, allowing us to easily recover the solution for the case of a single interface (Roberts, 1981a) when the slab width tends to zero.

In order to make analytical progress while fulfilling the conditions $m_1^2, m_2^2 > 0$ now we must take $\varepsilon^3 \ll \zeta \ll \varepsilon^2 \ll \varepsilon \ll 1$. The quasi-kink mode solution then becomes

$$\omega^2 \approx k^2 v_k^2 \left(1 + A\varepsilon^2 + B \frac{\zeta^2}{\varepsilon^2} \right), \quad \text{where } A, B \sim O(1). \quad (6.69)$$

Unfortunately, the limitations of the method start showing here. Namely, the term of size ζ^2/ε^2 is of comparable size to the terms ignored in order to decouple the full dispersion relation. Consequently, a valid solution that includes the first explicit term due to asymmetry cannot be determined. We could take a further ordering, say $\varepsilon^4 \ll \zeta \ll \varepsilon^3 \ll 1$, however, this work aims to analyse the effect of asymmetry, and the smaller we take the asymmetry to be, the less significant its effect must

become. The following solution can be found including terms up to ε^2 :

$$\omega_n^2 \approx \frac{n^2 \pi^2 v_k^2}{L^2} \left(1 - \varepsilon^2 \frac{n^2 \pi^2 \rho_0^2 (v_k^2 - v_{A0}^2)^2 (v_k^2 - c_1^2)}{v_k^6 \rho_1^2} \right). \quad (6.70)$$

Expression (6.70) is analogous to the results of Equation (18a) in Edwin and Roberts (1982). However, there is a small error in the paper there, as in Equation (18a) the factor $(1 - v_A^2/v_{Ae}^2)$ should have been squared. We must note that the method used in the derivation of this solution involves squaring terms, and so the final solution only satisfies the decoupled dispersion relation when the correct square-root is taken.

For a different possible quasi-kink mode solution, we define the average external tube speed, c_{TA} by:

$$c_{TA}^2 = \frac{c_{T1}^2 + c_{T2}^2}{2} \approx c_{T1}^2 \left(1 + \frac{\zeta c_{T1}^2}{2v_{A1}^2} \right). \quad (6.71)$$

To obtain the form of the quasi-kink mode solution given by $\omega^2 = k^2 c_{TA}^2 (1 + \alpha_2)$, where $\alpha_2 \sim O(\varepsilon^2)$, we assume $\varepsilon^3 \ll \zeta \ll \varepsilon^2 \ll \varepsilon \ll 1$, giving us the frequencies as

$$\omega_n^2 \approx \frac{n^2 \pi^2 c_{TA}^2}{L^2} \left(1 - \varepsilon^2 \frac{n^2 \pi^2 \rho_0^2 (c_{TA}^2 - v_{A0}^2)^2 (c_1^2 - c_{TA}^2)}{v_{A1}^4 c_{TA}^2 \rho_1^2} \right), \quad (6.72)$$

valid only when $c_{TA} > v_{A0}$ and $c_{TA} < c_0$. An expression involving the first explicit asymmetry term cannot be determined (apart from the asymmetry contained within c_{TA}^2). This is similar to the expression obtained in Equation (18b) in Edwin and Roberts (1982), and we can reduce Equation (6.72) to that equation by setting $\zeta = 0$.

To clarify, neither of the quasi-kink mode solutions show any explicit dependence on the magnetic asymmetry parameter ζ . However, defining the speeds v_k and c_{TA} , the asymmetry dependence is contained in these quantities already in an implicit manner. Thus the effects of magnetic asymmetry are still present, acting through the speed that the expansion is about.

The frequency ratio of the first harmonic eigenmode to the fundamental mode is not calculated for either of the quasi-kink frequency solutions, as they will not contain terms explicitly involving the magnetic asymmetry parameter ζ , and therefore not providing us with a useful tool to analyse magnetic asymmetry. Illustrations of the fundamental and first harmonic standing quasi-kink waves are still provided in Figures 6.17 and 6.18.

6.5.5 Amplitudes of Standing Harmonic Modes

In this subsection, we follow the method used in Section 6.3.2 to calculate the magnitude of the difference of the amplitudes of the standing oscillations at the two sides of the slab, denoting these by D_S and D_K for the quasi-sausage and quasi-kink modes, respectively. This amplitude difference can be found from the same expression in both cases:

$$D_S = D_K = \left| \left| \hat{\xi}_x(x_0) \right| - \left| \hat{\xi}_x(-x_0) \right| \right| = \left| \frac{1}{\omega} \left(\left| \hat{v}_x(x_0) \right| - \left| \hat{v}_x(-x_0) \right| \right) \right|. \quad (6.73)$$

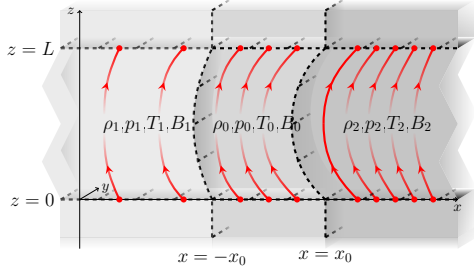


Figure 6.17: Illustration of a fundamental standing quasi-kink mode oscillation in the slab embedded in a magnetically asymmetric environment. The source of the Figure is: Oxley et al. (2020b).

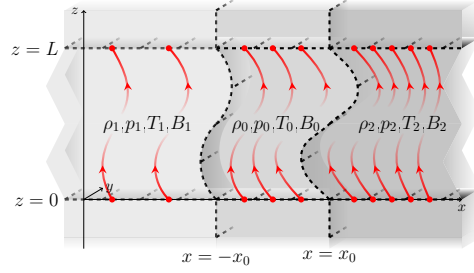


Figure 6.18: Same as Figure 6.17 but for the first harmonic. The source of the Figure is: Oxley et al. (2020b).

Quasi-sausage Modes

For quasi-sausage modes, $\hat{v}_x(x_0)$ and $\hat{v}_x(-x_0)$ (along with $\hat{\xi}_x(x_0)$ and $\hat{\xi}_x(-x_0)$) have opposite signs, so Equation (6.73) reduces to

$$D_S = \left| \hat{\xi}_x(x_0) + \hat{\xi}_x(-x_0) \right| = \left| \frac{1}{\omega} (\hat{v}_x(x_0) + \hat{v}_x(-x_0)) \right|. \quad (6.74)$$

The amplitude difference corresponding to the eigenfrequency given by Equation (6.60) is

$$D_S \approx \zeta \sqrt{\varepsilon} |C| \frac{\sqrt{-\tilde{\Pi}} L \rho_0 v_{A0}^2 (c_0^2 + v_{A0}^2)^{1/2} (c_1^2 - c_{T0}^2)^{1/2}}{\sqrt{n\pi} \rho_1 c_0^2 (c_{T0}^2 - v_{A1}^2)^{1/2} (c_{T0}^2 - c_{T1}^2)^{1/2} (c_1^2 + v_{A1}^2)^{1/2}} \times \left| \frac{v_{A1}^2}{2(v_{A1}^2 - c_{T0}^2)} \left(1 + \frac{(c_1^2 - c_{T0}^2)(v_{A1}^2 - c_{T0}^2)}{(c_{T1}^2 - c_{T0}^2)(c_1^2 + v_{A1}^2)} \right) - \frac{v_{A1}^2 \gamma}{2c_1^2 + v_{A1}^2 \gamma} \right|, \quad (6.75)$$

where $v_{A1} < c_{T0} < c_1$ is taken from the eigenfrequency solutions in Equation (6.60).

Next, the amplitude difference of the second type of quasi-sausage mode corresponding to the eigenfrequency given by Equation (6.65) is

$$D_S \approx \zeta \varepsilon |C| \frac{\rho_0 L \sqrt{|\tilde{\Pi}|} |v_{A0}^2 - c_1^2|^{1/2} |c_{T0}^2 - c_1^2|^{1/2} (c_0^2 + v_{A0}^2)^{1/2}}{\rho_1 c_1^2 |c_0^2 - c_1^2|^{1/2} |v_{A1}^2 - c_1^2|^{1/2}} \times \left| \frac{v_{A1}^2}{2(v_{A1}^2 - c_1^2)} - \frac{\gamma v_{A1}^2}{2c_1^2 + \gamma v_{A1}^2} \right|, \quad (6.76)$$

For both of these solutions, C is an arbitrary constant that can be set equal to one. The amplitude difference of oscillations between the two sides of the magnetic slab, for both quasi-sausage frequencies, shows a rather complex dependence on the characteristic speeds, a linear dependence on the magnetic asymmetry parameter ζ , and different dependences on ε . The first amplitude difference, given by Equation (6.75), shows a square-root dependence on ε , while the second one, given by Equation (6.76), simply shows a linear relationship with this slab width parameter.

Quasi-kink Modes

We can still calculate the amplitude difference between the two sides of the magnetic slab to leading order for quasi-kink modes, even though we did not do so for the frequency ratios. This is because, we only need to use a solution for eigenfrequency that includes the first correction term (i.e. the term of order ε^2). These solutions are given in Equations (6.70) and (6.72).

As a reminder, for the quasi-kink modes, $\hat{v}_x(x_0)$ and $\hat{v}_x(-x_0)$ have the same sign, so Equation (6.73) reduces to

$$D_K = \left| \hat{\xi}_x(x_0) - \hat{\xi}_x(-x_0) \right| = \left| \frac{1}{\omega} (\hat{v}_x(x_0) - \hat{v}_x(-x_0)) \right|. \quad (6.77)$$

The quasi-kink amplitude difference corresponding to the eigenfrequency given by Equation (6.70) is

$$D_K \approx \left| \zeta B \frac{Lv_k^5 \rho_1^2 (c_0^2 - v_k^2)}{2n\pi \rho_0^2 (c_{T0}^2 - v_k^2)(c_0^2 + v_{A0}^2)(v_{A0}^2 - v_k^2)(v_k^2 - c_1^2)} \right|, \quad (6.78)$$

while the quasi-kink amplitude difference corresponding to the eigenfrequency given by Equation (6.72) is

$$D_K \approx \zeta |B| \frac{Lv_{A1}^2 c_{TA}^3 \rho_1^2 (c_0^2 - c_{TA}^2)}{2n\pi \rho_0^2 (c_{TA}^2 - c_{T0}^2)(c_0^2 + v_{A0}^2)(c_{TA}^2 - v_{A0}^2)(c_1^2 - c_{TA}^2)}, \quad (6.79)$$

where the ordering $v_{A0} < c_{TA} < c_0$ is carried forward from the frequency solution given in Equation (6.72).

For both quasi-kink amplitude difference solutions, B is an arbitrary constant that can be set equal to one. The amplitude difference between the two sides of the slab, for both quasi-kink eigenfrequencies, also shows a complex dependence on the characteristic speeds, and a linear dependence on the magnetic asymmetry parameter ζ . However, they do not depend on ε to leading order.

6.6 Conclusion

In this Section, we investigated the dispersion of standing quasi-sausage and quasi-kink mode oscillations in asymmetric non-magnetic and magnetic slab systems. Referencing the steps of the equivalent derivations for propagating modes, in Section 6.2, we first obtained a standing wave dispersion relation for the case of a magnetic slab embedded in an asymmetric, non-magnetic environment that is subject to line-tying boundary conditions in the z -direction. Then we conducted an analytical and numerical study of the eigenfrequencies of quasi-sausage and quasi-kink modes, also examining their correspondence and therefore the limits of applicability of our approximations.

We proceeded to use the analytical expressions obtained for the thin slab and weak asymmetry limits to determine the frequency and amplitude differences of the different harmonics of each type of eigenmode, both of which can be useful tools of solar magneto-seismology. According to the Rayleigh-Ritz theorem, especially the amplitude differences should provide us a sensitive technique to measure the asymmetries present in a solar slab waveguide. We found this to be true for quasi-sausage modes, but not for their quasi-kink counterparts.

In Section 6.5, we generalised our results to standing waves in magnetic slabs sandwiched between magnetically asymmetric regions. Following similar steps to the non-magnetic study, we determined the dependence of the eigenfrequencies on the slab width and asymmetry parameters, and prepared magneto-seismological tools in the form of frequency ratios and amplitude differences. In the case of quasi-kink modes, we could not obtain a useful expression for the frequency ratios of the harmonics due to the assumptions we needed to take for analytical progress. However, an amplitude difference parameter depending on the magnetic asymmetry parameter could still be obtained for them. We did not encounter similar problems with the quasi-sausage modes, which provide useful diagnostic quantities for both frequency ratios and amplitude differences.

The inclusion of external asymmetric magnetic fields can potentially allow us to apply our model with greater precision to a wider variety of solar structures. Ideal candidates for application in the solar atmosphere would include e.g. prominences, elongated MBPs or sunspot light bridges. (For details on each of these structures analysed as magnetic slabs, see Chapter 4).

Chapter 7

Conclusion

7.1 Overview of the Thesis

This Thesis investigates the dispersion of magneto-acoustic waves in a family of asymmetric magnetic slab configurations. These Cartesian simple waveguide models provide a relatively simple and yet versatile tool for investigating oscillations in various solar atmospheric structures as a first approximation. Obtaining a concise theoretical description of MHD waves supported by slab-like solar environments then allows us to prepare techniques specifically geared towards practising solar magneto-seismology, that is, using our theoretical understanding of wave dispersion to guide observations and determine as of yet unknown physical parameters of certain phenomena in the solar atmosphere.

First, Chapter 1 provides a brief introduction to the topic of solar atmospheric seismology and the magnetohydrodynamic description of magnetised plasmas. The main layers of the solar atmosphere are described, along with the atmospheric heating problem, which is one of the greatest mysteries brought up by the temperature distribution between the solar surface and the highest layers of the atmosphere. Further details on both the study of the global structure of the atmosphere, as well as on elements of its fine structure are also given in later Chapters, as required (especially in Chapter 4 focused on suggested applications of the first slab model we investigate). To provide a background understanding for the calculations in later Chapters, we summarise the fundamental assumptions of magnetohydrodynamics and gather the linear MHD equations. These are then used to give a description of MHD waves first in a uniform medium, and then in a structured atmosphere. Before we move on towards developing and applying our own models, an introduction to a few historical milestones of solar magneto-seismology are presented.

The first model described in this Thesis is that of a static magnetic slab embedded in an asymmetric magnetic environment. Chapter 2 sets up this equilibrium configuration and includes a detailed derivation of the dispersion relation from the linearised ideal MHD equations. The structure of the dispersion relation is investigated, before we introduce the weak asymmetry approximation to decouple the dispersion relation into two separate equations, similarly to the case of a symmetric slab. It must be emphasized that in the general case of an asymmetric slab, a single equation describes both main types of eigenmodes, which are called quasi-sausage and quasi-kink in order to emphasise the influence that the environmental asymmetry has on their classical structure. We proceed to describe this new, asymmetric

behaviour in further detail, also illustrating it through a comparison to a coupled mechanical oscillator system. The concept of quasi-symmetric modes is introduced, which oscillations in an asymmetric waveguide which appear to have symmetric amplitudes at the slab boundaries due to the competing effects of the pressure gradient and the magnetic forces. We proceed to conduct a parametric study of the eigenmodes in asymmetric magnetic slab systems characterised by various sound-, Alfvén- and tube speeds, as well as density ratios. The effect of a changing density asymmetry is described in detail, and the resultant avoided crossings of eigenmodes are discussed.

Next, in Chapter 3, the dispersion relation and its solutions are studied in a number of analytical approximations relevant to applications in solar physics. We investigate thin- and wide slabs filled with high- and low- β plasmas, and we provide a few examples of numerical solutions to complement our analytical description. These calculations are carried out in order to understand wave behaviour in some relatively simple, analytically tractable limiting cases, and to prepare the tools we need for developing solar applications of the model in Chapter 4. A simple multi-layered asymmetric Cartesian waveguide is a simple but adaptable configuration, and therefore we put forward several features of the solar atmosphere which may be modelled by such slab systems, at least as a first approximation to understand their interactions with their asymmetric environments. As the solar atmosphere is a highly complex and dynamic medium (Banerjee et al., 2007), it is reasonable to expect that asymmetries on either side of its many waveguides might be present; and if the symmetry of a waveguide environment is indeed broken, that can fundamentally change the oscillations supported by the system, as we have illustrated in our Chapters 2 - 3. The solar applications we suggest go from the widest, global scales, through large coronal features to small photospheric structures. In each case, an overview of the applied waveguide model is provided, along with wave observations of key importance in the chosen waveguides. Next, a few simple approximations from Chapter 3 are applied to the model solar waveguides, and numerical results for the expected observable waves are presented.

Chapter 5 continues this line of investigation, and it details the generalisation of two magneto-seismological techniques introduced by Allcock and Erdélyi (2017). The asymmetric nature of the eigenmodes is utilised to find simple quantities which we could obtain from wave detections and use in an inversion process to determine more elusive parameters, such as the Alfvén speed inside the slab. The amplitude ratios and minimum perturbation shifts of quasi-sausage and quasi-kink modes are calculated, and the concept of quasi-symmetric modes is elaborated upon.

Next, in Chapter 6, we take a detour to investigate standing waves in asymmetric waveguides and provide further tools for SMS applications. First, to clearly set out the methods and boundary conditions, we present some results obtained for an asymmetric, externally non-magnetic slab system. Then, the key steps of the derivation are repeated for an asymmetric, externally magnetic slab system, too. We provide analytical expressions and numerical results for the frequency and amplitude ratios of standing quasi-sausage and quasi-kink modes in both cases, and we briefly mention the suggested solar applications of these techniques.

7.2 Summary of the main results

7.2.1 The Magnetic Slab Embedded in an Asymmetric Magnetic Environment

In Chapters 2 - 5, we investigate propagating waves in an asymmetric magnetic slab system. We start from setting up the equilibrium in Chapter 2, and finish this main part by providing tools for the purposes of magneto-seismology in Chapter 5.

Chapter 2

We describe the equilibrium configuration of a magnetised plasma slab embedded between two environmental regions, which are asymmetric both in their plasma parameters and magnetic field strengths. Upon introducing small perturbations into this system, we proceed to describe wave dispersion in the configuration. We linearise the ideal MHD equations, and look for plane wave solutions propagating parallel to the magnetic field lines and along the slab. Through this process, we arrive at an ordinary differential equation governing the behaviour of the plasma in each region. We match the solutions across the two interface separating the slab from its environment, requiring the continuity of total pressure and velocity perturbations across the boundaries. This allows us to derive the general dispersion relation for magneto-acoustic waves propagating in the asymmetric magnetic slab system. For the case of weak asymmetry in the environment, we further obtain an approximate (decoupled) version of the dispersion relation. We show that the asymmetric magnetic slab system is a generalisation of both the configuration of a slab embedded in an asymmetric, non-magnetic environment (Allcock and Erdélyi, 2017) and that of a magnetic slab enclosed in a symmetric, magnetic environment (Edwin and Roberts, 1982). The dispersion relations of both of these preceding studies are recovered.

We determine that the eigenmodes of the asymmetric magnetic slab, just like those of the asymmetric non-magnetic slab, are not “purely” of kink or sausage types. Rather, they show a mixture of the characteristics of these two modes, and their appearance is not (generally) symmetric, either, and therefore we call them quasi-sausage and quasi-kink modes. Mathematically, this mixed behaviour is represented by the fact that the full dispersion relation (Equation 2.31) does not decouple into two separate equations governing kink or sausage modes for an arbitrary magnitude of asymmetry.

To illustrate the reasons behind, as well as the appearance of the behaviour of asymmetric eigenmodes, we expand upon the mechanical analogy introduced by Allcock and Erdélyi (2017). Representing the pressure gradient and the magnetic forces in each domain with a system of coupled springs can reproduce many of the main features of the asymmetric eigenmodes. Both the waves guided by the slab, and their mechanical representation, may oscillate in phase, resulting in quasi-kink oscillations of an asymmetric slab; or the oscillations might happen in anti-phase, resulting in quasi-kink modes of a slab waveguide. This analogy highlights an interesting, although in practice, possibly rare case that becomes possible due to having competing, asymmetric forces in the two external plasma regions. Namely, an asymmetric slab system might show oscillations with symmetric perturbations at the boundaries, even though it is not a symmetric waveguide that supports the

waves. We call these special oscillations quasi-symmetric modes, and we revisit their magneto-seismological importance later, in Chapter 5.

After providing a couple of examples of numerical solutions illustrating the relation between the wavenumbers and angular frequencies of the eigenmodes supported by an asymmetric slab system with a particular ordering of characteristic speeds, we conduct a parametric investigation of the influence that (a) density or (b) magnetic asymmetry has on the phase speeds of eigenmodes. By focusing on slow surface eigenmodes of the asymmetric magnetic slab system, we show that any changes in the magnitudes of density and/or magnetic asymmetry result in a change of phase speeds and transverse velocity distributions of the guided oscillations, specifically, in a manner so that the phase speeds of quasi-sausage and quasi-kink waves perform avoided crossings. We show that while in the absence of external magnetic fields, the closest approach between the phase speeds of the two modes happens when the external densities are set to be symmetric, this is not the case when asymmetric magnetic fields are also present in the environment. Similarly, the presence of symmetric magnetic fields alone is not enough to ensure the occurrence of the closest phase speed approach, either.

Our findings presented here become relevant for the rest of the Chapters as well. Mathematically, it is the full and decoupled dispersion relations derived here that any further calculations until and including Chapter 5 will be based upon. From an observational point of view, the insights gained in this Chapter about the behaviour of asymmetric eigenmodes is indispensable e.g. when we apply the model to various solar environments and describe the waves we might expect to observe (see Chapter 4), or when we define quantities of solar magneto-seismological interest in Chapter 5.

Chapter 3

In this Chapter, we present a detailed theoretical (analytical and numerical) analysis of the eigenmodes supported by various asymmetric magnetic slab systems. The aim of this Chapter is to understand the behaviour of the asymmetric magneto-acoustic waves in limiting cases of e.g. slab width or plasma- β parameters, so that more complex cases may be constructed from these building blocks, and applications to the solar atmosphere may be suggested.

In general, we find that most of the waves supported by an asymmetric magnetic slab have equivalents either in an asymmetric non-magnetic slab, or in a symmetric magnetic slab system. Following methods similar to those employed by Edwin and Roberts (1982), we provide approximate expressions for the angular frequencies of waves in the thin- and wide-slab limits, and we point out how they are connected to their symmetric equivalents, when those exist.

We then proceed to provide expansion for magnetic slab systems filled with low- or high- β plasmas all throughout. This is motivated by some simpler possible applications, as the photosphere and the corona of the Sun are considered high- and low- β environments, respectively. Since they are both parts of the complex, dynamic coupled system that is the solar atmosphere, and they both possess numerous smaller-scale structures, it seems almost inevitable that asymmetric configurations should occur in both of these atmospheric layers.

For the ease of calculations, we present simplified dispersion relations for the extreme cases of infinite and zero plasma- β s, as well as the incompressible limit,

before we proceed to provide numerical solutions to the full dispersion relation under various possible characteristic speed orderings within both the high- and low- β regimes.

We conclude that both surface- and body modes of the slab are affected by the presence of magnetic and plasma asymmetries. However, this dependence appears directly in the case of approximations we provided for the surface modes, while it is only featured indirectly for body mode solutions, through introducing new and different cut-off frequencies as compared to the symmetric case.

Chapter 4

In Chapter 4, we summarise six possible applications of an asymmetric magnetic slab configuration for the purposes of modelling solar atmospheric waveguides. All of the structures within the solar atmosphere that we describe in this Chapter have already been shown to function as guiding environments for various waves, and we provide a brief overview of these earlier findings in each Section.

Firstly, we put forward two global applications of the model to the layers of the solar atmosphere. In both cases, we examine what physical scales or wavelengths a slab approximation might be appropriate for, before we detail the results of the applications. The first environment we approximate with an asymmetric magnetic slab system is that of the photosphere–interface region–corona system. Due to the large differences between the background parameters throughout this system, there are only limited phase speed bands in which trapped oscillations may exist. We find that some waves in this model may become leaky only on one interface, the one between the interface region and the photosphere. This is, however, a result that should be re-investigated in a more complex model that incorporates the small scale heights within the photosphere and therefore the substantial density increase that the current model cannot take into account. To refine this application somewhat further, we also investigate the types of wave expected to propagate in the chromosphere – transition region – corona system.

Next, we describe two coronal applications of the model. First, we consider the boundary regions of coronal holes and plumes as low- β asymmetric magnetic slab system. Next, the same application is carried out for a prominence and its asymmetric environment of coronal plasma. A richer variety of waves is found to be able to propagate in these configurations. However, we also establish that in practice, we should be careful about what wavelength or slab width regimes we accept the results for when we employ thin- or wide-slab approximations of these waveguides.

Last but not least, two lower atmospheric applications are discussed in the form of light bridges and magnetic bright points. Light bridges separating two, not necessarily symmetric umbral cores and MBPs wedged inside the intergranular lanes, the two sides of which are connected to separate granules, both are particularly illustrative examples of asymmetric configurations occurring in the solar atmosphere. Since the information available on light bridges and light walls, we examine various plasma- β values that might describe the plasma inside them, as well as in the sunspot umbrae in their environment. The variety of trapped oscillations possible within these light bridge systems is shown to be vastly different depending on the choice of plasma- β regime, even for similar general magnitudes of characteristic speeds.

MBPs are a recurring topic of this study, as some of them show elongated forms and can be approximated as magnetic slab systems. The static asymmetric magnetic slab model applied in this Chapter shows that under a wide range of characteristic speed orderings, MBPs may only guide surface modes.

Chapter 5

In Chapter 5, we revisit the description we gave of quasi-sausage, quasi-kink and quasi-symmetric oscillations of asymmetric magnetic slab waveguides in Chapter 2. The effects that the asymmetric background has on the appearance of the modes is utilised to generalise the techniques of solar magneto-seismology described by Allcock and Erdélyi (2017). We derive expressions for the amplitude ratios and minimum perturbation shifts of both quasi-kink and quasi sausage modes. The general expressions are then subjected to e.g. thin-slab approximations, which lets us arrive at formulae which we can invert and rearrange for the internal Alfvén speed of the slab system.

In practice, this means that measuring wave parameters (periods and wavenumbers), observing information about the spatial distribution of wave power, and combining them with e.g. density information lets us use these formulae to estimate a parameter of a solar atmospheric waveguide (the Alfvén speed) which might be difficult to measure directly.

In addition, the quasi-symmetric waves are also revisited, and they lead us to a relationship between the wave- and external plasma parameters that may also be used for estimations of missing characteristic speeds. Finally, we carry out a brief analytical and numerical investigation of the effect that different sources of asymmetry (density or magnetic) has on the amplitude ratio and minimum perturbation shift parameters. This concludes our study of propagating waves in an asymmetric magnetic slab system.

7.2.2 Standing Waves in Asymmetric Slab Waveguides

Chapter 6

We take a brief detour from propagating waves and “close down” the top and bottom part of the previously infinite slab models in the z -direction to examine standing waves in Chapter 6. Just like their propagating counterparts, standing waves are also expected to occur in various asymmetric solar waveguides, such as prominences or MBPs. This provides the motivation for deriving the dispersion relations for standing waves of asymmetric slabs in first a non-magnetic, and then a magnetic environment. Formally, these relations are analogous to those describing their propagating counterparts. However, as the slabs supporting standing waves are under line-tying boundary conditions at their top and bottom, the wavenumbers are now quantised and depend on the height of the slab.

We employ the thin slab and weak asymmetry approximations to derive analytical expressions for the frequencies of the harmonics of slow surface quasi-sausage and quasi kink waves in both cases, first for a slab in an asymmetric non-magnetic environment, and then for one in an isothermal, asymmetric magnetic environment. These frequencies are then used to construct the frequency ratio of the fundamental mode to the first harmonic in each case, and show the dependence of this quantity

on the asymmetry present in the system. We also derive expressions for the difference of oscillation amplitudes on either side of the slab, and in the case of the non-magnetic environment, the difference of the oscillation amplitude from the symmetric case as well. These are all parameters of solar magneto-seismological interest, as they describe observable parameters in terms of the equilibrium quantities and their asymmetries present in the system.

Of both theoretical and observational interest is the fact that, as we show in this Chapter, for the frequency and amplitude differences of quasi-sausage oscillations from their symmetric counterparts, the prediction of the Rayleigh-Riz technique hold true, and the amplitudes of the waves (which are of interest to methods of spatial seismology) are more sensitive to asymmetries added to the system than the frequencies (which are of interest to methods of temporal seismology).

7.3 Asymmetric Slab Waveguides and Their Applications in Solar Magneto-Seismology

As it has been mentioned in the introduction, the two universally utilised fundamental building blocks of modelling solar atmospheric structures are flux tubes and slabs filled with plasmas of various kinds and often permeated by magnetic fields. Depending on the exact structure under investigation, however, we generally want to introduce additional elements into these models which will bring them closer to realistic solar structures. These additional elements might come into play in what framework is chosen, eg. focusing on linear or nonlinear wave phenomena, ignoring or incorporating dissipation effects, or in setting up discontinuities or gradients within the starting configuration, and even in varying the geometry to a certain extent. These steps sacrifice some of the simplicity of calculations both on the analytical and on the numerical side, in the hopes of the advantage of reflecting the physical characteristics of and phenomena within the solar plasma more accurately.

The family of slab models presented in this study takes the avenue of preserving simplicity in the interactions of the plasma and the magnetic field, as well as the geometry, and introducing “complications” in the distribution of plasma parameters within the model (at least, compared to its classical, symmetric predecessors). These choices determine both the strengths and the weaknesses of the asymmetric slab family. Although a major advantage of slab models is their versatility when it comes to applications, as demonstrated in Chapter 4, still, whichever asymmetric slab system we choose for modelling a solar atmospheric structure, there will always be limitations to consider, too. Firstly, there is a shortcoming common to all infinite flux tube and slab models, symmetric (Roberts (1981b); Edwin and Roberts (1982); Edwin and Roberts (1983)) and asymmetric (Allcock and Erdélyi (2017); Zsámberger et al. (2018); Allcock et al. (2019)) ones alike: our Sun, and therefore the features of its atmosphere as well, are all finite.

This discrepancy is possible to mitigate if we decide to close the “top” and “bottom” of the slab (Joarder and Roberts (1992a); Oxley et al. (2020a); Oxley et al. (2020b)) or tube (McEwan et al. (2006)), as it is done when studying standing waves. This approach closes the tube fully, and it leaves one direction in which a slab can still be considered unbounded. As it was illustrated in the previous Chapters, this limitation definitely has to be taken into account when comparing our theoretical expectations to any observational results, and various solar waveguides

will have to be considered thin or wide slabs (or tubes) depending on the observed wavelengths of oscillations.

A further question to be considered is whether the part of the solar atmosphere we aim to model shows significant gravitational stratification or not. As demonstrated in Chapter 4, a slab model can serve as a basic first approximation of gravitational stratification on large scales, such as in the case of the global atmospheric layers or in that of prominences. However, as we pointed out in the relevant sections, the reality is that even within these solar structures, there can be significant stratification. In these cases, as well as in various other structures, the plasma and magnetic parameters in the solar atmosphere actually go through a continuous change, and not a sharp jump, like in the classical flux tubes or slabs. In the setting of the solar atmosphere, the presence of these transitions and various driving forces provide plenty of opportunities to transform wave energy through processes such as resonant absorption or phase mixing (Priest (2014); Erdélyi and Nelson (2016b)), which also fell outside the scope of the current study, which based itself on linear MHD theory.

From the above discussion it is clear that the analytical tractability and numerical simplicity of asymmetric slab models does limit their applications. However, our studies of the past few years suggest that they still represent an important step in understanding solar wave phenomena. Thanks to the initial assumptions and the series of approximations made throughout the Chapters of this thesis, it has become possible to generalise the quasi-sausage and quasi-kink modes described by Allcock and Erdélyi (2017). We have been able to investigate the amplitudes and minimum perturbations shifts of asymmetric eigenmodes, as well as their relation to the asymmetric plasma parameters and magnetic fields present in the environment of the slab. The process allowed us to describe avoided crossings and to understand the changes in the character of the MHD waves guided by certain solar structures as the width of their central (slab) region or their plasma- β parameter is changed. Throughout this work, we have specifically focused on diving into the details of the various effects on the frequencies, amplitudes, and transverse displacement distributions of eigenfunctions that are caused by incorporating asymmetry into classical slab models. As the solar atmosphere itself is a highly structured and dynamic environment, it seems reasonable to expect that perfectly symmetric features within it might not be the norm, but rather the exception.

Of course, introducing certain changes into the geometry of the model could also help capture additional physical effects that play an important role in the atmosphere of our star. Incorporating gradual transitions in place of the discontinuities of the asymmetric slab geometry could serve to further refine our understanding, now that we possess the fundamental building blocks. Another avenue of refinement could be extending the investigation to magnetic flux tube models. But the obvious choice of setting up an asymmetric or non-uniform background, in which a flux tube is embedded, involves unforeseen difficulties. To maintain total pressure balance in the equilibrium state of such a system, a parameter gradient would have to be both inside and outside the tube as well, which can easily lead to losing the analytical ease and physical clarity of the model.

Instead, a comparison between a flux tube surrounded by an annulus (see eg. Erdélyi and Carter (2006); Ruderman and Erdélyi (2009b)) and the asymmetric slab system could be made. However, they both still retain their ideal candidates for application in the solar atmosphere, in the form of structures with a circular

cross-section and elongated features, respectively. As the example of MBPs shows, sometimes the same solar structure can even have both appearances, and thus it can be approached with different models. Once more, specifically in the case of MBPs, a transitional step between the strictly cylindrical or Cartesian models could be that of the elliptical flux tube (Erdélyi and Morton (2009); Aldhafeeri et al. (2021)).

Overall, the Sun provides mathematical and physical minds with plenty of interesting and complicated structuring, due to the presence of both gravity and ubiquitous magnetic fields in its atmosphere. Deciphering the theory behind everything we can observe is a gargantuan task, and it can only be accomplished by carefully studying various minor and major building blocks. In this final discussion, we have provided a brief overlook of both the advantages and disadvantages of employing relatively simple flux tube or slab models. The aim of the asymmetric slab models described in this thesis was to be one such building block, and explore an aspect of solar waveguides not considered in this form before: the effect of background asymmetry on the well-known symmetric eigenmodes of MHD waveguides. However, even this one topic provides such a rich problem that there are still plenty of tasks to accomplish when it comes to studying asymmetric structures and the MHD waves propagating through them.

7.4 Future Aims

There are numerous ways to further develop the family of Cartesian multi-layered waveguide models. We have carried out a fairly exhaustive study of the rich problem of the static slab placed in an asymmetric magnetic environment. We have calculated frequency and amplitude ratios of standing and propagating modes for applications in solar magneto-seismology, and we have also suggested various solar environments to be considered as slab-like configurations. However, so far it has been outside the scope of this research to carry out a full practical application. For an externally non-magnetic asymmetric slab system, Allcock et al. (2019) applied their model to chromospheric fibrils and obtained estimates of the local Alfvén speed. A logical next step is to use the parameters defined in the previous Chapters and conduct a similar investigation. A comparison can be made between Alfvén speed estimates determined using externally magnetic or non-magnetic configurations as well. Furthermore, as the spatio-temporal resolution of telescopes keeps improving, new applications of the model become possible. In this Thesis, we have proposed to consider elongated MBPs as a slab environment, and we expect that e.g. DKIST observations can have the required sensitivity to resolve some MBPs, thus allowing us to use the methods of spatial seismology described here.

On the theoretical side, the next big leap in the generalisation of asymmetric Cartesian waveguide models is to carry out a detailed investigation of the effects that incorporating bulk background flows into the system can have on propagating and standing waves. Some initial steps have been taken in this direction by Barbulescu and Erdélyi (2018) and Allcock et al. (2019), and it is the topic of my continued research as well. Introducing a steady flow in one or more layers of the slab system opens it up to the Kelvin-Helmholtz instability, and the various sources of asymmetry (kinetic, magnetic, flow) can influence the instability threshold of the KHI in different ways. These initial studies so far have all worked with a constant flow in a region of the slab system. Once these investigations are completed, a bigger

leap forward can be the study of different flow profiles in one or more regions of the slab system, rather than restricting our studies to constant flows in each layer of the waveguide.

Bibliography

- T. E. Abdelatif. Magneto-atmospheric waves. *Solar Phys.*, 129:201–219, Oct. 1990. doi: 10.1007/BF00159037.
- A. A. Aldhafeeri, G. Verth, W. Brevis, D. B. Jess, M. McMurdo, and V. Fedun. Magnetohydrodynamic Wave Modes of Solar Magnetic Flux Tubes with an Elliptical Cross Section. *Astrophys. J.*, 912(1):50, May 2021. doi: 10.3847/1538-4357/abec7a.
- M. Allcock and R. Erdélyi. Magnetohydrodynamic Waves in an Asymmetric Magnetic Slab. *Solar Phys.*, 292:35, Feb. 2017. doi: 10.1007/s11207-017-1054-y.
- M. Allcock and R. Erdélyi. Solar Magnetoseismology with Magnetoacoustic Surface Waves in Asymmetric Magnetic Slab Waveguides. *Astrophys. J.*, 855(2):90, Mar 2018. doi: 10.3847/1538-4357/aaad0c.
- M. Allcock, D. Shukhobodskaia, N. K. Zsámberger, and R. Erdélyi. Magnetohydrodynamic waves in multi-layered asymmetric waveguides: solar magneto-seismology theory and application. *Frontiers in Astronomy and Space Sciences*, 6:48, July 2019. doi: 10.3389/fspas.2019.00048.
- J. Andries, T. van Doorselaere, B. Roberts, G. Verth, E. Verwichte, and R. Erdélyi. Coronal Seismology by Means of Kink Oscillation Overtones. *Space Sci. Rev.*, 149: 3–29, Dec. 2009. doi: 10.1007/s11214-009-9561-2.
- I. Arregui. Wave heating of the solar atmosphere. *Philosophical Transactions of the Royal Society of London Series A*, 373:20140261–20140261, Apr. 2015. doi: 10.1098/rsta.2014.0261.
- I. Arregui and J. L. Ballester. Damping Mechanisms for Oscillations in Solar Prominences. *Space Sci. Rev.*, 158(2-4):169–204, July 2011. doi: 10.1007/s11214-010-9648-9.
- I. Arregui and M. Goossens. No unique solution to the seismological problem of standing kink magnetohydrodynamic waves. *Astron. Astrophys.*, 622:A44, Feb. 2019. doi: 10.1051/0004-6361/201833813.
- I. Arregui, R. Oliver, and J. L. Ballester. Prominence Oscillations. *Living Reviews in Solar Physics*, 9:2, Apr. 2012. doi: 10.12942/lrsp-2012-2.
- M. Aschwanden. *Physics of the Solar Corona*. Springer-Verlag, Berlin Heidelberg, 2005.
- M. J. Aschwanden, L. Fletcher, C. J. Schrijver, and D. Alexander. Coronal Loop Oscillations Observed with the Transition Region and Coronal Explorer. *Astrophys. J.*, 520(2):880–894, Aug 1999. doi: 10.1086/307502.

- E. H. Avrett and R. Loeser. Models of the Solar Chromosphere and Transition Region from SUMER and HRTS Observations: Formation of the Extreme-Ultraviolet Spectrum of Hydrogen, Carbon, and Oxygen. *The Astrophysical Journal Supplement Series*, 175(1): 229–276, Mar. 2008. doi: 10.1086/523671.
- D. Banerjee, R. Erdélyi, R. Oliver, and E. O’Shea. Present and Future Observing Trends in Atmospheric Magnetoseismology. *Solar Phys.*, 246:3–29, Nov. 2007. doi: 10.1007/s11207-007-9029-z.
- M. Barbulescu and R. Erdélyi. Magnetoacoustic Waves and the Kelvin-Helmholtz Instability in a Steady Asymmetric Slab. I: The Effects of Varying Density Ratios. *Solar Phys.*, 293(6):86, Jun 2018. doi: 10.1007/s11207-018-1305-6.
- T. E. Berger, C. J. Schrijver, R. A. Shine, T. D. Tarbell, A. M. Title, and G. Scharmer. New Observations of Subarcsecond Photospheric Bright Points. *Astrophys. J.*, 454:531, Nov. 1995. doi: 10.1086/176504.
- D. Berghmans and F. Clette. Active region EUV transient brightenings - First Results by EIT of SOHO JOP80. *Solar Phys.*, 186:207–229, May 1999. doi: 10.1023/A:1005189508371.
- L. Bharti. Fine structure above a light bridge in the transition region and corona. *Mon. Not. Roy. Astron. Soc.*, 452:L16–L20, Sept. 2015. doi: 10.1093/mnrasl/slv071.
- J. M. Borrero and K. Ichimoto. Magnetic Structure of Sunspots. *Living Reviews in Solar Physics*, 8(1):4, Sept. 2011. doi: 10.12942/lrsp-2011-4.
- B. Bovelet and E. Wiehr. Dynamics of the solar active region finestructure. *Astron. Astrophys.*, 412:249–255, Dec. 2003. doi: 10.1051/0004-6361:20031305.
- P. J. Bushby. Magnetic fields in the solar photosphere. *Philosophical Transactions of the Royal Society of London Series A*, 366(1884):4465–4476, Dec. 2008. doi: 10.1098/rsta.2008.0158.
- M. Carlsson, V. H. Hansteen, B. De Pontieu, S. McIntosh, T. D. Tarbell, D. Shine, S. Tsuneta, Y. Katsukawa, K. Ichimoto, Y. Suematsu, T. Shimizu, and S. Nagata. Can High Frequency Acoustic Waves Heat the Quiet Sun Chromosphere? *Pub. Astron. Soc. Japan*, 59:S663–S668, Nov. 2007. doi: 10.1093/pasj/59.sp3.S663.
- B. K. Carter and R. Erdélyi. Sausage and kink oscillations in incompressible annular magnetic cylinders. *Astron. Astrophys.*, 475:323–331, Nov. 2007. doi: 10.1051/0004-6361:20077160.
- P. J. Crockett, M. Mathioudakis, D. B. Jess, S. Shelyag, F. P. Keenan, and D. J. Christian. The Area Distribution of Solar Magnetic Bright Points. *Astrophys. J. Lett.*, 722:L188–L193, Oct. 2010. doi: 10.1088/2041-8205/722/2/L188.
- M. Cuntz, W. Rammacher, and Z. E. Musielak. Acoustic Heating of the Solar Chromosphere: Present Indeed and Locally Dominant. *Astrophys. J. Lett.*, 657:L57–L60, Mar. 2007. doi: 10.1086/512973.
- I. De Moortel. An overview of coronal seismology. *Philosophical Transactions of the Royal Society of London Series A*, 363:2743–2760, Dec. 2005. doi: 10.1098/rsta.2005.1665.
- I. de Moortel. Longitudinal Waves in Coronal Loops. *Space Sci. Rev.*, 149(1-4):65–81, Dec 2009. doi: 10.1007/s11214-009-9526-5.

- I. De Moortel and V. M. Nakariakov. Magnetohydrodynamic waves and coronal seismology: an overview of recent results. *Philosophical Transactions of the Royal Society of London Series A*, 370:3193–3216, July 2012. doi: 10.1098/rsta.2011.0640.
- B. De Pontieu and R. Erdélyi. The nature of moss and lower atmospheric seismology. *Philosophical Transactions of the Royal Society of London Series A*, 364:383–394, Feb. 2006. doi: 10.1098/rsta.2005.1704.
- B. De Pontieu, R. Erdélyi, and S. P. James. Solar chromospheric spicules from the leakage of photospheric oscillations and flows. *Nature*, 430:536–539, July 2004. doi: 10.1038/nature02749.
- B. De Pontieu, R. Erdélyi, and I. De Moortel. How to Channel Photospheric Oscillations into the Corona. *Astrophys. J. Lett.*, 624:L61–L64, May 2005. doi: 10.1086/430345.
- B. De Pontieu, V. H. Hansteen, L. Rouppe van der Voort, M. van Noort, and M. Carlsson. High-Resolution Observations and Modeling of Dynamic Fibrils. *Astrophys. J.*, 655(1): 624–641, Jan. 2007a. doi: 10.1086/509070.
- B. De Pontieu, S. W. McIntosh, M. Carlsson, V. H. Hansteen, T. D. Tarbell, C. J. Schrijver, A. M. Title, R. A. Shine, S. Tsuneta, Y. Katsukawa, K. Ichimoto, Y. Suematsu, T. Shimizu, and S. Nagata. Chromospheric Alfvénic Waves Strong Enough to Power the Solar Wind. *Science*, 318:1574, Dec. 2007b. doi: 10.1126/science.1151747.
- C. E. DeForest and J. B. Gurman. Observation of Quasi-periodic Compressive Waves in Solar Polar Plumes. *Astrophys. J. Lett.*, 501:L217–L220, July 1998. doi: 10.1086/311460.
- A. Devaquet. Avoided crossings in photochemistry. *Pure and Applied Chemistry*, 41: 455–473, 1975. doi: 10.1351/pac197541040455. URL <http://dx.doi.org/10.1351/pac197541040455>.
- P. M. Edwin and B. Roberts. Wave propagation in a magnetically structured atmosphere. III - The slab in a magnetic environment. *Solar Phys.*, 76:239–259, Mar. 1982. doi: 10.1007/BF00170986.
- P. M. Edwin and B. Roberts. Wave Propagation in a Magnetic Cylinder. *Solar Phys.*, 88: 179–191, Oct. 1983. doi: 10.1007/BF00196186.
- R. Erdélyi. Magnetic coupling of waves and oscillations in the lower solar atmosphere: can the tail wag the dog? *Philosophical Transactions of the Royal Society of London Series A*, 364:351–381, Feb. 2006a. doi: 10.1098/rsta.2005.1703.
- R. Erdélyi. Magnetic seismology of the lower solar atmosphere. In *Proceedings of SOHO 18/GONG 2006/HELAS I, Beyond the spherical Sun*, volume 624 of *ESA Special Publication*, page 15.1, Oct. 2006b.
- R. Erdélyi and B. K. Carter. Wave propagation in incompressible MHD wave guides: the twisted magnetic Annulus. *Astron. Astrophys.*, 455(1):361–370, Aug. 2006. doi: 10.1051/0004-6361:20064926.
- R. Erdélyi and V. Fedun. Are There Alfvén Waves in the Solar Atmosphere? *Science*, 318:1572, Dec. 2007. doi: 10.1126/science.1153006.

- R. Erdélyi and R. J. Morton. Magnetohydrodynamic waves in a compressible magnetic flux tube with elliptical cross-section. *Astron. Astrophys.*, 494(1):295–309, Jan. 2009. doi: 10.1051/0004-6361:200810318.
- R. Erdélyi and C. J. Nelson. On The Role of MHD Waves in Heating Localised Magnetic Structures. In I. Dorotovic, C. E. Fischer, and M. Temmer, editors, *Coimbra Solar Physics Meeting: Ground-based Solar Observations in the Space Instrumentation Era*, volume 504 of *Astronomical Society of the Pacific Conference Series*, page 153, Apr. 2016a.
- R. Erdélyi and C. J. Nelson. On The Role of MHD Waves in Heating Localised Magnetic Structures. In I. Dorotovic, C. E. Fischer, and M. Temmer, editors, *Coimbra Solar Physics Meeting: Ground-based Solar Observations in the Space Instrumentation Era*, volume 504 of *Astronomical Society of the Pacific Conference Series*, page 153, Apr. 2016b.
- ESA. Anatomy of our Sun, 2019. URL https://www.esa.int/ESA_Multimedia/Images/2019/10/Anatomy_of_our_Sun.
- T. Felipe, M. Collados, E. Khomenko, C. Kuckein, A. Asensio Ramos, H. Balthasar, T. Berkefeld, C. Denker, A. Feller, M. Franz, A. Hofmann, J. Joshi, C. Kiess, A. Lagg, H. Nicklas, D. Orozco Suárez, A. Pastor Yabar, R. Rezaei, R. Schlichenmaier, D. Schmidt, W. Schmidt, M. Sigwarth, M. Sobotka, S. K. Solanki, D. Soltau, J. Staude, K. G. Strassmeier, R. Volkmer, O. von der Lühe, and T. Waldmann. Three-dimensional structure of a sunspot light bridge. *Astron. Astrophys.*, 596:A59, Nov. 2016. doi: 10.1051/0004-6361/201629586.
- A. Fossum and M. Carlsson. Detectability of High Frequency Acoustic Waves with TRACE. In H. Lacoste, editor, *SOHO 13 Waves, Oscillations and Small-Scale Transients Events in the Solar Atmosphere: Joint View from SOHO and TRACE*, volume 547 of *ESA Special Publication*, page 125, Jan. 2004.
- A. Fossum and M. Carlsson. Detectability of high frequency acoustic waves with TRACE. In A. Hanslmeier, A. Veronig, and M. Messerotti, editors, *Solar Magnetic Phenomena*, volume 320 of *Astrophysics and Space Science Library*, pages 239–242, 2005.
- H. Goedbloed and S. Poedts. *Principles of Magnetohydrodynamics*. Cambridge University Press, Cambridge, 2004.
- J. P. H. Goedbloed and S. Poedts. *Principles of Magnetohydrodynamics. With Applications to Laboratory and Astrophysical Plasmas*. Cambridge University Press, Cambridge, New York, 2004.
- L. Golub and J. M. Pasachoff. *The Solar Corona*. 2009.
- M. Goossens, A. de Groof, and J. Andries. Waves and oscillations in magnetic fields. In *SOLMAG 2002. Proceedings of the Magnetic Coupling of the Solar Atmosphere Euro-conference*, volume 505, pages 137–144, Oct. 2002.
- M. Goossens, J. Terradas, J. Andries, I. Arregui, and J. L. Ballester. On the nature of kink MHD waves in magnetic flux tubes. *Astron. Astrophys.*, 503(1):213–223, Aug. 2009. doi: 10.1051/0004-6361/200912399.
- M. Goossens, R. Erdélyi, and M. S. Ruderman. Resonant MHD Waves in the Solar Atmosphere. *Space Science Reviews*, 158(2):289–338, Jul 2011. ISSN 1572-9672. doi: 10.1007/s11214-010-9702-7. URL <https://doi.org/10.1007/s11214-010-9702-7>.

- S. R. Habbal, T. E. Holzer, and E. Leer. Heating of Coronal Loops by Fast Mode Mhd-Waves. In E. Jensen, P. Maltby, and F. Q. Orrall, editors, *IAU Colloq. 44: Physics of Solar Prominences*, page 228, Jan 1979.
- V. H. Hansteen and M. Carlsson. *The Solar Atmosphere*, volume 778, page 129. 2009.
- W. D. Heiss and A. L. Sannino. Avoided level crossing and exceptional points. *Journal of Physics A: Mathematical and General*, 23(7):1167, 1990. URL <http://stacks.iop.org/0305-4470/23/i=7/a=022>.
- A. Hillier and A. van Ballegooijen. On the Support of Solar Prominence Material by the Dips of a Coronal Flux Tube. *Astrophys. J.*, 766(2):126, Apr. 2013. doi: 10.1088/0004-637X/766/2/126.
- Y. J. Hou, T. Li, S. H. Yang, and J. Zhang. Light walls around sunspots observed by the Interface Region Imaging Spectrograph. *Astron. Astrophys.*, 589:L7, May 2016. doi: 10.1051/0004-6361/201628216.
- N. E. Hurlburt, D. Alexander, and A. M. Rucklidge. Complete Models of Axisymmetric Sunspots: Magnetoconvection with Coronal Heating. *Astrophys. J.*, 577(2):993–1005, Oct. 2002. doi: 10.1086/342154.
- D. B. Jess, M. Mathioudakis, R. Erdélyi, P. J. Crockett, F. P. Keenan, and D. J. Christian. Alfvén Waves in the Lower Solar Atmosphere. *Science*, 323:1582, Mar. 2009. doi: 10.1126/science.1168680.
- R. L. Jiang, K. Shibata, H. Isobe, and C. Fang. Fan-shaped Jets in Three-dimensional Reconnection Simulation as a Model of Ubiquitous Solar Jets. *Astrophys. J. Lett.*, 726(2):L16, Jan. 2011. doi: 10.1088/2041-8205/726/2/L16.
- P. S. Joarder and B. Roberts. The modes of oscillation of a prominence. I - The slab with longitudinal magnetic field. *Astron. Astrophys.*, 256:264–272, Mar. 1992a.
- P. S. Joarder and B. Roberts. The modes of oscillation of a prominence. II - The slab with transverse magnetic field. *Astron. Astrophys.*, 261:625–632, Aug. 1992b.
- P. S. Joarder and B. Roberts. The modes of oscillation of a prominence. III. The slab in a skewed magnetic field. *Astron. Astrophys.*, 277:225, Sept. 1993.
- P. H. Keys, M. Mathioudakis, D. B. Jess, S. Shelyag, D. J. Christian, and F. P. Keenan. Tracking magnetic bright point motions through the solar atmosphere. *Mon. Not. Roy. Astron. Soc.*, 428:3220–3226, Feb. 2013. doi: 10.1093/mnras/sts268.
- E. Khomenko and M. Collados. Oscillations and waves in sunspots. *Living Reviews in Solar Physics*, 12(1):6, 2015. ISSN 1614-4961. doi: 10.1007/lrsp-2015-6. URL <http://dx.doi.org/10.1007/lrsp-2015-6>.
- L. Kleint, P. Antolin, H. Tian, P. Judge, P. Testa, B. De Pontieu, J. Martínez-Sykora, K. K. Reeves, J. P. Wuelser, S. McKillop, S. Saar, M. Carlsson, P. Boerner, N. Hurlburt, J. Lemen, T. D. Tarbell, A. Title, L. Golub, V. Hansteen, S. Jaeggli, and C. Kankelborg. Detection of Supersonic Downflows and Associated Heating Events in the Transition Region above Sunspots. *Astrophys. J. Lett.*, 789(2):L42, July 2014. doi: 10.1088/2041-8205/789/2/L42.
- J. Kohl and S. Crammer. *Coronal Holes and Solar Wind Acceleration*. Springer Science and Business Media, Dordrecht, 2013.

- R. Komm, I. De Moortel, Y. Fan, S. Ilonidis, and O. Steiner. Sub-photosphere to Solar Atmosphere Connection. *Space Sci. Rev.*, 196:167–199, Dec. 2015. doi: 10.1007/s11214-013-0023-5.
- A. Lagg, S. K. Solanki, M. van Noort, and S. Danilovic. Vigorous convection in a sunspot granular light bridge. *Astron. Astrophys.*, 568:A60, Aug. 2014. doi: 10.1051/0004-6361/201424071.
- C. Liu, Y. Xu, W. Cao, N. Deng, J. Lee, H. S. Hudson, D. E. Gary, J. Wang, J. Jing, and H. Wang. Flare differentially rotates sunspot on Sun’s surface. *Nature Communications*, 7:13104, Oct. 2016. doi: 10.1038/ncomms13104.
- Y. Liu, Y. Xiang, R. Erdélyi, Z. Liu, D. Li, Z. Ning, Y. Bi, N. Wu, and J. Lin. Studies of Isolated and Non-isolated Photospheric Bright Points in an Active Region Observed by the New Vacuum Solar Telescope. *Astrophys. J.*, 856:17, Mar. 2018. doi: 10.3847/1538-4357/aab150.
- J. T. Mariska. The quiet solar transition region. *Annual Rev. Astron. Astrophys.*, 24:23–48, Jan. 1986. doi: 10.1146/annurev.aa.24.090186.000323.
- J. F. Mather and R. Erdélyi. Magneto-acoustic waves in a gravitationally stratified magnetized plasma: Eigen-solutions and their applications to the solar atmosphere. *The Astrophysical Journal*, 822(2):116, 2016. URL <http://stacks.iop.org/0004-637X/822/i=2/a=116>.
- M. Mathioudakis, D. B. Jess, and R. Erdélyi. Alfvén Waves in the Solar Atmosphere. From Theory to Observations. *Space Sci. Rev.*, 175:1–27, June 2013. doi: 10.1007/s11214-012-9944-7.
- M. P. McEwan, G. R. Donnelly, A. J. Díaz, and B. Roberts. On the period ratio $P_1/2P_2$ in the oscillations of coronal loops. *Astron. Astrophys.*, 460(3):893–899, Dec. 2006. doi: 10.1051/0004-6361:20065313.
- S. W. McIntosh, B. De Pontieu, M. Carlsson, V. Hansteen, P. Boerner, and M. Goossens. Alfvénic waves with sufficient energy to power the quiet solar corona and fast solar wind. *Nature*, 475:477–480, July 2011. doi: 10.1038/nature10235.
- R. J. Morton, G. Verth, D. B. Jess, D. Kuridze, M. S. Ruderman, M. Mathioudakis, and R. Erdélyi. Observations of ubiquitous compressive waves in the Sun’s chromosphere. *Nature Communications*, 3:1315, Dec. 2012. doi: 10.1038/ncomms2324.
- R. J. Morton, G. Verth, V. Fedun, S. Shelyag, and R. Erdélyi. Evidence for the Photospheric Excitation of Incompressible Chromospheric Waves. *Astrophys. J.*, 768:17, May 2013. doi: 10.1088/0004-637X/768/1/17.
- D. J. Mullan. *Physics of the Sun: A First Course*. Boca Raton, CRC Press, London, New York, 2009.
- V. M. Nakariakov. Magnetohydrodynamic waves in coronal polar plumes. *Philosophical Transactions of the Royal Society of London Series A*, 364:473–483, Feb. 2006. doi: 10.1098/rsta.2005.1711.
- V. M. Nakariakov and E. Verwichte. Coronal Waves and Oscillations. *Living Reviews in Solar Physics*, 2:3, May 2005. doi: 10.12942/lrsp-2005-3.

- V. M. Nakariakov, L. Ofman, E. E. Deluca, B. Roberts, and J. M. Davila. TRACE observation of damped coronal loop oscillations: Implications for coronal heating. *Science*, 285:862–864, Aug. 1999. doi: 10.1126/science.285.5429.862.
- K. R. Naqvi and W. B. Brown. The non-crossing rule in molecular quantum mechanics. *International Journal of Quantum Chemistry*, 6(2):271–279, 1972. ISSN 1097-461X. doi: 10.1002/qua.560060206. URL <http://dx.doi.org/10.1002/qua.560060206>.
- G. Newkirk, Jr. and J. Harvey. Coronal Polar Plumes. *Solar Phys.*, 3:321–343, Feb. 1968. doi: 10.1007/BF00155166.
- G. Nisticò, V. Polito, V. M. Nakariakov, and G. Del Zanna. Multi-instrument observations of a failed flare eruption associated with MHD waves in a loop bundle. *Astron. Astrophys.*, 600:A37, Apr. 2017. doi: 10.1051/0004-6361/201629324.
- L. Novotny. Strong coupling, energy splitting, and level crossings: A classical perspective. *American Journal of Physics*, 78(11):1199–1202, 2010. doi: 10.1119/1.3471177. URL <http://dx.doi.org/10.1119/1.3471177>.
- L. Ofman, V. M. Nakariakov, and C. E. DeForest. Slow Magnetosonic Waves in Coronal Plumes. *Astrophys. J.*, 514:441–447, Mar. 1999. doi:10.1086/306944.
- L. Ofman, V. M. Nakariakov, and N. Sehgal. Dissipation of Slow Magnetosonic Waves in Coronal Plumes. *Astrophys. J.*, 533:1071–1083, Apr. 2000. doi: 10.1086/308691.
- R. Oliver. Prominence Seismology Using Small Amplitude Oscillations. *Space Sci. Rev.*, 149(1-4):175–197, Dec. 2009. doi: 10.1007/s11214-009-9527-4.
- W. Oxley, N. K. Zsámberger, and R. Erdélyi. Standing MHD Waves in a Magnetic Slab Embedded in an Asymmetric Plasma Environment: Slow Surface Waves. *Astrophys. J.*, 890(2):109, Feb. 2020a. doi: 10.3847/1538-4357/ab67b3.
- W. Oxley, N. K. Zsámberger, and R. Erdélyi. Standing MHD Waves in a Magnetic Slab Embedded in an Asymmetric Magnetic Plasma Environment: Surface Waves. *Astrophys. J.*, 898(1):19, July 2020b. doi: 10.3847/1538-4357/ab9639.
- G. Poletto. Solar Coronal Plumes. *Living Reviews in Solar Physics*, 12(1):7, Dec. 2015. doi: 10.1007/lrsp-2015-7.
- E. Priest. *Magnetohydrodynamics of the Sun*. Cambridge University Press, Cambridge, 2014.
- N. E. Raouafi, J. W. Harvey, and S. K. Solanki. Properties of Solar Polar Coronal Plumes Constrained by Ultraviolet Coronagraph Spectrometer Data. *Astrophys. J.*, 658(1): 643–656, Mar. 2007. doi: 10.1086/510286.
- B. Roberts. Wave propagation in a magnetically structured atmosphere. I - Surface waves at a magnetic interface. *Solar Phys.*, 69:27–38, Jan. 1981a. doi: 10.1007/BF00151253.
- B. Roberts. Wave Propagation in a Magnetically Structured Atmosphere - Part Two - Waves in a Magnetic Slab. *Solar Phys.*, 69:39–56, Jan. 1981b. doi: 10.1007/BF00151254.
- B. Roberts. The creation of fine structure by magnetic fields. *Advances in Space Research*, 4:17–27, Jan. 1984. doi: 10.1016/0273-1177(84)90361-2.

- B. Roberts, P. M. Edwin, and A. O. Benz. On coronal oscillations. *Astrophys. J.*, 279: 857–865, Apr. 1984. doi: 10.1086/161956.
- H. Rosenberg. Evidence for MHD Pulsations in the Solar Corona. *Astron. Astrophys.*, 9: 159, Nov. 1970.
- L. H. M. Rouppe van der Voort, V. H. Hansteen, M. Carlsson, A. Fossum, E. Marthinussen, M. J. van Noort, and T. E. Berger. Solar magnetic elements at 0.1 arcsec resolution. II. Dynamical evolution. *Astron. Astrophys.*, 435:327–337, May 2005. doi: 10.1051/0004-6361:20042561.
- M. S. Ruderman and R. Erdélyi. Transverse Oscillations of Coronal Loops. *Space Sci. Rev.*, 149:199–228, Dec. 2009a. doi: 10.1007/s11214-009-9535-4.
- M. S. Ruderman and R. Erdélyi. Transverse Oscillations of Coronal Loops. *Space Sci. Rev.*, 149(1-4):199–228, Dec. 2009b. doi: 10.1007/s11214-009-9535-4.
- M. Ryutova. The “Magnetosonic Streaming”. *Astrophysical Letters and Communications*, 34:71, 1996.
- J. Sánchez Almeida, I. Márquez, J. A. Bonet, I. Domínguez Cerdeña, and R. Müller. Bright Points in the Internetwork Quiet Sun. *Astrophys. J. Lett.*, 609:L91–L94, July 2004. doi: 10.1086/422752.
- E. Scullion, R. Erdélyi, and J. G. Doyle. Waves in the Transition Region. *Astrophysics and Space Science Proceedings*, 19:426–428, 2010.
- D. Shukhobodskaya and R. Erdélyi. Propagation of Surface Magnetohydrodynamic Waves in Asymmetric Multilayered Plasma. *Astrophys. J.*, 868(2):128, Dec. 2018. doi: 10.3847/1538-4357/aae83c.
- M. Sobotka, M. Švanda, J. Jurčák, P. Heinzel, D. Del Moro, and F. Berrilli. Dynamics of the solar atmosphere above a pore with a light bridge. *Astron. Astrophys.*, 560:A84, Dec. 2013. doi: 10.1051/0004-6361/201322148.
- S. K. Solanki, B. Inhester, and M. Schüssler. The solar magnetic field. *Reports on Progress in Physics*, 69(3):563–668, Mar. 2006. doi: 10.1088/0034-4885/69/3/R02.
- S. K. Solanki, P. Barthol, S. Danilovic, A. Feller, A. Gandorfer, J. Hirzberger, T. L. Riethmüller, M. Schüssler, J. A. Bonet, V. Martínez Pillet, J. C. del Toro Iniesta, V. Domingo, J. Palacios, M. Knölker, N. Bello González, T. Berkefeld, M. Franz, W. Schmidt, and A. M. Title. SUNRISE: Instrument, Mission, Data, and First Results. *Astrophys. J. Lett.*, 723:L127–L133, Nov. 2010. doi: 10.1088/2041-8205/723/2/L127.
- Y. Taroyan and R. Erdélyi. Heating Diagnostics with MHD Waves. *Space Sci. Rev.*, 149: 229–254, Dec. 2009. doi: 10.1007/s11214-009-9506-9.
- J. O. Thurgood, R. J. Morton, and J. A. McLaughlin. First Direct Measurements of Transverse Waves in Solar Polar Plumes Using SDO/AIA. *Astrophys. J. Lett.*, 790:L2, July 2014. doi: 10.1088/2041-8205/790/1/L2.
- A. Tritschler, T. R. Rimmele, S. Berukoff, R. Casini, S. C. Craig, D. F. Elmore, R. P. Hubbard, J. R. Kuhn, H. Lin, J. P. McMullin, K. P. Reardon, W. Schmidt, M. Warner, and F. Woger. DKIST: Observing the Sun at High Resolution. In G. T. van Belle and H. C. Harris, editors, *18th Cambridge Workshop on Cool Stars, Stellar Systems, and the Sun*, volume 18 of *Cambridge Workshop on Cool Stars, Stellar Systems, and the Sun*, pages 933–944, Jan. 2015.

BIBLIOGRAPHY

- Y. Uchida. Propagation of Hydromagnetic Disturbances in the Solar Corona and Moreton's Wave Phenomenon. *Solar Phys.*, 4:30–44, May 1968. doi: 10.1007/BF00146996.
- Y. Uchida. Diagnosis of Coronal Magnetic Structure by Flare-Associated Hydromagnetic Disturbances. *Pub. Astron. Soc. Japan*, 22:341, 1970.
- D. Utz, A. Hanslmeier, C. Möstl, R. Müller, A. Veronig, and H. Muthsam. The size distribution of magnetic bright points derived from Hinode/SOT observations. *Astron. Astrophys.*, 498:289–293, Apr. 2009. doi: 10.1051/0004-6361/200810867.
- M. Vazquez. A Morphological Study of the Light-Bridges in Sunspots. *Solar Phys.*, 31: 377–387, Aug. 1973. doi: 10.1007/BF00152814.
- P. Venkatakrisnan. Inhibition of convective collapse of solar magnetic flux tubes by radiative diffusion. *Nature*, 322:156, July 1986. doi: 10.1038/322156a0.
- T. Wang. Standing Slow-Mode Waves in Hot Coronal Loops: Observations, Modeling, and Coronal Seismology. *Space Sci. Rev.*, 158:397–419, July 2011. doi: 10.1007/s11214-010-9716-1.
- T. Wang, D. E. Innes, and J. Qiu. Determination of the Coronal Magnetic Field from Hot-Loop Oscillations Observed by SUMER and SXT. *Astrophys. J.*, 656(1):598–609, Feb. 2007. doi: 10.1086/510424.
- T. J. Wang and S. K. Solanki. Vertical oscillations of a coronal loop observed by TRACE. *Astron. Astrophys.*, 421:L33–L36, July 2004. doi: 10.1051/0004-6361:20040186.
- S. Wedemeyer-Böhm, O. Steiner, J. Bruls, and W. Rammacher. What is Heating the Quiet-Sun Chromosphere? In P. Heinzel, I. Dorotovič, and R. J. Rutten, editors, *The Physics of Chromospheric Plasmas*, volume 368 of *Astronomical Society of the Pacific Conference Series*, page Heinzel, May 2007.
- S. Wedemeyer-Böhm, E. Scullion, O. Steiner, L. Rouppe van der Voort, J. de La Cruz Rodriguez, V. Fedun, and R. Erdélyi. Magnetic tornadoes as energy channels into the solar corona. *Nature*, 486:505–508, June 2012. doi: 10.1038/nature11202.
- E. Wiehr, B. Bovelet, and J. Hirzberger. Brightness and size of small-scale solar magnetic flux concentrations. *Astron. Astrophys.*, 422:L63–L66, July 2004. doi: 10.1051/0004-6361:200400019.
- S. Yang, J. Zhang, F. Jiang, and Y. Xiang. Oscillating light wall above a sunspot light bridge. *The Astrophysical Journal Letters*, 804(2):L27, 2015. URL <http://stacks.iop.org/2041-8205/804/i=2/a=L27>.
- S. Yang, J. Zhang, and R. Erdélyi. Enhancement of a Sunspot Light Wall with External Disturbances. *Astrophys. J.*, 833(2):L18, Dec 2016. doi: 10.3847/2041-8213/833/2/L18.
- S. Yang, J. Zhang, R. Erdélyi, Y. Hou, X. Li, and L. Yan. Sunspot Light Walls Suppressed by Nearby Brightenings. *Astrophys. J.*, 843(1):L15, Jul 2017. doi: 10.3847/2041-8213/aa7b2c.
- D. Yuan and R. W. Walsh. Abnormal oscillation modes in a waning light bridge. *Astron. Astrophys.*, 594:A101, Oct. 2016. doi: 10.1051/0004-6361/201629258.

- D. Yuan, V. M. Nakariakov, Z. Huang, B. Li, J. Su, Y. Yan, and B. Tan. Oscillations in a Sunspot with Light Bridges. *Astrophys. J.*, 792(1):41, Sep 2014. doi: 10.1088/0004-637X/792/1/41.
- T. V. Zaqarashvili and R. Erdélyi. Oscillations and Waves in Solar Spicules. *Space Sci. Rev.*, 149:355–388, Dec. 2009. doi: 10.1007/s11214-009-9549-y.
- N. K. Zsámberger and R. Erdélyi. Magnetoacoustic Waves in a Magnetic Slab Embedded in an Asymmetric Magnetic Environment. II. Thin and Wide Slabs, Hot and Cold Plasmas. *Astrophys. J.*, 894(2):123, May 2020. doi: 10.3847/1538-4357/ab8791.
- N. K. Zsámberger and R. Erdélyi. Magnetoacoustic Waves in a Magnetic Slab Embedded in an Asymmetric Magnetic Environment. III. Applications to the Solar Atmosphere. *Astrophys. J.*, 906(2):122, Jan. 2021. doi: 10.3847/1538-4357/abca9d.
- N. K. Zsámberger and R. Erdélyi. Solar magneto-seismology of a magnetic slab in an asymmetric magnetic environment. *Astrophys. J.*, 2022. [submitted].
- N. K. Zsámberger, M. Allcock, and R. Erdélyi. Magneto-acoustic Waves in a Magnetic Slab Embedded in an Asymmetric Magnetic Environment: The Effects of Asymmetry. *Astrophys. J.*, 853:136, Feb. 2018. doi: 10.3847/1538-4357/aa9ffe.